Fault Reactivation And Rock Deformation Mechanisms Under Stress/Pressure Cycling

Naderloo, M.

DOI
10.4233/uuid:ee8d984b-26d6-4cec-a354-95131cbb3c17

Publication date
2024

Document Version
Final published version

Citation (APA)
Naderloo, M. (2024). *Fault Reactivation And Rock Deformation Mechanisms Under Stress/Pressure Cycling*. [Dissertation (TU Delft), Delft University of Technology]. https://doi.org/10.4233/uuid:ee8d984b-26d6-4cec-a354-95131cbb3c17

FAULT REACTIVATION AND ROCK DEFORMATION MECHANISMS UNDER STRESS/PRESSURE CYCLING

FAULT REACTIVATION AND ROCK DEFORMATION MECHANISMS UNDER STRESS/PRESSURE CYCLING

Proefschrift

ter verkrijging van de graad van doctor
aan de Technische Universiteit Delft,
op gezag van de Rector Magnificus prof. ir. T.H.J.J. van der Hagen,
voorzitter van het College voor Promoties,
in het openbaar te verdedigen op vrijdag, 13 september 2024 om 12:30 uur

door

Milad NADERLOO

Master of Science in Mining Engineering-Rock Mechanics,
University of Tehran, Tehran, Iran,

geboren te Abhar, Iran.

Dit proefschrift is goedgekeurd door de

Samenstelling promotiecommissie:

Rector Magnificus	voorzitter
Dr. A. Barnhoorn	Technische Universiteit Delft
Prof. dr. ir. J.D. Jansen	Technische Universiteit Delft
Onafhankelijke leden:	
Prof. dr. H. Hajibeygi	Technische Universiteit Delft
Dr. A. R. Niemeijer	Universiteit Utrecht
Dr. A. Kushnir	Swiss Federal Institute of Technology Lausanne
Prof. dr. R. M. Holt	Norwegian University of Science and Technology
Dr. ir. D. Draganov	Technische Universiteit Delft
Prof. dr. S. Geiger,	Technische Universiteit Delft, reservelid

This thesis is part of the project 'Science4Steer: A Scientific Basis for Production and Reinjection Strategies to Minimize Induced Seismicity in Dutch Gas Fields' (project number DEEP.NL.2018.046) under the research programme 'DeepNL,' funded by the Dutch Research Council (NWO).

Keywords: Induced Seismicity, Cyclic Injection, Underground Energy Storage, Seismicity Mitigation, Rock Deformation, Acoustic Emission, Fault Reactivation, Fault Offset

Printed by: Gildeprint

Front & Back: Pictures by Marieke de Lorijn

ISBN 978-94-6384-624-0

An electronic version of this dissertation is available at
http://repository.tudelft.nl/.

Dedicated to my late father

This too shall pass.

Contents

SUMMARY

Addressing climate change and transitioning to renewable energy will involve subsurface activities like carbon storage, geothermal exploitation, and underground energy storage. However, fluid injection and extraction in the subsurface can alter the pressure, temperature, stress, and rock geochemistry, potentially leading to seismicity and subsidence. Understanding the mechanisms of fault reactivation and the geomechanical response of intact reservoir rock to variations in pore fluid pressure from injection and depletion operations is thus crucial. In this thesis, we integrate our findings from multiple studies to explore the impact of parameters related to injection and depletion, such as pattern (monotonic, cyclic) and rate, on the deformation of intact reservoir rock, slip behaviour in faulted reservoir rock, and the evolution of microseismicity, with a focus on how we can mitigate induced seismicity.

Our experimental investigations employ uniaxial compressive tests on intact Red Felser sandstone samples, subjecting them to cyclic recursive (CR), cyclic progressive (CP), and monotonic stress patterns at varying stress rates. The recording of Acoustic Emission (AE) waveforms revealed that cyclic stress patterns, especially CP, are characterized by lower maximum AE amplitudes compared to the monotonic pattern. By reducing the stress rate, the maximum AE energy and final mechanical strength both decrease significantly. Moreover, high-stress rates were found to alter the AE signature of events, suggesting that cyclic stress patterns combined with low-stress rates may mitigate induced seismicity in subsurface injection operations.

For underground energy storage, we investigate the geomechanical response of Red Felser sandstone to cyclic loading, crucial for safe and efficient underground porous reservoir operations. Experimental results, complemented by constitutive modeling, revealed various deformation mechanisms, including linear elastic, viscoelastic, and inelastic responses. Our study shows that the magnitude of inelastic deformations is influenced by mean stress, amplitude, and frequency of the stress waveform, with our models closely fitting the experimental data.

As part of our investigation into mitigating induced seismicity, we examine how stress and sliding patterns affect fault slip behaviour and seismicity evolution. To achieve this we carry out displacement-driven fault reactivation experiments on saw-cut Red Felser sandstones. Our results indicated that cyclic sliding, compared to continuous sliding, reduces seismicity but can accelerate slip velocity during the reloading phase due to the healing of gouge material on the fault plane. Additionally, under-threshold cycling effectively prevents seismicity and shear slip but poses a risk of increased seismicity if shear stress exceeds critical levels.

Furthermore, we explore the influence of injection pattern and rate on fault reactivation in porous Red Felser sandstone. High injection rates were linked to increased slip velocity and seismicity. Furthermore, our results from samples subjected to various injection patterns demonstrate that the cyclic recursive pattern exhibits a higher maximum slip velocity, more episodes of slow slip, and greater radiated AE energy than a monotonic pattern. A proper injection strategy must consider fault drainage, critical shear stress, injection rate, and injection pattern. Our results demonstrate that a monotonic injection pattern and low pressurization rate may mitigate seismicity on pre-existing faults in a highly permeable porous reservoir.

Finally, we investigate the fault slip nucleation within a displaced fault system. Our triaxial experiments on displaced faults reveal that differential compaction intensifies from the top of the sample towards the internal corner at the centre of the fault, indicating a variation in the stress field surrounding the fault plane. Our direct measurements near the displaced fault plane confirm the anomalies and peaks in stress observed in previous numerical and analytical studies.

This thesis offers new insights into the mechanical behaviour and seismicity evolution of intact and faulted reservoir rocks under variations in stress patterns and rates. These findings may contribute to mitigating injection-induced seismicity in intact and porous faulted rock settings. Furthermore, they enhance our understanding of the behaviour of deep geo-reservoirs subjected to diverse injection strategies, thereby expanding our knowledge of reservoir-related phenomena.

SAMENVATTING

Om klimaatverandering tegen te gaan en over te schakelen op hernieuwbare energie zijn activiteiten in de ondergrond nodig zoals koolstofopslag, geothermische exploitatie en ondergrondse energieopslag. Vloeistofinjectie en -extractie in de ondergrond kunnen echter de druk, temperatuur, spanning en geochemie van het gesteente veranderen, wat kan leiden tot aardbevingen en bodemdaling. Het is dus van cruciaal belang om de mechanismen van reactivering van breuken en de geomechanische respons van intact reservoirgesteente op variaties in de poriënvloeistofdruk als gevolg van injectie en depletie te begrijpen. Dit proefschrift integreert de bevindingen van meerdere studies om de invloed te onderzoeken van parameters gerelateerd aan injectie en depletie, zoals patroon (monotoon, cyclisch) en snelheid, op de vervorming van intact reservoirgesteente, slipgedrag in verbreukt reservoirgesteente en de ontwikkeling van microseismiciteit, met de nadruk op hoe we geïnduceerde seismiciteit kunnen beperken.

Onze experimentele onderzoeken bestonden uit eenassige drukproeven op intacte monsters van Red Felser zandsteen, waarbij ze werden onderworpen aan cyclisch recursieve (CR), cyclisch progressieve (CP) en monotone spanningspatronen bij variërende spanningsgroeisnelheden. Het opnemen van akoestische emissie (AE) golfvormen toonde aan dat cyclische spanningspatronen, vooral CP, gekenmerkt worden door lagere maximale AE amplitudes. Een significante afname van de maximale AE-energie en de uiteindelijke mechanische sterkte werd waargenomen bij lagere spanningsgroeisnelheden. Bovendien bleek dat hoge spanningsgroeisnelheden de AE-signatuur van gebeurtenissen veranderden, wat suggereert dat cyclische spanningspatronen in combinatie met lage spanningssnelheden geïnduceerde seismiciteit bij injectieactiviteiten in de ondergrond kunnen verminderen.

Op het gebied van ondergrondse energieopslag onderzochten we de geomechanische respons van Red Felser zandsteen op cyclische belasting, cruciaal voor veilige en efficiënte ondergrondse poreuze reservoiroperaties. Experimentele resultaten, aangevuld met constitutieve modellering, onthulden verschillende vervormingsmechanismen, waaronder lineair-elastische, visco-elastische en inelastische reacties. Het onderzoek toonde aan dat cyclische inelastische vervormingen worden beïnvloed door de gemiddelde spanning, amplitude en frequentie van de spanningsgolfvorm, waarbij onze modellen nauw aansluiten bij de experimentele gegevens.

Als onderdeel van ons onderzoek naar het verminderen van geïnduceerde seismiciteit, onderzochten we hoe spannings- en glijpatronen het slipgedrag van breuken en de seismiciteitsevolutie beïnvloeden. Om dit te bereiken hebben we verplaatsingsgedreven breukreactiveringsexperimenten uitgevoerd op doorgezaagde Red Felser zandsteenmonsters. De resultaten gaven aan dat cyclisch glijden, in vergelijking met continu glijden, de seismiciteit vermindert, maar de glijsnelheid tijdens de herlaadfase kan versnellen door het helen van gutsmateriaal op het breukvlak. Bovendien voorkomt cyclisch glijden onder de drempelwaarde effectief seismiciteit en pure afschuiving, maar brengt het risico van verhoogde seismiciteit met zich mee als de afschuifspanning de kritische niveaus overschrijdt.

Verder onderzochten we de invloed van het injectiepatroon en de injectiesnelheid op de reactivering van breuken in poreus rood Felser zandsteen. Hoge injectiesnelheden werden in verband gebracht met een verhoogde glijsnelheid en seismiciteit. Bovendien laten de resultaten van monsters die werden onderworpen aan verschillende injectiepatronen zien dat het cyclische recursieve patroon een hogere maximale slipsnelheid, meer episodes van langzame slip en meer uitgestraalde AE-energie vertoont dan een monotoon patroon. Een goede injectiestrategie moet rekening houden met de drainage van de breuk, de kritische schuifspanning, de injectiesnelheid en het injectiepatroon. Onze resultaten tonen aan dat een monotoon injectiepatroon en een lage drukgroeisnelheid seismiciteit op reeds bestaande breuken in een zeer doorlatend poreus reservoir kunnen verminderen.

Tot slot onderzocht en we de detail van glijgedrag binnen een verplaatst breuksysteem. Triaxiale experimenten op verplaatste breuken toonden aan dat differentiële compactie toeneemt vanaf de bovenkant van het monster naar de binnenhoek in het midden van de breuk, wat duidt op een variatie in het spanningsveld rond het breukvlak. Onze directe metingen in de buurt van het verplaatste breukvlak bevestigen de anomalieën en spanningspieken die in eerdere numerieke en analytische studies zijn waargenomen.

Deze studie biedt nieuwe inzichten in het mechanische gedrag en de seismiciteitsevolutie van intacte en verbreukte reservoirgesteenten onder variaties in spanningspatronen en -groeisnelheden. Deze bevindingen kunnen bijdragen aan het verminderen van seismiciteit door injectie in intact en poreus gesteente met breuken. Bovendien vergroten ze ons begrip van het gedrag van diepe georeservoirs die worden blootgesteld aan verschillende injectiestrategieën, waardoor onze kennis van reservoirgerelateerde fenomenen wordt uitgebreid.

1

INTRODUCTION

1

1.1. MOTIVATION

Reaching the Paris Agreement's target of limiting global temperature rise to below 2.0 °C, preferably below 1.5 °C, necessitates reaching net-zero emissions by 2050 (Renné, 2022). This ambitious goal can only be realized through a combination of various strategies. The International Energy Agency highlights that up to 20–30% of the total reduction in CO_2 emissions could be attributed to subsurface solutions (Hasanbeigi et al., 2012; Ürge-Vorsatz et al., 2007). Key contributions include geological carbon sequestration, geothermal energy exploitation, and underground energy storage (Barbier, 2002; Birkholzer et al., 2009; Naderloo et al., 2023). As renewable energy sources are intermittent, they do not always align with real-time energy requirements, which underscores the importance of subsurface energy storage (Panwar et al., 2011). Therefore, storing surplus energy and retrieving it during periods of high demand is crucial. Due to their limited capacity, traditional batteries are not wholly sufficient for this purpose (Bauer et al., 2017). Alternative methods like underground hydrogen storage, Compressed Air Energy Storage (CAES), or Aquifer Thermal Energy Storage (ATES) are therefore anticipated to be pivotal in enhancing energy storage efficiency (see Figure 1.1) (Bauer et al., 2013).

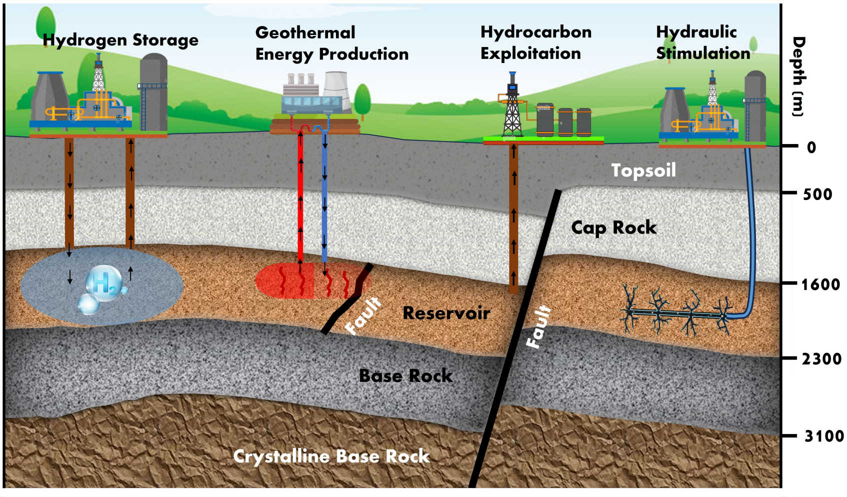

Figure 1.1: Various industrial activities that involve fluid injection and extraction, which can cause subsidence and induce seismicity by reactivating preexisting faults or creating large fractures resulting from hydraulic stimulation.

The potential drawbacks of geo-energy activities arise from the fact that injecting or withdrawing fluids from underground formations can alter pore pressure, temperature, stress conditions, and the geochemical properties of the reservoir rock. These changes can destabilize fractures or preexisting faults, potentially triggering seismic events (Keranen & Weingarten, 2018b; Kisslinger, 1976). Additionally, pore pressure fluctuations can induce subsidence and uplifting, with severity depending on magnitude and spatial gradient (Benetatos et al., 2020). Consequently, two major concerns associated with subsurface activities are the compromise of structural integrity and the disruption of daily life, affecting ongoing and future projects. Understanding the mechanisms of fault reactivation and the geomechanical response of intact reservoir rock to variations in pore fluid pressure from injection and depletion operations is thus crucial.

1.2. RESERVOIR-ROCK DEFORMATION MECHANISM

Geological formations, such as porous reservoirs and salt caverns, have proved to be a good option for storing energy-rich or energy-carrier fluids, such as compressed air, hot water, and hydrogen (Amid et al., 2016; Menéndez et al., 2019; Ramesh Kumar et al., 2021). Porous media, like depleted gas reservoirs, can provide significantly more storage capacity in different locations. All underground energy storage methods, including compressed air energy storage and hydrogen storage, involve cyclic loading due to the sequence of production and injection operations. Thus, understanding the geomechanical behavior of porous reservoir rock under cyclic loading is essential for designing and operating underground storages.

1.2.1. BRITTLE DEFORMATION OF SANDSTONE

In most rock deformation studies, inelastic behavior is observed as either brittle or ductile. Brittle deformation involves substantial permanent strain with and without visible fractures, while ductile behavior includes a range of mechanisms, like crystal plasticity and diffusional mass transfer, beyond mere fracturing (Paterson & Wong, 2005; Wong & Baud, 2012). Rock's transition from brittle faulting to ductile flow occurs under higher pressures and temperatures (Walton, 2021). The brittle-ductile transition also depends on the rock's initial porosity and its alteration under stress, which can either expand (dilatant) or shrink (compactant) the rock's volume (Brace, 1978; Wong & Baud, 2012).

As most potentially interesting depleted gas reservoirs for energy storage are located in shallower subsurface areas (not under high-stress regimes and temperatures), our research will primarily focus on brittle deformation. Numerous experimental researchers have studied sandstone's mechanical behavior and deformation processes under conventional deviatoric testing or triaxial compression in the brittle field (Baud et al., 2006; Brantut et al., 2013; Cai, 2010; Hoek, 1965; H. L. Wang et al., 2017). Typically, this behavior is represented through graphs plotting mean effective stress against total porosity reduction or deviatoric stress against axial deformation (Wong & Baud, 2012; Zhang et al., 2021). Figure 1.2 illustrates the four stages of Red Felser sandstone deformation, leading up to the point of maximum strength (Martin & Chandler, 1994; Pijnenburg et al., 2019):

1. Stage 1 (From Start to σ_{cc}): This stage demonstrates non-linear behavior, indicative of the closure of pre-existing cracks or damage, coupled with poro-elastic deformation.

2. Stage 2 (From σ_{cc} to σ_{bp}): The sandstone exhibits a near-linear response, typically considered as purely elastic (poroelastic) deformation. Elastic properties, such as Young's Modulus and Poisson's Ratio, are derived from this phase. Also, inelastic deformation can be identified at this stage.

3. Stage 3 (From σ_{bp} to σ_{cd}): In this stage, the sandstone begins to display non-linear

deformation, primarily due to the initiation and stable growth of new microcracks. The commencement of this stage, marked by σ_{bp}, is also referred to as the brittle yield point. The sample starts to expand beyond a certain stress threshold, marked by an inflection in the stress-strain curve.

4. Stage 4 (From σ_{cd} to σ_f): Here, the sandstone exhibits concave-down behavior, attributed to the emergence of grain crushing, unstable crack propagation, and the localization of shear cracks. Moreover, dilatancy becomes more pronounced at elevated stress levels than compaction behaviors.

5. Stage 5: As the stress continues to increase, it peaks (σ_f, representing sample strength), leading to the sample's failure through shear fractures. The macroscopic fracture originates from merging cracks that begin to expand from stage 4. Eventually, the stress reduces to a residual level, which is the stress required to slide along the formed fractures.

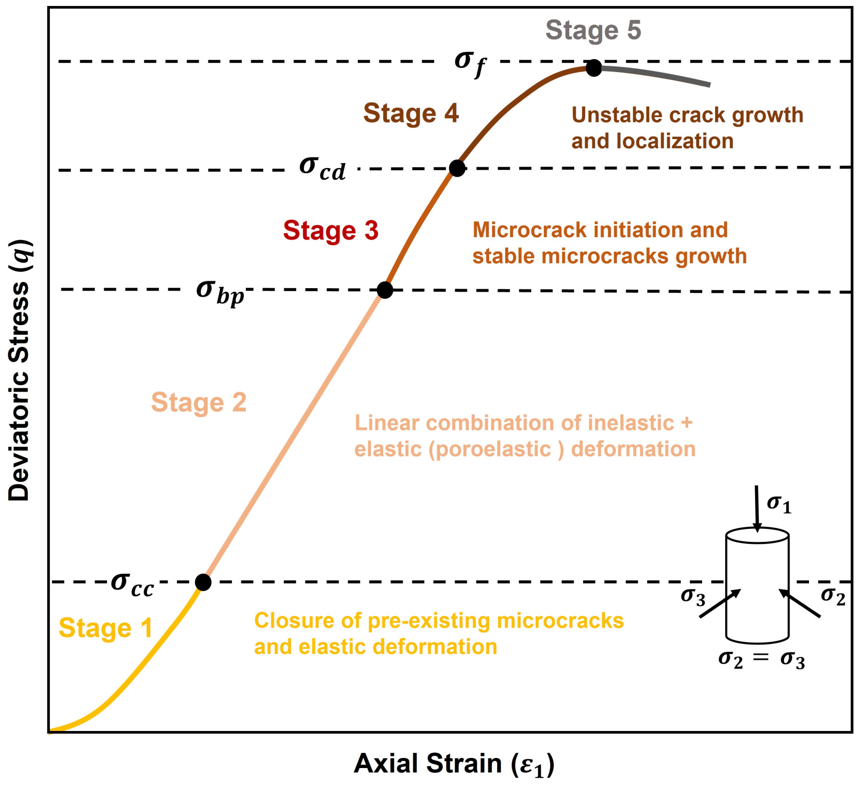

Figure 1.2: Typical stress-strain curve in the brittle field, illustrating the deformation stages of sandstone subject to constant confining pressure. Adopted from Martin and Chandler (1994) and Pijnenburg et al. (2019).

Among the various deformation stages, Stage 2 and the early phase of Stage 3 are particularly important for energy storage applications. This importance stems from the necessity of operating all energy storage systems below the yield point and within a safe zone (avoiding damage) (Naderloo et al., 2023). Adhering to these constraints is crucial to prevent failure and the accumulation of inelastic deformation. Recent and previous experimental studies have reported a significant contribution of inelastic deformation within stage 2, which is known as the fully elastic zone (Naderloo et al., 2023; Pijnenburg et al., 2019).

1.2.2. INELASTIC DEFORMATION IN THE LINEAR ZONE (STAGE 2)

Inelastic deformations of sandstone reservoirs can be translated as compaction of sandstone reservoirs. Compaction affects the stress path and alters the available elastic energy budget for seismic activity (Pijnenburg et al., 2018). While extensive research has been devoted to studying the elastic component, more comprehensive studies must be conducted on the occurrence of inelastic deformation in the linear zone (Baud et al., 2004; E. H. Rutter & Glover, 2012). In sandstone reservoirs, several inelastic deformation processes occur. These encompass: (1) microcracking along grain boundaries, (2) slipping between grains, (3) microcracking within and across grains, and (4) pressure solution at grain interfaces (Baud et al., 2006; Bernabe et al., 1994; Pijnenburg et al., 2018). In the stage 2 or linear regime inelastic strains are caused by intergranular fracturing, clay crushing and grain sliding. Higher initial porosity is known to favor these deformation mechanisms in sandstones (Pijnenburg et al., 2018; Vermeer, 1998). As a result, porous rocks do not necessarily exhibit a pure elastic regime. Pijnenburg et al. 2019 conducted triaxial cyclic experiments on Slochteren sandstone under reservoir conditions. Their results revealed that 30-50% of the total strain observed is inelastic, which includes the near-linear stage.

1.2.3. EFFECT OF CYCLIC STRESS ON RESERVOIR-ROCK DEFORMATION

In underground energy storage, if the rock behaves elastically, the pressure limits are expected to remain consistent over time, avoiding hysteresis on fault stress paths and allowing subsidence recovery (Heinemann et al., 2021). However, sandstone subjected to cyclic loading may accumulate inelastic deformation and damage, increasing with the number of cycles and affecting its mechanical, petrophysical, and acoustic properties (Taheri et al., 2016; H. L. Wang et al., 2017). The extent of this damage varies based on the stress level and cycle-related factors. Thus, it is crucial to focus on how the amplitude and frequency of these cycles and stress regimes influence deformation behavior both within and outside the elastic zone (stage 2 and 3, see Figure 1.2).

Few studies have focused on the effect of frequency of cycles on sandstone deformation (He et al., 2016; Peng et al., 2019, 2020). Peng et al. (2020) investigated the effect of loading frequency on the sandstone deformation under triaxial compression tests. Results showed that higher frequencies, by shortening load cycles, limited fracture development and increased rock strength, but low-frequency loading cycles led to more compact rock and reduced strength. Using three frequency settings (0.1, 1.0, and 10 Hz) under uniaxial cyclic loading tests on sandstone showed that frequency strongly influences the dynamic deformation and stiffness (Bagde & Petroš, 2005). Also, researchers studied the effect of the amplitude of cycles on the lifetime of sandstone. Taheri et al. (2016) demonstrated that in sandstone subjected to uniaxial loading conditions, damage increases with the amplification of unloading amplitude. Thus, the lifetime (before reaching yield point or brittle failure) of sandstone is shorter when the cycle amplitude is greater (Zhenyu & Haihong, 1990).

In addition, various research efforts have been directed toward understanding how the mechanical characteristics of reservoir sandstone change under diverse operational conditions (Geranmayeh Vaneghi et al., 2020; Liang et al., 2019; Peng et al., 2020; Sun et al., 2017). However, investigations into how parameters related to cyclic processes influence the measurement of inelastic deformation, particularly from an energy storage viewpoint, still need to be made available.

1.3. MECHANISMS OF INDUCED SEISMICITY

Induced seismicity, often called seismic activity caused by human actions, occurs due to alterations in subsurface stresses. These changes can be attributed to various processes, such as the injection or extraction of fluids, mining activities, and the creation of reservoirs. Four notable instances of induced seismicity include (i) a moment magnitude 5.4 earthquake in Pohang, South Korea, attributed to a geothermal energy project (Kim et al., 2018); (ii) a magnitude 5.7 earthquake in Oklahoma, US, linked to wastewater injection (Keranen & Weingarten, 2018a); (iii) three events exceeding magnitude 3 in Basel, Switzerland, during an Enhanced Geothermal Systems (EGS) project (Bachmann et al., 2012); and (iv) an increase in both frequency and magnitude of seismic events in the Groningen gas field, Netherlands, as a consequence of gas extraction (van Thienen-Visser & Breunese, 2015).

Indeed, as highlighted earlier, induced seismicity poses a significant risk in the context of subsurface projects and activities. Understanding the physical mechanisms responsible for initiating, propagating, and arresting fault slip is crucial for comprehending and managing this risk. Three primary mechanisms generate seismicity. The following sections provide detailed explanations of each mechanism and their key contributing factors (Doglioni, 2018).

1.3.1. INJECTION-DRIVEN FAULT REACTIVATION

The Mohr-Coulomb failure criterion and the effective stress law are most often used to describe shear failure in rocks. The Mohr-Coulomb criterion in the presence of pore pressure can be represented as follows (Hoek, 1990; Jaeger et al., 2009):

$$\tau_s = C + \mu(\sigma_n - p), \tag{1.1}$$

where τ_s is the shear strength of the fault plane, σ_n is the normal stress acting across the fault, C is cohesion, μ is the coefficient of friction, and p is pore pressure (note that we employ the rock mechanics convention in which positive normal stresses correspond to compression). Regarding equation 1.1, normal stress resolved on the fault plane decreases by increasing pore pressure. As a result of the increase in pore pressure, the Mohr circle shifts toward the failure envelope (see Figure 1.3a). Hence, a reduction in shear strength occurs during injection or pore pressure increase which causes fault reactivation (Kisslinger, 1976). Injection-induced fault reactivation is likely the most prevalent cause of induced seismic activity.

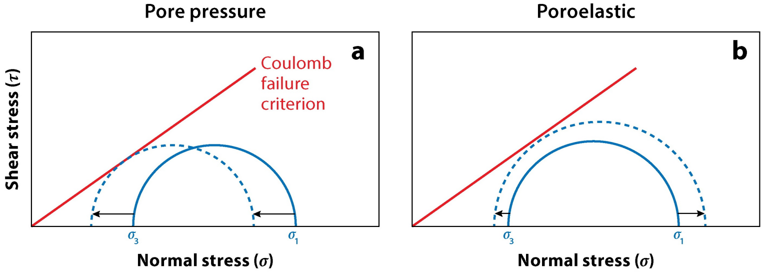

Figure 1.3: (a) Increasing fluid pressure reduces the effective normal stress resolved on the fault plane (shifting the Mohr circle toward the left). This reduction in shear resistance allows slip under tectonic shear stresses in the field. (b) Increasing differential stress in which Mohr circle become bigger and finally reactivation occurs (Keranen & Weingarten, 2018b).

1.3.2. PRODUCTION-INDUCED FAULT REACTIVATION

Fluid extraction causes the pore pressure to decrease, and, consequently, pore space in the rock reservoir is compressed or closed (Segall, 1985). Jin and Zoback (2015) and Segall (1985) proposed that the reactivation of normal faults around the reservoir is due to the stress path change caused by fluid extraction. Considering an anisotropic, porous, elastic reservoir with significantly smaller thickness than extensiveness, the horizontal total stress change (ΔS_{h}) due to a pore pressure change (ΔP_{p}) is described by the following equation (Addis, 1997; Chan & Zoback, 2007; Engelder & Fischer, 1994; Segall & Fitzgerald, 1998):

$$A = \frac{\Delta S_{\mathrm{hmin}}}{\Delta P_{\mathrm{p}}} = \alpha \frac{(1-2\nu)}{(1-\nu)}, \tag{1.2}$$

where α is the Biot coefficient, ν is Poisson's ratio, and A is the stress path. In uniaxial strain conditions (a thin reservoir in which the thickness of the reservoir is considerably smaller than its horizontal extension), the vertical total stress is assumed unchanged during depletion. Field operations such as hydraulic fracturing measurements show a decrease in minimum horizontal stresses, indicating stresses become more tensile with depletion (Addis, 1997). This poroelastic effect increases the differential stress and causes fault reactivation (see Figure 1.3b).

Also, Orlic and Wassing (2013) demonstrated the significance of reservoir geometry in the redistribution of stresses induced by fluid production. The presence of differential compaction in scenarios involving offset or displaced faults, combined with the superimposition of stress changes induced by external factors, is proposed to be a key factor in the reactivation of faults in seismic events triggered by production activities (Haug et al., 2018; Mulders, 2003; Yerkes & Castle, 1976). Differential compaction is associated with variations in total production, production rates, reservoir thicknesses, and elastic or poroelastic properties.

Analytical approaches (Jansen et al., 2019; Lehner, 2019) and numerical studies (Buijze et al., 2019; van Wees et al., 2018) showed that during production, the nucleation of slip along displaced faults starts from the internal corners of the reservoir/fault (see Figure 1.4). The initiation of slip nucleation at these corners is due to positive peak shear stresses, with two patches gradually growing towards the reservoir and merging with further depletion (see Figure 1.4). While numerous numerical and analytical studies address fault reactivation driven by production or injection in the context of displaced fault geometry (Buijze et al., 2019; Jansen et al., 2019; Lehner, 2019; van Wees et al., 2018), to our knowledge, no experimental work directly investigates fault reactivation and slip nucleation in such a displaced fault setting.

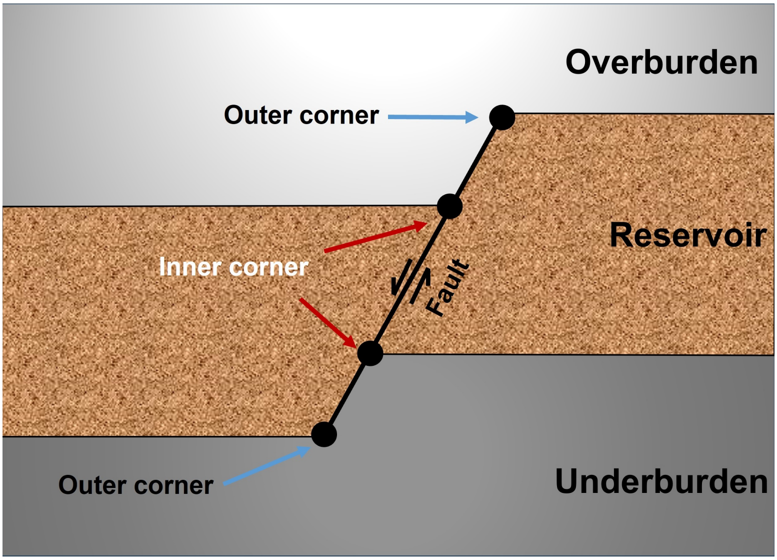

Figure 1.4: Schematic illustration of the displaced reservoir, including two inner and two outer corners.

1.3.3. HYDROFRACTURING (HYDRAULIC STIMULATION)

Induced seismicity is linked to hydraulic fracturing (HF) operations, which enhances the permeability and flow of fluids in tight (low permeable) reservoirs (Schultz et al., 2020). The HF process leads to new tensile failures and shearing along natural fractures (Rinaldi & Rutqvist, 2019). The generated fractures can cause earthquakes that are small in magnitude ($M_w < 0$) (Eaton et al., 2018). However, if the HF operation is performed close to preexisting faults, it can result in fault reactivation (Atkinson et al., 2020). The HF operation alters the equilibrium between effective normal and shear stresses on the preexisting fault, pushing it towards a failure state akin to injection-induced fault reactivation.

1.4. FAULT SLIP BEHAVIOUR

Fault reactivation can be explained by the Mohr-Coulomb failure criteria, which illustrate the threshold and required shear stress at a specific level or given normal stress to induce the start of slippage (Hoek, 1990; Jaeger et al., 2009). In essence, this criterion describes the strength of the fault plane. Friction along the fault interface (μ) can be measured as the ratio between the shear stress (τ) and the effective normal stress ($\sigma_n - P_p$):

$$\mu = \frac{\sigma_n - P_p}{\tau}, \tag{1.3}$$

with the shear stress, τ, defined as

$$\tau = \frac{\sigma_1 - \sigma_2}{2} \sin 2\theta. \tag{1.4}$$

And the normal stress, σ_n, described by the equation

$$\sigma_n = \frac{\sigma_1 + \sigma_2}{2} + \frac{\sigma_1 - \sigma_2}{2} \cos 2\theta. \tag{1.5}$$

where σ_1 and σ_3 represent the axial and confining pressure, respectively, and θ denotes the angle between the axial stress and the fault plane. The Mohr-Coulomb failure criterion is insufficient to explain the behavior of slip, whether it be stable or unstable sliding. Stable sliding refers to the steady, controlled movement of a fault, where any displacement results in a proportional and predictable response, without leading to sudden, large-scale slip events. In contrast, unstable sliding involves sudden, rapid movement along a fault, with decreased friction causing potential seismic events. In distinguishing stable from unstable movement, two key factors are considered: 1) the velocity-dependent characteristics of friction, specifically its evolution in response to a velocity change applied to the fault, and 2) the ability of the surrounding medium to store energy relative to the energy released by the fault, commonly linked to the discrepancy between the stiffness of the fault and that of the surrounding medium (note that in case of slip-weakening friction, the slope of the slip-weakening friction law alone determines the stability of the fault) (Chen et al., 2023; Linker & Dieterich, 1992; C. Noël et al., 2019; Rice, 1993; Rice & Ruina, 1983; Uenishi & Rice, 2003). This section provides a brief overview of the rate-and-state and spring-slider models, which are employed to differentiate the sliding behaviors of a fault.

The rate-and-state friction law (RSF) is widely applied to examine the behavior of fault slip post-reactivation. From the standpoint of RSF, the frictional behavior of the fault plane depends on the slip rate, state variables, and the loading history. By the RSF law, the subsequent equation illustrates the evolution of the frictional coefficient during slip (Dieterich, 1979; Ruina, 1983):

$$\mu = \mu_0 + a \ln\left(\frac{V}{V_0}\right) + b \ln\left(\frac{V_0 \theta}{D_c}\right), \tag{1.6}$$

where, considering the so-called slip law, the state variable θ evolution is expressed as

1

$$\frac{d\theta}{dt} = -\frac{V\theta}{D_c}\ln\left(\frac{V\theta}{D_c}\right). \tag{1.7}$$

Here, μ_0 represents the reference friction coefficient at velocity V_0, D_c denotes the critical slip distance, and V signifies the slip velocity. When $a - b > 0$, the friction exhibits rate-strengthening (or velocity strengthening) characteristics, allowing only stable sliding. Conversely, if $a - b < 0$, the friction is rate-weakening (or velocity weakening), potentially leading to dynamic instability in the fault (see Figure 1.5).

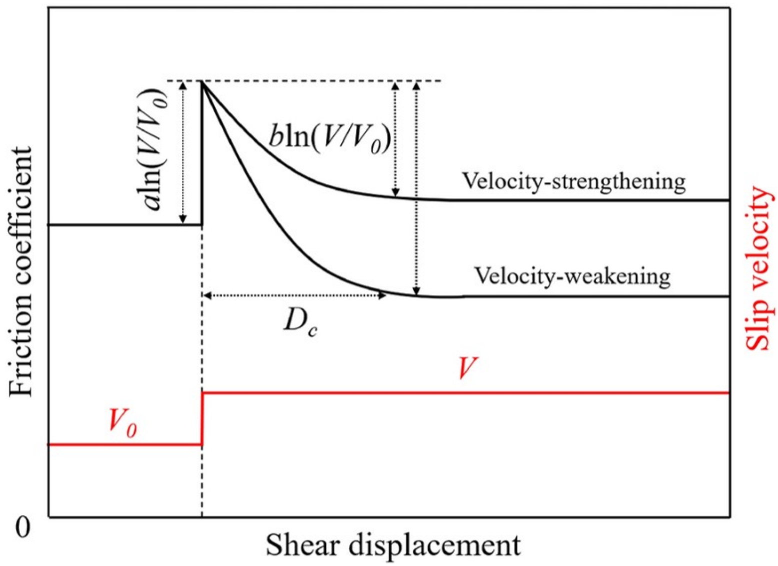

Figure 1.5: The schematic diagram for the rate and state friction law (Fang & Wu, 2022).

In situations involving rate-weakening (also known as velocity weakening), the stability of fault slip hinges on the medium's stiffness (K) relative to the fault's critical stiffness (K_{Fault}). In the spring-slider model, the fault is mimicked by a frictional surface under stress, connected to a spring that represents the medium's stiffness (K), (see Figure 1.6). The fault's own stiffness (K_{Fault}) is crucial: if K_{Fault} exceeds K, it leads to an unstable slip due to a rapid force decrease during fault loading. If K_{Fault} is less than K, the sliding remains stable, exhibiting either creep or no movement. This interplay results in stick-slip behavior, where the fault alternates between periods of stable sliding and sudden, unstable movements.

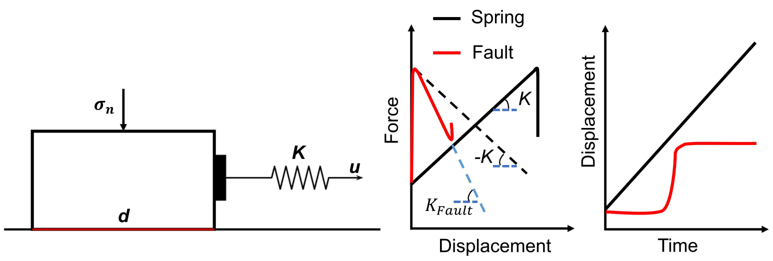

Figure 1.6: Illustrative sketch of the spring-slider model accompanied by characteristic mechanical graphs depicting unstable slip behavior. It includes both force-displacement and displacement-time graphs. The red lines illustrate the fault slip, while the black lines represent the spring's displacement (C. J.-M. R. Noël, 2021)

By integrating the rate-and-state friction methodology with a one-dimensional spring-slider model, the shift from stable to unstable slip is identifiable at a point of critical stiffness (Dieterich, 1979; Rice, 1993; Ruina, 1983):

$$K_c = \frac{(b-a)(\sigma_n - p_f)}{D_c} \tag{1.8}$$

If $a-b<0$ and $K>K_c$ the system is conditionally stable, however, if $a-b<0$ and $K<K_c$, the system is unstable.

1.5. MITIGATION STRATEGY

While most of the mechanisms that cause induced seismic events are well understood, few studies have focused on mitigating and reducing fluid-induced seismicity. For example, the aim can be to reduce the magnitude of the largest events triggered by fluid injection. It is essential to consider and investigate factors that can influence injection-induced seismicity, especially large-magnitude events. Various factors are believed to elevate the risk of large-magnitude seismic events (LMEs). These include operational parameters such as the volume, rate, and pressure of injections, along with permeability of the reservoir and geological aspects like in-situ stress, formation depth, and temperature, proximity to significant faults, and their orientation (McClure & Horne, 2014; Raleigh et al., 1976; Wilson et al., 2018). Although the precise interplay of these factors is not fully grasped, based on diverse studies and observations, several mitigation strategies have been proposed to reduce the seismic hazard concerns the probability of occurrence of large ground accelerations associated with fluid injection-induced seismicity (Hofmann et al., 2018). These strategies include:

1. **Low Seismic Risk Site Selection:** Choosing sites with minimal seismic risk is crucial. Such sites typically feature attenuating layers that dampen seismic waves and lack active fault zones in the current stress field. Examples of effective attenuating layers include thick sequences of unconsolidated sediments, clay-rich formations, and certain types of sedimentary rocks like shale. Lithologies that are particularly effective include claystone, siltstone, and certain limestone formations due to

their energy-absorbing properties. It is also important to select locations without critically stressed faults, or in simpler terms, areas that are not seismically active. (Kwiatek et al., 2010).

2. **Multi-stage Stimulation:** Instead of injecting large volumes of fluid into one part of the reservoir, spreading the injection across multiple stages in separate reservoir parts can reduce the risk of larger seismic events (Hofmann et al., 2018; Johri & Zoback, 2013; Zimmermann et al., 2015).

3. **Traffic Light Systems (TLS):** TLS involves adjusting fluid injection based on seismic magnitudes, peak ground velocities, or other factors. While standard in hydraulic stimulation treatments, their effectiveness varies, with some TLSs showing increased magnitudes after shut-in (Bachmann et al., 2011; Bommer et al., 2015; Hofmann et al., 2018).

4. **Advanced injection/production protocol:** Controlling the pressure, flow rate, fluid volume, fluid type, and the injection scheme can mitigate seismicity risks. Cyclic injection, where fluid injection alternates between active and paused phases, has shown potential in reducing seismicity (Zang et al., 2013).

Several experimental studies have focused on the fourth strategy (advanced injection protocol). Proposed solutions to mitigate and avoid larger induced earthquakes in different studies have been formulated such that the seismic response of cyclic fluid injection differs from the response to monotonic injection, thereby reducing induced seismicity (Patel et al., 2017; Yoon et al., 2014; Zang et al., 2013, 2019). Zang et al. (2019) concluded that by using cyclic injection (hydraulic fatigue), the magnitude of the largest induced seismic event can be reduced. Experiments on mine-scale hydraulic stimulation, employing three distinct injection patterns, revealed that a reduced rate of seismicity and lower maximum magnitudes mark the cyclic progressive scheme. Moreover, it exhibits significantly larger b-values, indicating a higher frequency of small events in comparison to larger ones (Niemz et al., 2020). In other words, cyclic injection increases the potential mechanism to replace big-magnitude events with many small ones (Niemz et al., 2020; Zang et al., 2019; Zhuang et al., 2020). Yet, it is noteworthy that the majority of studies proposing cyclic injection as a method for mitigating seismicity focus on intact rocks with low permeability.

Few experimental studies focus on the effect of injection patterns on seismicity mitigation in faulted rock medium (Ji, Yoon, et al., 2021; Ji, Zhuang, et al., 2021; C. Noël et al., 2019). Li et al. (2020) conducted an injection-induced fault reactivation test on a critically stressed natural fracture in granite to investigate the slip behaviour under cyclic and monotonic injection patterns (Ji, Yoon, et al., 2021; Ji, Zhuang, et al., 2021). When cyclic injection is conducted with a limited peak injection pressure, it induces aseismic fault slip at significantly lower peak slip rates compared to those observed during the monotonic injection. The more uniform reduction in effective normal stress caused by cyclic injection promotes gradual and stable fault slip, characterized by smaller peak slip rates (Ji, Yoon, et al., 2021). Cyclic fluid injection facilitates the diffusion of fluid pressure along faults. Yet, the decrease in seismic moment release hinges on various cycle-related elements, including the critical injection pressure and injection frequency (Ji, Zhuang, et al., 2021). Oscillating fluid pressure during a fault reactivation experiment on permeable sandstone promoted seismic behavior rather than aseismic slip. This was interpreted to be due to the alterations in critical stiffness of the fault plane (C. Noël et al., 2019). The conflicting conclusions drawn regarding the effectiveness of cyclic injection primarily stem from the influence of the different fault's drainage and different boundary conditions (Ji, Yoon, et al., 2021; Ji, Zhuang, et al., 2021; C. Noël et al., 2019; Samuelson et al., 2011). Therefore, it is essential to investigate and compare the effects of different injection patterns under the same boundary conditions on a simulated fault in permeable rock.

Also, lowering fluid injection rates has been shown to lead to reduced seismic hazard and risk (Alghannam & Juanes, 2020; Ciardo & Rinaldi, 2022; French et al., 2016; Ji et al., 2022; Passelègue et al., 2018; L. Wang et al., n.d.). High injection rates during experiments performed on a saw-cut Westerly granite sample under triaxial stress conditions facilitated the transition from drained to locally undrained conditions. High injection rates create local fluid pressure perturbations (heterogeneous distribution of fluid pressure) capable of reactivating faults (Passelègue et al., 2018). Injection-induced fault slip experiments on the high-permeable saw-cut sandstone using high and low fluid pressurization rates showed that slip behaviour is determined by pressurization rate rather than injection pressure (L. Wang et al., n.d.). While several studies have explored the mechanism of fault reactivation with different injection rates on impermeable rocks, few studies have been allocated to reveal fundamental physical mechanisms linking the rate of fluid injection to induced earthquakes in permeable rocks (Alghannam & Juanes, 2020; Ji et al., 2022; Passelègue et al., 2018; E. Rutter & Hackston, 2017; Ye & Ghassemi, 2018, 2020). A systematic experimental study that focuses on whether different injection rates, which influence the stress path (effective normal and shear stress), will cause different slip behaviors is currently lacking. The increased use of the subsurface, particularly of permeable reservoirs, underlines the urgency of understanding the impact of slip behaviors on the evolution of microseismicity.

1.6. Objectives of the thesis

The NWO DeepNL program aims to provide fundamental contributions to understanding the processes in the subsurface of the Netherlands resulting from human activities, such as gas extraction, geothermal energy production, CO_2 injection, salt mining, and other geological storage and mining activities ("NWO Research Programme: DeepNL", 2017). The DeepNL program is composed of different projects, and one of them is Science4Steer. Science4Steer is a joint numerical-experimental research project to understand the effects of time-varying gas production and re-injection operations in Dutch gas fields in the Rotliegend formation. One of the experimental sub-groups of the Science4Steer project involved research reported in the current thesis, which mainly focuses on evolution in mechanical and seismicity properties due to the cycling of stress/fluid pressure in intact and faulted porous reservoir rocks.

As previously noted, the potential hazards associated with geo-energy activities, such as fluid injection or extraction from underground formations, include subsidence and seismicity. Therefore, it is crucial to comprehend the mechanisms that cause subsidence and seismicity and to develop mitigation protocols that consider parameters related to injection and depletion, such as rate, amplitude, and frequency. Building upon the challenges and scientific gaps identified above, this thesis centers around five main objectives, which are as follows:

1. How do different stress patterns and rates affect the seismicity evolution and mechanical evolution of intact reservoir sandstone? Can varying stress rates and patterns reduce seismicity?
2. How does cyclic stress with different amplitude and frequency influence the deformation of intact reservoir rock?
3. How does stress pattern affect fault slip and microseismic evolution?
4. How do different injection rates and patterns affect injection-induced seismicity in a faulted porous medium?
5. What is the mechanism of fault slip in a displaced fault system?

1.7. ORGANIZATION OF THE CHAPTERS

This thesis is structured into eight main chapters to address the previously outlined questions, each devoted to exploring one specific question. These chapters consist of a collection of articles published or submitted to peer-reviewed journals.

- **Chapter 2:** This chapter elaborates on the effect of stress cycling patterns and rates on seismic evolution and failure patterns of highly porous Red Felser sandstone. It includes uniaxial compression tests and Acoustic Emission (AE) monitoring on 18 samples under three different stress patterns and rates. It provides insights into which stress patterns and rates yield lower seismicity.
- **Chapter 3:** This chapter aims to address the Red Felser sandstone deformation under triaxial cyclic loading above and below the onset of dilatant cracking, under different frequencies and loading amplitudes. Axial strains and AEs are measured in both regimes to quantify the rock's total deformation (strain) and its AE characteristics. Additionally, efforts are made to model the cyclic deformation behavior of sandstone by comparing experimental data with simulation results. Results provide information about the inelastic deformation and AE response of the reservoir rock relevant for underground energy storage.
- **Chapter 4:** The research described in this chapter aims to combine passive and active acoustic monitoring methods to monitor fault sliding and reactivation under triaxial conditions. It attempts to improve the monitoring of different phases of fault reactivation and fault reactivation processes under stress cycling, including early aseismic creep (pre-slip), fault slip, and continuous sliding.
- **Chapter 5:** This chapter details a displacement-driven triaxial fault reactivation experiment conducted on saw-cut Red Felser sandstone. It explores seismicity evolution using various approaches: under-threshold cyclic sliding, cyclic sliding, and monotonic sliding.

- **Chapter 6:** This chapter elaborates on the effect of different pressurization rates and patterns on a porous faulted reservoir rock. It includes injection-driven fault reactivation experiments on saw-cut Red Felser sandstone under three injection rates and three injection patterns (cyclic, stepwise, and monotonic injection). It provides insight into a proper injection strategy that could help reduce injection-induced seismicity.
- **Chapter 7:** The aim of this chapter is to investigate fault slip and nucleation in a displaced fault setting. It encompasses both large-scale true-triaxial experiments on a partially displaced normal fault and small-scale triaxial experiments on a fully displaced vertical fault. The primary focus is to examine and validate the initiation of slip nucleation patches in both the inner and outer corners of the displaced fault setting.
- **Chapter 8:** This chapter summarizes the conclusions for the entire thesis. It also provides recommendations for future research and development related to the topics covered in this thesis.

1.8. DATA AVAILABILITY

In the 4TU.ResearchData repository, all data from each chapter have been stored and organized with the following DOI addresses:

- **Chapter 2**: https://doi.org/10.4121/97e9d9e2-ff89-4d8c-b875-f691762f7b8c
- **Chapter 3**: https://doi.org/10.4121/8bf07c75-86b9-4a10-a301-0b35d19e2090
- **Chapter 4**: https://doi.org/10.4121/d40d3812-c3db-46bb-8394-24473c735b23
- **Chapter 5**: https://doi.org/10.4121/be1630f9-b57b-4001-954d-ae291c9c7eaf
- **Chapter 6**: https://doi.org/10.4121/02c46099-0f1e-486b-91b9-b5f0ecb30bc4
- **Chapter 7**: https://doi.org/10.4121/38262dab-3eea-4991-87a0-1b7e849efbfb and https://doi.org/10.4121/01b669fd-d757-4f63-8e2b-cf25c994f02b

Bibliography

Addis, M. A. (1997). The stress-depletion response of reservoirs. *SPE annual technical conference and exhibition*.

Alghannam, M., & Juanes, R. (2020). Understanding rate effects in injection-induced earthquakes. *Nature communications*, *11*(1), 3053.

Amid, A., Mignard, D., & Wilkinson, M. (2016). Seasonal storage of hydrogen in a depleted natural gas reservoir. *International journal of hydrogen energy*, *41*(12), 5549–5558.

Atkinson, G. M., Eaton, D. W., & Igonin, N. (2020). Developments in understanding seismicity triggered by hydraulic fracturing. *Nature Reviews Earth Environment*, *1*(5), 264–277.

Bachmann, C. E., Wiemer, S., Goertz-Allmann, B. P., & Woessner, J. (2012). Influence of pore-pressure on the event-size distribution of induced earthquakes. *Geophysical Research Letters*, *39*(9).

Bachmann, C. E., Wiemer, S., Woessner, J., & Hainzl, S. (2011). Statistical analysis of the induced Basel 2006 earthquake sequence: introducing a probability-based monitoring approach for Enhanced Geothermal Systems. *Geophysical Journal International*, *186*(2), 793–807.

Bagde, M. N., & Petroš, V. (2005). Waveform effect on fatigue properties of intact sandstone in uniaxial cyclical loading. *Rock mechanics and rock engineering*, *38*, 169–196.

Barbier, E. (2002). Geothermal energy technology and current status: an overview. *Renewable and sustainable energy reviews*, *6*(1-2), 3–65.

Baud, P., Klein, E., & Wong, T.-f. (2004). Compaction localization in porous sandstones: spatial evolution of damage and acoustic emission activity. *Journal of Structural Geology*, *26*(4), 603–624.

Baud, P., Vajdova, V., & Wong, T.-f. (2006). Shear-enhanced compaction and strain localization: Inelastic deformation and constitutive modeling of four porous sandstones. *Journal of Geophysical Research: Solid Earth*, *111*(B12).

Bauer, S., Beyer, C., Dethlefsen, F., Dietrich, P., Duttmann, R., Ebert, M., Feeser, V., Görke, U., Köber, R., & Kolditz, O. (2013). Impacts of the use of the geological subsurface for energy storage: an investigation concept. *Environmental earth sciences*, *70*, 3935–3943.

Bauer, S., Dahmke, A., & Kolditz, O. (2017). Subsurface energy storage: geological storage of renewable energy—capacities, induced effects and implications.

Benetatos, C., Codegone, G., Ferraro, C., Mantegazzi, A., Rocca, V., Tango, G., & Trillo, F. (2020). Multidisciplinary analysis of ground movements: an underground gas storage case study. *Remote Sensing*, *12*(21), 3487.

1

Bernabe, Y., Fryer, D. T., & Shively, R. M. (1994). Experimental observations of the elastic and inelastic behaviour of porous sandstones. *Geophysical Journal International*, *117*(2), 403–418.

Birkholzer, J. T., Zhou, Q., & Tsang, C.-F. (2009). Large-scale impact of CO2 storage in deep saline aquifers: A sensitivity study on pressure response in stratified systems. *international journal of greenhouse gas control*, *3*(2), 181–194.

Bommer, J. J., Crowley, H., & Pinho, R. (2015). A risk-mitigation approach to the management of induced seismicity. *Journal of Seismology*, *19*(2), 623–646.

Brace, W. F. (1978). Volume changes during fracture and frictional sliding: A review. *pure and applied geophysics*, *116*, 603–614.

Brantut, N., Heap, M. J., Meredith, P. G., & Baud, P. (2013). Time-dependent cracking and brittle creep in crustal rocks: A review. *Journal of Structural Geology*, *52*, 17–43.

Buijze, L., Van den Bogert, P. A. J., Wassing, B. B. T., & Orlic, B. (2019). Nucleation and arrest of dynamic rupture induced by reservoir depletion. *Journal of Geophysical Research: Solid Earth*, *124*(4), 3620–3645.

Cai, M. (2010). Practical estimates of tensile strength and Hoek–Brown strength parameter mi of brittle rocks. *Rock Mechanics and Rock Engineering*, *43*(2), 167–184.

Chan, A. W., & Zoback, M. D. (2007). The role of hydrocarbon production on land subsidence and fault reactivation in the Louisiana coastal zone. *Journal of Coastal Research*, *23*(3 (233)), 771–786.

Chen, J., Hunfeld, L. B., Niemeijer, A. R., & Spiers, C. J. (2023). Fault weakening during short seismic slip pulse experiments: The role of pressurized water and implications for induced earthquakes in the groningen gas field. *Journal of Geophysical Research: Solid Earth*, *128*(2), e2022JB025729.

Ciardo, F., & Rinaldi, A. P. (2022). Impact of injection rate ramp-up on nucleation and arrest of dynamic fault slip. *Geomechanics and Geophysics for Geo-Energy and Geo-Resources*, *8*(1), 28.

Dieterich, J. H. (1979). Modeling of rock friction: 1. Experimental results and constitutive equations. *Journal of Geophysical Research: Solid Earth*, *84*(B5), 2161–2168.

Doglioni, C. (2018). A classification of induced seismicity. *Geoscience Frontiers*, *9*(6), 1903–1909.

Eaton, D. W., Igonin, N., Poulin, A., Weir, R., Zhang, H., Pellegrino, S., & Rodriguez, G. (2018). Induced seismicity characterization during hydraulic-fracture monitoring with a shallow-wellbore geophone array and broadband sensors. *Seismological Research Letters*, *89*(5), 1641–1651.

Engelder, T., & Fischer, M. P. (1994). Influence of poroelastic behavior on the magnitude of minimum horizontal stress, S h in overpressured parts of sedimentary basins. *Geology*, *22*(10), 949–952.

Fang, Z., & Wu, W. (2022). Laboratory friction-permeability response of rock fractures: A review and new insights. *Geomechanics and Geophysics for Geo-Energy and Geo-Resources*, *8*, 1–16.

French, M. E., Zhu, W., & Banker, J. (2016). Fault slip controlled by stress path and fluid pressurization rate. *Geophysical Research Letters*, *43*(9), 4330–4339. https://doi.org/10.1002/2016GL068893

Geranmayeh Vaneghi, R., Thoeni, K., Dyskin, A. V., Sharifzadeh, M., & Sarmadivaleh, M. (2020). Strength and damage response of sandstone and granodiorite under different loading conditions of multistage uniaxial cyclic compression. *International Journal of Geomechanics*, *20*(9), 04020159.

Hasanbeigi, A., Price, L., & Lin, E. (2012). Emerging energy-efficiency and CO2 emission-reduction technologies for cement and concrete production: A technical review. *Renewable and Sustainable Energy Reviews*, *16*(8), 6220–6238.

Haug, C., Nüchter, J.-A., & Henk, A. (2018). Assessment of geological factors potentially affecting production-induced seismicity in North German gas fields. *Geomechanics for Energy and the Environment*, *16*, 15–31. https://doi.org/https://doi.org/10.1016/j.gete.2018.04.002

He, M., Li, N., Chen, Y., & Zhu, C. (2016). Strength and fatigue properties of sandstone under dynamic cyclic loading. *Shock and Vibration*, *2016*.

Heinemann, N., Alcalde, J., Miocic, J. M., Hangx, S. J. T., Kallmeyer, J., Ostertag-Henning, C., Hassanpouryouzband, A., Thaysen, E. M., Strobel, G. J., & Schmidt-Hattenberger, C. (2021). Enabling large-scale hydrogen storage in porous media–the scientific challenges. *Energy Environmental Science*, *14*(2), 853–864.

Hoek, E. (1990). Estimating Mohr-Coulomb friction and cohesion values from the Hoek-Brown failure criterion. *International Journal of Rock Mechanics and Mining Sciences Geomechanics Abstracts*, *27*(3), 227–229.

Hoek, E. (1965). Rock fracture under static stress conditions.

Hofmann, H., Zimmermann, G., Zang, A., & Min, K. B. (2018). Cyclic soft stimulation (CSS): a new fluid injection protocol and traffic light system to mitigate seismic risks of hydraulic stimulation treatments. *Geothermal Energy*. https://doi.org/10.1186/s40517-018-0114-3

Jaeger, J. C., Cook, N. G. W., & Zimmerman, R. (2009). *Fundamentals of rock mechanics*. John Wiley Sons.

Jansen, Singhal, P., & Vossepoel, F. C. (2019). Insights From Closed-Form Expressions for Injection- and Production-Induced Stresses in Displaced Faults. https://doi.org/10.1029/2019JB017932

Ji, Y., Wang, L., Hofmann, H., Kwiatek, G., & Dresen, G. (2022). High-Rate Fluid Injection Reduces the Nucleation Length of Laboratory Earthquakes on Critically Stressed Faults in Granite. *Geophysical Research Letters*, *49*(23), e2022GL100418.

Ji, Y., Yoon, J. S., Zang, A., & Wu, W. (2021). Mitigation of injection-induced seismicity on undrained faults in granite using cyclic fluid injection: A laboratory study. *International Journal of Rock Mechanics and Mining Sciences*, *146*, 104881.

Ji, Y., Zhuang, L., Wu, W., Hofmann, H., Zang, A., & Zimmermann, G. (2021). Cyclic Water Injection Potentially Mitigates Seismic Risks by Promoting Slow and Stable Slip of a Natural Fracture in Granite. *Rock Mechanics and Rock Engineering*, 1–17.

Jin, L., & Zoback, M. D. (2015). An Analytical Solution for Depletion-induced Principal Stress Rotations In 3D and its Implications for Fault Stability. *AGUFM*, *2015*, S13B–2816.

Johri, M., & Zoback, M. D. (2013). The evolution of stimulated reservoir volume during hydraulic stimulation of shale gas formations. *SPE/AAPG/SEG Unconventional Resources Technology Conference*, URTEC–1575434.

1

Keranen, K. M., & Weingarten, M. (2018a). Induced seismicity. *Annual Review of Earth and Planetary Sciences*.

Keranen, K. M., & Weingarten, M. (2018b). Induced seismicity. *Annual Review of Earth and Planetary Sciences*, *46*, 149–174.

Kim, K.-H., Ree, J.-H., Kim, Y., Kim, S., Kang, S. Y., & Seo, W. (2018). Assessing whether the 2017 Mw 5.4 Pohang earthquake in South Korea was an induced event. *Science*, *360*(6392), 1007–1009.

Kisslinger, C. (1976). A review of theories of mechanisms of induced seismicity. *Engineering Geology*, *10*(2-4), 85–98.

Kwiatek, G., Bohnhoff, M., Dresen, G., Schulze, A., Schulte, T., Zimmermann, G., & Huenges, E. (2010). Microseismicity induced during fluid-injection: A case study from the geothermal site at Groß Schönebeck, North German Basin. *Acta Geophysica*, *58*, 995–1020.

Lehner, F. (2019). An analysis of depletion-induced fault stressing-new closedform analytical solutions. *Assen: Nederlandse Aardolie Maatschappij BV*.

Liang, D., Zhang, N., Xie, L., Zhao, G., & Qian, D. (2019). Damage and fractal evolution trends of sandstones under constant-amplitude and tiered cyclic loading and unloading based on acoustic emission. *International Journal of Distributed Sensor Networks*, *15*(7), 1550147719861020.

Linker, M. F., & Dieterich, J. H. (1992). Effects of variable normal stress on rock friction: Observations and constitutive equations. *Journal of Geophysical Research: Solid Earth*, *97*(B4), 4923–4940.

Martin, C. D., & Chandler, N. A. (1994). The progressive fracture of Lac du Bonnet granite. *International journal of rock mechanics and mining sciences geomechanics abstracts*, *31*(6), 643–659.

McClure, M. W., & Horne, R. N. (2014). Correlations between formation properties and induced seismicity during high pressure injection into granitic rock. *Engineering geology*, *175*, 74–80.

Menéndez, J., Ordóñez, A., Álvarez, R., & Loredo, J. (2019). Energy from closed mines: Underground energy storage and geothermal applications. *Renewable and Sustainable Energy Reviews*, *108*, 498–512.

Mulders, F. M. M. (2003). Modelling of stress development and fault slip in and around a producing gas reservoir.

Naderloo, M., Veltmeijer, A., Jansen, J. D., & Barnhoorn, A. (2023). Laboratory study on the effect of stress cycling pattern and rate on seismicity evolution. *Geomechanics and Geophysics for Geo-Energy and Geo-Resources*, *9*(1), 137. https://doi.org/10.1007/s40948-023-00678-1

Niemz, P., Cesca, S., Heimann, S., Grigoli, F., Specht, S. V., Hammer, C., Zang, A., & Dahm, T. (2020). Full-waveform-based characterization of acoustic emission activity in a mine-scale experiment : a comparison of conventional and advanced hydraulic fracturing schemes, 189–206. https://doi.org/10.1093/gji/ggaa127

Noël, C., Passelègue, F. X., Giorgetti, C., & Violay, M. (2019). Fault Reactivation During Fluid Pressure Oscillations : Transition From Stable to Unstable Slip Journal of Geophysical Research : Solid Earth, 940–953.

Noël, C. J.-M. R. (2021). *On the effects of fluid pressure variations on rock-mass and fault mechanical behaviour* (tech. rep.). EPFL.

NWO Research Programme: DeepNL [Accessed on: 2017-01-01]. (2017).

Orlic, B., & Wassing, B. B. T. (2013). A study of stress change and fault slip in producing gas reservoirs overlain by elastic and viscoelastic caprocks. *Rock mechanics and rock engineering*, *46*(3), 421–435.

Panwar, N. L., Kaushik, S. C., & Kothari, S. (2011). Role of renewable energy sources in environmental protection: A review. *Renewable and sustainable energy reviews*, *15*(3), 1513–1524.

Passelègue, F. X., Brantut, N., & Mitchell, T. M. (2018). Fault Reactivation by Fluid Injection: Controls From Stress State and Injection Rate. *Geophysical Research Letters*, *45*(23), 12, 837–12, 846. https://doi.org/10.1029/2018GL080470

Patel, S. M., Sondergeld, C. H., & Rai, C. S. (2017). Laboratory studies of hydraulic fracturing by cyclic injection. *International Journal of Rock Mechanics and Mining Sciences*, *95*(March), 8–15. https://doi.org/10.1016/j.ijrmms.2017.03.008

Paterson, M. S., & Wong, T.-f. (2005). *Experimental rock deformation: the brittle field* (Vol. 348). Springer.

Peng, K., Zhou, J., Zou, Q., & Song, X. (2020). Effect of loading frequency on the deformation behaviours of sandstones subjected to cyclic loads and its underlying mechanism. *International Journal of Fatigue*, *131*, 105349.

Peng, K., Zhou, J., Zou, Q., Zhang, J., & Wu, F. (2019). Effects of stress lower limit during cyclic loading and unloading on deformation characteristics of sandstones. *Construction and Building Materials*, *217*, 202–215.

Pijnenburg, R. P. J., Verberne, B. A., Hangx, S. J. T., & Spiers, C. J. (2018). Deformation behavior of sandstones from the seismogenic Groningen gas field: Role of inelastic versus elastic mechanisms. *Journal of Geophysical Research: Solid Earth*, *123*(7), 5532–5558.

Pijnenburg, R. P., Verberne, B. A., Hangx, S. J., & Spiers, C. J. (2019). Inelastic Deformation of the Slochteren Sandstone: Stress-Strain Relations and Implications for Induced Seismicity in the Groningen Gas Field. *Journal of Geophysical Research: Solid Earth*, *124*(5), 5254–5282. https://doi.org/10.1029/2019JB017366

Raleigh, C. B., Healy, J. H., & Bredehoeft, J. D. (1976). An experiment in earthquake control at Rangely, Colorado. *Science*, *191*(4233), 1230–1237.

Ramesh Kumar, K., Makhmutov, A., Spiers, C. J., & Hajibeygi, H. (2021). Geomechanical simulation of energy storage in salt formations. *Scientific Reports*, *11*(1), 1–24.

Renné, D. S. (2022). Progress, opportunities and challenges of achieving net-zero emissions and 100% renewables. *Solar Compass*, *1*, 100007.

Rice, J. R. (1993). Spatio-temporal complexity of slip on a fault. *Journal of Geophysical Research: Solid Earth*, *98*(B6), 9885–9907.

Rice, J. R., & Ruina, A. L. (1983). Stability of steady frictional slipping.

Rinaldi, A. P., & Rutqvist, J. (2019). Joint opening or hydroshearing? Analyzing a fracture zone stimulation at Fenton Hill. *Geothermics*, *77*, 83–98.

Ruina, A. (1983). Slip instability and state variable friction laws. *Journal of Geophysical Research: Solid Earth*, *88*(B12), 10359–10370.

Rutter, E. H., & Glover, C. T. (2012). The deformation of porous sandstones; are Byerlee friction and the critical state line equivalent? *Journal of Structural Geology*, *44*, 129–140.

Rutter, E., & Hackston, A. (2017). On the effective stress law for rock-on-rock frictional sliding, and fault slip triggered by means of fluid injection. *Philosophical Transactions of the Royal Society A: Mathematical, Physical and Engineering Sciences*, *375*(2103), 20160001.

Samuelson, J., Elsworth, D., & Marone, C. (2011). Influence of dilatancy on the frictional constitutive behavior of a saturated fault zone under a variety of drainage conditions. *Journal of Geophysical Research: Solid Earth*, *116*(B10).

Schultz, R., Skoumal, R. J., Brudzinski, M. R., Eaton, D., Baptie, B., & Ellsworth, W. (2020). Hydraulic fracturing-induced seismicity. *Reviews of Geophysics*, *58*(3), e2019RG000695.

Segall, P. (1985). Stress and subsidence resulting from subsurface fluid withdrawal in the epicentral region of the 1983 Coalinga earthquake. *Journal of Geophysical Research: Solid Earth*, *90*(B8), 6801–6816.

Segall, P., & Fitzgerald, S. D. (1998). A note on induced stress changes in hydrocarbon and geothermal reservoirs. *Tectonophysics*, *289*(1-3), 117–128.

Sun, B., Zhu, Z., Shi, C., & Luo, Z. (2017). Dynamic mechanical behavior and fatigue damage evolution of sandstone under cyclic loading. *International Journal of Rock Mechanics and Mining Sciences*, *94*, 82–89.

Taheri, A., Yfantidis, N., Olivares, C. L., Connelly, B. J., & Bastian, T. J. (2016). Experimental study on degradation of mechanical properties of sandstone under different cyclic loadings. *Geotechnical Testing Journal*, *39*(4), 673–687.

Uenishi, K., & Rice, J. R. (2003). Universal nucleation length for slip-weakening rupture instability under nonuniform fault loading. *Journal of Geophysical Research: Solid Earth*, *108*(B1).

Ürge-Vorsatz, D., Danny Harvey, L. D., Mirasgedis, S., & Levine, M. D. (2007). Mitigating CO2 emissions from energy use in the world's buildings. *Building Research Information*, *35*(4), 379–398.

van Thienen-Visser, K., & Breunese, J. (2015). Induced seismicity of the groningen gas field: History and recent developments. *The Leading Edge*, *34*(6), 664–671.

van Wees, J.-D., Osinga, S., Van Thienen-Visser, K., & Fokker, P. A. (2018). Reservoir creep and induced seismicity: inferences from geomechanical modeling of gas depletion in the Groningen field. *Geophysical Journal International*, *212*(3), 1487–1497.

Vermeer, P. A. (1998). Non-associated plasticity for soils, concrete and rock. In *Physics of dry granular media* (pp. 163–196). Springer.

Walton, G. (2021). A new perspective on the brittle–ductile transition of rocks. *Rock Mechanics and Rock Engineering*, *54*(12), 5993–6006.

Wang, H. L., Xu, W. Y., Cai, M., Xiang, Z. P., & Kong, Q. (2017). Gas permeability and porosity evolution of a porous sandstone under repeated loading and unloading conditions. *Rock Mechanics and Rock Engineering*, *50*, 2071–2083.

Wang, L., Kwiatek, G., Rybacki, E., & Bonnelye, A. (n.d.). Laboratory Study on Fluid - Induced Fault Slip Behavior : The Role of Fluid Pressurization Rate Geophysical Research Letters, 1–12. https://doi.org/10.1029/2019GL086627

Wilson, M. P., Worrall, F., Davies, R. J., & Almond, S. (2018). Fracking: How far from faults? *Geomechanics and Geophysics for Geo-Energy and Geo-Resources*, *4*, 193–199.

Wong, T.-f., & Baud, P. (2012). The brittle-ductile transition in porous rock: A review. *Journal of Structural Geology*, *44*, 25–53.

Ye, Z., & Ghassemi, A. (2018). Injection-induced shear slip and permeability enhancement in granite fractures. *Journal of Geophysical Research: Solid Earth*, *123*(10), 9009–9032.

Ye, Z., & Ghassemi, A. (2020). Heterogeneous Fracture Slip and Aseismic-Seismic Transition in a Triaxial Injection Test. *Geophysical Research Letters*, *47*(14), 1–9. https://doi.org/10.1029/2020GL087739

Yerkes, R. F., & Castle, R. O. (1976). Seismicity and faulting attributable to fluid extraction. *Engineering Geology*, *10*(2-4), 151–167.

Yoon, J. S., Zang, A., & Stephansson, O. (2014). Numerical investigation on optimized stimulation of intact and naturally fractured deep geothermal reservoirs using hydro-mechanical coupled discrete particles joints model. *Geothermics*, *52*, 165–184.

Zang, A., Yoon, J. S., Stephansson, O., & Heidbach, O. (2013). Fatigue hydraulic fracturing by cyclic reservoir treatment enhances permeability and reduces induced seismicity. *Geophysical journal international*, *195*(2), 1282–1287.

Zang, A., Zimmermann, G., Hofmann, H., Stephansson, O., Min, K.-B., & Kim, K. Y. (2019). How to reduce fluid-injection-induced seismicity. *Rock Mechanics and Rock Engineering*, *52*(2), 475–493.

Zhang, J.-c., Lin, Z.-n., Dong, B., & Guo, R.-x. (2021). Triaxial compression testing at constant and reducing confining pressure for the mechanical characterization of a specific type of sandstone. *Rock Mechanics and Rock Engineering*, *54*, 1999–2012.

Zhenyu, T. A. O., & Haihong, M. O. (1990). An experimental study and analysis of the behaviour of rock under cyclic loading. *Intl J of Rock Mech Mining Sci Geomechanic Abs*, *27*(1).

Zhuang, L., Gyu, S., Melvin, J., Kwang, D., Kim, Y., Hofmann, H., Bok, K., & Arno, M. (2020). Laboratory True Triaxial Hydraulic Fracturing of Granite Under Six Fluid Injection Schemes and Grain - Scale Fracture Observations.

Zimmermann, G., Hofmann, H., Babadagli, T., Yoon, J.-S., Zang, A., Deon, F., Urpi, L., Blöcher, G., Hassanzadegan, A., & Huenges, E. (2015). Multi-fracturing and cyclic hydraulic stimulation scenarios to develop Enhanced Geothermal Systems–Feasability and mitigation strategies to reduce seismic risk. *World Geothermal Congress*, 6.

2

EFFECT OF STRESS CYCLING PATTERN AND RATE ON SEISMICITY EVOLUTION[1]

Abstract: *Recent laboratory and field studies suggest that temporal variations in injection patterns (e.g., cyclic injection) might trigger less seismicity than constant monotonic injection. This study presents results from uniaxial compressive experiments performed on Red Felser sandstone samples providing new insights on the effect of stress pattern and rate on seismicity evolution. Red Felser sandstone samples were subjected to three stress patterns: cyclic recursive (CR), cyclic progressive (CP), and monotonic stress. Three different stress rates (displacement controlled) were also applied: low, medium, and high rates of* 10^{-4} *mm/s,* 5×10^{-4} *mm/s, and* 5×10^{-3} *mm/s, respectively. Acoustic Emission (AE) waveforms were recorded throughout the experiments using 11 AE transducers placed around the sample. Microseismicity analysis shows that: (i) cyclic stress patterns and especially cyclic progressive patterns are characterized by a high number of AE events and lower maximum AE amplitude; (ii) among the three different stress patterns, the largest b-value (slope of the log frequency-magnitude distribution) resulted from the cyclic progressive (CP) stress pattern, (iii) by reducing the stress rate, the maximum AE energy and final mechanical strength both decrease significantly. In addition, stress rate remarkably affects the detailed AE signature of the events classified by the distribution of events in the average frequency (AF) – rise angle (RA) space. High stress rates increase the number of events with low AF and high RA signatures. Considering all elements of the AE analysis, it can be concluded that applying cyclic stress patterns in combination with low-stress rates may potentially lead to a more favourable induced seismicity effect in subsurface-related injection operations.*

[1]This chapter was published in (Naderloo et al., 2023)

2.1. Introduction

2.1.1. Scientific Background

In the last few decades, human activities concerning geo-reservoirs, including natural gas production, water waste disposal (Hincks et al., 2018), hydraulic fracturing (Davies et al., 2013), CO2 storage, and geothermal energy production (Grünthal, 2014), have caused induced seismicity. Many anthropogenic earthquake events and earthquake sequences are attributed to injection or extraction operations (Ellsworth, 2013). For example, in the Groningen gas field in the Netherlands, induced seismic events have been reported to have increased in frequency and magnitude over time due to gas extraction (Lele et al., 2016). The largest event, M = 3.6 at the center of the gas field, was recorded in 2012. An earthquake of magnitude 5.5 in Pohang, South Korea, which occurred during the site development of the geothermal project, was provoked by the injection process (Grigoli et al., 2018).

Multiple studies have been conducted to better understand the causes of induced seismicity (Keranen & Weingarten, 2018; Raleigh et al., 1976; Zoback & Gorelick, 2012). Increasing the fluid pressure reduces the effective normal stress resolved on the fault plane. As a result, the shear resistance is reduced, allowing slip under tectonic shear stresses in the field (Kisslinger, 1976; Segall, 1989). Also, increasing the pore pressure during injection for hydraulic fracturing purposes can create fractures causing seismicity (Grigoli et al., 2018). Moreover, there is convincing evidence that a decline in the pore pressure (production) can induce seismicity in gas fields (Segall & Fitzgerald, 1998). A decrease in fluid pressures causes poroelastic changes and differential compaction, perturbing the stress path around the reservoir that, under appropriate circumstances, can lead to earthquakes.

While most of the mechanisms that cause induced seismic events are well understood, few studies have focused on mitigating and reducing fluid-induced seismicity. For example, the aim can be to reduce the magnitude of the largest events triggered by fluid injection. Thus, each field must be assessed individually to determine the maximum allowable magnitude (Hofmann, Zimmermann, Zang, & Min, 2018; Westaway & Younger, 2014). Another possibility can be replacing or compensating the largest magnitude event with a group of smaller events (Yoon et al., 2014). Regarding this goal, injection rate, protocol, volume, and temperature can play an important role (Hofmann, Zimmermann, Zang, & Min, 2018; Zang et al., 2019). Proposed solutions to mitigate and avoid larger induced earthquakes in numerical and experimental studies have been formulated that the seismic response of cyclic fluid injection differs from the response to monotonic injection, thereby reducing induced seismicity (Patel et al., 2017; Yoon et al., 2014; Zang et al., 2013). Zang et al. (2019) concluded that by using cyclic injection (hydraulic fatigue), the magnitude of the largest induced seismic event can be reduced. Also, a seismic traffic light system is sometimes adopted in which injection rates and pressures are modified based on predefined thresholds of recorded seismic magnitudes or other factors (Baisch et al., 2019; Bommer et al., 2015; Hofmann, Zimmermann, Zang, & Min, 2018).

The few existing studies into the mitigation of induced seismicity have focused on low-porosity or non-porous rocks and not on high-porosity rocks (Ji et al., 2021; Niemz et al., 2020; Zang et al., 2019). Furthermore, most studies focus on mechanical evolution rather than seismicity patterns. In this chapter, the differences in seismicity patterns in high-porosity Red Felser sandstone samples are studied by subjecting them to three different stress patterns and rates. In particular, we focus on the energy, maximum amplitude, amplitude-frequency distribution of seismicity events, and failure pattern under different stress patterns and rates.

2.1.2. STRESS PATTERN AND RATE EFFECT

Cyclic loading may cause different forms of mechanical behaviour in the rock material (Fuenkajorn & Phueakphum, 2010; Peng et al., 2020; Stavrogin & Tarasov, 2001). Rocks experience accumulation of damage, cycle after cycle, which, depending on the stress regime (deformation regime), can be in the form of compaction and dilation (Eberhardt et al., 1999; Hernandez et al., 2022; Pijnenburg et al., 2019). Damage accumulation can alter elastic parameters and the failure pattern of the rocks. Few studies confirmed that, in contrast with a monotonic injection or loading pattern that produces a large extensive planar fracture, cyclic patterns induce a more complex fracture pattern (Cerfontaine & Collin, 2018; Erarslan, 2016; Niemz et al., 2020; Yin et al., 2023; Zang et al., 2019). Also, the amplitude and waveform of cycles influences the mechanical behaviour (Fuenkajorn & Phueakphum, 2010; Y. Liu & Dai, 2021; L.-j. Ma et al., 2013).

In addition to stress patterns, stress rate can significantly influence the deformation behavior of the rock. The stress-rate dependence of failure mechanisms in rock can be attributed to the rate-dependent behaviour of microcrack and fractures in the rock medium (Fuenkajorn et al., 2012; Y. Li & Xia, 2000). Fracture toughness is another parameter that can be changed by changing the stress rate (Q. B. Zhang & Zhao, 2013a). Dynamic fracture toughness and crack propagation velocities increase with loading rates, while static fracture toughness remains constant (Swanson, 1984; Z. X. Zhang et al., 1999). According to Imani et al. (2017), the number of tensile and shear fractures increases simultaneously as the strain rate increases; while the number of shear fractures increases more than the number of tensile fractures. However, most of the studies mentioned above on the effect of stress patterns and rates are concentrated on the mechanical evolution compared to the acoustic and seismicity response.

2.2. EXPERIMENTAL METHODOLOGY

2.2.1. STARTING SAMPLE AND APPARATUS

The Rotliegend formation was formed during the early Permian, and consists of fluvial, sandstones, and shales. The Red Felser sandstone used in our experiments was obtained from the Palatine forest near Kaiserslautern, Germany, as part of the Rotliegend formation. Red Felser sandstone is composed of 95% grain minerals, including 89% quartz and 6% orthoclase, and 5% matrix minerals, featuring 4% kaolinite, 1% albite, and trace amounts of haematite, chlorite, Ca-apatite, pyrite, and halite (van Uijen, 2013). The Red Felser is a homogeneous and isotropic sandstone at the scale of a large block (50 × 50 × 20 cm). Cylindrical Red Felser sandstones used in this study were obtained from the same large block by diamond drilling. They were cut into cylinders of 30 mm and 75 mm in diameter and length, respectively. Multiple cylindrical samples of the Red Felser were subjected to preliminary tests to extract the basic mechanical and physical properties of the samples. The connected porosity of the samples was determined using a gas expansion (Helium) pycnometer to be 23% ± 0.5%. We selected samples with porosity falling within the range of the average porosity ±1% standard deviation for the tests. This selection was made to ensure optimal reproducibility among the samples. In addition, we performed three repeat experiments with each stress pattern to ensure that the results are not affected by other factors. Table 2.1 summarizes the key parameters of the Red Felser sandstone, including physical and mechanical properties. We performed uniaxial compression tests with an aluminum dummy sample of known elastic properties to correct the deformation of the loading machine for calculating the elastic parameters.

Table 2.1: Key mechanical and physical parameters of the Red Felser sandstone

Uniaxial Strength (MPa)	P-wave Velocity (m/s)	Porosity (%)	Young's Modulus (GPa)	Poisson's Ratio
44 ± 3	2700 ± 25	23 ± 0.5	15 ± 1.5	0.28 ± 0.02

2.2.2. LOADING SYSTEM AND AE DATA ACQUISITION SYSTEM

Uniaxial compression tests were performed using a servo-control loading machine manufactured by the TU Delft. The loading system can provide static and dynamic loading conditions with a maximum capacity of 500 kN (Figure 2.1). Note that the deformation of the loading machine was corrected using an aluminum dummy sample with a known elastic modulus. A Richter acoustic emission system was used to record and detect microseismic activities during various stress patterns and rates (Figure 2.1). The Richter system is a multi-purpose, multi-channel, 16-bit ADC resolution data acquisition. The system provides simultaneous and synchronous sampling of all input channels. Using the ExStream software, continuous waveforms were meticulously recorded at a sampling rate of 2 MHz, with an input impedance of 50 Ω. While the ExStream software of the Richter system records the acoustic emission data, the raw continuous waveform data is processed and managed by the Insite Seismic Processor software.

The continuous waveform data is converted to single waveforms for further analysis using a predefined trigger logic. An event is recorded if five or more transducers exceed a voltage threshold of about 1mV within a time window of 480 μs and a sampling rate of 2 MHz. The amplitude threshold was carefully established at 1mV, employing the widely accepted 'pencil lead break test (PLB)' method, as used in previous investigations (de Almeida et al., 2014; Grosse & Ohtsu, 2008). This threshold was selected, taking into account the diverse sources of background noise prevalent in the laboratory environment. Also, a thin layer of acoustic coupling agent was used between the sensors and the rock surface to enhance the quality of signal recording (Bi et al., 2023). Each test was conducted using an array of 11 AE transducers, and an identical sensor configuration was consistently employed for all tests (Figure 2.1). To maintain data integrity, any initial recorded events, attributed to the settling of loading plates and friction between the loading piston and the rock sample at the onset of the loading process, were excluded from the dataset.

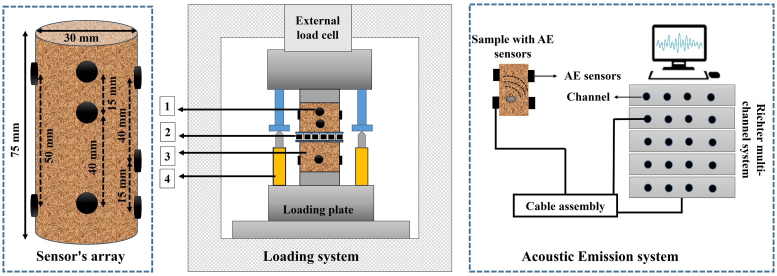

Figure 2.1: 1 Schematic illustration of the loading and acoustic emission system. 1) AE sensor (11 sensors were used); 2) radial strain gauge; 3) rock sample embedded in the loading machine; and 4) Linear Variable Differential Transformer (LVDT) for measuring axial deformation.

2.2.3. EXPERIMENTAL PROCEDURE

Three different stress schemes (six schemes considering different rates) were used in this study, which are shown in Figure 2.2: 1) a monotonic stress scheme, equivalent to a conventional uniaxial test, 2) a cyclic recursive (CR) stress scheme in which, after each cycle, stress is reduced to 5 MPa as a reference stress level, and stress increases 5 MPa per cycle up to achieving the final strength of the sample, 3) a cyclic progressive (CP) stress scheme in which, unlike the CR scheme, stress is not reduced to a reference stress level and instead is reduced with an amount of 5 MPa, and similar to CR, is increased with 5 MPa in each following cycle. In addition, three different stress rates (displacement control) were applied for the monotonic and cyclic recursive stress patterns: low, medium, and high rates that are 10^{-4} mm/s, 5×10^{-4} mm/s, and 5×10^{-3} mm/s, respectively. Please note that these are displacement rates, not direct linear stress rates. Following ISRM and ASTM recommendations, we selected the medium strain rate aiming for sample failure within 2 to 15 minutes (Fairhurst & Hudson, 1999; Standard, 2014). We used a standard strain rate of 5×10^{-4} mm/s, causing Red Felser sandstone to fail within 10 minutes. Additionally, we tested rates ten times faster and five times slower to explore the effect of stress rates on seismicity evolution. The cyclic stress was applied approximately within the elastic (linear) zone of the stress-strain plot, which means between 10% - 85% of the final strength of the sample. Concerning the final strength, elastic zone, and cyclic pattern (stress step of 5 MPa), seven cycles were applied before the failure of the sample. Therefore, the upper limit of the last stress cycle for both cyclic recursive and cyclic progressive was approximately 85% of the final strength (yield zone) of the Red Felser sandstone under UCS test conditions. The naming of the experiments is based on the stress pattern and rate applied (cyclic recursive high rate is thus named CRH).

2.2.4. ACOUSTIC EMISSION MONITORING

2.2.5. AE ENERGY

The true AE energy is proportional to the area beneath and along the acoustic emission waveform. Electrical signals are assumed to have energy proportional to the square of

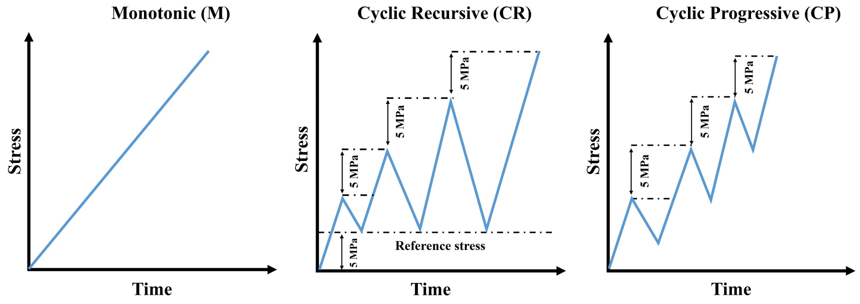

Figure 2.2: Schematic illustration of three stress schemes: from left to right monotonic, cyclic recursive, and cyclic progressive.

their voltage (Grosse & Ohtsu, 2008; Khazaei et al., 2015; Naderloo et al., 2019):

$$E_i = \frac{1}{R}\int_{t_0}^{t_1} V_i(t)^2\,dt, \tag{2.1}$$

where V_i is the voltage of each trace point that exceeds the threshold amplitude; t_0 and t_i are the starting and ending times of the transient voltage record, and R is equal to 50 Ω representing the input impedance of the AE system. By using equation (2.1), the AE energy was calculated for the entire recorded signals of each stress pattern.

2.2.6. B-VALUE ANALYSIS (FREQUENCY-MAGNITUDE DISTRIBUTION)

According to earthquake seismology, the occurrence frequency of events with large magnitudes is lower than of events with smaller magnitudes. This concept can be described or quantified in terms of a magnitude-frequency relationship proposed by Gutenberg and Richter (Gutenberg & Richter, 1944; Lombardi, 2003):

$$\log_{10} N = a - bM_l, \tag{2.2}$$

where N is the number of events with a magnitude larger than or equal to M_l, and a and b are empirical constants. The b value is the negative slope of the log frequency-magnitude graph. A high b value implies a high number of small events relative to large ones, which is desirable for seismicity mitigation (Lei et al., 2018). The maximum-likelihood technique is one of the most appropriate methods to estimate the b-value (Woessner & Wiemer, 2005):

$$b = \frac{\log_{10}(e)}{[M - (M_c - \Delta M_{\text{bin}}/2)]'}, \tag{2.3}$$

where M is the mean magnitude of the sample, ΔM_{bin} is the binning width of the catalog, and M_c is defined as the minimum magnitude in which 100% of the events in a space-time volume are detected (Aki, 1965; Kurz et al., 2006; X. Liu et al., 2020; Lockner, 1993; Woessner & Wiemer, 2005).

Based on the discussion above, the *b*-value was estimated for each stress pattern and rate. The *b*-value was calculated for the entire AE events of each experiment after filtering the events below the threshold and early events from the adjustment of loading pistons. The number of events (cluster) required to calculate the *b*-value meets the condition of having more than 200 events (Amorese et al., 2010; Roberts et al., 2015).

2.2.7. AE PARAMETERS ANALYSIS (RA AND AF VALUE)

Crack growth has been observed to have a different acoustic emission signature depending on the crack growth mode (shear, tensile, and mixed; see Figure 2.3). The AE signals with short rise times (the time needed to achieve maximum amplitude after the first arrival) and high frequencies are characteristics of tensile crack mode, which involves opposing movement of crack surfaces (Figure 2.3b). In contrast, longer rise time (RT) and low-frequency waveforms are attributed to shear-type of cracks (Figure 2.3c) (Aggelis, 2011; Niu et al., 2020). The shear waveforms are slower, and the maximum peak of the waveform takes longer to achieve after the initial longitudinal arrivals (Figure 2.3c) (Ohno & Ohtsu, 2010).

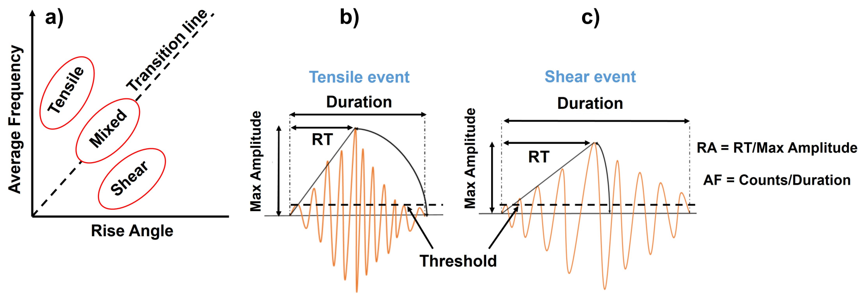

Figure 2.3: Crack classification the AF and RA value: a) Relationship between the Rise Angle (RA) and Average Frequency (AF) value; b) The tensile event with short rise time and duration; c) shear event with long rise time and duration (Zhu et al., 2022)

The cracking mode influences two critical parameters: the average frequency (AF), which is the ratio of the number of threshold crossings and the signal length, and the rise angle (RA), which is the rise time divided by the maximum amplitude. As illustrated in Figure 2.3a, the RA value and AF ratio can distinguish the crack modes as shear, mixed, and tensile by considering an empirical transition line (Aggelis, 2011). This method can be considered a relative classification method due to the assumptions for determining the transition line, the amplitude threshold selection, and the limitation of AE recording devices for triggering. The transition line is mainly derived from an empirical relationship that can be different for materials. According to Z.-H. Zhang and Deng (2020), the optimal ratio of the RA and the AF values for brittle rock is approximately between 1:100 to 1:500 under compressional loading conditions. Various studies have employed diverse approaches, including clustering, Gaussian mixture modeling, and kernel density estimation (KDE) function, to determine optimal transition lines and crack classification (Lian et al., 2023). Nonetheless, the most dependable approach involves applying these methods to test the same material under varying loading conditions, such as shearing, tensile, and compression (J. Li et al., 2022; Lian et al., 2023; G. Ma & Wu, 2023). Since the dominant cracking mode can play an essential role in fracturing, we aim to investigate the possible effects of stress pattern and rate on the distribution of AE events in the AF-RA space.

2.3. Experimental Results and Analysis

2.3.1. AE events pattern

Figure 2.4 shows the typical stress-time graph, the amplitude of AE events, and cumulative AE for the three different stress schemes at the same rate. During loading with the monotonic medium rate (MM) stress pattern, AE events (clusters) were detected as of approximately 80% of the final strength, typically known as the yield zone (Figure 2.4a). However, for cyclic stress schemes, either cyclic recursive medium rate (CRM) or cyclic regressive medium rate (CPM), AE events were observed from approximately 33% of the final strength, i.e., within the fully linear region. Additionally, the Kaiser effect can be observed after the second cycle during both CRM and CPM experiments (Figures 2.4b and c). The Kaiser effect is defined as the absence of detectable acoustic emissions until the previously applied stress level is exceeded (Lavrov, 2003). During the reloading phase of each cycle, AE events appear when the previous maximum stress level is exceeded, as shown in Figures 2.4b and c. After the fifth cycle in both the CRM and CPM stress patterns, the AE events start to appear before achieving the maximum previous stress (see Figures 2.4b and c, points A1-A3 and points B1-B3, which shows the turning point of the cumulative curve of AE). This phenomenon implies a hysteric behaviour or memory effect in the Red Felser sandstone (Y. Zhang et al., 2017). Considering the CRM stress pattern, the axial inelastic deformation accumulates cycle after cycle (Figure 2.5b). At the end of the last cycle, on average, 33% of the total deformation is inelastic. Total inelastic deformation was calculated from the stress-strain curves shown in Figure 2.4b. The accumulation of inelastic deformation within the elastic zone occurs through compaction and grain (micro-cracks) sliding (Pijnenburg et al., 2019). Therefore, the cyclic stress pattern induces inelastic deformation, which we interpret as the reason behind observing the Kaiser effect and the appearance of the memory effect. Figure 2.5a shows the average total number of AE events for each stress scheme at the same rate (medium rate), in which cyclic stress patterns, especially CPM, are characterized by a high number of total generated events. The high number of total events can be due to the induced damage (inelastic deformation) and hysteresis from cyclic stress. However, the question is, can we replace the large events with small events using cyclic stress patterns? To answer this question, we will analyse the microseismicity in terms of maximum amplitude, maximum energy, and magnitude-frequency distribution (b-value).

2.3.2. Amplitude and radiated AE energy

Reducing the maximum magnitude and seismic energy radiation is desirable from a seismicity mitigation perspective. Figure 2.6 shows the recorded maximum AE amplitude for each stress pattern and rate versus final strength (breakdown stress). Although there is no strong correlation between maximum AE amplitude and final strength, one trend can be observed with increasing final strength; the maximum AE amplitude increases as well.

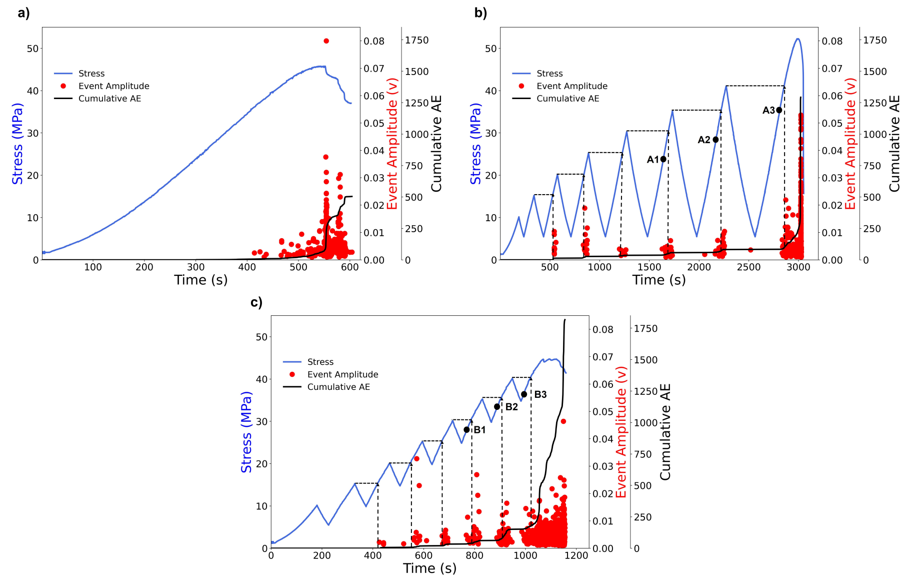

Figure 2.4: Typical stress-time graph, AE amplitude and cumulative AE events for the three different stress schemes at the same rate (medium rate). a monotonic stress (MM, RF29); b cyclic recursive (CRM, RF30); c cyclic progressive (CPM, RF37). Cumulative AE is denoted by the solid black line, and the memory effect is denoted by black dots.

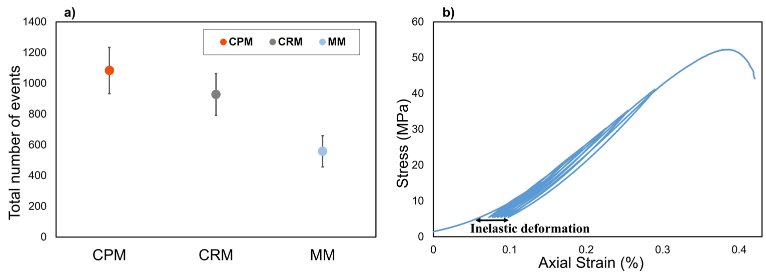

Figure 2.5: a Average total number of events from three different stress patterns with the same rate (medium rate); b Calculation of the inelastic strain from the stress-strain data of the CRM test (sample RF39).

In Figure 2.6, the red and grey dashed lines indicate the average values of the maximum AE amplitudes obtained from the monotonic and cyclic tests, respectively. The average amplitude for cyclic stress patterns is 20% lower than monotonic loadings (grey dashed line in Figure 2.6). In general, a high recorded maximum AE amplitude characterizes samples subjected to a monotonic stress pattern. The CRL pattern results in a 74% and 30% decrease in maximum amplitude and final strength, respectively, compared to the high monotonic rate (MH).

Figure 2.7 indicates the effect of stress rate on the maximum radiated AE energy and final strength (breakdown stress). The horizontal and vertical dotted lines show the av-

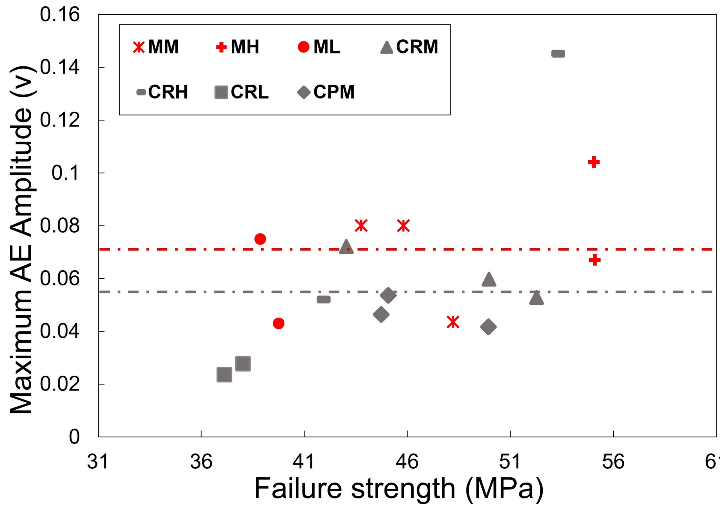

Figure 2.6: The maximum observed amplitude of AE events and final strength for each stress pattern and rate. Red and grey dashed lines indicate average values of amplitude for monotonic and cyclic tests, respectively.

erage maximum radiated AE energy and the average final strength for each stress rate. The stress rate has a significant effect on the final strength. By increasing the stress rate from low to medium to high, the final strength increases on average by 33% and 10%, respectively (Figure 2.7). The stress rate also significantly affects the maximum radiated AE energy. As is shown in Figure 2.7, the maximum radiated AE energy for experiments with a low-stress rate (violet markers) is very small compared to samples subjected to a high-stress rate (red markers).

2.3.3. B-VALUE ANALYSIS (FREQUENCY-AMPLITUDE DISTRIBUTION)

Figure 2.8 shows the frequency-amplitude distributions of the events for different stress patterns. Considering three different stress patterns with the same rate (medium rate), the CPM pattern has an increased number of small events relative to the large ones as indicated by a high b-value (see Figure 2.8). The MM and CRM patterns lead to the generation of more large events and have a lower b-value. A detailed analysis of the amplitude distribution is provided in Figure 2.9. The CPM pattern is characterized by the highest frequency of low amplitude events (Figure 2.9e), while the MM pattern shows a low frequency in the zone with low-amplitude events (Figure 2.9a). Focusing on the tail of the frequency-amplitude distributions shows that the frequencies of events with medium and large amplitudes for the CRM and MM are higher than the frequency for the CPM pattern (Figures 2.9b, d, and f). Additionally, the tail of the distribution for the MM pattern ends at a high amplitude (80 mV) as shown by the arrow in Figure 2.9b. While the frequency-amplitude distribution for the CRM pattern shows a high frequency of small events compared to the MM, the estimated b-value for both patterns is approximately equal. In other words, the CRM pattern shows an increased number of both small and large events.

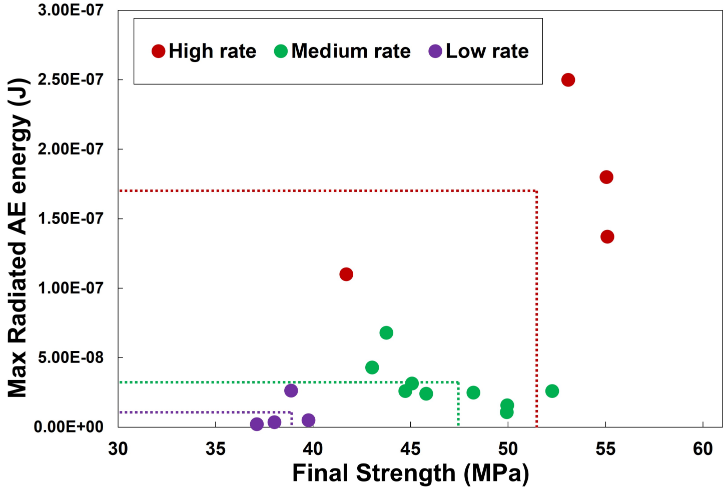

Figure 2.7: The maximum radiated AE energy versus final strength for different stress rates. The horizontal and vertical dotted lines indicate the average maximum radiated AE energy, and the average final strength, for each stress rate.

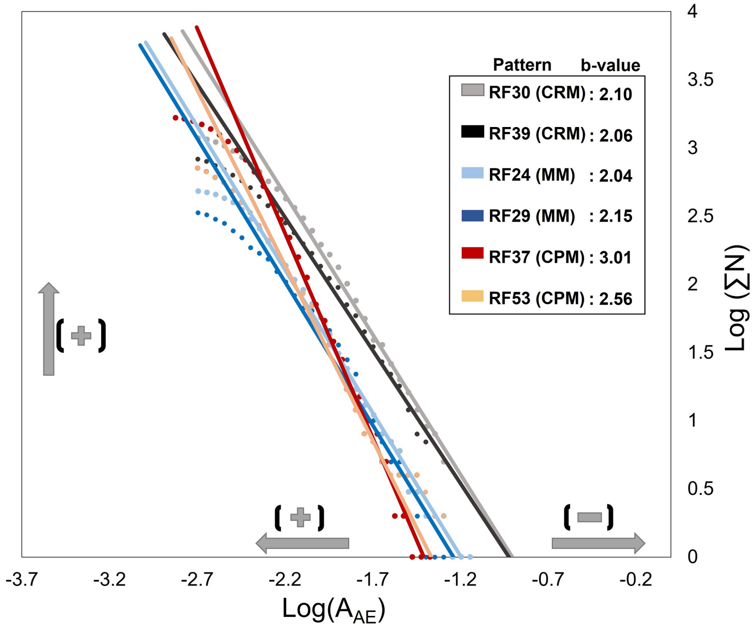

Figure 2.8: The frequency-amplitude distributions of the events for three types of stress patterns. The bottom left plus sign indicates an increase in the number of small events, and the minus sign indicates an increase in the number of high-amplitude events. Thus, a high b-value corresponds to observations of more events toward the low amplitudes relative to the higher amplitudes resulting in a steeper gradient. Note that each rock is labeled with the RF abbreviation, with full details provided in Table 2.2.

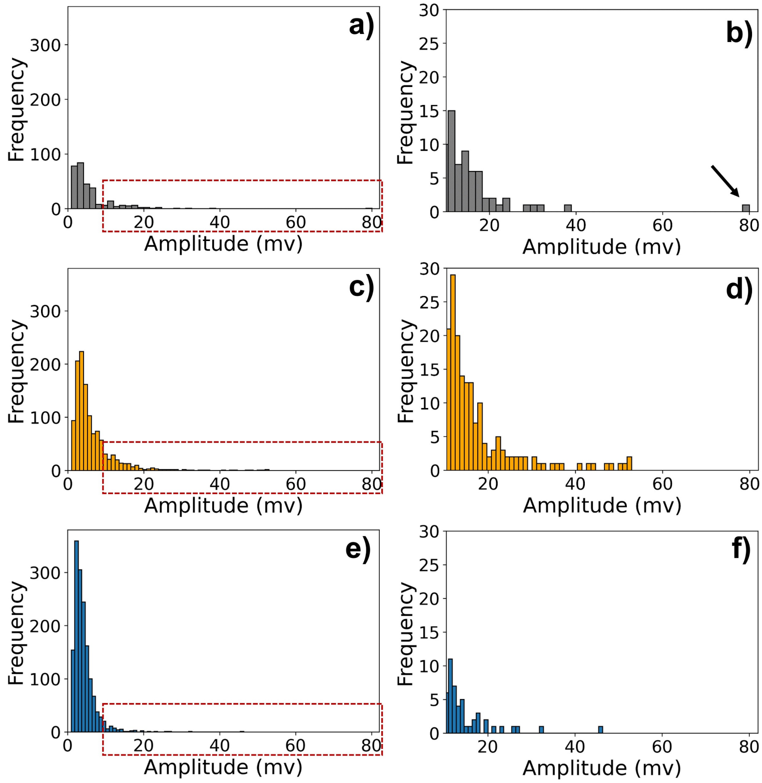

Figure 2.9: A comparison of AE amplitude distributions for three different stress patterns at the medium rate. Figures a, c, and e show the frequency-amplitude distribution for MM, CRM, and CPM, respectively. Figures b, d, and f show the tails of the frequency-amplitude distributions from 10 mv to 82 mv (red dotted box) for MM, CRM, and CPM, respectively.

2.3.4. MECHANICAL EVOLUTION

Cyclic loading patterns can influence the fracturing process by changing the fracture process zone, accumulating inelastic deformation, and adding hysteresis behaviour (Erarslan, 2016; Naderloo et al., 2023; Pijnenburg et al., 2019). As shown in Figure 2.10, samples subjected to cyclic stress display more complex fracture patterns and disintegration, whereas samples with monotonic experiments display one large fracture and less disintegration (decohesion). This difference in failure pattern can be due to the accumulation of the damage cycle after cycle and creating more possible routes for fracture to propagate. In addition to the stress pattern, the stress rate also clearly affects the fracture pattern of the samples. Experiments at low-stress rates are characterized by intense disintegration and crushing (Figure 2.11), especially for low-rate cyclic cases (CRL). Thus, combining cyclic stress patterns and low-stress rates leads to more intense disintegration and powdering of the sample. Besides, the stress rate significantly affects final strength, and applying the high-stress rate increases the average final strength by 33% and 10% in comparison to low and medium rates, respectively (see the final strength

(σ_c) for each test in Table 2.2).

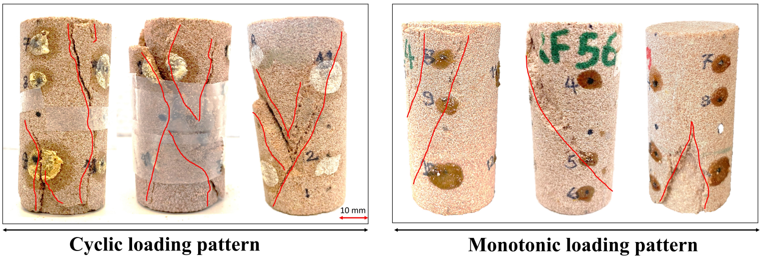

Figure 2.10: Illustration of fracture patterns in the samples after subjecting them to cyclic and monotonic stress patterns.

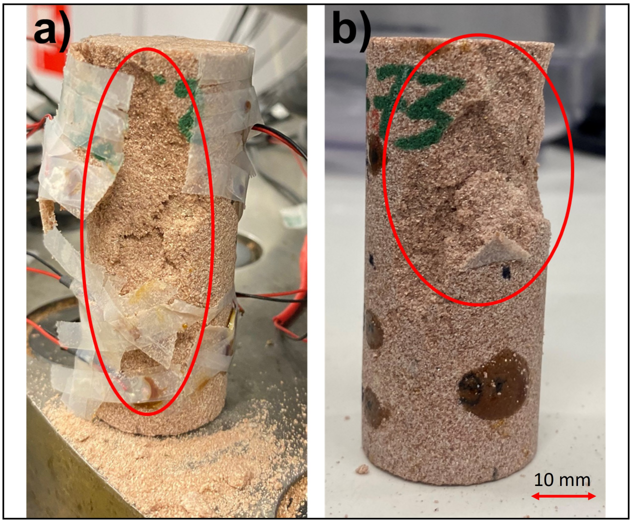

Figure 2.11: Disintegration and fragmentation in samples subjected to low stress rate after final failure: a Cyclic recursive low rate (CRL); b Monotonic low rate (ML).

2.3.5. AE SIGNAL ANALYSIS (STRESS PATTERN AND RATE EFFECT))

As mentioned before, we can obtain information about the failure and cracking mode by using the RA and AF parameters. Note that the transition line depends on the material and type of test. We used two transition lines (AF=100×RA and AF=500×RA) from the study conducted by Z.-H. Zhang and Deng (2020) to investigate event distribution from different stress patterns and rates in the AF-RA space. In Figure 2.12, AF versus RA is depicted with two transition lines for the experiments from three different stress rates. Stress rate significantly affects the crack classification or event distribution in the AF-RA space. Based on Figure 2.12, events from samples subjected to low-stress rates are concentrated on the side with higher AF and lower RA, and by increasing the stress rate, events are more spread to the zone with low AF and high RA values (shear zone and below transition lines). This agrees with the study by Imani et al. (2017). They observed that tensile and shear fractures increase with increasing strain rate; however, the number of shear fractures increases more than the number of tensile fractures. Also, Liang et al. (2023) showed that the contribution of shear failure increases with increasing the strain rate. Figures 2.13b, d, and f illustrate the AF-RA density map for three dif-

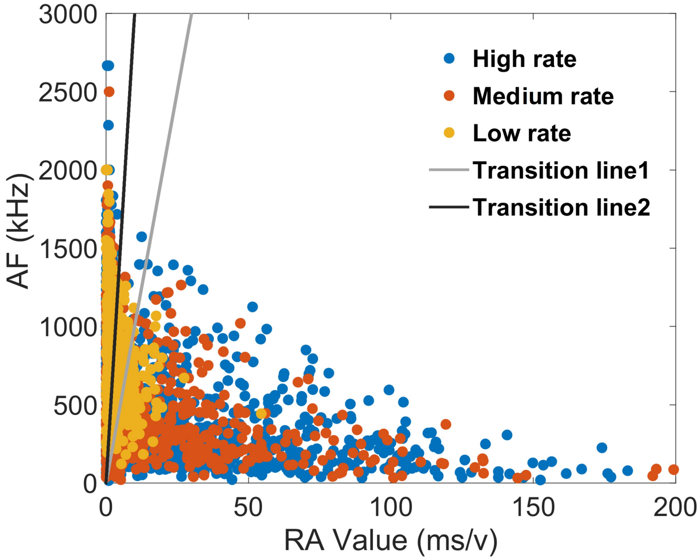

Figure 2.12: Plotting AF versus RA with two transition lines for cyclic recursive experiments at three different rates. The grey and black lines represent the transition lines corresponding to AF values of $100 \times RA$ and $500 \times RA$, respectively.

ferent stress rates. To create the density maps (Figure 2.13 and Figure 2.14), we utilized a 2D histogram-based density estimation with a predetermined number of bins (Eilers & Goeman, 2004). Following the density estimation, we employed a Kernel smoothing function to assign weights to data points based on their proximity to each point of interest. These weights are determined by the distance between data points and the point of interest, with closer points receiving higher weights. As shown in Figures 2.13b, d, and f the maximum density zone moves towards lower AF values with increasing stress rates. Additionally, an extension of events toward a high RA zone can be observed for medium and high-stress rate cases. Alongside density maps, 3D plots were generated by combining the energy of events with the AF-RA diagram. The low-stress rate case shows the occurrence of low energy events concentrated in the high AF and low RA regions (Figures 2.13e and f). Samples subjected to medium and high-stress rates show scattered high-energy events in AF-RA space (Figures 2.13a-d). Therefore, increasing the stress rate generates high rise angle and high energy events.

Moreover, AF-RA space density maps were generated for the samples subjected to different stress patterns but at the same stress rate (Figure 2.14). Events from samples subjected to the CPM stress pattern are more concentrated in the high AF zone than those from the other stress patterns. The AF-RA patterns for the MM and CRM stress schemes are approximately similar (Figure 2.14). Therefore, stress patterns, and especially stress rate, appear to influence fracturing mode and consequently signal proper-

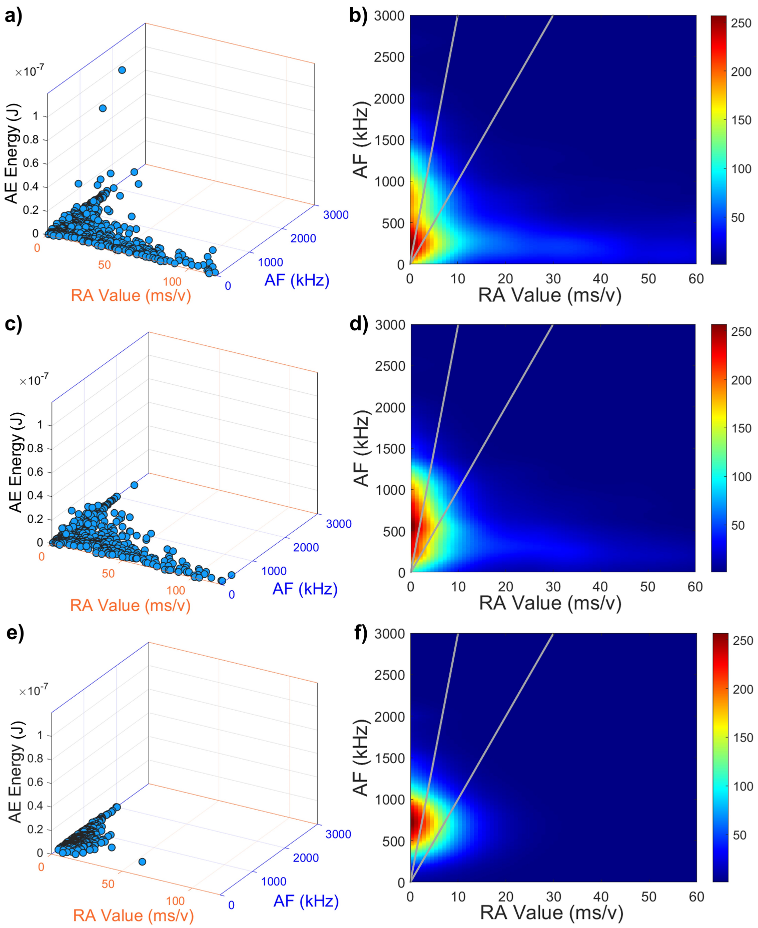

Figure 2.13: AF-RA density and 3D plots for three different stress rates including events energy; a and b High rate; c and d Medium rate; and e and f Low rate.

ties of AE events.

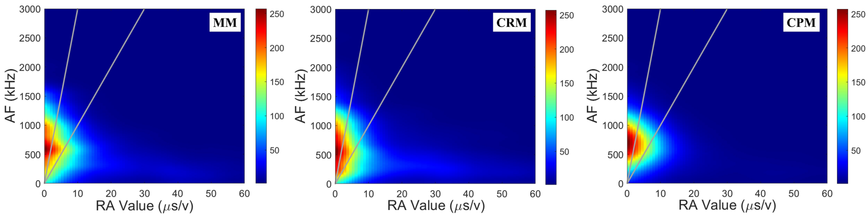

Figure 2.14: Density map distribution of events in AF-RA space for three different stress schemes with medium rate; Cyclic progressive (CPM); Cyclic recursive (CRM); and Monotonic (MM)).

2.4. Interpretation and Discussion

In recent years, the interest into controlled adjustment of injection operations for different purposes, such as geothermal projects, hydraulic fracturing, and temporal energy storage projects, is increasing. The main goals are mitigating induced seismicity and increasing injection efficiency (Patel et al., 2017; Zang et al., 2013). Different behaviour in seismicity and fracturing patterns due to different stress rates and cyclic schemes in our experiments may provide more information to adjust injection operations to large-scale hydraulic stimulation and traffic light systems for subsurface-related projects (Hofmann, Zimmermann, Zang, Yoon, et al., 2018).

2.4.1. Effect of stress pattern

Patel et al. (2017) and Zhuang et al. (2020) reported an increase in the total number of AE events using cyclic injection. We also observed an increase in the total number of AE events for samples subjected to medium rate cyclic recursive (CRM) and the cyclic progressive (CPM) stress patterns compared to the medium rate monotonic (MM) stress pattern (Figure 2.5a). The details of seismic responses under different stress patterns merit further discussion.

First, from a mitigation perspective, reducing the amplitude (magnitude) of the biggest event is important. Zhuang et al. (2020) observed a reduction in the largest event (maximum amplitude) using a cyclic progressive injection pattern. In general, in the present study, samples subjected to cyclic stress patterns are characterized by a lower maximum amplitude (Figure 2.6). The lowest maximum AE amplitude and final strength are attributed to the low-rate cyclic recursive stress pattern (CRL). These differences in maximum recorded amplitude can be related to mechanical and failure responses under different stress patterns. Recent experiments using the hydraulic fatigue concept showed that fractures resulting from continuous injection are elongated fracture planes with stable orientations, while cyclic progressive injection induces a more complex fracture pattern with branching (Niemz et al., 2020; Yin et al., 2023; Zang et al., 2000, 2013). Also, many studies confirmed the differences between the Fracture Process Zone (FPZ) formed during monotonic and cyclic mechanical loading (Cerfontaine & Collin, 2018; Erarslan, 2016; Y. Liu et al., 2017). In the present study (Figure 2.10), samples subjected to cyclic stress displayed more complex fracture patterns and disintegration, whereas samples with monotonic experiments displayed large fractures and less disintegration (decohesion). This observation is similar to those from earlier studies. Although we applied a cyclic pattern within the so-called "fully elastic zone", approximately 33% of inelastic strain was captured at the end of the last cycle for the CR experiments (Figure 2.5b). Pijnenburg et al. (2019) observed inelastic deformation within the fully elastic zone by performing a cyclic triaxial experiment on the Slochteren sandstone. They showed that inelastic deformation within the elastic zone is due to the intergranular normal and/or shear displacements, squeezing clay films at grain contacts, and damage closure from the early loading stage. Hence, it can be speculated that the seismic energy is released through many small events and reduced maximum induced magnitude. In other words, for cyclic stress cases, the fracture plane propagates through a rock volume that previously has experienced inelastic damage and micro-fracturing. Thus, less fracture energy is required, and less AE energy is radiated (Zang et al., 2019).

Also, seismicity mitigation cannot be achieved by just decreasing either maximum magnitude or energy. The amplitude (magnitude) distribution obtained from the entire experiment is important. Niemz et al. (2020) performed a mine-scale experiment with both continuous and cyclic injection. They concluded that the cyclic progressive pattern is characterized by a lower maximum magnitude and significantly larger b-values. A comparison of the frequency–amplitude distributions of the AE events from our experiments showed that there are three ranges of b-value (Table 2.2); 1) lower range ($b-value \leq 2.1$), 2) medium range ($2.1 < b-value < 2.5$), and 3) higher range ($2.5 \leq b-value$). The seismicity induced by the cyclic progressive medium rate (CPM) has an increased number of small events relative to the large ones, indicating a high b-value (Figures 2.8 and 2.9e). All estimated b-values from the CPM pattern are categorized as a high-range b-value group ($2.5 \leq b-value$), which on average, shows higher values than the samples subjected to the MM and CRM patterns at the medium rate (see Table 2.2). Although both CRM and CPM stress patterns result in a high total number of events and lower maximum amplitudes, however; estimated b-values to the CRM pattern are lower than those to the CPM pattern. Compared to the CPM pattern, cycles in the CRM pattern have a higher amplitude and also are reduced down to reference stress (5 MPa), which causes compaction and closure of microcracks. Compaction and closure require more energy (strain) to be removed, and consequently, more large amplitude events are generated during the the CRM experiments. We speculate that the accumulation of inelastic deformation and micro-cracks per cycle induced by cyclic stress could reduce large events through increasing the occurrence of small events. All observations show that with the same stress rate, the CPM stress pattern results in better seismicity mitigation in terms of maximum amplitude and b-value compared to the CRM and MM patterns.

2.4.2. EFFECT OF STRESS RATE

We observed a significant effect of stress rate on seismicity and mechanical properties of samples. Decreasing the stress rate decreases the maximum radiated AE energy and final strength (Figure 2.7). Besides, the stress rate significantly affected event distribution in the AF-RA space (Figures 2.12 and 2.13). Most of the events from low-stress rate cases occur in the high AF or tensile mode zones, while events from high-stress rate cases extend into the shear zone (high RA zones). Differences in the AF-RA distribution can be also seen in the failure pattern of the samples. As shown in Figure 2.11, samples subjected to a low-stress rate are characterized by intense disintegration and crushing instead of extended shear failure planes. Several studies show that by decreasing the strain/stress rate, Young's modulus decreases, which shows that time-dependent behaviour is involved in the elastic zone (Wasantha et al., 2015; Q. B. Zhang & Zhao, 2013b; Zhou et al., 2015). The time-dependent process can accelerate deformation and disintegration. Also, Zhao et al. (2021) showed that at low strain rates, numerous tiny fragments adhere to fractures, filling intergranular cracks with debris. Higher strain rates reduce the number of fragments, focusing fractures on grain cementation surfaces. With high loading rates, trans-granular and inter-granular cracks intersect, further reducing tiny fragments. Therefore, due to the decrease in final strength and the disintegration of grains using a low-stress rate, the possibility of an extensive shear fracture plane is low during failure. Consequently, smaller and low-energy events are generated by splitting and disintegration. The low-stress rate and cyclic recursive composition resulted in the highest b-value, which is 75% higher than the lowest b-value (Table 2.2). Inelastic deformation and grain disintegration induced by a combination of cyclic patterns and low-stress rates result in lower seismicity.

Table 2.2: Summary of the experiments and key parameters based on different stress patterns—MM (monotonic medium rate), CRM (cyclic recursive medium rate), CPM (cyclic progressive medium rate), MH (monotonic high rate), CRH (cyclic recursive high rate), ML (monotonic low rate), and CRL (cyclic recursive low rate)—and rates. Additionally, information on maximum radiated AE energy (E_{max}), maximum AE amplitude (A_{max}), and uniaxial compressive strength (σ_c) is provided.

Sample	Pattern	Rate (mm/s)	σ_c (MPa)	b-value	E_{max}	A_{max} (v)	Events	Porosity (%)
RF31	MM	0.0005	48.2	2.61 ± 0.09	2.48×10^{-8}	0.0435	750	22.1
RF24	MM	0.0005	43.7	2.04 ± 0.087	6.80×10^{-8}	0.0801	534	23.3
RF29	MM	0.0005	45.8	2.15 ± 0.11	2.41×10^{-8}	0.0800	380	23.7
RF30	CRM	0.0005	52.2	2.10 ± 0.06	2.60×10^{-8}	0.0528	1200	23.2
RF39	CRM	0.0005	49.9	2.06 ± 0.065	1.58×10^{-8}	0.0598	912	22.4
RF27	CRM	0.0005	43.0	2.14 ± 0.08	4.30×10^{-8}	0.0722	587	23.8
RF37	CPM	0.0005	44.7	3.01 ± 0.73	2.60×10^{-8}	0.0463	1720	23.1
RF47	CPM	0.0005	49.93	2.50 ± 0.10	1.08×10^{-8}	0.0417	753	23.5
RF53	CPM	0.0005	45.07	2.56 ± 0.088	3.14×10^{-8}	0.0532	930	22.1
RF56	MH	0.005	55.09	2.61 ± 0.054	1.37×10^{-7}	0.0670	1837	22,9
RF55	MH	0.005	55.05	2.43 ± 0.068	1.80×10^{-7}	0.1041	1159	23.4
RF50	CRH	0.005	41.71	2.40 ± 0.07	1.10×10^{-7}	0.0520	1158	24.1
RF51	CRH	0.005	53.09	2.08 ± 0.057	2.50×10^{-7}	0.1451	1300	22.6
RF73	ML	0.0001	39.77	2.30 ± 0.11	5.00×10^{-9}	0.0428	467	24.2
RF72	ML	0.0001	38.87	2.25 ± 0.068	2.63×10^{-8}	0.0748	1100	22.8
RF54	CRL	0.0001	38.02	3.40 ± 0.010	3.5×10^{-9}	0.0277	1156	23.2
RF52	CRL	0.0001	37.11	3.51 ± 0.013	2.18×10^{-9}	0.0236	752	22.8

2.5. IMPLICATIONS FOR INDUCED SEISMICITY

Our experimental results demonstrate that applying cyclic stresses even within a fully elastic zone can help seismicity mitigation. Besides, a low-stress rate can complement a cyclic stress pattern. From a seismicity mitigation perspective, low rate and cyclic stress composition lead to a lower seismicity pattern.

Increasing permeability and reaching a safe (avoiding seismicity) or target fluid pressure is crucial for hydraulic fracturing, geothermal energy production, and waste-water disposal (Hofmann, Zimmermann, Zang, & Min, 2018; Ji et al., 2021; Zang et al., 2019). Seismicity mitigation can be considered a balance between different parameters, including maximum magnitude, radiated energy, total number of events, and *b*-value (magnitude distribution). It will be desirable to reduce maximum magnitude and energy and increase the *b*-value by generating more low-magnitude events compared to large-magnitude events. The maximum allowable magnitude depends on the local surface infrastructure and the vicinity to populated areas. One policy is to replace a single large-magnitude event by many low magnitudes ones (Yoon et al., 2014). Our experiments indicate that more total events were generated by applying cyclic stress patterns. As illustrated by the increase in b-value in the cyclic progressive stress pattern, this results in replacing the largest magnitudes by many low magnitudes events.

Another policy for seismicity management is using a traffic light system (TLS) (Bommer et al., 2015; Hofmann, Zimmermann, Zang, & Min, 2018). For designing the TLS systems, the injection scheme and flow rate are important. In our current study, besides stress patterns, we investigated the effect of stress rates on seismicity patterns. According to our results, the composition of a cyclic stress scheme with a low stress rate can result in a significantly higher b-value and low maximum magnitude and energy. Therefore, results from our study may be of help to design injection protocols.

2.6. CONCLUSION

We conducted uniaxial compression tests on high porous Red Felser sandstone under different stress schemes by changing the stress pattern and rates to investigate their role on seismicity and failure. Our findings are summarized as follows:

1. Cyclic stress patterns, and especially cyclic progressive patterns, are characterized by a high number of AE events.
2. Generally, cyclic stress patterns lower the maximum AE amplitude, where a low-rate cyclic recursive stress pattern results in the lowest maximum AE amplitude and final strength.
3. The stress rate strongly affects the maximum AE energy and final strength; by reducing the stress rate, they both decrease.
4. Considering the same stress rate, a medium-rate cyclic progressive stress pattern results in the highest b-value, implying an increased number of small events relative to large ones.
5. Stress rate remarkably affects the distribution of events in the average frequency vs. rise angle (AF-RA) space. While events from low stress rates are concentrated in the zone with high AF (above the transition line), events are more spread towards the zone with low AF and high RA values when increasing the stress rate.
6. An intense disintegration and powdering characterize experiments at low stress rates.

Bibliography

Aggelis, D. G. (2011). Classification of cracking mode in concrete by acoustic emission parameters. *Mechanics Research Communications*, *38*(3), 153–157.

Aki, K. (1965). Maximum likelihood estimate of b in the formula log N= a-bM and its confidence limits. *Bull. Earthq. Res. Inst., Tokyo Univ.*, *43*, 237–239.

Amorese, D., Grasso, J.-R., & Rydelek, P. A. (2010). On varying b-values with depth: results from computer-intensive tests for Southern California. *Geophysical Journal International*, *180*(1), 347–360.

Baisch, S., Koch, C., & Muntendam-Bos, A. (2019). Traffic light systems: To what extent can induced seismicity be controlled? *Seismological Research Letters*, *90*(3), 1145–1154.

Bi, J., Du, C., Zhao, Y., Wang, C., Lian, S., & Xiong, X. (2023). Characterization of shear behavior and damage mechanism of periodic thermal loading sandstone based on NMR technique. *Engineering Geology*, 107272.

Bommer, J. J., Crowley, H., & Pinho, R. (2015). A risk-mitigation approach to the management of induced seismicity. *Journal of Seismology*, *19*(2), 623–646.

Cerfontaine, B., & Collin, F. (2018). Cyclic and fatigue behaviour of rock materials: review, interpretation and research perspectives. *Rock Mechanics and Rock Engineering*, *51*(2), 391–414.

Davies, R., Foulger, G., Bindley, A., & Styles, P. (2013). Induced seismicity and hydraulic fracturing for the recovery of hydrocarbons. *Marine and petroleum geology*, *45*, 171–185.

de Almeida, V. A. D., Baptista, F. G., & de Aguiar, P. R. (2014). Piezoelectric transducers assessed by the pencil lead break for impedance-based structural health monitoring. *IEEE Sensors Journal*, *15*(2), 693–702.

Eberhardt, E., Stead, D., & Stimpson, B. (1999). Quantifying progressive pre-peak brittle fracture damage in rock during uniaxial compression. *International Journal of Rock Mechanics and Mining Sciences*, *36*(3), 361–380.

Eilers, P. H. C., & Goeman, J. J. (2004). Enhancing scatterplots with smoothed densities. *Bioinformatics*, *20*(5), 623–628.

Ellsworth, W. L. (2013). Injection-Induced Earthquakes. *341*(July), 1–8.

Erarslan, N. (2016). Microstructural investigation of subcritical crack propagation and Fracture Process Zone (FPZ) by the reduction of rock fracture toughness under cyclic loading. *Engineering Geology*, *208*, 181–190. https://doi.org/https://doi.org/10.1016/j.enggeo.2016.04.035

Fairhurst, C. E., & Hudson, J. A. (1999). Draft ISRM suggested method for the complete stress-strain curve for intact rock in uniaxial compression. *International journal of rock mechanics and mining sciences (1997)*, *36*(3), 279–289.

Fuenkajorn, K., & Phueakphum, D. (2010). Effects of cyclic loading on mechanical properties of Maha Sarakham salt. *Engineering Geology*, *112*(1-4), 43–52.

Fuenkajorn, K., Sriapai, T., & Samsri, P. (2012). Effects of loading rate on strength and deformability of Maha Sarakham salt. *Engineering Geology*, *135*, 10–23.

Grigoli, F., Cesca, S., Rinaldi, A. P., Manconi, A., Lopez-Comino, J. A., Clinton, J. F., Westaway, R., Cauzzi, C., Dahm, T., & Wiemer, S. (2018). The November 2017 Mw 5.5 Pohang earthquake: A possible case of induced seismicity in South Korea. *Science*, *360*(6392), 1003–1006.

Grosse, C. U., & Ohtsu, M. (2008). *Acoustic emission testing*. Springer Science Business Media.

Grünthal, G. (2014). Induced seismicity related to geothermal projects versus natural tectonic earthquakes and other types of induced seismic events in Central Europe. *Geothermics*, *52*, 22–35.

Gutenberg, B., & Richter, C. F. (1944). Frequency of earthquakes in California. *Bulletin of the Seismological society of America*, *34*(4), 185–188.

Hernandez, E., Naderloo, M., Kumar, K. R., Hajibeygi, H., & Barnhoorn, A. (2022). Modeling of Cyclic Deformation of Sandstones Based on Experimental Observations. *EAGE GET 2022*, *2022*(1), 1–5.

Hincks, T., Aspinall, W., Cooke, R., & Gernon, T. (2018). Oklahoma's induced seismicity strongly linked to wastewater injection depth. *Science*, *359*(6381), 1251–1255.

Hofmann, H., Zimmermann, G., Zang, A., Yoon, J. S., Stephansson, O., Kim, K. Y., Zhuang, L., Diaz, M., & Min, K.-B. (2018). Comparison of cyclic and constant fluid injection in granitic rock at different scales. *ARMA US Rock Mechanics/Geomechanics Symposium*, ARMA–2018.

Hofmann, H., Zimmermann, G., Zang, A., & Min, K. B. (2018). Cyclic soft stimulation (CSS): a new fluid injection protocol and traffic light system to mitigate seismic risks of hydraulic stimulation treatments. *Geothermal Energy*. https://doi.org/10.1186/s40517-018-0114-3

Imani, M., Nejati, H. R., & Goshtasbi, K. (2017). Dynamic response and failure mechanism of brazilian disk specimens at high strain rate. *Soil Dynamics and Earthquake Engineering*, *100*, 261–269.

Ji, Y., Yoon, J. S., Zang, A., & Wu, W. (2021). Mitigation of injection-induced seismicity on undrained faults in granite using cyclic fluid injection: A laboratory study. *International Journal of Rock Mechanics and Mining Sciences*, *146*, 104881.

Keranen, K. M., & Weingarten, M. (2018). Induced seismicity. *Annual Review of Earth and Planetary Sciences*.

Khazaei, C., Hazzard, J., & Chalaturnyk, R. (2015). Damage quantification of intact rocks using acoustic emission energies recorded during uniaxial compression test and discrete element modeling. *Computers and Geotechnics*, *67*, 94–102.

Kisslinger, C. (1976). A review of theories of mechanisms of induced seismicity. *Engineering Geology*, *10*(2-4), 85–98.

Kurz, J. H., Finck, F., Grosse, C. U., & Reinhardt, H.-W. (2006). Stress drop and stress redistribution in concrete quantified over time by the b-value analysis. *Structural health monitoring*, *5*(1), 69–81.

Lavrov, A. (2003). The Kaiser effect in rocks: principles and stress estimation techniques. *International Journal of Rock Mechanics and Mining Sciences*, *40*(2), 151–171.

Lei, X., Li, S., & Liu, L. (2018). Seismic b-value for foreshock AE events preceding repeated stick-slips of pre-cut faults in granite. *Applied Sciences*, *8*(12), 2361.

Lele, S. P., Hsu, S.-Y., Garzon, J. L., DeDontney, N., Searles, K. H., Gist, G. A., Sanz, P. F., Biediger, E. A. O., & Dale, B. A. (2016). Geomechanical Modeling to Evaluate Production-Induced Seismicity at Groningen Field. https://doi.org/10.2118/183554-MS

Li, J., Lian, S., Huang, Y., & Wang, C. (2022). Study on crack classification criterion and failure evaluation index of red sandstone based on acoustic emission parameter analysis. *Sustainability*, *14*(9), 5143.

Li, Y., & Xia, C. (2000). Time-dependent tests on intact rocks in uniaxial compression. *International Journal of Rock Mechanics and Mining Sciences*, *37*(3), 467–475.

Lian, S., Zhao, Y., Bi, J., Wang, C., & sen Huang, Y. (2023). Investigation the effect of freeze–thaw cycle on fracture mode classification in concrete based on acoustic emission parameter analysis. *Construction and Building Materials*, *362*, 129789.

Liang, Y., Kong, F., Zou, Q., & Zhang, B. (2023). Effect of strain rate on mechanical response and failure characteristics of horizontal bedded coal under quasi-static loading. *Geomechanics and Geophysics for Geo-Energy and Geo-Resources*, *9*(1), 52. https://doi.org/10.1007/s40948-023-00587-3

Liu, X., Han, M., He, W., Li, X., & Chen, D. (2020). A new b value estimation method in rock acoustic emission testing. *Journal of Geophysical Research: Solid Earth*, *125*(12), e2020JB019658.

Liu, Y., & Dai, F. (2021). A review of experimental and theoretical research on the deformation and failure behavior of rocks subjected to cyclic loading. *Journal of Rock Mechanics and Geotechnical Engineering*.

Liu, Y., Dai, F., Fan, P., Xu, N., & Dong, L. (2017). Experimental investigation of the influence of joint geometric configurations on the mechanical properties of intermittent jointed rock models under cyclic uniaxial compression. *Rock Mechanics and Rock Engineering*, *50*, 1453–1471.

Lockner, D. (1993). The role of acoustic emission in the study of rock fracture. *International Journal of Rock Mechanics and Mining Sciences Geomechanics Abstracts*, *30*(7), 883–899.

Lombardi, A. M. (2003). The maximum likelihood estimator of b-value for mainshocks. *Bulletin of the Seismological Society of America*, *93*(5), 2082–2088.

Ma, G., & Wu, C. (2023). Crack type analysis and damage evaluation of BFRP-repaired pre-damaged concrete cylinders using acoustic emission technique. *Construction and Building Materials*, *362*, 129674.

Ma, L.-j., Liu, X.-y., Wang, M.-y., Xu, H.-f., Hua, R.-p., Fan, P.-x., Jiang, S.-r., Wang, G.-a., & Yi, Q.-k. (2013). Experimental investigation of the mechanical properties of rock salt under triaxial cyclic loading. *International Journal of Rock Mechanics and Mining Sciences*, *62*, 34–41.

Naderloo, M., Moosavi, M., & Ahmadi, M. (2019). Using acoustic emission technique to monitor damage progress around joints in brittle materials. *Theoretical and Applied Fracture Mechanics*, *104*, 102368.

Naderloo, M., Veltmeijer, A., Jansen, J. D., & Barnhoorn, A. (2023). Laboratory study on the effect of stress cycling pattern and rate on seismicity evolution. *Geomechanics and Geophysics for Geo-Energy and Geo-Resources*, *9*(1), 137. https://doi.org/10.1007/s40948-023-00678-1

Niemz, P., Cesca, S., Heimann, S., Grigoli, F., Specht, S. V., Hammer, C., Zang, A., & Dahm, T. (2020). Full-waveform-based characterization of acoustic emission activity in a mine-scale experiment : a comparison of conventional and advanced hydraulic fracturing schemes, 189–206. https://doi.org/10.1093/gji/ggaa127

Niu, Y., Zhou, X.-P., & Berto, F. (2020). Evaluation of fracture mode classification in flawed red sandstone under uniaxial compression. *Theoretical and Applied Fracture Mechanics*, *107*, 102528.

Ohno, K., & Ohtsu, M. (2010). Crack classification in concrete based on acoustic emission. *Construction and Building Materials*, *24*(12), 2339–2346.

Patel, S. M., Sondergeld, C. H., & Rai, C. S. (2017). Laboratory studies of hydraulic fracturing by cyclic injection. *International Journal of Rock Mechanics and Mining Sciences*, *95*(March), 8–15. https://doi.org/10.1016/j.ijrmms.2017.03.008

Peng, K., Zhou, J., Zou, Q., & Song, X. (2020). Effect of loading frequency on the deformation behaviours of sandstones subjected to cyclic loads and its underlying mechanism. *International Journal of Fatigue*, *131*, 105349.

Pijnenburg, R. P., Verberne, B. A., Hangx, S. J., & Spiers, C. J. (2019). Inelastic Deformation of the Slochteren Sandstone: Stress-Strain Relations and Implications for Induced Seismicity in the Groningen Gas Field. *Journal of Geophysical Research: Solid Earth*, *124*(5), 5254–5282. https://doi.org/10.1029/2019JB017366

Raleigh, C. B., Healy, J. H., & Bredehoeft, J. D. (1976). An experiment in earthquake control at Rangely, Colorado. *Science*, *191*(4233), 1230–1237.

Roberts, N. S., Bell, A. F., & Main, I. G. (2015). Are volcanic seismic b-values high, and if so when? *Journal of Volcanology and Geothermal Research*, *308*, 127–141.

Segall, P. (1989). Earthquakes triggered by fluid extraction. *Geology*, *17*(10), 942–946.

Segall, P., & Fitzgerald, S. D. (1998). A note on induced stress changes in hydrocarbon and geothermal reservoirs. *Tectonophysics*, *289*(1-3), 117–128.

Standard, A. (2014). Standard test method for compressive strength and elastic moduli of intact rock core specimens under varying states of stress and temperatures. *ASTM International*, *10*, D7012–D7014.

Stavrogin, A. N., & Tarasov, B. G. (2001). *Experimental physics and rock mechanics*. CRC Press.

Swanson, P. L. (1984). Subcritical crack growth and other time-and environment-dependent behavior in crustal rocks. *Journal of Geophysical Research: Solid Earth*, *89*(B6), 4137–4152.

van Uijen, W. M. (2013). Rotliegend geology in the Southern Permian Basin: the development of synrift sediments and its relation to seismic imaging.

Wasantha, P. L. P., Ranjith, P. G., Zhao, J., Shao, S. S., & Permata, G. (2015). Strain rate effect on the mechanical behaviour of sandstones with different grain sizes. *Rock mechanics and rock engineering*, *48*(5), 1883–1895.

Westaway, R., & Younger, P. L. (2014). Quantification of potential macroseismic effects of the induced seismicity that might result from hydraulic fracturing for shale gas exploitation in the UK. *Quarterly Journal of Engineering Geology and Hydrogeology*, *47*(4), 333–350.

Woessner, J., & Wiemer, S. (2005). Assessing the quality of earthquake catalogues: Estimating the magnitude of completeness and its uncertainty. *Bulletin of the Seismological Society of America*, *95*(2), 684–698.

Yin, P.-F., Yang, S.-Q., Gao, F., & Tian, W.-L. (2023). Experiment and DEM simulation study on mechanical behaviors of shale under triaxial cyclic loading and unloading conditions. *Geomechanics and Geophysics for Geo-Energy and Geo-Resources*, *9*(1), 10.

Yoon, J. S., Zang, A., & Stephansson, O. (2014). Numerical investigation on optimized stimulation of intact and naturally fractured deep geothermal reservoirs using hydro-mechanical coupled discrete particles joints model. *Geothermics*, *52*, 165–184.

Zang, A., Wagner, F. C., Stanchits, S., Janssen, C., & Dresen, G. (2000). Fracture process zone in granite. *Journal of Geophysical Research: Solid Earth*, *105*(B10), 23651–23661.

Zang, A., Yoon, J. S., Stephansson, O., & Heidbach, O. (2013). Fatigue hydraulic fracturing by cyclic reservoir treatment enhances permeability and reduces induced seismicity. *Geophysical journal international*, *195*(2), 1282–1287.

Zang, A., Zimmermann, G., Hofmann, H., Stephansson, O., Min, K.-B., & Kim, K. Y. (2019). How to reduce fluid-injection-induced seismicity. *Rock Mechanics and Rock Engineering*, *52*(2), 475–493.

Zhang, Q. B., & Zhao, J. (2013a). Effect of loading rate on fracture toughness and failure micromechanisms in marble. *Engineering Fracture Mechanics*, *102*, 288–309.

Zhang, Q. B., & Zhao, J. (2013b). Effect of loading rate on fracture toughness and failure micromechanisms in marble. *Engineering Fracture Mechanics*, *102*, 288–309.

Zhang, Y., Chen, Y., Yu, R., Hu, L., & Irfan, M. (2017). Effect of loading rate on the felicity effect of three rock types. *Rock Mechanics and Rock Engineering*, *50*(6), 1673–1681.

Zhang, Z. X., Kou, S. Q., Yu, J.-h., Yu, Y., Jiang, L. G., & Lindqvist, P.-A. (1999). Effects of loading rate on rock fracture. *International Journal of Rock Mechanics and Mining Sciences*, *36*(5), 597–611.

Zhang, Z.-H., & Deng, J.-H. (2020). A new method for determining the crack classification criterion in acoustic emission parameter analysis. *International Journal of Rock Mechanics and Mining Sciences*, *130*, 104323.

Zhao, Z., Jing, H., Shi, X., Wu, J., & Yin, Q. (2021). Experimental investigation on fracture behaviors and acoustic emission characteristics of sandstone under different strain rates. *Environmental Earth Sciences*, *80*, 1–16.

Zhou, H., Yang, Y., Zhang, C., & Hu, D. (2015). Experimental investigations on loading-rate dependency of compressive and tensile mechanical behaviour of hard rocks. *European Journal of Environmental and Civil Engineering*, *19*(sup1), s70–s82.

Zhu, J., Deng, J., Chen, F., & Wang, F. (2022). Failure analysis of water-bearing rock under direct tension using acoustic emission. *Engineering Geology*, *299*, 106541.

Zoback, M. D., & Gorelick, S. M. (2012). Earthquake triggering and large-scale geologic storage of carbon dioxide. *Proceedings of the National Academy of Sciences, 109*(26), 10164–10168.

2

3

SANDSTONE DEFORMATION UNDER CYCLING LOADING[1]

Abstract: *Considering the storage capacity and already existing infrastructures, underground porous reservoirs are highly suitable to store green energy, for example, in the form of green gases such as hydrogen and compressed air. Depending on the energy demand and supply, the energy-rich fluids are injected and produced, which induces cyclic change of state-of-the-stress in the reservoir and its surroundings. Detailed analyses of the geomechanical deformations under variable storage conditions i.e., storage frequency and fluid fluctuating pressures, are crucially important for safe and efficient operations. The present chapter presents an integrated analysis, based on experimental and constitutive modeling aspects, to investigate sandstones' geomechanical response to cyclic loading relevant to underground energy storage (UES). To this end, sandstone rock samples were subjected to cyclic loading above and below the onset of dilatant cracking under different frequencies and loading amplitudes. Axial strains and Acoustic Emissions (AE) were measured in both regimes to quantify the total deformation (strain) of the rock and its AE characteristics. It is found that the inelastic strain and number of AE events is the highest in the first cycle and reduce subsequently cycle after cycle. Moreover, cyclic inelastic deformations are affected by the mean stress, amplitude, and frequency of the stress waveform. On the one hand, the higher the mean stress and the amplitude, the higher the total inelastic strains. On the other hand, the lower the frequency, the higher the total inelastic strain. From the modeling perspectives, five types of deformation mechanisms were identified based on the governing physics: elastic, viscoelastic, compaction-based cyclic inelastic, inelastic brittle creep, and dilatation-based inelastic deformation. To model elastic, viscoelastic, and brittle creep, the Nishihara model was used. A cyclic modified cam clay model (MCC) and hardening-softening model were applied to capture plastic deformation. The results show a very good fit of the constitutive model with the experimental re-*

[1] This chapter, a joint collaboration, was published in (Naderloo et al., 2023) and partly presented in (KUMAR, 2023). The numerical portion of this work was completed by Kishan Ramesh Kumar and Edgar Hernandez.

sults, which could help in studying the response of reservoirs to injection and production.

3.1. INTRODUCTION

In the advent of climate change, a successful transition towards cleaner renewable energy calls for effective large-scale (i.e., in the order of TWh) storage technologies (Krevor et al., 2023). To overcome the challenge of intermittency in renewable energy, subsurface storage technology needs to be efficiently developed (Matos et al., 2019). One of the established options is underground gas storage (UGS), in which imported gas is stored in subsurface reservoirs during the summer when prices and demand are low, for heating during winter (Evans & Chadwick, 2009; Sadeghi & Sedaee, 2022; G. Zhang et al., 2017). However, global concerns about climate change are driving more attention to renewable energy sources and storage, such as compressed air energy storage CAES" (Bazdar et al., 2022), underground hydrogen storage UHS" (Boon & Hajibeygi, 2022; Hashemi et al., 2021; Takach et al., 2022), and aquifer thermal energy storage (ATES) (Fleuchaus et al., 2018). A detailed review of energy storage types can be found in references (Feng et al., 2022; Koohi-Fayegh & Rosen, 2020; Olabi & Abdelkareem, 2022; Tarkowski, 2019). The geological formations such as porous reservoirs and salt caverns, has proved to be a good option for storing energy-rich or energy-carrier fluids, such as compressed air, hot water, and hydrogen (Amid et al., 2016; Bauer et al., 2013; Menéndez et al., 2019; Ramesh Kumar et al., 2021). Porous media, such as depleted gas reservoirs, can provide significantly more storage capacity in different locations (Bai & Tahmasebi, 2022; Sainz-Garcia, 2017). The high permeability and availability of porous rocks, such as sandstone reservoirs, make them promising for storage (Amid et al., 2016; Crotogino et al., 2018; Heinemann et al., 2021). Therefore, further research on porous rocks, especially sandstone reservoirs, which contain a large-fraction of the world reserves, is crucial to designing and operating underground storage (Bo et al., 2023).

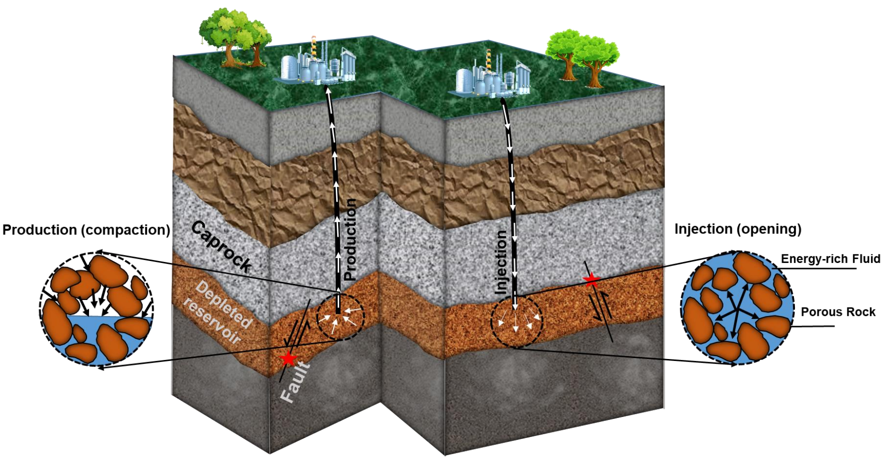

Figure 3.1: Illustration of potential geological storage (depleted gas reservoir) sites for energy-rich fluids.

Subsurface storage technology is based on the injection and production of energy-rich fluids into underground reservoirs depending on the demand and supply (Heinemann et al., 2021; Luboń & Tarkowski, 2020), resulting in cyclic loading as shown in Figure 3.1. Thus, the reservoir experiences cyclic changes in porous pressure and temperature. As a result, the in-situ effective stresses are altered accordingly, which influences the stress conditions on the reservoir rock and surrounding elements, such as caprock, faults, and wells (Chen et al., 2016; Kumar et al., 2022; Liu et al., 2020; X. Zhang & Tahmasebi, 2019). For instance, a decrease or increase in fluid pressure can induce fault reactivation and seismicity (earthquakes) by perturbing the stress path (Orlic et al., 2013; Silverii et al., 2021). The pressure fluctuation during storage can also induce subsidence, which damages the infrastructures nearby (Janna et al., 2012; Teatini et al., 2011). Therefore, it is essential to understand about deformation behavior of sandstone reservoirs and the effect of all the different injection/depletion-related parameters, including amplitude and frequency of cycles, to reduce the risk of delaying projects and optimize the utility of the energy storage operations (Bai & Tahmasebi, 2022).

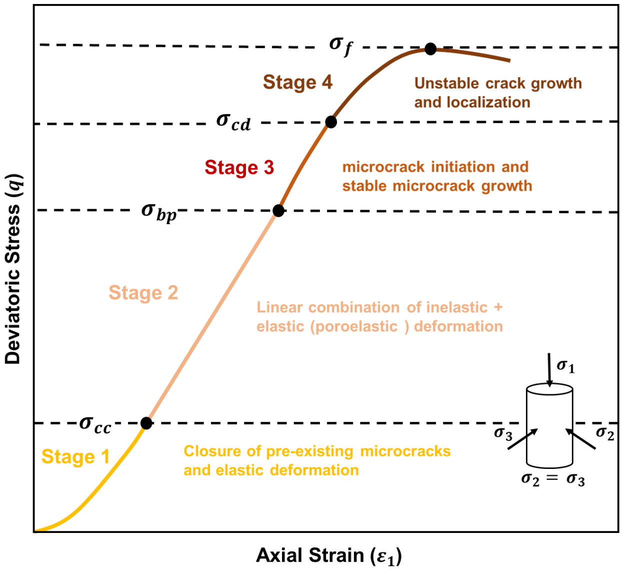

Figure 3.2: Stress-strain curve showing deformation stages of Red Felser sandstone under the condition of constant confining pressure (10 MPa). The four stages of stress levels are: the initial crack closure ($\boldsymbol{\sigma}_{cc}$), brittle yield point stress ($\boldsymbol{\sigma}_{bp}$), crack damage stress ($\boldsymbol{\sigma}_{cd}$) and maximum strength ($\boldsymbol{\sigma}_f$).

Many experimental researchers have identified the mechanical behavior and deformation process of sandstone subjecting to conventional deviatoric testing (Baud et al., 2006; Brantut et al., 2013; Cai, 2010; Hoek, 1965; H. L. Wang et al., 2017). This behavior is normally represented in terms of mean effective stress versus total porosity reduction or deviatoric stress versus axial deformation (Wong & Baud, 2012; J.-c. Zhang et al., 2021). As shown in Figure 3.2, the four stages of the Red Felser sandstone deformation up to reaching maximum strength are as follows (Martin & Chandler, 1994; Pijnenburg et al., 2019):

- Stage 1 (from the start to $\boldsymbol{\sigma}_{cc}$): A non-linear behavior that reflects the closure of pre-existing cracks or damage alongside poro-elastic deformation.

- Stage 2 (from $\boldsymbol{\sigma}_{cc}$ to $\boldsymbol{\sigma}_{bp}$): Near-linear behavior of sandstone which is known as purely elastic (poroelastic) deformation.
- Stage 3 (from $\boldsymbol{\sigma}_{bp}$ to $\boldsymbol{\sigma}_{cd}$): The deformation shows non-linear behavior due to the initiation of new microcracks and stable crack growth.
- Stage 4 (from $\boldsymbol{\sigma}_{cd}$ to $\boldsymbol{\sigma}_{f}$): The concave-down behavior in this regime is attributed to the onset of grain crushing, unstable crack growth, and shear crack localization.

Among different stages of deformation, stage 2 and the early part of stage 3 are important from an energy storage perspective. This is because all the energy storage systems should be operated below the yield point and within a safe zone to avoid failure and accumulation of inelastic deformation. Recent and previous experimental studies on applying cyclic loading have reported a significant contribution of inelastic deformation within stage 2 (fully linear zone), where the inelastic deformation can contribute from 20% to 70% of total deformation (Hernandez et al., 2022; Pijnenburg et al., 2018, 2019; Shalev et al., 2014). Thus, applying cyclic stress conditions can change the deformation mechanism of sandstone resulting in an accumulation of inelastic deformation and damage as the number of cycles increases, which accordingly influences mechanical, acoustic and other petrophysical properties (Peng et al., 2019; Shen et al., 2020; Taheri et al., 2016). The intensity and quantity of this change (damage) can be different according to stress level (Figure 3.2) and cyclic-related parameters (amplitude and frequency of cycles).

A few researchers have focused on the effect of frequency of the cycles on sandstone (Bagde & Petroš, 2005; Fuenkajorn & Phueakphum, 2010; Ma et al., 2013; Peng et al., 2020). They observed that by increasing the frequencies, damage and axial deformation decrease because of the prevention of the growth of new fractures in both compaction and inelastic stages. Also, a few researchers studied the effect of the amplitude of cycles on the lifetime of sandstone (Z. Li et al., 2022; Taheri et al., 2016; Zhenyu & Haihong, 1990). Studies into the effect of amplitude indicated that by increasing the stress amplitude, the residual strain accumulation rate in sandstone is increased, resulting in reduced fatigue life. Also, some studies have focused on the evolution of the mechanical properties of reservoir sandstone under different operating conditions (Geranmayeh Vaneghi et al., 2020; Liang et al., 2019; Peng et al., 2020; Sun et al., 2017). Nevertheless, there are very few studies into the effect of cyclic-related parameters on the quantification of inelastic deformation from the perspective of energy storage.

In addition to the study of mechanical evolution itself under cyclic loading, some studies have attempted to use non-destructive methods such as active and passive acoustics to monitor and correlate the number of cycles and cycles pattern with different acoustic parameters (Jiang et al., 2019; Meng et al., 2018; Shen et al., 2020; Yin & Xu, 2020). The Acoustic Emission (AE) technique is a non-destructive method defined as a transient elastic wave that is produced by released strain energy due to an internal phenomenon such as grain slides or crushing, plastic deformation, and microcrack initiation (Grosse & Ohtsu, 2008; Naderloo et al., 2019). However, the AE technique has not yet been used to correlate the different types of elastic and inelastic deformations occurring in sandstone under cyclic loading with AE events.

In this chapter, we perform cyclic triaxial experiments on the Red Felser sandstone to quantify the inelastic deformation occurring in sandstone under different cyclic-related parameters. Besides, the effect of the stress regime was investigated on types of deformation (time-dependent and instantaneous) and inelastic deformation. In particular, we focus on the evolution of the axial inelastic strain, the number of generated AE events per cycle, and the correlation between the cumulative inelastic strain and cumulative AE numbers. Experimental studies have limitations associated with the geometry scale, time scale, and heterogeneity. Thus, to explore the effects of cyclic loading for longer time scales and large-scale reservoir models, constitutive models are usually developed based on experimental data to determine the different types of deformations (elastic, viscoelastic, creep, plastic).

Several forms of constitutive models have been taken into account for various types of rocks in the literature, including rock salt (Khaledi et al., 2016; Pouya et al., 2016) and generalized models for brittle rocks (Cerfontaine et al., 2017). Models such as the Maxwell model, the Kelvin-Voigt model, and the Fractional Maxwell model, attempt to consider the viscoelastic strain in rocks (Ding et al., 2017; J. Wang et al., 2022). The time-dependent plastic creep strain is modeled using a power law for rock-salt, brittle porous rocks (He et al., 2022; Ramesh Kumar et al., 2021; Xu et al., 2018) and also modelled using viscoplastic deformation where the plastic strain starts accumulating above a certain stress level (X. Li & Yin, 2021; Tsai et al., 2008; Yang & Hu, 2018). Lastly, in a generalized form for soil and rocks, the time-independent plastic strain has been considered (Carter et al., 1979; de Borst, 1987; Pijnenburg et al., 2019; Vermeer & De Borst, 1984; Weng & Ling, 2013; Xu et al., 2018). Recently Modified Cam Clay model (MCC) (Carter et al., 1979) was employed to explain the inelastic deformation of sandstone below the brittle yield point (Pijnenburg et al., 2019). However, there are very few attempts by researchers trying to quantify all the deformations observed in different stress regimes under cyclic loading on sandstone.

To address the above challenge, based on the observed experimental results, different constitutive models were conglomerated in this chapter. The Kelvin-Voigt model has been employed to quantify viscoelastic deformation. Time-independent plastic deformation in the near-linear regime is accounted for using the MCC model, which is further modified, inspired by (Carter et al., 1979), to account for the effect of cyclic loading. A hardening-softening model is considered for time-independent plastic deformation in a brittle regime (de Borst, 1987; Vermeer & De Borst, 1984). Thus, the appropriate plasticity and creep model is employed depending on the measured brittle yield point from the experiments.

The rest of the paper is structured as follows. First, the experimental setup and methodology are described. Next, the employed constitutive laws are presented in detail. Experimental results are further elaborated, showing the effect of amplitude, frequency of the cycles, and stress regime on axial deformation and acoustic emission characteristics. Then, numerical results are calibrated and compared with experimental data. Based on the experimental and numerical results, conclusions are drawn.

3.2. EXPERIMENTAL DESIGN AND TEST SCHEME

3.2.1. SAMPLE PREPARATION AND LOADING APPARATUS

Red Felser sandstone was selected as the reservoir rock for the cyclic experiments. Red Felser sandstone is part of the Rotliegend formation, which originates from near Kaiserslautern, Germany. Its lithology and geological age make it relevant for storage applications in the Slochteren sandstone in the Netherlands. Red Felser sandstone is composed of 95% grain minerals, including 89% quartz and 6% orthoclase, and 5% matrix minerals, featuring 4% kaolinite, 1% albite, and trace amounts of haematite, chlorite, Ca-apatite, pyrite, and halite (van Uijen, 2013). All samples were drilled 30 mm in diameter from a unique rock slab to ensure the best possible reproducibility between samples. Next, the samples were cut to a nominal length of approximately 70 mm. The average density and porosity of the samples were 2.1 ± 0.015 g/cm^3 and 21.14 ± 0.7%. An example of prepared Red Felser sandstone is shown in Figure 3.4a.

To carry out the triaxial cyclic test, also known as the deviatoric cyclic test, a servo-control loading machine (with a maximum capacity of 500 kN) manufactured by the TU Delft was used (Figure 3.3) to apply axial stress ($\boldsymbol{\sigma}_1$). The loading machine is capable of achieving a maximum displacement rate of 1mm/s and a minimum displacement rate of 0.0001 mm/s. In order to apply the confining pressure or horizontal stress ($\boldsymbol{\sigma}_2$=$\boldsymbol{\sigma}_3$), an instrumented triaxial cell (capable of applying confining pressure up to a maximum of 70 MPa) as the one shown in Figure 3.3 was used together with the loading machine. The triaxial cell includes a special silicon jacket that, in addition to providing isolation between the confining fluid and the rock sample, has a total of 6 piezoelectric transducers. The vertical deformation of the rock sample is measured by two Linear Variable Displacement Transformer "LVDT" (Figure 3.3).

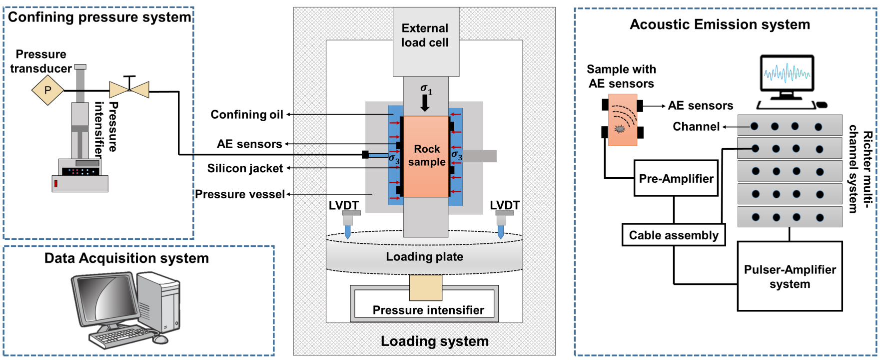

Figure 3.3: Schematic illustration of the experimental setup including loading system, data acquisition, and AE system.

3.2.2. ACOUSTIC EMISSION MONITORING

The Acoustic emission (AE) technique was used to detect the AE events and their correlation with inelastic deformation. The silicon jacket was instrumented with an array of 6 piezoceramic transducers to record AE events originating from rock samples during stress cycling. Next, the Richter system, a continuous data acquisition system was used to record AE activities captured by piezoelectric transducers. A schematic illustration of the AE system is given in Figure 3.3. The AE system consists of 4 units that can be synchronized to provide a fully expandable system with up to 20 channels. The ExStream software controls the acoustic emission system, whereas the Insite Seismic Processor software processes and manages the raw waveform data. A trigger logic is used to convert continuous waveform data into single waveforms for further analysis. Concerning background noise, the number of sensors (6 sensors were used), and array distribution, if three or more transducers exceed a voltage threshold of about 0.05 V within a time window of 480 μs and a sampling rate of 2 MHz, it can be recorded as an event.

3.2.3. TESTING PROTOCOL

In the beginning, two monotonic deviatoric tests were carried out at 10 MPa confining pressure until macroscopic sample failure occurred to determine the failure stages and deformation behavior of the Red Felser sandstone. After these tests, different deformation stages of the Red Felser sandstone were determined, such as stage 1, stage 2, and the start of stage 3, to design our experimental protocol (Figure 3.4b).

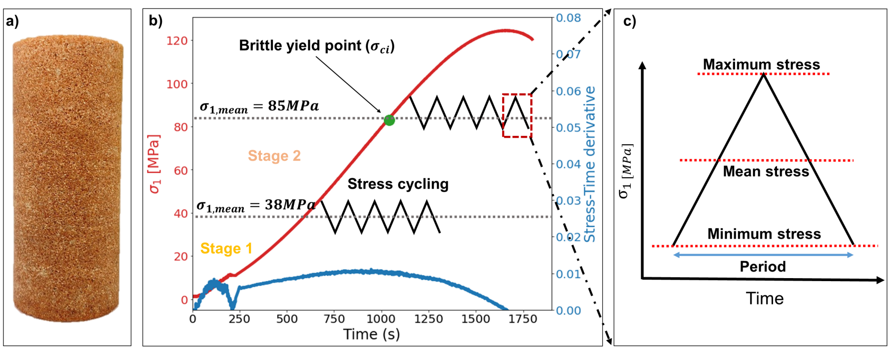

Figure 3.4: Illustration of the experimental protocol and Red Felser sandstone; a) the Red Felser sandstone sample after preparation, b) The stress-time curve together with mean stress levels (cycling stress level), and c) The triangular waveform of stress.

In total, 12 deviatoric cyclic tests were carried out, and all the samples were fully saturated with water before the tests. A vacuum saturation pump was used to saturate the samples. Due to their high porosity, all samples were fully saturated within one hour. Regarding the deviatoric cyclic test, two mean axial stresses ($\boldsymbol{\sigma}_{1,mean}$) were selected: one right at the start of stage 2 equal to 38MPa (Elastic regime) and the second one right above the brittle yield point equal to 85MPa (brittle regime). According to the stress-strain and stress-time derivatives, the brittle yield point is estimated to be 84.2 MPa (Figure 3.4b). Up to reaching the specified mean deviatoric stresses, a displacement-controlled rate of 5×10^{-5} mm/s was used to increase the stress. For the frequencies, three scenarios were evaluated F1=0.014 Hz (1.2 min/cycle), F2=0.0014 Hz (12 min/cycle), and F1=0.0002 Hz (83 min/cycle). It is difficult to apply real-field relevant frequencies (seasonal timescales) in our laboratory. We aimed to have a set of frequencies that could help shedding new lights on the time-dependent deformations, and their consistent modelling concepts. It should be mentioned that frequency is adjusted by increasing or decreasing the loading rate. Finally, two axial stress amplitudes were tested A1=20 MPa and A2=5.9 MPa. The latter is equivalent to the yearly pore pressure changes in the NORG gas field (Juez-Larre et al., 2016). These conditions were permuted, leading to 12 cyclic tests with a maximum of 8 cycles Table 3.1.

3

Table 3.1: Information about rock samples, cyclic parameters, total inelastic strain ($\boldsymbol{\varepsilon}_{1,total}^{\text{inelastic}}$), the total number of AE ($\boldsymbol{N}_{AE}$), Amplitude of the cycles (A), frequency of the cycles (f), stress regime ($\boldsymbol{\sigma}_{mean}$), and average events amplitude ($\boldsymbol{A}_{AE}^{\text{average}}$) for the cyclic tests and multi-stage (MS) creep test with confining pressure of $\boldsymbol{\sigma}_3$ = 10 MPa.

Sample	Test	$\boldsymbol{\sigma}_{mean}$ [MPa]	A [MPa]	f [Hz]	$\boldsymbol{\varepsilon}_{1,total}^{\text{inelastic}}$ [%]	$\boldsymbol{N}_{AE}$	$\boldsymbol{A}_{AE}^{\text{average}}$ $[V]$
RFD5	Cyclic	85	20	0.014	0.05	469	0.2±0.01
RFD6	Cyclic	85	20	0.0014	0.057	336	0.23±0.012
RFD7	Cyclic	85	20	0.0002	0.06	464	0.24±0.015
RFD8	Cyclic	38	20	0.014	0.031	328	0.14±0.005
RFD10	Cyclic	38	20	0.0014	0.031	310	0.17±0.008
RFD18	Cyclic	38	20	0.0002	0.045	323	0.18±0.007
RFD12	Cyclic	85	5.11	0.014	0.040	-	-
RFD16	Cyclic	85	5.11	0.0014	0.048	-	-
RFD20	Cyclic	85	5.11	0.0002	0.047	-	-
RFD14	Cyclic	38	5.11	0.014	0.016	-	-
RFD17	Cyclic	38	5.11	0.0014	0.01	-	-
RFD21	Cyclic	38	5.11	0.0002	0.027	-	-
RFD9	MS creep	-	-	-	-	-	-

A triangular waveform was selected to approximate the cyclic stress behavior of underground storage field applications. Thus the maximum stress of the waveform corresponds to the minimum pore pressure (compaction), while the minimum stress refers to the maximum stored volume or pore pressure (opening). The main parameter that defines the waveform, like mean axial stress, axial stress amplitude, and frequency (period), is shown in Figure 3.4c. It is important to mention that the waveform considers a constant stress rate during loading and unloading periods. Thus, the strain rate varies during these periods.

After designing the cyclic stress scheme, the first step for each test was reaching the desirable confining pressure ($\boldsymbol{\sigma}_3$) hydrostatically, which was 10 MPa. During the next phase, axial stress ($\boldsymbol{\sigma}_1$) was increased deviatorically by applying a constant displacement rate of 0.0005 mm/s to reach the two target mean stresses (38 MPa and 85 MPa) which was the mean stress of the waveform. After, the loading software was switched to stress control and used the built-in function to generate triangular waveforms. We applied a total of eight cycles since experiments had to be completed within a day.

In addition to 12 deviatoric tests, one multi-stage creep test was performed to provide the input parameters to model the cyclic test in the brittle regime. During the creep test, the rock sample was subjected to three axial stress ($\boldsymbol{\sigma}_1$) levels while keeping the confining pressure ($\boldsymbol{\sigma}_3$) constant at 10 MPa. The Multi-step creep test was carried out in axial stress levels of 85 MPa (8 hours), 105 MPa (3 hours), and 115 MPa (0.65 hours). In the next section, the constitutive laws are developed to model the relevant physics undergoing in sandstone.

3

3.3. CONSTITUTIVE LAW FORMULATION

Based on several experiments and observed physics, different deformation mechanisms were employed, and accordingly, the total strain ($\boldsymbol{\varepsilon}^{\mathrm{t}}$) is split into elastic strain $\boldsymbol{\varepsilon}^{\mathrm{e}}$, plastic strain $\boldsymbol{\varepsilon}^{\mathrm{p}}$, visco-elastic strain $\boldsymbol{\varepsilon}^{\mathrm{ve}}$ and creep strain $\boldsymbol{\varepsilon}^{\mathrm{cr}}$ as

$$\boldsymbol{\varepsilon}^{\mathrm{t}} = \boldsymbol{\varepsilon}^{\mathrm{e}} + \boldsymbol{\varepsilon}^{\mathrm{p}} + \boldsymbol{\varepsilon}^{\mathrm{ve}} + \boldsymbol{\varepsilon}^{\mathrm{cr}}. \tag{3.1}$$

Schematic illustration of the numerical model is shown in Figure 3.5.The elastic strain based on Hooke's law is given by,

$$\boldsymbol{\varepsilon}^{\mathrm{e}} = \frac{q}{E_1}. \tag{3.2}$$

Here q is the deviatoric stress, E_1 is the elastic Young's modulus. The viscoelastic strain is the time dependent strain which is given by

$$\boldsymbol{\varepsilon}^{\mathrm{ve}} = \frac{q}{E_2}\left(1 - \exp\left(\frac{-E_2}{\eta_1}t\right)\right). \tag{3.3}$$

Here E_2, η_1 are the Youngs modulus and viscosity of the viscoelastic unit. The creep strain is inelastic strain which is time dependent that is given by

$$\boldsymbol{\varepsilon}^{\mathrm{cr}} = \left(\frac{\sigma_1 - \sigma^{BP}}{\eta_2}\right)\Delta t. \tag{3.4}$$

Here σ^{BP} is the brittle yield point and η_2 is the viscosity of the brittle creep unit. Finally, the plastic strain is split into two components based on the mechanisms which are given by

$$\boldsymbol{\varepsilon}^{\mathrm{p}} = \boldsymbol{\varepsilon}^{\mathrm{p}}_{\mathrm{compaction}} + \boldsymbol{\varepsilon}^{\mathrm{p}}_{\mathrm{dilation}}. \tag{3.5}$$

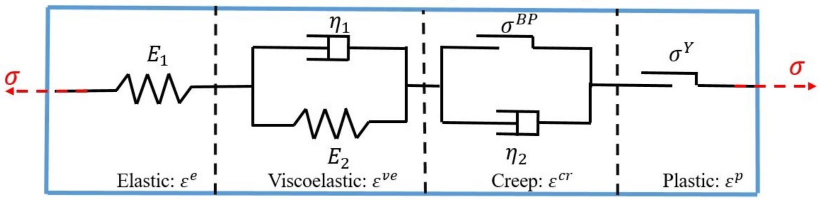

Figure 3.5: Schematic illustration of the constitutive model when a constant load is applied.

To compute $\boldsymbol{\varepsilon}^{\mathrm{p}}_{\mathrm{compaction}}$ Modified Cam Clay model (MCC) (Roscoe & Burland, 1968) and for $\boldsymbol{\varepsilon}^{\mathrm{p}}_{\mathrm{dilation}}$ hardening softening model was used (Vermeer & De Borst, 1984). Finally, the total strain in the rock is given based on the brittle yield point, i.e.,

$$\boldsymbol{\varepsilon}^{\mathrm{t}} = \begin{cases} \frac{q}{E_1} + \frac{q}{E_2}(1-\mathrm{e}^{-\frac{E_2}{\eta_1}t}) + f_1(q,\alpha_i) & \sigma_1 < \text{Brittle yield point} \\ \frac{q}{E_1} + \frac{q}{E_2}(1-\mathrm{e}^{-\frac{E_2}{\eta_1}t}) + \frac{\sigma_1-\sigma^{BP}}{\eta_2}\Delta t + f_2(q,\beta_i) & \sigma_1 > \text{Brittle yield point} \end{cases} \tag{3.6}$$

In the following subsections, the plasticity models are elaborated.

3.3.1. MODIFIED CAM CLAY MODEL

The MCC model uses a yield surface that determines whether rocks behave in an elastic or plastic behavior. The critical components are shown in the schematic Figure 3.6. This model has been used to account for inter-granular cracking, clay crushing, and grain sliding, which takes place below the brittle yield point (Pijnenburg et al., 2019).

In this chapter, the MCC model is extended to account for cyclic inelastic compaction inspired by the work done by (Carter et al., 1979). The yield function is given by

$$f = q^2 - M^2(p(p_c - p)). \tag{3.7}$$

Here M is the slope of the critical state line, p_c is the pre-consolidation pressure, and p is the volumetric stress. The pre-consolidation pressure is expressed as

$$\frac{\delta p_c}{p_c} = \frac{\delta p_l}{p_l}. \tag{3.8}$$

Here p_l is the loading parameter derived from the yield surface envelope, which is

$$p_l = p + \frac{q}{M}^2\left(\frac{1}{p}\right). \tag{3.9}$$

The plastic strain is computed from the consistency condition by normalizing the stresses (Coussy, 2004; Nikolinakou et al., 2012). The change in void ratio is given by

$$de = -(1+e)\times\boldsymbol{\varepsilon}^{\mathrm{p}}_{p}. \tag{3.10}$$

The volumetric and deviatoric parts of the incremental plastic strain is given by

$$\begin{bmatrix}\Delta\boldsymbol{\varepsilon}^{\mathrm{p}}_{p}\\ \Delta\boldsymbol{\varepsilon}^{\mathrm{p}}_{q}\end{bmatrix} = \Omega\times\begin{bmatrix} M^2-\eta & 2\eta \\ 2\eta & \frac{2\eta}{M^2-\eta^2}\end{bmatrix}\times\begin{bmatrix}dp\\ dq\end{bmatrix}. \tag{3.11}$$

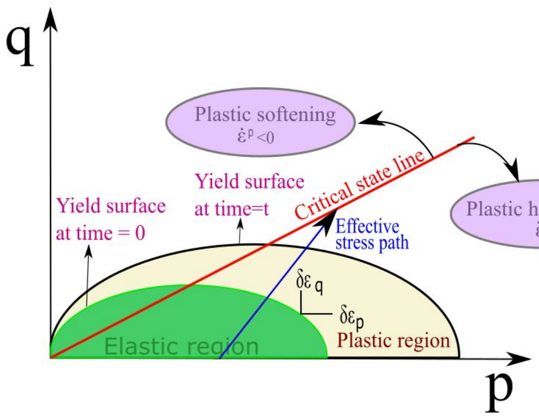

Figure 3.6: The schematic diagram of modified cam clay model showing the yield envelopes.

Here,

$$\Omega = \frac{\lambda_{MCC} - \kappa}{(1+e)\,p(M^2+\eta^2)} \tag{3.12}$$

in which

$$\kappa = \frac{1+e}{K} \tag{3.13}$$

and

$$K = \frac{E_{avg}}{3\,(1-2\upsilon)}. \tag{3.14}$$

Furthermore, $\eta = q/p$, $e = \phi/1-\phi$, ϕ is the porosity, and e is the void ratio. For a detailed derivation, refer to the literature (Coussy, 2004; Nikolinakou et al., 2012). Also, here dp and dq are the incremental volumetric stress and deviatoric stress, respectively. To account for the cyclic part of the inelastic strains, θ is the parameter employed which accounts for the cyclic element of the MCC model equation 3.8, which is given by

$$\frac{\delta p_c}{p_c} = \theta \frac{\delta p_l}{p_l}. \tag{3.15}$$

$$p_c^{new} = p_c^{old} \left(\frac{p_l^{max}}{p_c^{old}} \right)^{\theta} \tag{3.16}$$

So this ensures that a new pre-consolidation parameter p_c^{new} is established cycle after cycle. The evolution of the pre-consolidation parameter is ruled by equation 3.15 and equation 3.16 after integration. This p_c^{new} is lower than p_l^{max} but as the number of cycles increases p_c^{new} tends to the value of p_l^{max}. If θ is equal to 1, the model reduces to the standard MCC. This proposal is inspired by the work of (Carter et al., 1979), which dealt with the deformation of clays under cyclic loadings. So from this model, plastic strain from $\boldsymbol{\varepsilon}^{\mathrm{p}}_{\mathrm{compaction}}$ is computed.

3.3.2. HARDENING SOFTENING MODEL

The hardening-softening model is employed to model the plastic strains induced by the fracturing of the grains above the brittle yield point. The model is explained briefly here, and for a deeper understanding, the reader is referred to (de Borst, 1987; Vermeer & De Borst, 1984). The model for triaxial conditions ($\sigma_3 = \sigma_2$) is based on Coulomb-Mohrs yield surfaces f_1 and f_2 (equations 3.17 and 3.18), which is given by

$$f_1 = \frac{1}{2}(\sigma_3 - \sigma_1) + \frac{1}{2}(\sigma_1 + \sigma_3)\sin(\phi_f) - c \times \cos(\phi_f) = 0 \tag{3.17}$$

$$f_2 = \frac{1}{2}(\sigma_2 - \sigma_1) + \frac{1}{2}(\sigma_1 + \sigma_2)\sin(\phi_f) - c \times \cos(\phi_f) = 0. \tag{3.18}$$

Here c is the cohesion of the rock and ϕ_f is the internal friction angle. Similar surfaces are defined for the plastic potential flow, as can be seen in equations 3.19 and 3.20

$$g_1 = \frac{1}{2}(\sigma_3 - \sigma_1) + \frac{1}{2}(\sigma_1 + \sigma_3)\sin(\psi) + \text{constant} \tag{3.19}$$

$$g_2 = \frac{1}{2}(\sigma_2 - \sigma_1) + \frac{1}{2}(\sigma_1 + \sigma_2)\sin(\psi) + \text{constant.} \tag{3.20}$$

Here ψ is the dilation angle. These plastic potential functions (g_1 and g_2) are responsible for the magnitude of the plastic strain increments $\dot{\boldsymbol{\varepsilon}}^p$, as can be seen in the general plasticity rule depicted by equation 3.21 as well as in equations 3.22 and 3.23 for axial and volumetric plastic strains respectively. The rate of plastic strain is given by

$$\dot{\boldsymbol{\varepsilon}}^p = \lambda_1 \frac{\partial g_1}{\partial \boldsymbol{\sigma}} + \lambda_2 \frac{\partial g_2}{\partial \boldsymbol{\sigma}} \tag{3.21}$$

$$\dot{\varepsilon}_1^p = \frac{1}{2}(\lambda_1 + \lambda_2)(-1 + \sin(\psi)) \tag{3.22}$$

$$\dot{\varepsilon}_v^p = (\lambda_1 + \lambda_2)\sin(\psi). \tag{3.23}$$

The plastic multipliers are computed using the below expressions which are obtained from de Borst (1987), given by

$$\lambda_1 = \frac{\mu_4 \left(\frac{\partial f_1}{\partial \boldsymbol{\sigma}}\right)^T \mathbb{D}\dot{\boldsymbol{\varepsilon}} - \mu_2 \left(\frac{\partial f_2}{\partial \boldsymbol{\sigma}}\right)^T \mathbb{D}\dot{\boldsymbol{\varepsilon}}}{\mu_1\mu_4 - \mu_2\mu_3} \tag{3.24}$$

$$\lambda_2 = \frac{\mu_1 \left(\frac{\partial f_2}{\partial \boldsymbol{\sigma}}\right)^T \mathbb{D}\dot{\boldsymbol{\varepsilon}} - \mu_3 \left(\frac{\partial f_1}{\partial \boldsymbol{\sigma}}\right)^T \mathbb{D}\dot{\boldsymbol{\varepsilon}}}{\mu_1\mu_4 - \mu_2\mu_3}. \tag{3.25}$$

Where μ_1,μ_2,μ_3 and μ_4 are define as:

$$\mu_1 = \left(-\frac{\partial f_1}{\partial \bar{\varepsilon}^p}\frac{\partial \bar{\varepsilon}^p}{\partial \boldsymbol{\varepsilon}^p} + \mathbb{D}\frac{\partial f_1}{\partial \boldsymbol{\sigma}}\right)^T \frac{\partial g_1}{\partial \boldsymbol{\sigma}} \tag{3.26}$$

$$\mu_2 = \left(-\frac{\partial f_1}{\partial \bar{\varepsilon}^p}\frac{\partial \bar{\varepsilon}^p}{\partial \boldsymbol{\varepsilon}^p} + \mathbb{D}\frac{\partial f_1}{\partial \boldsymbol{\sigma}}\right)^T \frac{\partial g_2}{\partial \boldsymbol{\sigma}} \tag{3.27}$$

$$\mu_3 = \left(-\frac{\partial f_2}{\partial \bar{\varepsilon}^p}\frac{\partial \bar{\varepsilon}^p}{\partial \boldsymbol{\varepsilon}^p} + \mathbb{D}\frac{\partial f_2}{\partial \boldsymbol{\sigma}}\right)^T \frac{\partial g_1}{\partial \sigma} \tag{3.28}$$

3

$$\mu_4 = \left(-\frac{\partial f_2}{\partial \bar{\boldsymbol{\varepsilon}}^p}\frac{\partial \bar{\varepsilon}^p}{\partial \boldsymbol{\varepsilon}^p} + \mathbb{D}\frac{\partial f_2}{\partial \boldsymbol{\sigma}}\right)^T \frac{\partial g_2}{\partial \boldsymbol{\sigma}}. \tag{3.29}$$

$\mathbb{D}$ is the elasticity matrix, and the hardening parameter $\bar{\varepsilon}^p$ is given by

$$\bar{\varepsilon}^p = \int \sqrt{\frac{2}{3}(\dot{\varepsilon}_1^p\dot{\varepsilon}_1^p + \dot{\varepsilon}_2^p\dot{\varepsilon}_2^p + \dot{\varepsilon}_3^p\dot{\varepsilon}_3^p)}dt. \tag{3.30}$$

The expressions for the above parameters are elaborated in (KUMAR, 2023). Dilation-based plastic strain is computed from this model.

Next section, we discuss the experimental results obtained from imposing cyclic loading on sandstone.

3.4. EXPERIMENTAL RESULTS

3.4.1. BEHAVIOR OF STRESS AND STRAIN

The total inelastic strain was computed by subtracting the strain of the initial loading from the strain at the final unloading at a referential stress ($\boldsymbol{\sigma}_1$) of 15 MPa as shown by equation 3.31 and (Figure 3.7b). The stress was not decreased to exactly the confining pressure (10 MPa) to avoid damage to the cell's silicon jacket. The cumulative apparent inelastic axial strain over the cycle is estimated by subtracting the axial strain at the end of every cycle minus the strain at the beginning of the first cycle (Equation 3.32 and Figure 3.7b). All strains were measured at minimum axial stress of the cyclic test. This inelastic strain is considered apparent because it is affected by the time-dependent deformation of the rock such as visco-elastic deformation.

$$\boldsymbol{\varepsilon}_{1,total}^{\text{inelastic}} = \boldsymbol{\varepsilon}_{1f}^2 - \boldsymbol{\varepsilon}_{1in}^1 \tag{3.31}$$

$$\boldsymbol{\varepsilon}_{1,apparent}^{\text{inelastic}} = \boldsymbol{\varepsilon}_{1f}^4 - \boldsymbol{\varepsilon}_{1in}^3 \tag{3.32}$$

Figure 3.7a shows the imposed stress and strain behavior against time for the test with the lowest frequency (0.0002Hz) and larger amplitude (20 MPa) in the brittle regime. In this figure, it can be seen that the axial strain ($\boldsymbol{\varepsilon}_1$) increases from one cycle to the other, where the peaks and valleys show a clear rising trend. In the stress-strain curve (Figure 3.7b) the final unloading curve has a concave shape, and the apparent elastic strain is larger than the total inelastic strain, which can be due to the visco-elasticity. The total and the apparent inelastic strain were calculated for all 12 tests to investigate the effect of different stress regimes, frequencies, and amplitudes on inelastic deformation.

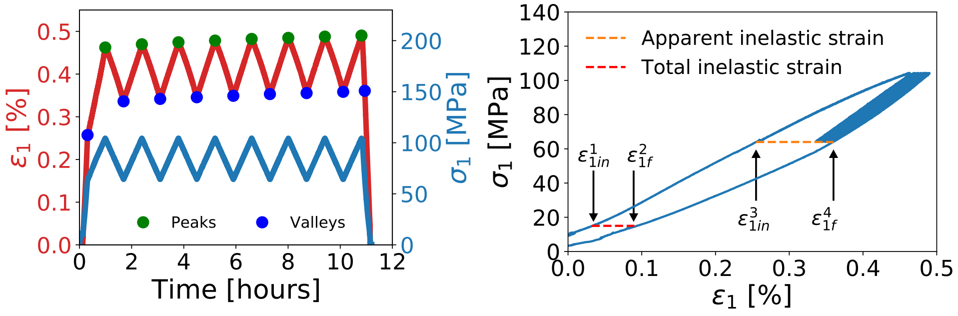

(a) (b)

Figure 3.7: Imposed cyclic stress and strain response during the time: (a) Evolution of peaks and valleys for the strain, (b) Calculation of total and apparent inelastic strain.

The total inelastic strain after eight cycles was estimated following equation 3.31 and the results are shown in Figure 3.8. As expected, there are inelastic strains when cyclic loading is applied in the brittle regime ($\boldsymbol{\sigma}_{mean1}$ > brittle yield point). In the fully linear regime, however, there are also inelastic deformations ($\boldsymbol{\sigma}_{mean1}$ < brittle yield point). Inelastic strains in the brittle regime are larger than in the elastic regime. Stress amplitude also has an impact on inelastic strain in both regimes. The larger the amplitude, the larger the inelastic strain. Frequency affects the total inelastic strain in both regimes. The effect of frequency is more pronounced in the elastic regime, and by reducing the frequency, total inelastic strain increases.

3.4.2. CUMULATIVE APPARENT INELASTIC STRAIN OVER CYCLES

Ideally, inelastic strain should be measured at deviatoric stress equal to zero. Nevertheless, the apparent inelastic strain is used as a qualitative estimation to understand the evolution of inelastic strain per cycle (Equation 3.32). Figure 3.9 shows typical results obtained in every test. The main observation is that the largest apparent inelastic strain occurs in the first cycle. For the following cycles, the rate of inelastic strain per cycle decreased. However, the rate of the decrease in inelastic strain for the test performed in an elastic regime is higher than the test in the brittle regime and approaching zero Figure 3.9b.

To complement the analysis, the results of the cumulative apparent inelastic strain of the 12 tests were plotted for the same amplitude and deformation regime as shown in Figure 3.10 and Figure 3.11. The apparent inelastic strain of the first cycle was removed to improve the comparison and focus on strain evolution over the cycles. Figure 3.10a and Figure 3.10b show that deformation in the brittle regime is time-dependent and inelastic strain increases per cycle. Reducing the frequency within the brittle zone increases the inelastic strain. This time-dependent deformation can be caused by visco-elastic and/or brittle creep behavior. For the tests in the elastic regime (Figure 3.11a and Figure 3.11b), there is no time-dependent deformation, and all the inelastic strains approach zero by increasing the number of cycles. According to Figure 3.10 and Figure 3.11, by reducing

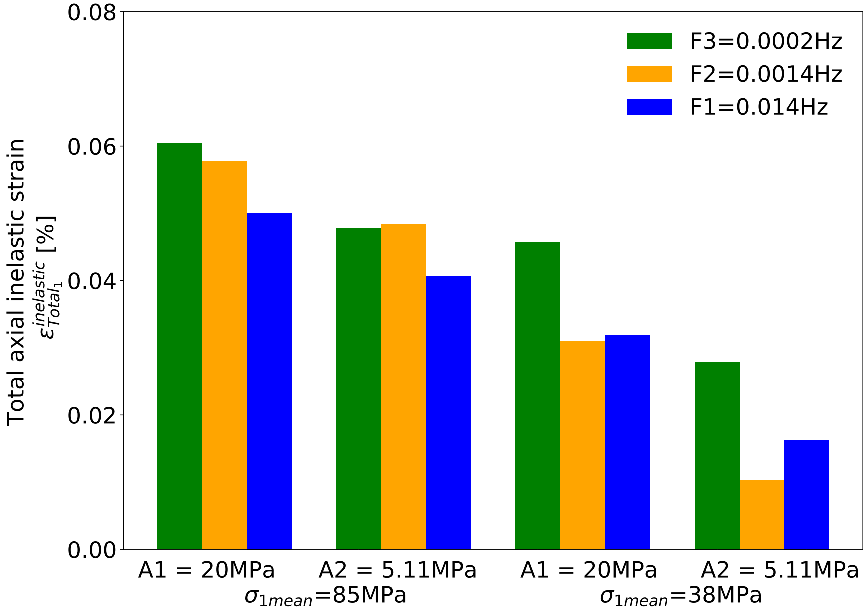

Figure 3.8: The left two bars illustrate the effect of amplitude and frequency on total inelastic deformation under a high-stress regime, while the right two bars demonstrate the effect of amplitude and frequency under a lower effective mean stress regime at the end of the experiments.

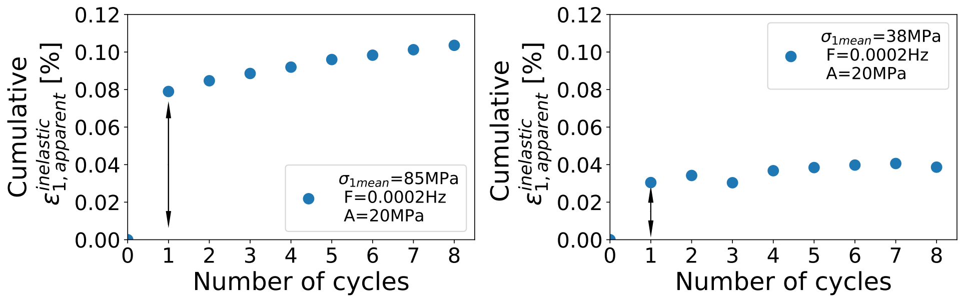

(a) σ_{mean} = 85 MPa

(b) σ_{mean} = 38 MPa

Figure 3.9: Apparent inelastic axial strain versus the number of cycles in both studied regime: (a) Brittle regime, and (b) the elastic regime, for the lowest frequency f = 0.0002 Hz and maximum amplitude (A = 20 MPa). Arrows indicate the inelastic deformation from the first cycle.

the amplitude of cycles, the magnitude of the inelastic strain decrease for both stress regimes. The effect of frequency within the elastic regime is not clear, which can be due to the instability or sensitivity of the machine to small deformations (Figure 3.11a and Figure 3.11b).

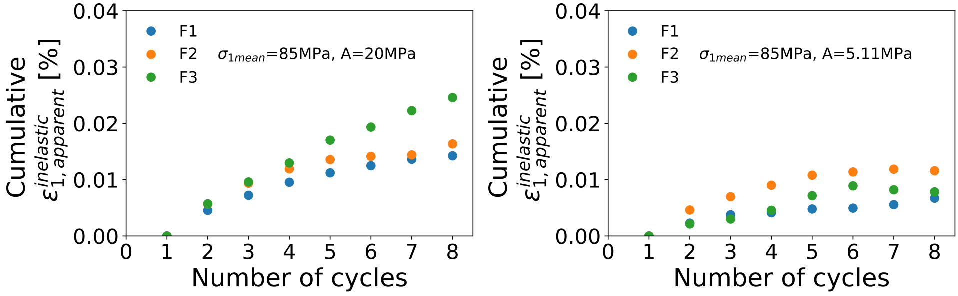

(a) (b)

Figure 3.10: Comparison of cumulative apparent inelastic strain evolution after removing the first cycle for the different tested frequencies (F1=0.014 Hz, F2=0.0014 Hz, F3=0.0002 Hz) within the brittle regime: (a) Results with amplitude of 20 MPa, (b) Results with amplitude of 5.11 MPa.

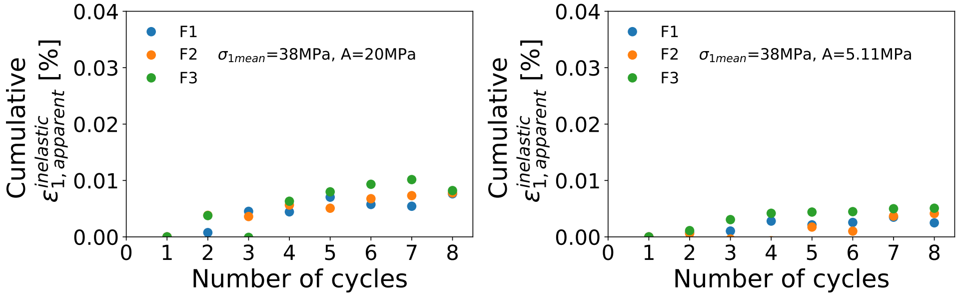

(a) (b)

Figure 3.11: Comparison of cumulative apparent inelastic strain evolution after removing the first cycle for the different tested frequencies (F1=0.014 Hz, F2=0.0014 Hz, F3=0.0002 Hz) within the elastic regime: (a) Results with amplitude of 20 MPa, (b) Results with amplitude of 5.11 MPa.

3.4.3. ACOUSTIC EMISSIONS AND INELASTIC STRAIN

The AE events were recorded only for the tests corresponding to the maximum stress amplitude (20 MPa). Different parameters from the AE technique, such as AE energy, amplitude, and the number of AE, can be used to interpret failure and deformation mechanisms. As shown in Figure 3.12a, the AE amplitude was plotted together with imposed axial stress versus time. AE events were recorded early in the first loading interval at axial stress slightly higher than the confining stress. After starting the cyclic loading, the maximum acoustic intensity and the number of events were recorded in the first cycle. In general, by increasing the number of cycles, the number of AE and amplitude decreased (Figure 3.12b).

Results concerning the effect of the deformation regime and frequency on the AE amplitude and number of AE events are shown in Figure 3.13. In terms of AE amplitude, the average AE amplitude for the tests in the brittle regime is higher than the average AE amplitude for the tests in the elastic regime (Table 3.1).

This was an anticipated result; micro-fracturing in the brittle regime is expected to re-

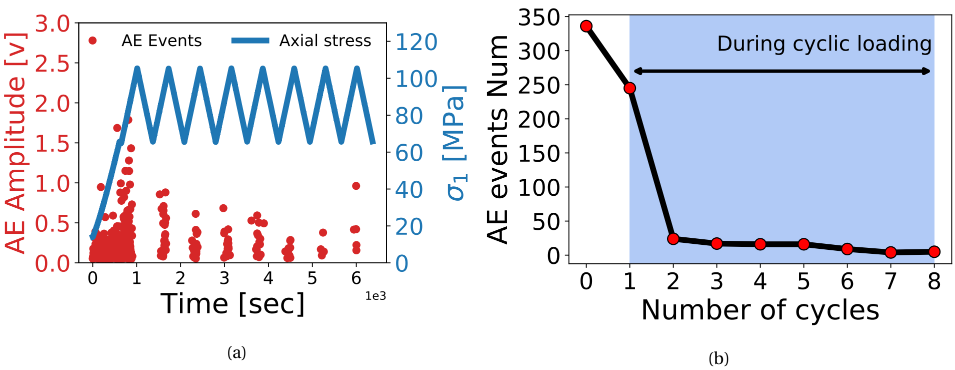

Figure 3.12: The results of acoustic emissions: (a) AE amplitude together with axial stress versus time, (b) Evolution of the number of AE events per cycle. The result is for the test with medium frequency (0.0014Hz) and larger amplitude (20 MPa) in the brittle regime.

lease more elastic energy than any other mechanism presented at a stress lower than the brittle yield point (such as clay compaction and pore closure). In addition to AE amplitude, the number of generated AE during the first cycle and the total number of AE events in the brittle regime is more than in the elastic regime. The total number of AE events for the elastic regime is similar for the three tested frequencies (Table 3.1).

Acoustic emissions are, in most cases, an indicator of inelastic strains, as mentioned by Lockner (1993). There is an interesting and similar observation between AE and inelastic strain per cycle. In essence, the maximum number of AE events and major inelastic strain were observed during the first cycle and then decreased by increasing the number of cycles (Figure 3.9 and Figure 3.13). Figure 3.14 indicates a strong linear correlation between a cumulative number of AE events and cumulative apparent inelastic strain. The linear regression slope for samples subjected to the brittle regime is more than those subjected to the elastic regime (Figure 3.14a). Besides, a change in frequency within the brittle regime influences the correlation slope; however, there is no significant influence of frequency change within the elastic regime.

3.4.4. DISCUSSION AND INTERPRETATION OF EXPERIMENTAL RESULTS

The possible reasons behind the obtained results regarding deformation and AE characteristics in both elastic and brittle regimes can be discussed separately. As expected, inelastic strains and AE were recorded when tests were carried out in the brittle regime (axial stresses higher than brittle yield point). When the maximum axial stress is higher than the brittle yield point, the critical and/or sub-critical micro-cracks are induced in the quartz grains (grain bridging and breakage), leading to irreversible changes in the rock microstructure and the release of elastic waves ((Brantut et al., 2013; Martin & Chandler, 1994)). An increase in the amplitude of cycles can create high-stress concentrations between grains, leading to more inter-granular and intra-granular cracks being induced. For the Red Felser sandstone, it is clear that the rock can experience time-dependent inelastic deformations when the stress is above the brittle yield point. This was proven by

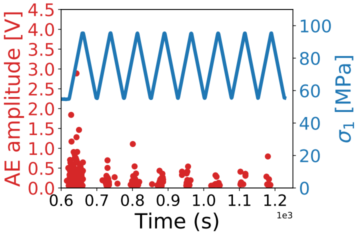

(a) $\boldsymbol{\sigma}_{mean}$ = 85, F=0.014 Hz, A= 20MPa

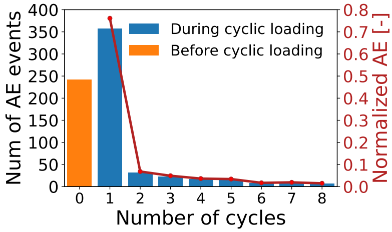

(b) $\boldsymbol{\sigma}_{mean}$ = 85, F=0.014 Hz, A= 20MPa

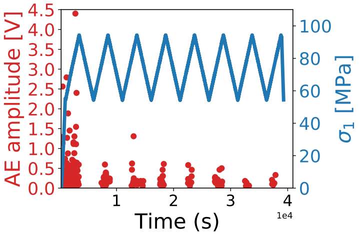

(c) $\boldsymbol{\sigma}_{mean}$ = 85, F=0.0002 Hz, A= 20MPa

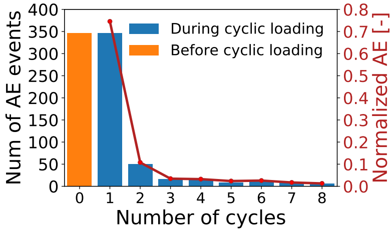

(d) $\boldsymbol{\sigma}_{mean}$ = 85, F=0.0002 Hz, A= 20MPa

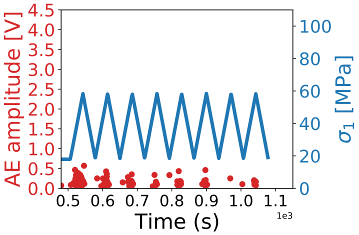

(e) $\boldsymbol{\sigma}_{mean}$ = 38, F=0.014 Hz, A= 20MPa

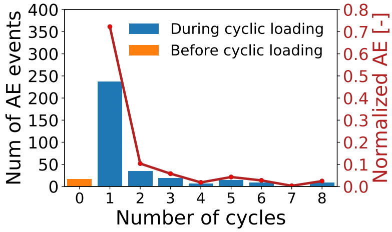

(f) $\boldsymbol{\sigma}_{mean}$ = 38, F=0.014 Hz, A= 20MPa

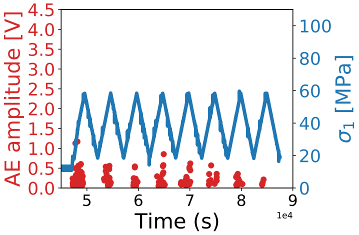

(g) $\boldsymbol{\sigma}_{mean}$ = 38, F=0.0002 Hz, A= 20MPa

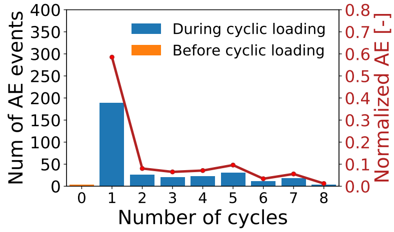

(h) $\boldsymbol{\sigma}_{mean}$ = 38, F=0.0002 Hz, A= 20MPa

Figure 3.13: Comparison of the AE event numbers and AE amplitude for tests in brittle (a, b, c, and d) and elastic (e, f, g, and h) regimes at different frequencies and fixed amplitude of 20MPa. Figures a, c, e, and g show the AE amplitude together with axial stress versus time, and figures b, d, f, and h illustrate the evolution of AE event numbers per cycle.

the results of the creep tests (see Figure 3.19) and by the effect of frequency on apparent inelastic strain during deviatoric cyclic tests (see Figure 3.10). This deformation mechanism is called brittle creep (Brantut et al., 2013). Therefore, using low frequency and high amplitude cycles induces more inelastic deformations (Figure 3.8).

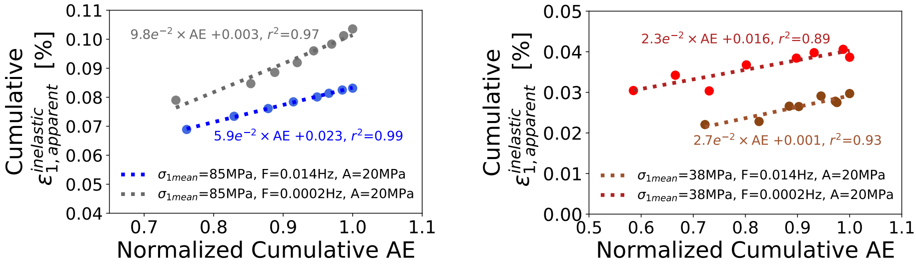

(a) (b)

Figure 3.14: Cross plot of cumulative AE vs cumulative inelastic strain. (a) The brittle regime, (b) The elastic regime.

Interestingly, inelastic strain and AE were also recorded in the elastic regime (axial stresses lower than brittle yield point), where only elastic strains are usually expected. Inelastic deformations at low-stress levels for sandstone have also been reported by (Gatelier et al., 2002; Pijnenburg et al., 2019). From the micro-structural point of view, inelastic strains in sandstones below the brittle yield point have been interpreted as irreversible rock compaction caused by crushing and slip of clay layers plus inter-granular cracking (Pijnenburg et al., 2018, 2019). Red Felser sandstone comprises low volumetric proportions of clay and orthoclase grains that could crush or breake at stress levels lower than the onset for intra-granular cracking of quartz grains. Regarding the cyclic inelastic strains, it has been related to the irreversible closure of induced and existing cracks (Cerfontaine et al., 2017).

For the same stress amplitude, the AE amplitude and the total number of AE differ between the two regimes, as shown in Figure 3.13, Figure 3.14, and Table 3.1. This indicates the different mechanisms that are taking place. For instance, micro-cracking of quartz grains that takes place above the brittle yield point is expected to release more energy than inter-granular cracking, clay crushing, or grain sliding, which are the possible mechanisms below the brittle yield point.

Based on the observations from the experiments, the comparison between the developed constitutive model in section 3.3 with experimental results are elaborated.

3.5. MODELLING RESULTS

3.5.1. BELOW BRITTLE YIELD POINT

Firstly, the constitutive laws are calibrated with the first cycle and further they are compared with the experimental results in the remaining cycles. From the Figure 3.14, it was found that the apparent inelastic strain (viscoelastic + inelastic) is directly proportional to the AE. Based on this observation, the number of recorded AE events for every cycle and only the estimate of inelastic strain from AE events is correlated by using a direct proportionality. Using normalized AE as presented in Figure 3.13, the estimate of inelastic strain for each cycle is given by

$$\varepsilon_1^{Inelastic,i} = \frac{AE_i}{AE_{\text{Total}}} \times \varepsilon_{Total}^{Inelastic}. \tag{3.33}$$

Here AE_{Total} is the total number of AE events during stress cycling, AE_i is the number of AE events recorded at each cycle 'i' and $\varepsilon_{Total}^{Inelastic}$ is the total inelastic strain from the experiments. Using the superposition principle (Kelly, 2013), the cyclic variation of 'q' with a deviatoric stress stepping scheme was employed. Young's modulus of the rock (elastic and viscoelastic) was initially calibrated with the first cycle of each experiment. Then, the MCC model parameters were fine-tuned using the inelastic strain from the first cycle. Using these parameters, the experimental results are compared with the analytical solutions.

Table 3.2 shows the parameters employed for the three frequencies at an amplitude of 20 MPa. Figure 3.15a and Figure 3.15c show the variation of axial strain with time for experimental and modeling results for frequencies 0.0014 Hz and 0.0002 Hz. The modeling results showed a very good fit compared to experimental results for all the frequencies. The difference between the total inelastic strain for experimental and modeling results is also presented in the last column of Table 3.2. The highest difference between them is around 7 % for the lowest frequency.

Table 3.2: Model input parameters and difference in total inelastic strain between the model and lab measurements for tests in the 'elastic regime' (σ_{mean2} = 38 MPa) and amplitude ($A1$) of 20 MPa.

Test	f [Hz]	λ_{MCC}	θ	η_1 GPa s	E_{avg}	p_c	$\varepsilon^{inelastic}$ Model/Lab
$\sigma_{mean2}/F1/A1$	F1=0.014	1.50e-04	0.005	250	23.3	10	0.0314 / 0.0319
$\sigma_{mean2}/F2/A1$	F2=0.0014	1.85e-04	0.005	1900	23.3	10	0.030 / 0.031
$\sigma_{mean2}/F3/A1$	F3=0.0002	2.30e-04	0.005	13000	23.3	10	0.042 / 0.045

Figure 3.15b and Figure 3.15d show the variation of inelastic strain with time obtained from the MCC model, which is compared with the inelastic strain estimated using the number of events of AE (Equation 3.33) for the same frequencies. It can be seen that the MCC model is successful in capturing the inelastic strain cycle after cycle. The increase in inelastic strain for every cycle which is based on AE, follows a similar trend as the cyclic MCC model and quantitatively captures well with the experiments.

The yield surface evolution for different input loading cycles is shown in Figure 3.16. As the number of cycles increase, the yield surface slowly evolves to reach the maximum-sized final yield envelope. The plasticity model employed here with the parameters calibrated from the first cycle showed maximum decrease in 0.2 % porosity at the end of the experiment. Though the decrease in porosity was not measured experimentally, previously few researchers have shown the decrease in porosity of sandstone under triaxial loading (Pijnenburg et al., 2019). In the energy storage perspective, porosity reduction implies the reduction in storage capacity of the subsurface reservoirs caused due to accumulated inelastic deformation. From the Table 3.2, it can also be seen that the parameters λ_{MCC} and viscosity η_1 are increasing with decreasing frequency. The rest of the parameters, such as θ, p_c pre-consolidation pressure, and E_{avg} are constant for all the frequencies. The viscosity of the rock increases with decreasing frequency of the applied load.

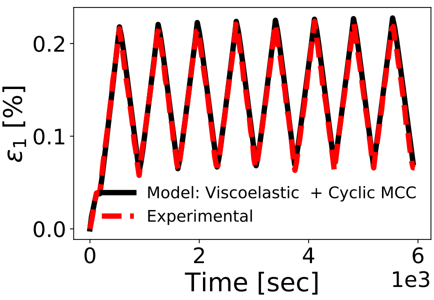

(a) Axial strain v/s time for $f = 0.0014$ Hz

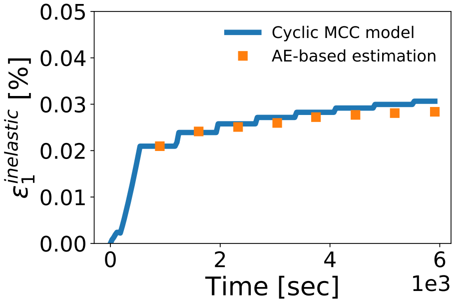

(b) Inelastic strain v/s time for $f = 0.0014$ Hz

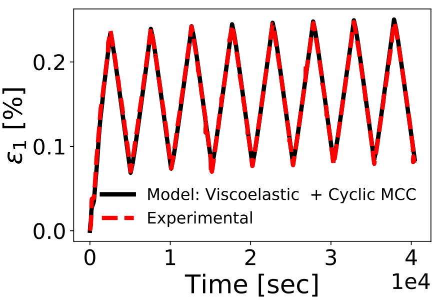

(c) Axial strain v/s time for $f = 0.0002$ Hz

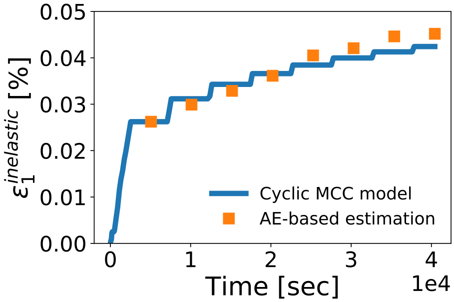

(d) Inelastic strain v/s time for $f = 0.0002$ Hz

Figure 3.15: **Below brittle yield point:** The above figures show the variation of axial strain with time (3.15a, 3.15c). The respective inelastic strain with time is shown in (3.15b, 3.15d).

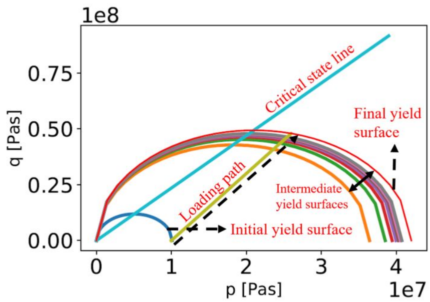

Figure 3.16: Illustration of the evolving yield envelope for every cycle of the rock using the MCC.

In the context of energy storage and upscaling the lab to energy storage conditions, viscoelastic frequency will become a key parameter when compared to rest of the material parameters used in the constitutive models. Viscoelastic frequency is a parameter directly influenced by cyclic loading frequency. It is interpreted that this viscosity could also be a function of strain rate as presented for the creep viscosity (Weijermars, 1997). Thus, as frequency decreases, the mean strain rate decreases, causing the viscosity to increase, which suggests a strain rate thinning-like behavior. To further support this,

Figure 3.17 shows the viscosity variation with the loading frequency. Authors (Fenix Consulting Delft BV, 2018), model sandstone-based Bergermeer gas field storage sites with the viscoelastic model. The viscosity used by them to compare the uplift with GPS stations was around 1e8 GPa s. Using this as evidence, it can be said that depending on the frequency of cyclic loading viscosity of the viscoelastic model needs to be modified accordingly.

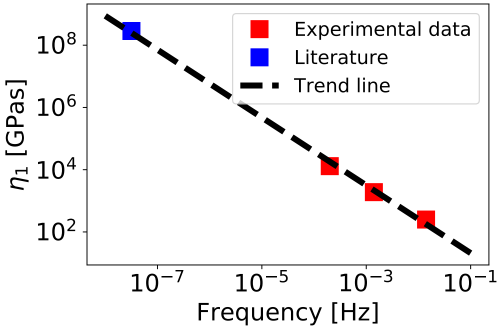

Figure 3.17: The variation of viscosity of rocks with the frequency of the cyclic loading. The field scale relevant data is from the literature (Fenix Consulting Delft BV, 2018) (Blue square)

3.5.2. ABOVE BRITTLE YIELD POINT

Here we employ the hardening softening model, and brittle creep additionally because the loading zone is above the brittle yield point. So the first step is defining the parameters of these two models, which are considered independent of the frequency of cyclic loading. For the calibration of the hardening-softening model, the range for cohesion and friction angle was established. This was done through monotonic test results for Red Felser sandstone at different confining pressures, as shown in Figure 3.18. It can be seen that cohesion could range between 12MPa and 32MPa while the internal friction angle could be between 25^o and 48^o for $\sigma_3 = 10MPa$.

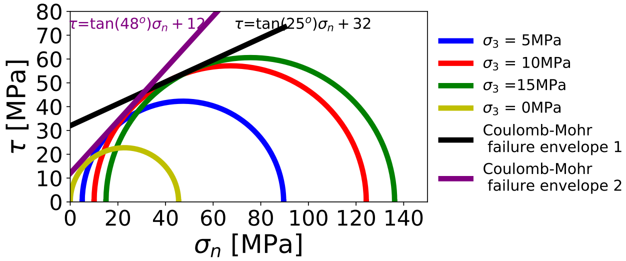

Figure 3.18: The figure shows the variation of shear stress with normal stress (failure envelop) with the equation of the Mohr-coulomb failure criteria can be seen.

The hardening softening (HS) model was further calibrated with the first loading cycle of the test case $\sigma_{mean}1/F3/A1$. This was done using the trial and error method. Next, the creep model was calibrated against the Multistage creep test. Thus, initial calibration of the viscoelastic and MCC model parameters also occurred. Figure 3.19a shows that it was possible to reproduce the strain of all the loading steps. The imposed axial load (σ_1) is shown in Figure 3.19a. In this test case, the model comprises all the models (elastic, viscoelastic, creep, MCC, and HS model). Table 3.3 shows all the parameters obtained from fitting the experimental data for only the multistage creep test. The critical state line 'M' slope was taken from (Pijnenburg et al., 2019).

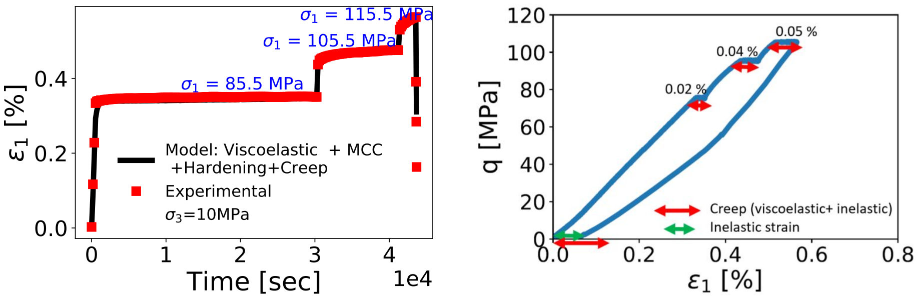

(a) Strain v/s time

(b) Stress v/s strain

Figure 3.19: The figure shows the variation of strain with time for the imposed stress (σ_1) as shown in the Figure 3.19a for a multi-stage creep test. The creep strain (viscoelastic+inelastic) and the inelastic strains are highlighted in red and green arrows, respectively as shown in Figure 3.19b.

Table 3.3: Model parameters used to reproduce experimental multistage creep test 2. These parameters will remain constant during modeling brittle cyclic tests, except for the viscosity of the visco-elastic unit, which changes depending on the frequency of the cyclic load.

Physics	Value	Value	Value	Value
Viscoelasticity	$E_1 = 46$ GPa	$E_2 = 49$ GPa	$\eta_1 = 13e3$ GPa s	$\nu = 0.125$
MCC	$M = 2.35$ (Pijnenburg et al., 2019)	$\lambda_{MCC} = 1.2e{-4}$	$p_c^0 = 10.1$ MPa	$\phi = 0.2056$
HS model	$E_{avg} = 23.7$	$c = 22$ MPa	$\phi_{friction} = 34.5$	$\varepsilon_f = 0.0015$
Brittle creep	$\eta_2 = 18e5$ GPa s	$\sigma^{BP} = 81$ GPa s		

Figure 3.19b shows the variation of deviatoric stress with axial strain for the multi-stage creep test. The red and green double-headed arrows highlight the creep (visco-elastic + inelastic) strains and only inelastic strains, respectively. Using this, the viscoelastic and inelastic strain contributions could be identified, which helps calibrate the constitutive model.

Table 3.4: Model parameters: θ and visco-elastic viscosity η_1 against frequency for tests in the brittle regime. It is also mentioned the difference in total inelastic strain between the model and lab measurements. $F1 > F2 > F3$. Here $\sigma_{mean1} = 85$ MPa and $A1 = 20$ MPa.

Test	Frequency [Hz]	θ	η_1 [Gpa.s]	Eavg. [GPa]	$\varepsilon^{inelastic}$[%] Model/Lab
$\sigma_{mean1}/F1/A1$	F1=0.014	0.005	650	21.8	0.05 / 0.07
$\sigma_{mean1}/F2/A1$	F2=0.004	0.005	7800	21.8	0.058 / 0.065
$\sigma_{mean1}/F3/A1$	F3=0.0002	0.005	40000	21.8	0.0604 / 0.079

Finally, the deviatoric cyclic tests performed in the brittle regime were compared with the proposed model (Equation 3.6) after the calibration as shown in Figure 3.20. Figure 3.20a and Figure 3.20c show the variation of axial strain with time for two frequencies $f = 0.0014$ Hz and $f = 0.0002$ Hz. The inelastic strain contributions with the time of the three models are shown in Figure 3.20b and Figure 3.20d, respectively, for the same two frequencies. It can be seen that brittle creep plays an important role as the frequency decreases because there is more time for this type of deformation to become significant. In addition, cyclic plasticity was required to reproduce the experimental results of all the tests at the amplitude of 20 MPa (A1). Cyclic plasticity was more significant for high-frequency tests because of the negligible creep contribution (Figure 3.20b). The results for f = 0.014 Hz also showed a good fit for both below the yield point and above the yield point regimes.

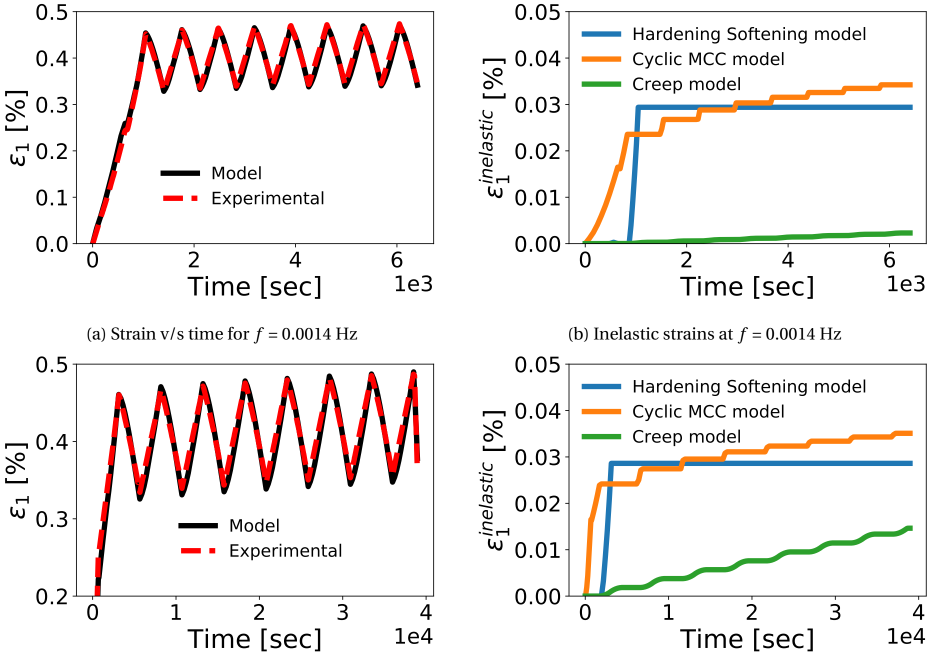

(a) Strain v/s time for $f = 0.0014$ Hz

(b) Inelastic strains at $f = 0.0014$ Hz

(c) Strain v/s time for $f = 0.0002$ Hz

(d) Inelastic strains at $f = 0.0002$ Hz

Figure 3.20: **Above brittle yield point:** The variation of axial strain with time and inelastic strains with time for all the frequencies are shown. The constitutive model comprises elastic, viscoelastic, creep, MCC, and HS model.

Similar to the previous tests conducted below the brittle yield point, the viscoelastic viscosity had to be increased when the frequency of loading of cyclic tests was reduced, as shown in Table 3.4. Also, the viscosity in these test cases is consistently higher than the tests conducted in the elastic regime. The difference between the total inelastic strain for experimental and modeling results is also presented in the last column of Table 3.4. Due to the higher number of parameters involved from constitutive models, this difference is higher when compared to the previous section of below brittle yield point. No powerful optimization algorithms were employed, and lastly, the cyclicity part of dilation-based plasticity constitutive law was not accounted for. They are beyond the scope of this chapter.

In the subsurface energy storage perspective, considering much higher time scales with very low frequencies (max. 1e-6 Hz), creep deformation can become the most significant inelastic mechanism compared to the rest. Visco-elasticity will become critical during the injection and production of the reservoir to ensure that the strain-thinning behavior of sandstone rocks is considered.

Next, the effect of amplitude of cyclic loading for different regimes of stresses can be seen in Figure 3.21. Figure 3.21a andFigure 3.21b show the variation of axial strain with time for mean stresses 38 MPa and 85 MPa, respectively. The parameters used in this amplitude are presented in Table 3.5.

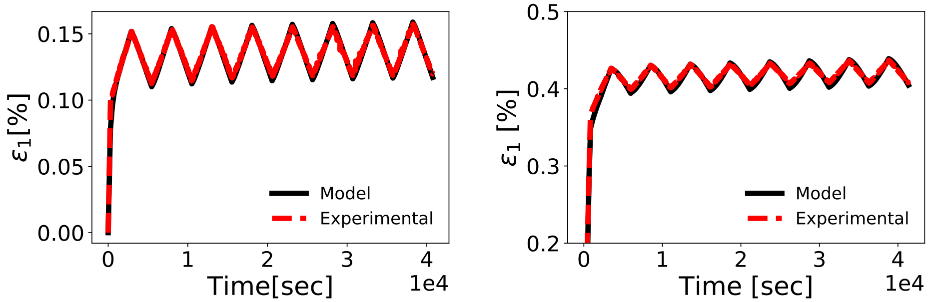

(a) σ_{mean2} = 38 MPa and A = 5.11 MPa

(b) σ_{mean1} = 85 MPa and A = 5.11 MPa

Figure 3.21: The variation of axial strains with time for lower amplitude A2 (A = 5.11 MPa), lowest frequency f = 0.0002 Hz and different mean stresses.

Table 3.5: Model parameters: θ and visco-elastic viscosity η_1 against frequency for tests in the brittle regime. The below parameters are for the amplitudes $A2$ = 5.11 MPa for both the means stresses at the lowest frequency.

Test	Frequency [Hz]	θ	η_1 [Gpa.s]	Eavg. [GPa]
$\sigma_{mean1}/F3/A2$	F3=0.0002	0.005	13000	20.9
$\sigma_{mean2}/F3/A2$	F3=0.0002	0.005	45000	23.11

Here we see that the constitutive model fits the experimental data even for lower amplitudes. The Young's modulus (Eavg) is slightly different for mean stress 1 and 2, irrespective of amplitude and frequency. However, we did not observe any trend in the variation of Eavg depending on the stress regimes. The values of the parameters involved in constitutive models can slightly change if powerful optimization algorithms are employed. However, we expect the qualitative behavior of sandstone rock based on the above operating conditions would remain the same.

3.6. CONCLUSION

We conducted an extensive experimental and modeling analysis for Red Felser sandstone rock subjected to cyclic loading. Three different frequencies, two amplitudes, and two different stress regimes of cyclic loading on sandstone were studied using axial strain and acoustic emissions. Further, a constitutive model was developed based on literature, which is specifically suitable for sandstone rocks but could be extended for other porous rocks. Major conclusions are

- The inelastic deformations occurred at stress conditions above and below the brittle yield point (onset of dilatant cracking). The inelastic strain per cycle decreased as the number of cycles increased. Therefore, fatigue was not registered within the number of cycles tested.
- The cyclic inelastic deformations were affected by the mean stress, amplitude, and frequency of the stress waveform imposed during testing. On the one hand, the higher the mean stress or amplitude, the higher the total inelastic strains. On the other hand, the lower the frequency, the higher the total inelastic strain.
- There is a strong correlation between the cumulative number of AE vs. cumulative apparent inelastic strain. They both decrease by increasing the number of cycles.
- The proposed constitutive model based on governing physics showed a very good fit with the experimental results. The viscosity of the rock was found to be the most critical parameter which needs to be accounted for depending on the frequency of the cyclic loading.
- The cyclic MCC model captures the estimation of inelastic deformation based on the increase in the number of AE events happening cycle after cycle.

Bibliography

Amid, A., Mignard, D., & Wilkinson, M. (2016). Seasonal storage of hydrogen in a depleted natural gas reservoir. *International journal of hydrogen energy*, *41*(12), 5549–5558.

Bagde, M. N., & Petroš, V. (2005). Waveform effect on fatigue properties of intact sandstone in uniaxial cyclical loading. *Rock mechanics and rock engineering*, *38*, 169–196.

Bai, T., & Tahmasebi, P. (2022). Coupled hydro-mechanical analysis of seasonal underground hydrogen storage in a saline aquifer. *Journal of Energy Storage*, *50*, 104308.

Baud, P., Vajdova, V., & Wong, T.-f. (2006). Shear-enhanced compaction and strain localization: Inelastic deformation and constitutive modeling of four porous sandstones. *Journal of Geophysical Research: Solid Earth*, *111*(B12).

Bauer, S., Beyer, C., Dethlefsen, F., Dietrich, P., Duttmann, R., Ebert, M., Feeser, V., Görke, U., Köber, R., Kolditz, O., et al. (2013). Impacts of the use of the geological subsurface for energy storage: An investigation concept. *Environmental earth sciences*, *70*(8), 3935–3943.

Bazdar, E., Sameti, M., Nasiri, F., & Haghighat, F. (2022). Compressed air energy storage in integrated energy systems: A review. *Renewable and Sustainable Energy Reviews*, *167*, 112701.

Bo, Z., Boon, M., Hajibeygi, H., & Hurter, S. (2023). Impact of experimentally measured relative permeability hysteresis on reservoir-scale performance of underground hydrogen storage (uhs). *International Journal of Hydrogen Energy*, *12*, in press. https://doi.org/10.1016/j.ijhydene.2022.12.270

Boon, M., & Hajibeygi, H. (2022). Experimental characterization of h2/water multiphase flow in heterogeneous sandstone rock at the core scale relevant for underground hydrogen storage (uhs). *Sci Rep*, *12*, 14604. https://doi.org/10.1038/s41598-022-18759-8

Brantut, N., Heap, M. J., Meredith, P. G., & Baud, P. (2013). Time-dependent cracking and brittle creep in crustal rocks: A review. *Journal of Structural Geology*, *52*, 17–43.

Cai, M. (2010). Practical estimates of tensile strength and Hoek–Brown strength parameter mi of brittle rocks. *Rock Mechanics and Rock Engineering*, *43*(2), 167–184.

Carter, J. P., Wroth, C. P., & Booker, J. R. (R. (1979, January). A critical state soil model for cyclic loading. In *Soil mechanics - transient and cylic loads* (pp. 219–252). John Wiley & Sons Ltd.

Cerfontaine, B., Charlier, R., Collin, F., & Taiebat, M. (2017). Validation of a New Elastoplastic Constitutive Model Dedicated to the Cyclic Behaviour of Brittle Rock Materials. *Rock Mechanics and Rock Engineering*, *50*(10), 2677–2694. https://doi.org/10.1007/S00603-017-1258-3/FIGURES/26

3

Chen, J., Du, C., Jiang, D., Fan, J., & He, Y. (2016). The mechanical properties of rock salt under cyclic loading-unloading experiments. *Geomechanics and Engineering*, *10*(3), 325–334.

Coussy, O. (2004). *Poromechanics*. Wiley. https://www.wiley.com/en-us/Poromechanics-p-9780470849200

Crotogino, F., Schneider, G.-S., & Evans, D. J. (2018). Renewable energy storage in geological formations. *Proceedings of the Institution of Mechanical Engineers, Part A: Journal of Power and Energy*, *232*(1), 100–114.

de Borst, R. (1987). Integration of plasticity equations for singular yield functions. *Computers & Structures*, *26*(5), 823–829. https://doi.org/https://doi.org/10.1016/0045-7949(87)90032-0

Ding, X., Zhang, G., Zhao, B., & Wang, Y. (2017). Unexpected viscoelastic deformation of tight sandstone: Insights and predictions from the fractional Maxwell model. *Scientific Reports 2017 7:1*, *7*(1), 1–11. https://doi.org/10.1038/s41598-017-11618-x

Evans, D. J., & Chadwick, R. (2009). Underground gas storage: Worldwide experiences and future development in the uk and europe.

Feng, L., Zhang, X., Li, X., Li, B., Li, Y., Xu, Y., Guo, H., Zhou, X., & Chen, H. (2022). Performance analysis of hybrid energy storage integrated with distributed renewable energy. *Energy Reports*, *8*, 1829–1838.

Fenix Consulting Delft BV. (2018). *3D Geomechanical Model for Gas Storage Bergermeer Report for TAQA Energy BV* (tech. rep.). TAQA Energy BV. Delft.

Fleuchaus, P., Godschalk, B., Stober, I., & Blum, P. (2018). Worldwide application of aquifer thermal energy storage–a review. *Renewable and Sustainable Energy Reviews*, *94*, 861–876.

Fuenkajorn, K., & Phueakphum, D. (2010). Effects of cyclic loading on mechanical properties of Maha Sarakham salt. *Engineering Geology*, *112*(1-4), 43–52.

Gatelier, N., Pellet, F., & Loret, B. (2002). Mechanical damage of an anisotropic porous rock in cyclic triaxial tests. *International Journal of Rock Mechanics and Mining Sciences*, *39*(3), 335–354.

Geranmayeh Vaneghi, R., Thoeni, K., Dyskin, A. V., Sharifzadeh, M., & Sarmadivaleh, M. (2020). Strength and damage response of sandstone and granodiorite under different loading conditions of multistage uniaxial cyclic compression. *International Journal of Geomechanics*, *20*(9), 04020159.

Grosse, C. U., & Ohtsu, M. (2008). *Acoustic emission testing*. Springer Science Business Media.

Hashemi, L., Blunt, M., & Hajibeygi, H. (2021). Pore-scale modelling and sensitivity analyses of hydrogen-brine multiphase flow in geological porous media. *Scientific reports*, *11*(1), 8348.

He, Q., Wu, F., & Gao, R. (2022). Nonlinear creep-damage constitutive model of surrounding rock in salt cavern reservoir. *Journal of Energy Storage*, *55*, 105520. https://doi.org/https://doi.org/10.1016/j.est.2022.105520

Heinemann, N., Alcalde, J., Miocic, J. M., Hangx, S. J., Kallmeyer, J., Ostertag-Henning, C., Hassanpouryouzband, A., Thaysen, E. M., Strobel, G. J., Schmidt-Hattenberger, C., et al. (2021). Enabling large-scale hydrogen storage in porous media–the scientific challenges. *Energy & Environmental Science*, *14*(2), 853–864.

Hernandez, E., Naderloo, M., Kumar, K. R., Hajibeygi, H., & Barnhoorn, A. (2022). Modeling of cyclic deformation of sandstones based on experimental observations. *2022*(1), 1–5. https://www.earthdoc.org/content/papers/10.3997/2214-4609.202221120

Hoek, E. (1965). Rock fracture under static stress conditions.

Janna, C., Castelletto, N., Ferronato, M., Gambolati, G., & Teatini, P. (2012). A geomechanical transversely isotropic model of the po river basin using psinsar derived horizontal displacement. *International Journal of Rock Mechanics and Mining Sciences*, *51*, 105–118.

Jiang, D., Xie, K., Chen, J., Zhang, S., Tiedeu, W. N., Xiao, Y., & Jiang, X. (2019). Experimental analysis of sandstone under uniaxial cyclic loading through acoustic emission statistics. *Pure and Applied Geophysics*, *176*(1), 265–277.

Juez-Larre, J., Remmelts, G., Breunese, J., Van Gessel, S., & Leeuwenburgh, O. (2016). Using underground gas storage to replace the swing capacity of the giant natural gas field of groningen in the netherlands. a reservoir performance feasibility study. *Journal of Petroleum Science and Engineering*, *145*, 34–53.

Kelly, P. (2013). Solid mechanics part i: An introduction to solid mechanics. *A Creative Commons Attributions, Mountain View, CA, 94042*.

Khaledi, K., Mahmoudi, E., Datcheva, M., & Schanz, T. (2016). Stability and serviceability of underground energy storage caverns in rock salt subjected to mechanical cyclic loading. *International Journal of Rock Mechanics and Mining Sciences*, *86*, 115–131. https://doi.org/10.1016/J.IJRMMS.2016.04.010

Koohi-Fayegh, S., & Rosen, M. A. (2020). A review of energy storage types, applications and recent developments. *Journal of Energy Storage*, *27*, 101047.

Krevor, S., De Coninck, H., Gasda, S. E., Ghaleigh, N. S., de Gooyert, V., Hajibeygi, H., Juanes, R., Neufeld, J., Roberts, J. J., & Swennenhuis, F. (2023). Subsurface carbon dioxide and hydrogen storage for a sustainable energy future. *Nature Reviews Earth & Environment*, *4*(2), 102–118.

KUMAR, K. R. (2023). Geomechanical study of underground hydrogen storage.

Kumar, K., Honorio, H., & Hajibeygi, H. (2022). Simulation of the inelastic deformation of porous reservoirs under cyclic loading relevant for underground hydrogen storage. *Scientific reports*, *12*, 21404.

Li, X., & Yin, Z. (2021). Study of creep mechanical properties and a rheological model of sandstone under disturbance loads. *Processes*, *9*. https://doi.org/10.3390/pr9081291

Li, Z., Yang, F., Fan, J., Jiang, D., & Ambre, J. (2022). Fatigue effects of discontinuous cyclic loading on the mechanical characteristics of sandstone. *Bulletin of Engineering Geology and the Environment*, *81*(8), 1–15.

Liang, D., Zhang, N., Xie, L., Zhao, G., & Qian, D. (2019). Damage and fractal evolution trends of sandstones under constant-amplitude and tiered cyclic loading and unloading based on acoustic emission. *International Journal of Distributed Sensor Networks*, *15*(7), 1550147719861020.

Liu, Y., Ma, T., Wu, H., & Chen, P. (2020). Investigation on mechanical behaviors of shale cap rock for geological energy storage by linking macroscopic to mesoscopic failures. *Journal of Energy Storage*, *29*, 101326.

Lockner, D. (1993). The role of acoustic emission in the study of rock fracture. *International Journal of Rock Mechanics and Mining Sciences Geomechanics Abstracts*, *30*(7), 883–899.

Luboń, K., & Tarkowski, R. (2020). Numerical simulation of hydrogen injection and withdrawal to and from a deep aquifer in nw poland. *international journal of hydrogen energy*, *45*(3), 2068–2083.

3

Ma, L.-j., Liu, X.-y., Wang, M.-y., Xu, H.-f., Hua, R.-p., Fan, P.-x., Jiang, S.-r., Wang, G.-a., & Yi, Q.-k. (2013). Experimental investigation of the mechanical properties of rock salt under triaxial cyclic loading. *International Journal of Rock Mechanics and Mining Sciences*, *62*, 34–41.

Martin, C. D., & Chandler, N. A. (1994). The progressive fracture of Lac du Bonnet granite. *International journal of rock mechanics and mining sciences geomechanics abstracts*, *31*(6), 643–659.

Matos, C. R., Carneiro, J. F., & Silva, P. P. (2019). Overview of large-scale underground energy storage technologies for integration of renewable energies and criteria for reservoir identification. *Journal of Energy Storage*, *21*, 241–258.

Menéndez, J., Ordóñez, A., Álvarez, R., & Loredo, J. (2019). Energy from closed mines: Underground energy storage and geothermal applications. *Renewable and Sustainable Energy Reviews*, *108*, 498–512.

Meng, Q., Zhang, M., Han, L., Pu, H., & Chen, Y. (2018). Acoustic emission characteristics of red sandstone specimens under uniaxial cyclic loading and unloading compression. *Rock Mechanics and Rock Engineering*, *51*(4), 969–988.

Naderloo, M., Moosavi, M., & Ahmadi, M. (2019). Using acoustic emission technique to monitor damage progress around joints in brittle materials. *Theoretical and Applied Fracture Mechanics*, *104*, 102368.

Naderloo, M., Kumar, K. R., Hernandez, E., Hajibeygi, H., & Barnhoorn, A. (2023). Experimental and numerical investigation of sandstone deformation under cycling loading relevant for underground energy storage. *Journal of Energy Storage*, *64*, 107198.

Nikolinakou, M. A., Luo, G., Hudec, M. R., & Flemings, P. B. (2012). Geomechanical modeling of stresses adjacent to salt bodies: Part 2 - Poroelastoplasticity and coupled overpressures. *AAPG Bulletin*, *96*(1), 65–85. https://doi.org/10.1306/04111110143

Olabi, A., & Abdelkareem, M. A. (2022). Renewable energy and climate change. *Renewable and Sustainable Energy Reviews*, *158*, 112111.

Orlic, B., Wassing, B., & Geel, C. (2013). Field scale geomechanical modeling for prediction of fault stability during underground gas storage operations in a depleted gas field in the netherlands. *47th US Rock Mechanics/Geomechanics Symposium*.

Peng, K., Zhou, J., Zou, Q., & Song, X. (2020). Effect of loading frequency on the deformation behaviours of sandstones subjected to cyclic loads and its underlying mechanism. *International Journal of Fatigue*, *131*, 105349.

Peng, K., Zhou, J., Zou, Q., Zhang, J., & Wu, F. (2019). Effects of stress lower limit during cyclic loading and unloading on deformation characteristics of sandstones. *Construction and Building Materials*, *217*, 202–215.

Pijnenburg, R. P. J., Verberne, B. A., Hangx, S. J. T., & Spiers, C. J. (2018). Deformation behavior of sandstones from the seismogenic Groningen gas field: Role of inelastic versus elastic mechanisms. *Journal of Geophysical Research: Solid Earth*, *123*(7), 5532–5558.

Pijnenburg, R. P., Verberne, B. A., Hangx, S. J., & Spiers, C. J. (2019). Inelastic Deformation of the Slochteren Sandstone: Stress-Strain Relations and Implications for Induced Seismicity in the Groningen Gas Field. *Journal of Geophysical Research: Solid Earth*, *124*(5), 5254–5282. https://doi.org/10.1029/2019JB017366

Pouya, A., Zhu, C., & Arson, C. (2016). Micro–macro approach of salt viscous fatigue under cyclic loading. *Mechanics of Materials*, *93*, 13–31. https://doi.org/https://doi.org/10.1016/j.mechmat.2015.10.009

Ramesh Kumar, K., Makhmutov, A., Spiers, C. J., & Hajibeygi, H. (2021). Geomechanical simulation of energy storage in salt formations. *Scientific Reports*, *11*(1), 1–24.

Roscoe, K. H., & Burland, J. B. (1968). On the Generalized Stress-Strain Behavior of Wet Clays. In J. Heyman & F. A. Leckie (Eds.), *Engineering plasticity*. https://www.researchgate.net/publication/264921746_On_the_Generalized_Stress-Strain_Behavior_of_Wet_Clays

Sadeghi, S., & Sedaee, B. (2022). Cushion and working gases mixing during underground gas storage: Role of fractures. *Journal of Energy Storage*, *55*, 105530.

Sainz-Garcia, A. A. (2017). *Dynamics of underground gas storage. insights from numerical models for carbon dioxide and hydrogen.* [Doctoral dissertation, Université Toulouse 3 Paul Sabatier (UT3 Paul Sabatier)].

Shalev, E., Lyakhovsky, V., Ougier-Simonin, A., Hamiel, Y., & Zhu, W. (2014). Inelastic compaction, dilation and hysteresis of sandstones under hydrostatic conditions. *Geophysical Journal International*, *197*(2), 920–925.

Shen, R., Chen, T., Li, T., Li, H., Fan, W., Hou, Z., & Zhang, X. (2020). Study on the effect of the lower limit of cyclic stress on the mechanical properties and acoustic emission of sandstone under cyclic loading and unloading. *Theoretical and Applied Fracture Mechanics*, *108*, 102661.

Silverii, F., Maccaferri, F., Richter, G., Gonzalez Cansado, B., Wang, R., Hainzl, S., & Dahm, T. (2021). Poroelastic model in a vertically sealed gas storage: A case study from cyclic injection/production in a carbonate aquifer. *Geophysical Journal International*, *227*(2), 1322–1338.

Sun, B., Zhu, Z., Shi, C., & Luo, Z. (2017). Dynamic mechanical behavior and fatigue damage evolution of sandstone under cyclic loading. *International Journal of Rock Mechanics and Mining Sciences*, *94*, 82–89.

Taheri, A., Yfantidis, N., Olivares, C. L., Connelly, B. J., & Bastian, T. J. (2016). Experimental study on degradation of mechanical properties of sandstone under different cyclic loadings. *Geotechnical Testing Journal*, *39*(4), 673–687.

Takach, M., Sarajlić, M., Peters, D., Kroener, M., Schuldt, F., & von Maydell, K. (2022). Review of hydrogen production techniques from water using renewable energy sources and its storage in salt caverns. *Energies*, *15*(4), 1415.

3

Tarkowski, R. (2019). Underground hydrogen storage: Characteristics and prospects. *Renewable and Sustainable Energy Reviews*, *105*, 86–94.

Teatini, P., Castelletto, N., Ferronato, M., Gambolati, G., Janna, C., Cairo, E., Marzorati, D., Colombo, D., Ferretti, A., Bagliani, A., et al. (2011). Geomechanical response to seasonal gas storage in depleted reservoirs: A case study in the po river basin, italy. *Journal of Geophysical Research: Earth Surface*, *116*(F2).

Tsai, L. S., Hsieh, Y. M., Weng, M. C., Huang, T. H., & Jeng, F. S. (2008). Time-dependent deformation behaviors of weak sandstones. *International Journal of Rock Mechanics and Mining Sciences*, *45*(2), 144–154. https://doi.org/10.1016/j.ijrmms.2007.04.008

van Uijen, W. M. (2013). Rotliegend geology in the Southern Permian Basin: the development of synrift sediments and its relation to seismic imaging.

Vermeer, P. A., & De Borst, R. (1984). Non-Associated Plasticity for Soils, Concrete and Rock. *HERON*, *29*(3). https://repository.tudelft.nl/islandora/object/uuid%3A4ee188ab-8ce0-4df3-adf5-9010ebfaabf0

Wang, H. L., Xu, W. Y., Cai, M., Xiang, Z. P., & Kong, Q. (2017). Gas permeability and porosity evolution of a porous sandstone under repeated loading and unloading conditions. *Rock Mechanics and Rock Engineering*, *50*, 2071–2083.

Wang, J., Zhang, Q., Song, Z., Feng, S., & Zhang, Y. (2022). Nonlinear creep model of salt rock used for displacement prediction of salt cavern gas storage. *Journal of Energy Storage*, *48*, 103951. https://doi.org/https://doi.org/10.1016/j.est.2021.103951

Weijermars, R. (1997). *Principles of rock mechanics*. Alboran Science Publishing.

Weng, M. C., & Ling, H. I. (2013). Modeling the behavior of sandstone based on generalized plasticity concept. *International Journal for Numerical and Analytical Methods in Geomechanics*, *37*(14), 2154–2169. https://doi.org/10.1002/NAG.2127

Wong, T.-f., & Baud, P. (2012). The brittle-ductile transition in porous rock: A review. *Journal of Structural Geology*, *44*, 25–53.

Xu, T., Zhou, G., Heap, M. J., Yang, S., Konietzky, H., & Baud, P. (2018). The Modeling of Time-Dependent Deformation and Fracturing of Brittle Rocks Under Varying Confining and Pore Pressures. *Rock Mechanics and Rock Engineering*, *51*(10), 3241–3263. https://doi.org/10.1007/s00603-018-1491-4

Yang, S. Q., & Hu, B. (2018). Creep and Long-Term Permeability of a Red Sandstone Subjected to Cyclic Loading After Thermal Treatments. *Rock Mechanics and Rock Engineering*, *51*(10), 2981–3004. https://doi.org/10.1007/s00603-018-1528-8

Yin, D., & Xu, Q. (2020). Comparison of sandstone damage measurements based on non-destructive testing. *Materials*, *13*(22), 5154.

Zhang, G., Li, B., Zheng, D., Ding, G., Wei, H., Qian, P., & Li, C. (2017). Challenges to and proposals for underground gas storage (ugs) business in china. *Natural Gas Industry B*, *4*(3), 231–237.

Zhang, J.-c., Lin, Z.-n., Dong, B., & Guo, R.-x. (2021). Triaxial compression testing at constant and reducing confining pressure for the mechanical characterization of a specific type of sandstone. *Rock Mechanics and Rock Engineering*, *54*, 1999–2012.

Zhang, X., & Tahmasebi, P. (2019). Effects of grain size on deformation in porous media. *Transport in Porous Media*, *129*(1), 321–341.

Zhenyu, T. A. O., & Haihong, M. O. (1990). An experimental study and analysis of the behaviour of rock under cyclic loading. *Intl J of Rock Mech Mining Sci Geomechanic Abs*, *27*(1).

4

Active and Passive Monitoring of Fault Reactivation[1]

Abstract: *Increased seismicity, due to subsurface activities has led to increased interest in monitoring and seismic risk mitigation. In this chapter we combined passive and active acoustic monitoring methods to monitor fault sliding and reactivation in the laboratory. Acoustic emission (AE) and ultrasonic transmission measurements were performed during stress-cycling to monitor stress-driven fault reactivation. We show the use of transmissivity and coda wave interferometry of the active acoustic measurements and the number of generated AE events for fault reactivation monitoring. Combining these two methods, we are able to detect different phases of the fault reactivation process under stress cycling including, early aseismic creep (pre-slip), fault slip, and continuous sliding. Combining both active and passive monitoring increases the accuracy of monitoring and may help to develop methods for better seismic risk mitigation.*

[1]This chapter, a joint collaboration with Aukje Veltmeijer, was presented and published in SEG and AAPG IMAGE Conference 2022 (Naderloo et al., 2022)

4.1. Introduction

Increasing human activities in the subsurface, due to rising renewable energy demand, has led to an increase in induced seismicity all over the world. Seismicity is recorded at different subsurface-related projects, such as waste water injection, gas extraction/storage, and geothermal energy production. Well-known example is the M5.4 earthquake in Pohang (Kim et al., 2018), and the high number of seismicity recordings in Groningen, caused by gas extraction (van Thienen-Visser & Breunese, 2015).

Monitoring and seismic risk mitigation have received much interest over the years. Multiple studies have been conducted to improve the monitoring system of induced seismicity (Eaton, 2018; Grigoli et al., 2017; Mahani et al., 2016). Verdon et al. (2010) showed there is a correlation between seismicity rate and injection or production activities, using passive monitoring. Using improved matching and locating techniques, Chen et al. (2018) demonstrated the detection of seismic events and the clustering of seismic activity associated with pre-existing faults and fractures, using passive monitoring and enhanced matching and locating techniques. Monitoring induced seismicity, however, still poses a number of challenges, including the need for near-real-time monitoring and limitations associated with seismic network quality (Grigoli et al., 2017). To improve the monitoring and managing system of induced seismicity, combining geophysical, geological, and hydrological data from the field with modelling is required. Potential seepage or leakage along faults or fracture zones was studied by Oye et al. (2021), using both active and passive monitoring techniques (Oye et al., 2021).

Similarly, active monitoring techniques are used to monitor changes in the subsurface prior to fault reactivation. Laboratory studies have shown the sensitivity of ultrasonic P-waves to the reactivation of faults for frictional sliding experiments (Kaproth & Marone, 2013; Shreedharan et al., 2021). Also at a larger scale, precursory signals can be observed using active acoustic monitoring. Chiarabba et al. (2020) observed at a larger (crustal) scale an increase, and near the hypocentre, a decrease in P-wave velocity before an M6.5 earthquake in Italy.

Most of the studies at field or laboratory scale are based on either passive monitoring or active monitoring; only a limited number combine both techniques. In active acoustic methods, controlled signals are transmitted through rocks to monitor changes in wave properties, revealing stress and damage. In contrast, passive acoustic methods record naturally occurring acoustic emissions to detect microcracks and stress-related events. It can be valuable and helpful for monitoring purposes to combine the active and passive acoustic methods. This chapter aims to shed light on using both passive and active acoustic methods for monitoring fault sliding under stress cycling on a laboratory scale. We perform stress-driven fault reactivation experiments on sandstones under stress cycling.

4.2. Methodology

In this chapter, high porosity Red Felser sandstones were used, which are analogous to the Rotliegend sandstones of the Groningen gas reservoir (in the North of the Netherlands). Cylindrical core samples were cut at an angle of 30° to the vertical cylinder axis to simulate a fault plane. The samples, including saw cut, had dimensions of 30±0.5 mm in diameter and 70±2 mm in length. A gas expansion (Helium) pycnometer was used to determine the average connected porosity of the samples: 19.14%±0.7%.

We used an instrumented Hoek cell in a 500 kN uniaxial loading machine (Figure 4.2). A three-step stress-driven protocol for fault reactivation was performed (Figure 4.1).

1. During the first step, axial stress and confining pressure increased hydrostatically up to the desired confining pressure of 20 MPa, while the sample was fully saturated.
2. During the second step, axial stress is increased to reach the pre-determined shear strength of the fault plane (Several fault reactivation tests were performed at a confining pressure of 20 MPa to determine the reactivation zone).
3. In step three, a cyclic reactivation scenario was conducted where, after fault slip, the axial stress (σ_1) was decreased by 12 MPa, reaching approximately the onset of the reactivation zone, and then increased again to the previous stress level (Figure 4.1).

Two sets of acoustic experiments were performed during stress-driven cyclic fault reactivation. Reactivation with passive acoustic emission (AE) monitoring and reactivation with active acoustic monitoring.

The active acoustic monitoring was performed using ultrasonic transmission measurements. Two P-wave transducers are integrated into the pistons in the loading system (Figure 4.2), with the source at the top and the receiver at the bottom of the sample. The transducers have a peak operating frequency of 1 MHz, and every 2 seconds, 512 P-waves were sent, recorded, and stacked to reduce the signal-to-noise ratio. The transmission data was analysed using the transmissivity: $T = |A_{\max}|$, which is the maximum amplitude of the recorded P-wave. Additionally, coda wave interferometry (CWI) (Snieder, 2006) is used to monitor the change in velocity (dv/v) between two consecutive recorded waves. Coda interferometry is a technique that detects small changes in a medium by analyzing the scattered "coda" waves from seismic events. Using a moving reference wavefield for the CWI, the changing medium is continuously monitored (Zotz-Wilson et al., 2019).

The passive acoustic monitoring (AE) was performed using an array of 10 piezo-ceramic transducers (Figure 4.2) to detect micro-seismic events. The AE transducers are 5 mm in diameter, with a dominant resonant frequency of about 1 MHz, and the signals were amplified using pre-amplifiers. The continuous recorded waveform data was cut into single waveforms (AE events) for further analysis, using a pre-defined trigger logic. These AE events were stored if, in five or more transducers, the waveforms recorded exceed a voltage threshold of 25 mV, within a time window of 480 points and a sampling rate of 2 MHz.

4.3. Discussion of Results

In total, 9 stress-reactivation cycles were performed, including acoustic monitoring. The stress-driven fault reactivation cycles can be divided into three parts:

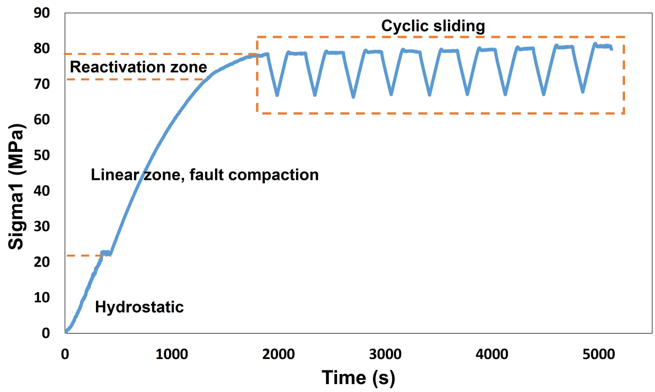

Figure 4.1: Axial stress (σ_1) as a function of time. Different phases of the fault reactivation experiment include hydrostatic, linear zone, reactivation zone, and cyclic sliding.

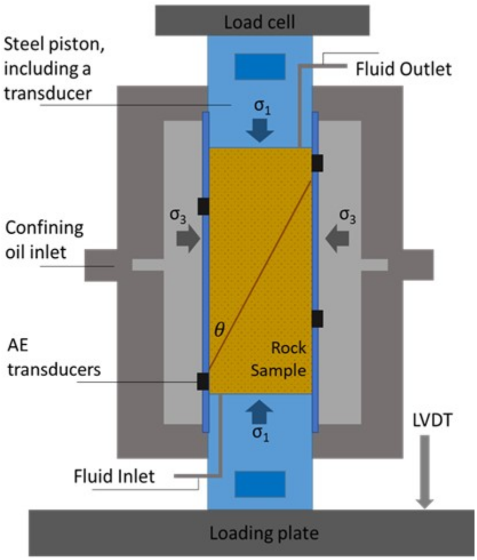

Figure 4.2: Schematic illustration of instrumented Hoek cell with AE sensors, and S-wave transducers. The shortening of the sample was recorded with two linear variable displacement transducers (LVDT's).

1. Stress increase, consisting of the pre-slip phase and the fault reactivation phase.
2. Constant sliding (pure fault slip), in which the sample was continued to be stressed, but constant fault slip counteracted this increase resulting in a more or less constant stress.
3. Stress decrease, after which a new cycle begins.

Figure 4.3 shows the AE results, the axial stress (σ_1), micro-seismic event amplitude and cumulative events are shown. A silence zone, showing zero generated AE event is caused by reducing the stress after fault slip. However, by increasing the stress, AE events start to appear before exceeding the previous reached maximum stress (maximum stress from the previous cycle) and before pure fault slip. AE events are generated from 97% of the maximum stress indicating the fault reactivation (Figure 4.3).

Prior to fault reactivation and pure fault slip, a pre-slip aseismic stage is present. During this pre-slip phase, the fault plane experiences creep (slow slip). During this stage, the stress continues to build up but shows a deviation from the linear increase (Figure 4.3a and Figure 4.3b, beige and blue colour). During this pre-slip phase (blue colour), low amplitude AE events (and a lower event rate) were recorded. After this phase, stress reaches its maximum value and then it drops, indicating fault reactivation.

During reactivation (Figure 4.3b, blue zone), the event rate and maximum amplitude for the individual AE events increase. After reactivation, we observe continuous sliding (pure slip). During this phase (Figure 4.3b, grey zone), continuous micro-seismic generation can be observed. Figure 4.4 shows the data from active acoustic monitoring. Shown is the axial stress (σ_1), the cumulative velocity change ($[\Delta v/v]_{\mathrm{sum}}$) obtained by CWI, and the transmissivity (T). The velocity and transmissivity (maximum amplitude of the waveform) show an overall decreasing trend, but within each cycle, different phases of fault reactivation can be identified. $[\Delta v/v]_{\mathrm{sum}}$ and T show an approx. linear increase due to the imposed increasing stress (Figure 4.4, beige zone). Before the early creep phase (or before 95% of maximum stress), strain is slowly accumulating on the fault plane and stress is building up, however, this stress is not enough to overcome the shear strength, thus the fault remains locked and the contact area between the two sides of the fault increases (the asperities lock). This results in a constant (linear) increase of T and $[\Delta v/v]_{\mathrm{sum}}$ with increasing pressure and micro-seismic events are not generated.

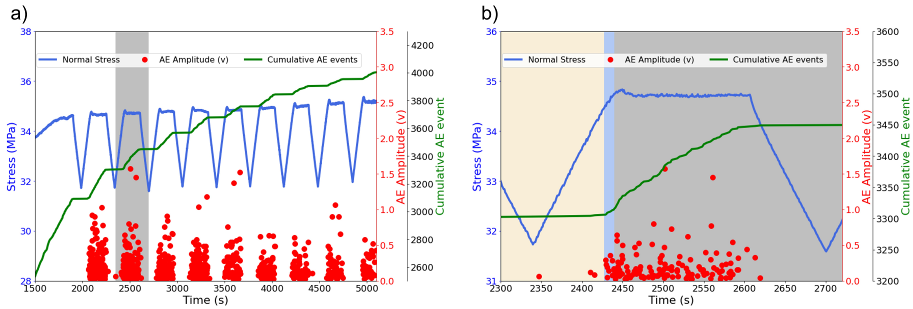

Figure 4.3: Passive acoustic data (AE) during cycling, showing axial stress (σ_1) as a function of time, and the appearance and amplitude of the single AE events and their cumulative. A. showing all the cycles, the cycle shaded grey is shown in B. showing the different phases of fault reactivation experiment; linear stress build up phase in beige, the pre-slip/ early creep phase in blue, fault reactivation and slip in green, and afterwards in grey the continuous sliding..

Before fault reactivation, both $[dv/v]_{\mathrm{sum}}$ and T show a deviation from their linear increase. This coincides with the early creep phase (aseismic stage) and this reduction is attributed to pre-slip and dilation (Shreedharan et al., 2021). During this aseismic phase, the contact area along the fault plane, or the asperities, are slowly destroyed, resulting in

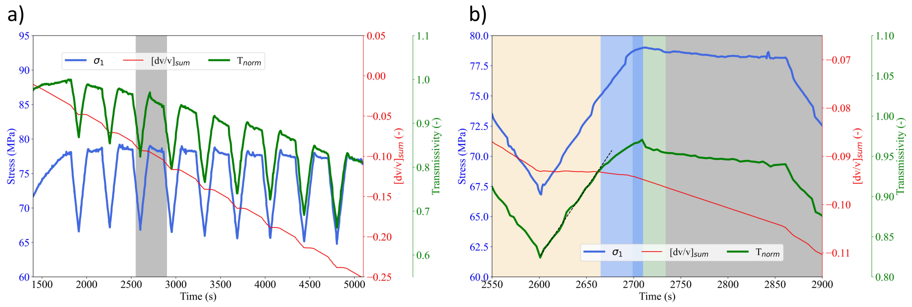

Figure 4.4: Active acoustic data during cycling, showing axial stress (σ_1) as a function of time, and the changing transmissivity (T) and cumulative velocity change $[dv/v]_{\text{sum}}$ during the cycling. The cycle shaded grey is shown in Figure 4.4B, illustrating the different phases of the fault reactivation experiment; linear stress build-up phase in beige, the pre-slip/early creep phase in blue, fault reactivation and slip in green, and afterwards in grey the continuous sliding. The trend line indicates the clear reduction in transmissivity at the start of the pre-slip phase. The pre-slip/early creep phase in blue has two shades, based on the extra decrease in velocity change prior to fault reactivation.

a reduction of T and $[dv/v]_{\text{sum}}$. The detection of the early creep phase using T and $[dv/v]_{\text{sum}}$ is at 95% of the maximum stress indicating the fault reactivation. After fault reactivation (stress drop) both parameters show a constant decrease, consistent with the continuous sliding and the continuous destruction of asperities along the fault plane.

Both the passive data and active data shows we can detect the early creep phase (aseismic stage), the fault reactivation (stress drop), and the continuous sliding phase. Therefore, both methods can be used as a monitoring method of pre-slip and can act as precursory signals to imminent fault slip.

The active monitoring shows precursory signals to fault slip from 95% to failure, whereas the passive (AE) method shows the first recorded events from 97% to failure. The active monitoring is independent of generated seismicity and can be deployed and used for monitoring at any stage of reactivation. Passive monitoring can provide valuable insight into the location and moment tensor of the fault reactivation and generated seismicity (Liu et al., 2022). Therefore, these methods complement each other and monitoring can be improved.

4.4. Conclusion

In this chapter, we used passive and active acoustic techniques to monitor stress-driven fault reactivation experiments under stress cycling.

1. We showed that both passive acoustic (acoustic emission) and active acoustic monitoring can be used to detect fault reactivation processes under stress cycling which include different phases: linear strain build up, early creep (pre-slip), stress drop (main slip), and continuous sliding.

2. The active acoustic technique detected the early creep phase at 95% before failure, and the AE method at 97% before failure. The active method is slightly more

sensitive, and is independent of seismicity-generated movement along the fault. Therefore, a combination of both methods can be beneficial to increase the accuracy of monitoring.

These results have shown that monitoring fault reactivation in the laboratory with a combination of active and passive techniques is feasible. As a result, such a combination may be useful for monitoring faulted or critically stressed reservoirs that are undergoing cyclic stress behaviour.

Bibliography

Chen, H., Meng, X., Niu, F., Tang, Y., Yin, C., & Wu, F. (2018). Microseismic monitoring of stimulating shale gas reservoir in SW China: 2. Spatial clustering controlled by the preexisting faults and fractures. *Journal of Geophysical Research: Solid Earth*, *123*(2), 1659–1672.

Chiarabba, C., De Gori, P., Segou, M., & Cattaneo, M. (2020). Seismic velocity precursors to the 2016 mw 6.5 norcia (italy) earthquake. *Geology*, *48*(9), 924–928.

Eaton, D. W. (2018). *Passive seismic monitoring of induced seismicity: Fundamental principles and application to energy technologies*. Cambridge University Press.

Grigoli, F., Cesca, S., Priolo, E., Rinaldi, A. P., Clinton, J. F., Stabile, T. A., Dost, B., Fernandez, M. G., Wiemer, S., & Dahm, T. (2017). Current challenges in monitoring, discrimination, and management of induced seismicity related to underground industrial activities: A European perspective. *Reviews of Geophysics*, *55*(2), 310–340.

Kaproth, B. M., & Marone, C. (2013). Slow earthquakes, preseismic velocity changes, and the origin of slow frictional stick-slip. *Science*, *341*(6151), 1229–1232.

Kim, K.-H., Ree, J.-H., Kim, Y., Kim, S., Kang, S. Y., & Seo, W. (2018). Assessing whether the 2017 Mw 5.4 Pohang earthquake in South Korea was an induced event. *Science*, *360*(6392), 1007–1009.

Liu, Q., Waheed, U. b., Borisov, D., Simons, F. J., Gao, F., & Williamson, P. (2022). Full-waveform centroid moment tensor inversion of passive seismic data acquired at the reservoir scale. *Geophysical Journal International*, *230*(3), 1725–1750.

Mahani, A. B., Kao, H., Walker, D., Johnson, J., & Salas, C. (2016). Performance evaluation of the regional seismograph network in northeast British Columbia, Canada, for monitoring of induced seismicity. *Seismological Research Letters*, *87*(3), 648–660.

Naderloo, M., Veltmeijer, A., & Barnhoorn, A. (2022). Active and passive monitoring of fault reactivation under stress cycling. *SEG/AAPG International Meeting for Applied Geoscience Energy*.

Oye, V., Anell, I., Braathen, A., Dichiarante, A. M., Evans, J., Hafner, A., Liberty, L., Midtkandal, I., Petrie, E., & Sauvin, G. (2021). Monitoring and imaging of active and passive CO2 seepage patterns. *Available at SSRN 3819197*.

Shreedharan, S., Bolton, D. C., Rivière, J., & Marone, C. (2021). Competition between preslip and deviatoric stress modulates precursors for laboratory earthquakes. *Earth and Planetary Science Letters*, *553*, 116623.

Snieder, R. (2006). The theory of coda wave interferometry. *Pure and Applied geophysics*, *163*, 455–473.

van Thienen-Visser, K., & Breunese, J. (2015). Induced seismicity of the groningen gas field: History and recent developments. *The Leading Edge*, *34*(6), 664–671.

Verdon, J. P., Kendall, J.-M., White, D. J., Angus, D. A., Fisher, Q. J., & Urbancic, T. (2010). Passive seismic monitoring of carbon dioxide storage at Weyburn. *The Leading Edge*, *29*(2), 200–206.

Zotz-Wilson, R., Boerrigter, T., & Barnhoorn, A. (2019). Coda-wave monitoring of continuously evolving material properties and the precursory detection of yielding. *The Journal of the Acoustical Society of America*, *145*(2), 1060–1068.

5

SEISMICITY EVOLUTION DURING FAULT REACTIVATION UNDER STRESS CYCLING

Abstract: *Human activities involving subsurface operations are widely acknowledged to potentially induce seismicity, raising public concern and highlighting safety risks associated with these projects. Numerous studies have suggested that regulating parameters related to injection and depletion, like the pattern and rate of injection, may help mitigate induced seismicity. In the research reported in this chapter, we conducted displacement-driven fault reactivation experiments on saw-cut Red Felser sandstone to gain fresh insights into how stress and sliding patterns affect fault slip behaviour and the evolution of seismicity. We applied three distinct stress patterns: continuous, cyclic, and under-threshold cyclic. Results showed that compared to continuous sliding, cyclic sliding triggers less seismicity in terms of total b-value and a reduction in the number of large AE events potentially due to the uniform reduction in roughness and normal stress on the fault plane; however, the healing of gouge material on the fault plane during the unloading phase can result in an increased slip velocity. Also, by increasing the number of cycles, the number of generated events and AE energy per cycle are generally reduced. The outcomes of the tests conducted under the under-threshold cycling scenario revealed that this pattern effectively prevents seismicity. However, if the shear stress surpasses the previously established maximum (critical) shear stress, seismicity escalates dramatically, as evidenced by an increase in both maximum AE energy and magnitude. These results underscore the significance of considering the amplitude of the cycles and the healing effect in the design of injection and depletion protocols.*

5.1. INTRODUCTION

It is widely acknowledged that human activities related to subsurface operations such as geothermal projects, water waste injection, and gas storage or production can induce seismicity (Bommer et al., 2015; Muntendam-Bos et al., 2022). Well-known examples of induced seismicity are Pohang, South Korea with a moment magnitude of M_w5.4 caused by a geothermal energy project (Kim et al., 2018), Oklahoma, US, an order of magnitude M_w5.7 earthquake due to the waste-water injection (Keranen & Weingarten, 2018), and seismicity associated with gas production in the Groningen gas field, Netherlands (Lele et al., 2016; van Thienen-Visser & Breunese, 2015). There are two major mechanisms of induced seismicity within faulted geological settings. First, injection-driven fault reactivation, which occurs due to the reduction in the shear strength of the fault plane during pore pressure increase (Ellsworth, 2013; Segall & Fitzgerald, 1998). The second mechanism is depletion-driven fault reactivation as a result of the stress path perturbation, which is caused by poroelastic effects (Chan & Zoback, 2007; Jansen et al., 2019; Jin & Zoback, 2015; Raleigh et al., 1976; Segall, 1989; Zoback & Gorelick, 2012). Induced seismicity can pose significant risks to nearby infrastructure and the well-being of local communities. Consequently, gaining a comprehensive understanding of how injection operations and related parameters impact seismic activity and fault displacement is crucial for the safe and effective implementation of geo-storage projects such as those involving hydrogen and geothermal energy (Lee et al., 2019).

5

Several experimental studies have attempted to investigate the possible mitigation of the seismic risks associated with fluid injection (Hofmann, Zimmermann, Zang, & Min, 2018; Patel et al., 2017; Zang et al., 2013). The recently developed hydraulic fatigue concept (cyclic fluid injection) showed an ability for permeability enhancement and mitigation of injection-induced seismic risks (Niemz et al., 2020; Zang et al., 2013). It has been suggested that cyclic fluid injection's seismic response differs from monotonic injection's, and cyclic injection may result in less induced seismicity (Naderloo et al., 2023; Zang et al., 2019). In addition to the cyclic injection itself, Niemz et al. (2020) showed that using a cyclic progressive pattern triggers less seismicity in terms of b-value (frequency-magnitude distribution) and large magnitude events compared to conventional monotonic injection. However, all the studies mentioned above have been carried out on intact rock media, and not faulted media. The mechanism of seismicity caused by the hydro-fracturing of intact rocks is expected to be different from hydro-shearing or fault reactivation (Gischig & Preisig, 2015).

Few experimental investigations have addressed the effect of injection pattern on the mitigation of seismicity in faulted rock media during fault reactivation (Ji, Yoon, et al., 2021; Ji, Zhuang, et al., 2021; Naderloo et al., 2022; Noël et al., 2019; Wang et al., n.d.). Regarding the effect of pressure cycling (pattern), Noël et al. (2019) performed a fault reactivation experiment on saw-cut sandstone under fluid oscillation. They concluded that pressure oscillation promotes unstable behavior rather than stable slip. In contrast, Ji, Zhuang, et al. (2021), by performing injection-driven fault reactivation on faulted granite samples, showed that cyclic injection with limited pore pressure results in lower peak slip velocity and aseismic slip compared with a monotonic pattern. In a similar experiment, cyclic fluid injection promotes the diffusion of fluid pressure along faults. However, the reduction in seismic moment release is influenced by several cycle-related factors, such as the critical injection pressure and injection frequency (Ji, Zhuang, et al., 2021). These contradictory results can be due to differences in the permeability of rock samples, drainage of faults, and different boundary conditions (Rathnaweera et al., 2020).

In addition, there are several numerical and field scale studies on mitigating and managing induced seismicity (Hager et al., 2021; Hofmann, Zimmermann, Zang, Yoon, et al., 2018; Sabah et al., 2022). A seismic traffic light system is employed, wherein adjustments to injection rates and pressures are made in accordance with predefined thresholds related to recorded seismic magnitudes or other pertinent factors (Hofmann, Zimmermann, Zang, Yoon, et al., 2018). Field experiments conducted in the early 1970s at the Rangely, Colorado (USA) oil field indicated that seismic activity could potentially be triggered or mitigated by cyclically altering subsurface fluid pressure above or below a specific threshold (Raleigh et al., 1976). Ji et al. (2022) employed both numerical and analytical models to examine cyclic fluid injection into a fault zone characterized by pressure-sensitive permeability. Results showed that automatically adjusting cyclic injection parameters, guided by near-real-time and high-resolution reservoir monitoring, has the potential to optimize flow rates for economically and environmentally sustainable operation of Enhanced Geothermal Systems (EGS).

Although there are several studies addressing the effect of cyclic stress/pressure on fault reactivation behavior and its mitigation, some aspects and issues remain unclear, such as the effect of number cycles and amplitude (threshold) of the cycles on microseismicity evolution and fault slip (Naderloo et al., 2023). Additionally, the impact of cyclic normal stress on fault slip, compared to constant normal stress when the fault slides or reactivates, is poorly understood (Hong & Marone, 2005). In the research reported in this chapter, we carried out a triaxial fault reactivation experiment on saw-cut Red Felser sandstone using an instrumented triaxial cell to investigate a possible solution for seismicity mitigation. Microseismicity (number of events, b-value, and energy) results obtained from continuous and cycling sliding are compared first. Second, we show the effect of the number of cycles on microseismicity evolution. Ultimately, under-threshold stress cycling was studied.

5.2. MATERIAL AND METHODS

5.2.1. SAMPLE PREPARATION

We selected a high-porosity Red Felser sandstone as the reservoir rock for our displacement-driven fault reactivation experiments. This sandstone was sourced from the vicinity of Kaiserslautern, Germany. Initially, a specific rock block was identified for drilling cylindrical samples with a 30 mm diameter, which were subsequently cut to a nominal length of approximately 75 mm. The samples were characterized with an average density of $2.1 \pm 0.015\,\mathrm{g/cm^3}$ and porosity of $21.14 \pm 0.7\%$, determined using a gas expansion (Helium) pycnometer. Samples falling within the range of the average porosity $\pm 1\%$ standard deviation were exclusively chosen to ensure consistent results. To simulate a fault plane, cylindrical samples measuring 75 mm in length and 30 mm in diameter were cut at a $30°$ angle relative to the vertical cylinder axis. Careful cleaning of the saw-cut surfaces was conducted to remove the rock grains from the fault surface across all samples. Table 5.1 shows important information about the saw-cut samples used for the fault reactivation experiment.

Table 5.1: Information about the samples, sliding scenarios—monotonic sliding (MS), cyclic sliding (CS), and under-threshold sliding (UTS)—total radiated energy (E_{total}), total number of events (N_{total}), porosity, confining pressure, and displacement rate.

Sample	Pattern	b-value	E_{total}	N_{total}	Porosity (%)	Confining Pressure (MPa)	Displacement Rate (mm/s)
RF125	CS	2.61	0.00019	1001	21.6	20	0.0005
RF119	CS	2.30	0.00025	1306	20.7	20	0.0005
RF116	MS	2.03	0.00047	1650	21.3	20	0.0005
RF121	MS	2.02	0.0004	1549	21.8	20	0.0005
RF130	UTS	-	-	-	21.5	20	0.0005

5.2.2. TESTING APPARATUS

5

To conduct the triaxial fault reactivation experiments, we utilized an instrumented Hoek cell with a maximum confining pressure capacity of 70 MPa. This instrumented Hoek cell was positioned beneath a uniaxial servo-control loading machine (with maximum capacity of 500 kN), offering a resolution of ±0.05 kN, responsible for applying the axial stress (σ_1) (see Figure 5.1). The loading machine is capable of achieving a maximum displacement rate of 1 mm/s and a minimum displacement rate of 0.0001 mm/s. We employed a specialized silicon jacket to safeguard the rock sample from the confining oil. We embedded eight piezoelectric transducers within this silicon jacket, which are 5 mm in diameter and 1 mm in thickness. These transducers were in direct contact with the rock surface to capture microseismic events or acoustic emissions (AE). To improve the data acquisition, the emitted signals were amplified using pre-amplifiers, which were subsequently linked to Richter continuous data acquisition system. We employed a Richter acoustic emission system to capture and detect microseismic activities across a range of stress patterns and rates, as illustrated in Figure 5.1. The Richter system is a versatile, multi-channel data acquisition system with 16-bit ADC resolution, allowing for simultaneous and synchronous sampling of all input channels. Continuous waveforms were recorded at a sampling rate of 2 MHz, with an input impedance of 50 Ω, using the ExStream software. While the ExStream software of the Richter system handled the recording of acoustic emission data, the raw continuous waveform data underwent processing and management through the Insite Seismic Processor software. This processing included the conversion of continuous waveform data into individual waveforms for subsequent analysis, following a predefined trigger logic. For an event to be recorded, was necessary for five or more transducers to exceed a voltage threshold of approximately 25 mV within a time window of 480 μs, all at the 2 MHz sampling rate. The amplitude threshold of 25 mV was carefully established, considering the various sources of background noise commonly present in the laboratory environment. To further enhance the quality of signal recording, a thin layer of acoustic coupling agent was applied between the sensors and the rock surface. To ensure data integrity, any initial recorded events attributed to the settling of loading plates and friction between the loading piston and the rock sample at the beginning or any stage of the loading process were excluded from the dataset.

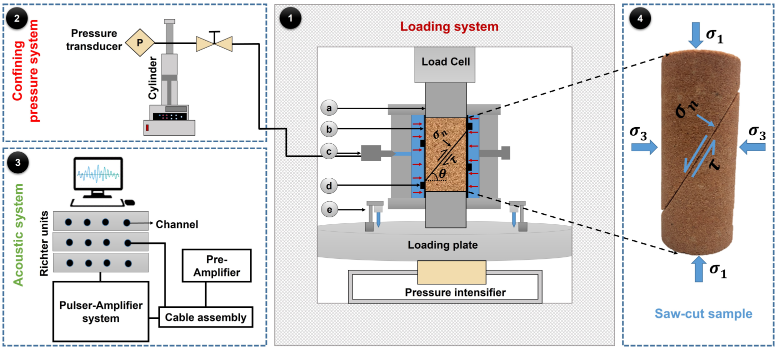

Figure 5.1: Schematic of the experimental setup including different units: 1) Loading system ((a) loading piston, (b) silicon jacket, (c) confining oil inlet, (d) acoustic emission sensor, (e) Linear Variable Differential Transformer (LVDT) for measuring axial deformation, 2) Confining pressure system, 3) Acoustic system, and 4) saw-cut sample.

We implemented a four-step displacement-driven fault reactivation protocol, illustrated in Figure 5.2. In the first step, axial stress and confining pressure were increased hydrostatically up to the desired confining pressure of 20 MPa while the sample was fully saturated (as indicated by the grey-shaded zone). In the second step, axial stress was incremented at a rate of 0.0005 mm/s to reach the shear strength of the fault plane (depicted in the orange shaded area) while maintaining constant confining pressure. During this phase, both rock matrix deformation and fault compaction occurred, and this behavior was not entirely linear. In the subsequent step, step three, fault reactivation commenced with slow sliding (creep) and continued to induce more slip (within the reactivation zone). Identifying an exact stress point as the reactivation point proved challenging. However, based on stress–strain and stress-time derivatives, we estimated the reactivation zone, denoted by the green-shaded region in Figure 5.2. In other words, by analyzing the stress–strain and stress–time data and aligning the results at the same stress levels, the point at which drastic non-linear stress behavior begins was identified, which is assumed to mark the onset of fault reactivation zone. Finally, after reactivation, three different fault sliding scenarios were executed as follows:

1. Continuous or monotonic sliding of the fault plane (Figure 5.2a).

2. Cyclic sliding, in which after a specific amount of fault slip (2.5 min sliding, consistent across all cycles), axial stress (σ_1) was decreased by 12 MPa (down to the stress level at which reactivation begins) and subsequently increased to attain the shear strength, resulting in fault slip (Figure 5.2b).

3. Under-threshold cycling sliding, similar to cyclic sliding but with the maximum stress during the cycles remaining below the previously reached maximum stress (96% of previous maximum stress) (as shown in Figure 5.2c). The under-threshold cycling starts in the same manner as the cyclic sliding pattern, and after three cycles with restricted peak stress, it transitions to cycles with peak stress levels below the previous maximum. After 12 such restricted cycles, stress is once again in-

creased to exceed the previous maximum stress and is followed by six cycles similar to the initial three cycles. The purpose of combining normal stress cycling with under-threshold cycling was to investigate the changes in cycle amplitude during operation and their impact on seismicity. This approach also allows for a meaningful comparison between the two types of cyclic sliding within the same experiment.

It is important to note that the same amount of sliding or strain was applied for both continuous and cycling sliding patterns to ensure comparability across different parameters (Figure 5.2b and 5.2c). The normal stress (σ_n) and shear stress (τ) on the fault plane were calculated from the principal stresses following:

$$\sigma_n = \frac{1}{2}(\sigma_1 + \sigma_3) - \frac{1}{2}(\sigma_1 - \sigma_3)\cos 2\theta, \tag{5.1}$$

and

$$\tau = \frac{1}{2}(\sigma_1 - \sigma_3)\sin 2\theta. \tag{5.2}$$

5

The axial stress is represented by σ_1 and the radial stress by σ_3 while θ is the angle between the axial stress and the fault plane.

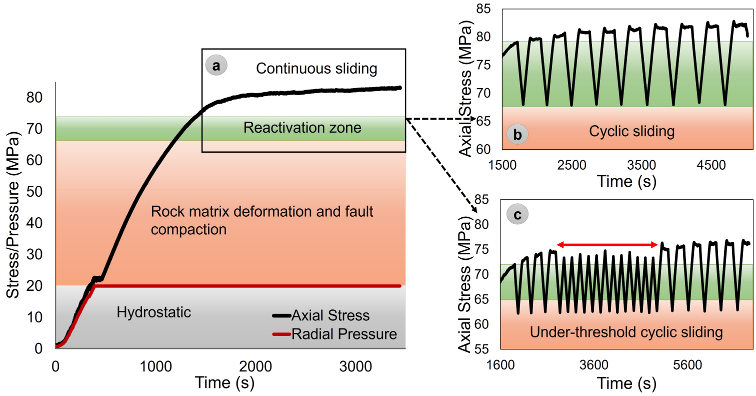

Figure 5.2: Illustration of the experimental protocol and stress path: a) continuous sliding, b) cyclic sliding, and c) under-threshold cyclic sliding.

5.3. RESULTS

5.3.1. CONTINUOUS SLIDING VERSUS CYCLIC SLIDING

Figure 5.3 shows the evolution of microseismic (MS) events, slip velocity, and axial shortening by further increasing the axial stress (advancing the axial loading piston). In the case of continuous sliding (Figure 5.3a and Figure 5.4a), there is no significant change in axial stress and normal stress on the fault plane, and there is a slight hardening of both. MS events are generated from the start of the fault reactivation (events also generated before fault reactivation due to fault compaction, grain crushing, and some inelastic deformation in the rock matrix) continuously until the end of the slip. The rate of MS event generation decreases as the experiment approaches its conclusion. Additionally, axial shortening increases at a constant rate until the end of the experiment, totaling 0.82 mm (approximately a total strain of 2.47%) (Figure 5.4a).

During fault reactivation using cyclic sliding (Figure 5.3b and Figure 5.4b), there is an oscillation in axial stress and normal stress acting on the fault plane. After decreasing the axial stress after each cycle, when it increases again to reach the shear strength, there is a slight drop in stress, and fault sliding continues. Fault reactivation begins with an increase in slip velocity, and after reaching a maximum slip, the velocity slightly drops and becomes constant until the moment axial stress decreases. Also, at the start of fault reactivation in each cycle, microseismic (MS) events are generated until the start of the stress reversal. Similar to continuous sliding, stress is slightly built up by further sliding and increasing the number of cycles. The number of events and the amplitude of each event decreases with an increasing number of cycles. Additionally, the amplitude of the events varies.

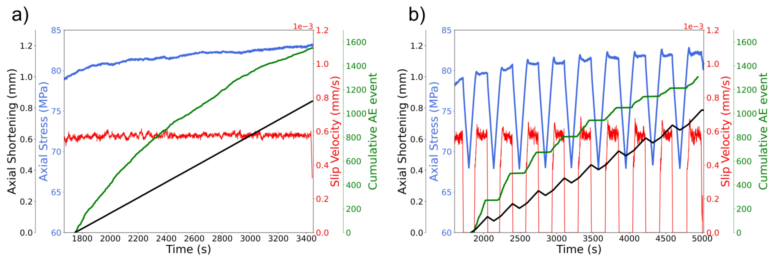

Figure 5.3: The evolution of microseismicity (MS) events, slip velocity, and axial shortening by further increasing the axial stress (advancing the axial loading piston). a) continuous sliding and b) cyclic sliding.

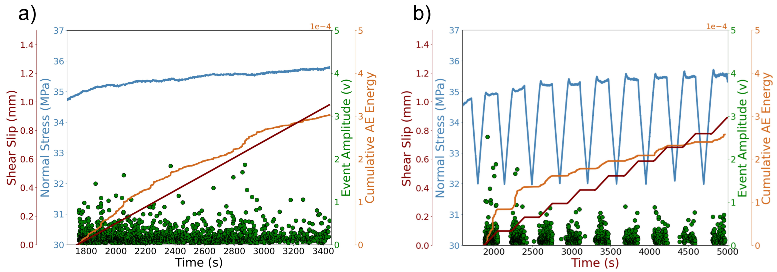

Figure 5.4: The evolution of normal stress, induced shear slip, and MS events amplitude by further increasing the axial stress (advancing the axial loading piston). a) continuous sliding and b) cyclic sliding.

Figure 5.5a presents a detailed view of the initial two cycles for the cyclic sliding experiment. Within each cycle, there is an escalation in slip velocity and microseismic (MS) events prior to surpassing the previously attained maximum stress. Essentially, fault reactivation commences with a period of creep and requires time to surpass the ultimate strength, after which it undergoes continuous movement at a steady slip velocity. Notably, no reverse sliding occurs during stress reduction (axial shortening diminishes as axial stress lessens), as evidenced by the absence of MS events. A reduction in axial stress leads to the decompaction of both the rock matrix and the fault plane during stress reversal. Additionally, Figure 5.5b illustrates that shear slip begins with events of small amplitude, which, upon exceeding the ultimate strength, are followed by the occurrence of large amplitude events. Furthermore, Figure 5.6 demonstrates that, generally, as the number of cycles increases, there is a decline in the overall count of acoustic emission (AE) events produced, the maximum amplitude, and the total AE energy radiated. This decline is particularly pronounced within the initial four cycles, becoming less severe thereafter, and eventually levels off.

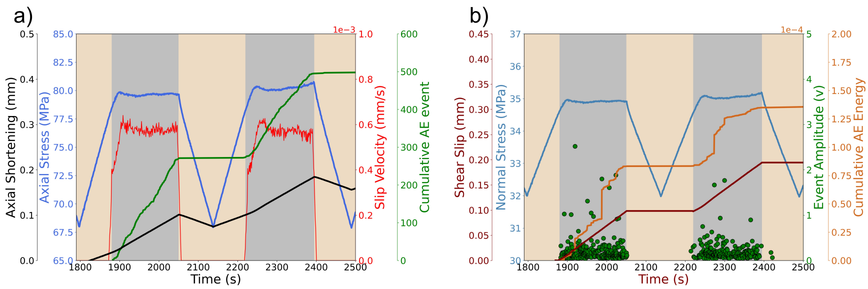

Figure 5.5: Zoomed view of first two-cycle from Figure 5.3b and Figure 5.4b. a) The evolution of microseismicity (MS) events, slip velocity, and axial shortening. b) The evolution of normal stress, induced shear slip, and MS events amplitude. The grey area represents the period of fault reactivation in each cycle, from its initiation to its conclusion.

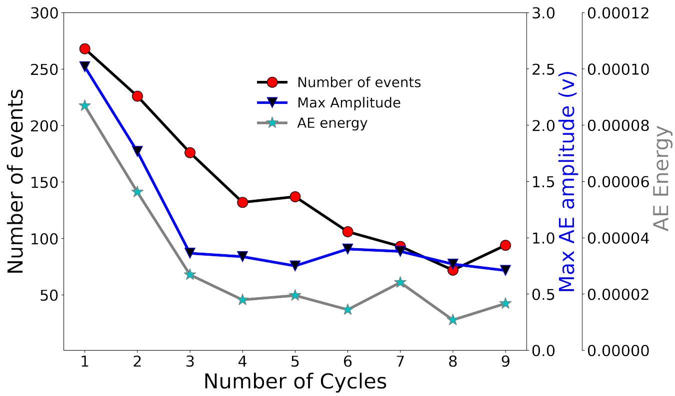

Figure 5.6: Evolution of the number of events, maximum AE amplitude, and AE radiated energy per cycle for the cyclic sliding scenario.

5.3.2. UNDER-THRESHOLD CYCLIC SLIDING

Figure 5.7 illustrates the change in different parameters after fault reactivation using both cyclic and under-threshold sliding. The first three cycles exhibit a pattern similar to stress cycling sliding. However, after this (point A), axial stress does not exceed the previous maximum stress (Figure 5.7a and Figure 5.8a). Microseismic (MS) events are generated in the first three cycles, but with the start of under-threshold cycling (Figure 5.7a, point A), the number of generated events decreases drastically, becoming almost absent with only a few MS events. After 12 under-threshold cycles, axial stress increases again to reach the maximum previous stress level, marking the start of cyclic sliding. Subsequent to reaching the previous maximum stress, stress builds up (approximately 1.5 MPa) and then drops, initiating continuous sliding. Both Figure 5.7b and 5.8b show that MS events generate again, and slip velocity accelerates. Slip velocity reaches its maximum, drops, recovers, and continues with nearly constant velocity.

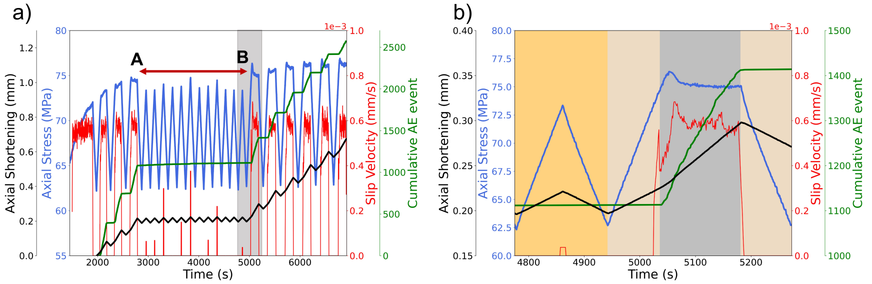

Figure 5.7: a) The evolution of microseismicity (MS) events, slip velocity, and axial stress. b) Zoomed view of the grey-shaded area in Figures 5.7.

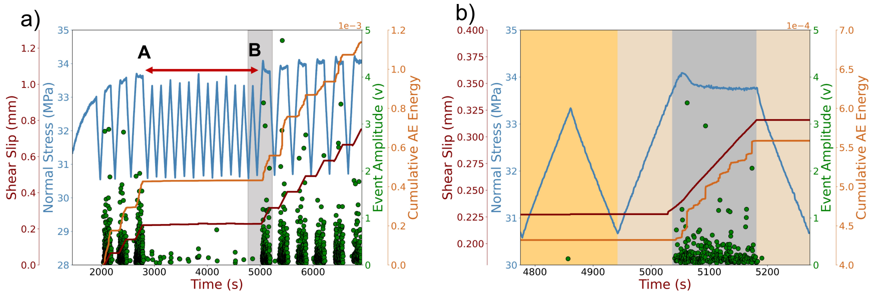

Figure 5.8: The evolution of normal stress, induced shear slip and MS events amplitude. b) Zoomed view of the grey-shaded area in Figures 5.8.

Figure 5.9 displays the progression of the number of events, the maximum acoustic emission (AE) amplitude, and the AE radiated energy per cycle for both under-threshold and regular cyclic sliding. During the initial three cycles of cyclic sliding, there is a decrease in the total number of AE events, the maximum amplitude, and the overall AE energy. With the onset of under-threshold cyclic sliding, there is a drastic drop in the number of events, maximum AE amplitude, and AE radiated energy (indicated by the grey shaded zone in Figure 5.9). Resuming cyclic sliding (highlighted by the light brown shaded zone) leads to a significant increase in the number of events, maximum AE amplitude, and AE radiated energy. Consequently, the maximum AE amplitude and AE radiated energy surpass the levels observed during the first three cycles of sliding. Therefore, using under-threshold cycling can reduce or stop the generation of microseismic (MS) events compared to cyclic and continuous sliding. However, increasing the stress again up to a level completely overcoming the fault strength can even induce larger events or high-energy events.

5.4. Discussion

5.4.1. Effect of stress pattern

While the total shear displacement (total strain of 2.47% in the system) remained fairly consistent between continuous and cyclic sliding patterns, variations were observed in

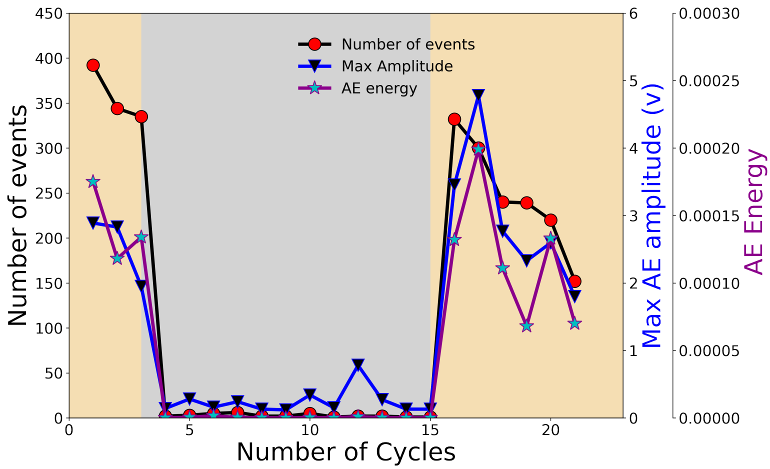

Figure 5.9: Evolution of the number of events, maximum AE amplitude, and AE radiated energy per cycle for the under-threshold cyclic sliding scenario.

seismicity and slip patterns. Figure 5.10 highlights key parameters essential for seismicity mitigation, such as the total number of events, the b-value, and the total radiated Acoustic Emission (AE) energy derived from the experiments for both continuous and cyclic sliding patterns. In continuous sliding, there is a higher total number of events and greater total radiated AE energy compared to the cyclic sliding pattern. Additionally, the b-value observed in continuous sliding is lower than that in the cyclic pattern, indicating a relatively higher frequency of larger events compared to smaller ones. Figure 5.11 shows the frequency-amplitude distributions of the events for two sliding patterns in which events from the cyclic sliding pattern have an increased number of small events relative to the large ones as indicated by a high b-value (see Figure 5.11). Therefore, the cyclic sliding pattern indicates a lower potential for inducing large-magnitude events compared to continuous sliding.

The study by Ji, Yoon, et al. (2021) on injection-induced fault reactivation in faulted granite, using both monotonic and cyclic injection, revealed that cyclic injection leads to a uniform reduction in effective normal stress. This results in slow and stable fracture slip, as indicated by lower peak slip rates. The cause is attributed to the sequence of fluid flowback and re-injection, which encourages gradual and more even fluid pressure distribution on the fault plane. However, this observation holds only under conditions of restricted peak injection and a certain amount of total slip. In addition, increased permeability aids in achieving a more uniform distribution of fluid pressure along the fracture, thereby reducing the injection pressure required to activate the fracture (Ji et al., 2020; Passelègue et al., 2018). In a similar study, Ji, Zhuang, et al. (2021) observed that cyclic fluid injection equalizes the fluid pressure distribution across the fault plane. Nonetheless, its efficiency in reducing seismic moment release depends on various injection cycle-related factors, including the critical injection pressure and injection frequency. In our results, oscillation of the normal stress acting on the fault plane induces compaction and relaxation, which can potentially lead to a uniform reduction in both roughness and asperities (see Figure 5.4a). We hypothesize that instead of abrupt asperity damage during slip via continuous sliding, cyclic sliding gradually reduces and removes asperities. This process lowers the likelihood of slip nucleation. During both continuous sliding and cyclic sliding, the number of generated events decreases as the experiments approach their end (see Figures 5.3 and 5.4). However, large AE events can still occur (Figure 5.3a). In cyclic sliding, the amplitude of large events diminishes as the number of cycles increases and the experiment nears completion.

At the beginning of fault reactivation in each cycle (Figure 5.3b), we notice a buildup and drop in stress, leading to a slight increase in slip velocity, which then stabilizes after reaching a peak. This pattern might result from the healing of the quartz-rich gouge during periods of inactivity of the fault plane, resembling a 'hold' condition for the fault plane. The fault plane in this hold condition is more likely to experience healing even over short periods (the unloading ramp duration), enhancing the shear strength of the quartz-rich fault plane ((Hunfeld et al., 2017; Seyler et al., 2023)). In effect, frictional healing contributes to the fault's strengthening, and stress build-up during the start of reactivation. Therefore, although cyclic sliding can reduce sudden asperity breakage, the number of events, and the magnitude of events as cycles increase (compared to continuous sliding), it also exhibits peak slip velocities slightly higher than during the oscillations in slip velocity seen in continuous sliding (Figure 5.3). Consequently, careful consideration of cyclic operation parameters, such as maximum amplitude and rock medium type, is essential.

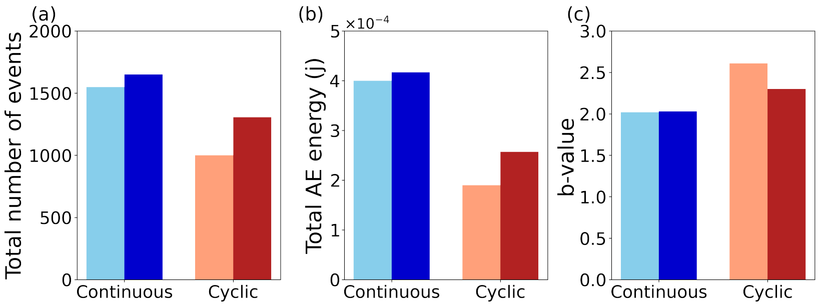

Figure 5.10: Comparison of different seismicity parameters obtained from the experiment with different sliding patterns (The light blue and dark blue bars represent the continuous sliding pattern, while the light orange and dark red bars represent the cyclic sliding pattern): a) the total number of MS events, b) total radiated AE energy, and c) estimated b-value.

5.4.2. HEALING AND UNDER-THRESHOLD SLIDING

As previously stated, it is crucial to carefully consider cyclic operation parameters, such as limiting the peak amplitude of the cycle, to reduce seismicity (Ji, Yoon, et al., 2021; Ji, Zhuang, et al., 2021). Our findings indicate that employing under-threshold cycling can diminish or halt the generation of microseismic (MS) events, in contrast to both cyclic and continuous sliding. However, re-escalating the stress to a level that completely overcomes the fault strength may trigger larger or more energetic events, as illustrated in

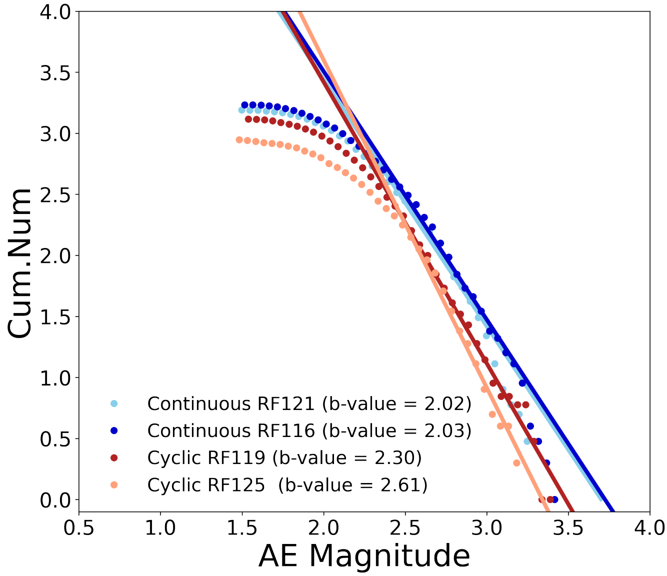

Figure 5.11: b-value estimation for the tests from continuous and cyclic sliding.

Figures 5.7, 5.8, and 5.9. This phenomenon could be attributed to the healing effect observed after 12 under-threshold cycles, during which the fault remains semi-stationary and in a held state. In other words, the fault plane experiences a sequence of compaction and relaxation without reactivation (sliding). We conducted a slide-hold-slide experiment using saw-cut Red Felser sandstone. The slide-hold-slide experiment is commonly used for studying material healing (Hunfeld et al., 2017; Richardson & Marone, 1999; Tesei et al., 2012). This experiment also incorporated two cycles of under-threshold cycling. Figure 5.12 presents the evolution of shear stress and friction coefficient when applying two under-threshold sliding cycles with three different holding times (1 minute, 10 minutes, and 20 minutes). The data from these varying holding periods suggest that even a one-minute hold can initiate a healing effect, and longer hold times further enhance the fault's strengthening (stress buildup), as marked at points A, B, and C. Moreover, even just two under-threshold cycles can lead to a healing effect and fault strengthening. Therefore, while under-threshold cycles can mitigate seismicity, the consequent healing of the gouge material on the fault plane means that if stress escalates to match the fault strength, it could induce larger events due to the resultant higher stress drop.

5.5. Conclusion

In this chapter, we carried out displacement-driven fault reactivation experiments on saw-cut Red Felser sandstones. These experiments were designed to examine the impact of different sliding patterns on seismicity and slip evolution. We employed three distinct sliding patterns: continuous sliding, cyclic sliding, and under-threshold sliding. The outcomes of these experiments revealed several key findings:

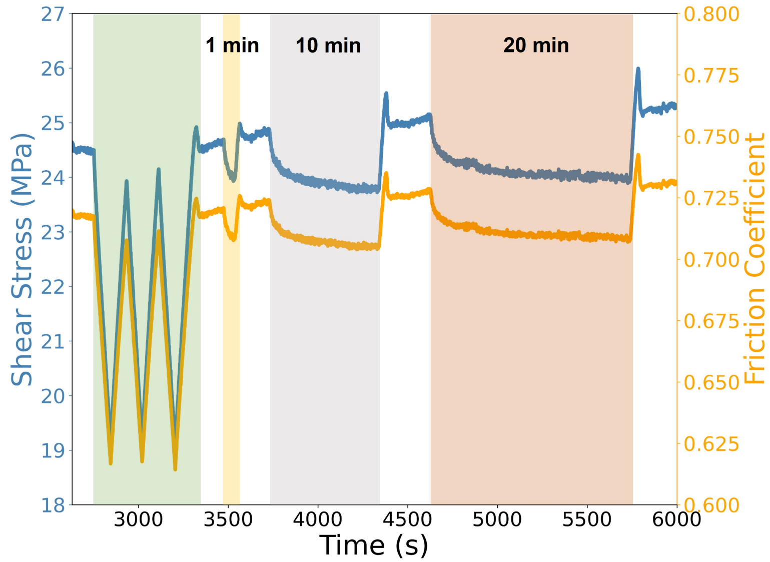

Figure 5.12: The evolution of shear stress and friction coefficient when applying two under-threshold sliding cycles with three different holding times (1 minute, 10 minutes, and 20 minutes).

1. Compared to continuous sliding, cyclic sliding triggers less seismicity in terms of total b-value and large Acoustic Emission (AE) events, probably through a uniform reduction in roughness and normal stress on the fault plane.
2. By increasing the number of cycles, in general, the number of generated events and AE energy are reduced. Nevertheless, there is a continued risk of generating large AE events during the first cycles.
3. The under-threshold cycling scenario prevents seismicity and pure shear slip; however, if shear stress exceeds the previous maximum (critical) shear stress, seismicity hazard increases drastically in terms of maximum AE energy, and magnitude.
4. The healing of gouge material on the fault plane during the unloading phase of the cycles probably causes shear strengthening and stress buildup, leading to a subsequent stress drop. This process can result in an increase of slip velocity.

Bibliography

Bommer, J. J., Crowley, H., & Pinho, R. (2015). A risk-mitigation approach to the management of induced seismicity. *Journal of Seismology*, *19*(2), 623–646.

Chan, A. W., & Zoback, M. D. (2007). The role of hydrocarbon production on land subsidence and fault reactivation in the Louisiana coastal zone. *Journal of Coastal Research*, *23*(3 (233)), 771–786.

Ellsworth, W. L. (2013). Injection-Induced Earthquakes. *341*(July), 1–8.

Gischig, V. S., & Preisig, G. (2015). Hydro-fracturing versus hydro-shearing: a critical assessment of two distinct reservoir stimulation mechanisms. *ISRM Congress*, ISRM–13CONGRESS.

Hager, B. H., Dieterich, J., Frohlich, C., Juanes, R., Mantica, S., Shaw, J. H., Bottazzi, F., Caresani, F., Castineira, D., & Cominelli, A. (2021). A process-based approach to understanding and managing triggered seismicity. *Nature*, *595*(7869), 684–689.

Hofmann, H., Zimmermann, G., Zang, A., Yoon, J. S., Stephansson, O., Kim, K. Y., Zhuang, L., Diaz, M., & Min, K.-B. (2018). Comparison of cyclic and constant fluid injection in granitic rock at different scales. *ARMA US Rock Mechanics/Geomechanics Symposium*, ARMA–2018.

Hofmann, H., Zimmermann, G., Zang, A., & Min, K. B. (2018). Cyclic soft stimulation (CSS): a new fluid injection protocol and traffic light system to mitigate seismic risks of hydraulic stimulation treatments. *Geothermal Energy*. https://doi.org/10.1186/s40517-018-0114-3

Hong, T., & Marone, C. (2005). Effects of normal stress perturbations on the frictional properties of simulated faults. *Geochemistry, Geophysics, Geosystems*, *6*(3).

Hunfeld, L. B., Niemeijer, A. R., & Spiers, C. J. (2017). Frictional properties of simulated fault gouges from the seismogenic Groningen Gas Field under in situ P–T-chemical conditions. *Journal of Geophysical Research: Solid Earth*, *122*(11), 8969–8989.

Jansen, Singhal, P., & Vossepoel, F. C. (2019). Insights From Closed-Form Expressions for Injection- and Production-Induced Stresses in Displaced Faults. https://doi.org/10.1029/2019JB017932

Ji, Y., Wang, L., Hofmann, H., Kwiatek, G., & Dresen, G. (2022). High-Rate Fluid Injection Reduces the Nucleation Length of Laboratory Earthquakes on Critically Stressed Faults in Granite. *Geophysical Research Letters*, *49*(23), e2022GL100418.

Ji, Y., Wanniarachchi, W. A. M., & Wu, W. (2020). Effect of fluid pressure heterogeneity on injection-induced fracture activation. *Computers and Geotechnics*, *123*, 103589.

Ji, Y., Yoon, J. S., Zang, A., & Wu, W. (2021). Mitigation of injection-induced seismicity on undrained faults in granite using cyclic fluid injection: A laboratory study. *International Journal of Rock Mechanics and Mining Sciences*, *146*, 104881.

Ji, Y., Zhuang, L., Wu, W., Hofmann, H., Zang, A., & Zimmermann, G. (2021). Cyclic Water Injection Potentially Mitigates Seismic Risks by Promoting Slow and Stable Slip of a Natural Fracture in Granite. *Rock Mechanics and Rock Engineering*, 1–17.

Jin, L., & Zoback, M. D. (2015). An Analytical Solution for Depletion-induced Principal Stress Rotations In 3D and its Implications for Fault Stability. *AGUFM*, *2015*, S13B–2816.

Keranen, K. M., & Weingarten, M. (2018). Induced seismicity. *Annual Review of Earth and Planetary Sciences*.

Kim, K.-H., Ree, J.-H., Kim, Y., Kim, S., Kang, S. Y., & Seo, W. (2018). Assessing whether the 2017 Mw 5.4 Pohang earthquake in South Korea was an induced event. *Science*, *360*(6392), 1007–1009.

Lee, K.-K., Ellsworth, W. L., Giardini, D., Townend, J., Ge, S., Shimamoto, T., Yeo, I.-W., Kang, T.-S., Rhie, J., & Sheen, D.-H. (2019). Managing injection-induced seismic risks. *Science*, *364*(6442), 730–732.

Lele, S. P., Hsu, S.-Y., Garzon, J. L., DeDontney, N., Searles, K. H., Gist, G. A., Sanz, P. F., Biediger, E. A. O., & Dale, B. A. (2016). Geomechanical Modeling to Evaluate Production-Induced Seismicity at Groningen Field. https://doi.org/10.2118/183554-MS

Muntendam-Bos, A. G., Hoedeman, G., Polychronopoulou, K., Draganov, D., Weemstra, C., van der Zee, W., Bakker, R. R., & Roest, H. (2022). An overview of induced seismicity in the Netherlands. *Netherlands Journal of Geosciences*, *101*.

Naderloo, M., Veltmeijer, A., Jansen, J. D., & Barnhoorn, A. (2023). Laboratory study on the effect of stress cycling pattern and rate on seismicity evolution. *Geomechanics and Geophysics for Geo-Energy and Geo-Resources*, *9*(1), 137. https://doi.org/10.1007/s40948-023-00678-1

Naderloo, M., Veltmeijer, A., Pluymakers, A., & Barnhoorn, A. (2022). Experimental Investigation of the Effect of Stress Cycling on Seismicity Evolution During Fault Reactivation Process. *83rd EAGE Annual Conference Exhibition*, *2022*(1), 1–5.

Niemz, P., Cesca, S., Heimann, S., Grigoli, F., Specht, S. V., Hammer, C., Zang, A., & Dahm, T. (2020). Full-waveform-based characterization of acoustic emission activity in a mine-scale experiment : a comparison of conventional and advanced hydraulic fracturing schemes, 189–206. https://doi.org/10.1093/gji/ggaa127

Noël, C., Passelègue, F. X., Giorgetti, C., & Violay, M. (2019). Fault Reactivation During Fluid Pressure Oscillations : Transition From Stable to Unstable Slip Journal of Geophysical Research : Solid Earth, 940–953.

Passelègue, F. X., Brantut, N., & Mitchell, T. M. (2018). Fault Reactivation by Fluid Injection: Controls From Stress State and Injection Rate. *Geophysical Research Letters*, *45*(23), 12, 837–12, 846. https://doi.org/10.1029/2018GL080470

Patel, S. M., Sondergeld, C. H., & Rai, C. S. (2017). Laboratory studies of hydraulic fracturing by cyclic injection. *International Journal of Rock Mechanics and Mining Sciences*, *95*(March), 8–15. https://doi.org/10.1016/j.ijrmms.2017.03.008

Raleigh, C. B., Healy, J. H., & Bredehoeft, J. D. (1976). An experiment in earthquake control at Rangely, Colorado. *Science*, *191*(4233), 1230–1237.

Rathnaweera, T. D., Wu, W., Ji, Y., & Gamage, R. P. (2020). Understanding injection-induced seismicity in enhanced geothermal systems: From the coupled thermo-hydro-

5

mechanical-chemical process to anthropogenic earthquake prediction. *Earth-Science Reviews*, *205*, 103182.

Richardson, E., & Marone, C. (1999). Effects of normal stress vibrations on frictional healing. *Journal of Geophysical Research: Solid Earth*, *104*(B12), 28859–28878.

Sabah, M., Ameri, M. J., Hofmann, H., & Ebrahimi, M. (2022). Numerical modeling of injection-induced earthquakes based on fully coupled thermo-poroelastic boundary element method. *Geothermics*, *105*, 102481.

Segall, P. (1989). Earthquakes triggered by fluid extraction. *Geology*, *17*(10), 942–946.

Segall, P., & Fitzgerald, S. D. (1998). A note on induced stress changes in hydrocarbon and geothermal reservoirs. *Tectonophysics*, *289*(1-3), 117–128.

Seyler, C. E., Shreedharan, S., Saffer, D. M., & Marone, C. (2023). The role of clay in limiting frictional healing in fault gouges. *Geophysical Research Letters*, *50*(20), e2023GL104984.

Tesei, T., Collettini, C., Carpenter, B. M., Viti, C., & Marone, C. (2012). Frictional strength and healing behavior of phyllosilicate-rich faults. *Journal of Geophysical Research: Solid Earth*, *117*(B9).

van Thienen-Visser, K., & Breunese, J. (2015). Induced seismicity of the groningen gas field: History and recent developments. *The Leading Edge*, *34*(6), 664–671.

Wang, L., Kwiatek, G., Rybacki, E., & Bonnelye, A. (n.d.). Laboratory Study on Fluid - Induced Fault Slip Behavior : The Role of Fluid Pressurization Rate Geophysical Research Letters, 1–12. https://doi.org/10.1029/2019GL086627

Zang, A., Yoon, J. S., Stephansson, O., & Heidbach, O. (2013). Fatigue hydraulic fracturing by cyclic reservoir treatment enhances permeability and reduces induced seismicity. *Geophysical journal international*, *195*(2), 1282–1287.

Zang, A., Zimmermann, G., Hofmann, H., Stephansson, O., Min, K.-B., & Kim, K. Y. (2019). How to reduce fluid-injection-induced seismicity. *Rock Mechanics and Rock Engineering*, *52*(2), 475–493.

Zoback, M. D., & Gorelick, S. M. (2012). Earthquake triggering and large-scale geologic storage of carbon dioxide. *Proceedings of the National Academy of Sciences*, *109*(26), 10164–10168.

5

6

Injection-induced Seismicity in Porous Media

Abstract: *To effectively mitigate the risks associated with induced seismicity, it is crucial to comprehend how fluid injection-related factors influence seismicity response and evolution. In this chapter, we perform injection-driven fault reactivation experiments on porous saw-cut Red Felser sandstone to provide new insight into the effect of injection pattern and rate on fault slip behavior and seismicity evolution. Three different injection rates were applied: high, medium, and low rates of 2 MPa/min, 1 MPa/min, and 0.2 MPa/min, respectively. Three injection patterns were also used: cyclic recursive, monotonic, and stepwise injections. Our results reveal that high injection rates lead to increased slip velocity, more microseismic events, higher total AE energy, and a lower b-value compared to low injection rate tests. We postulate that a high injection rate enhances the likelihood of a sudden reduction in effective normal stress, leading to fault opening and the disruption of asperity contacts. Regardless of the injection rate, all experiments consistently showed frictional strengthening. Furthermore, results from samples subjected to various injection patterns demonstrate that the cyclic recursive pattern exhibits a higher maximum slip velocity, more episodes of slow slip, and greater radiated AE energy than a monotonic pattern. In the case of the cyclic recursive pattern, increasing the number of cycles and available hydraulic energy budget increases shear stress drop, shear slip, and maximum slip velocity. A proper injection strategy must consider fault drainage, critical shear stress, injection rate, and injection pattern. Our results demonstrate that using a monotonic injection pattern and low pressurization rate may mitigate seismicity on pre-existing faults in a highly permeable porous reservoir.*

6.1. INTRODUCTION

Many human activities related to the subsurface, such as geothermal projects, water waste injection, and gas storage, involve the injection of pressurized fluids into the subsurface. The injection of pressurized fluids into underground formations can induce seismicity by reactivating pre-existing faults, which sometimes includes large-magnitude earthquakes (Deichmann & Giardini, 2009; Ellsworth, 2013b; Grigoli et al., 2018; Ji, Yoon, et al., 2021). Three well-known examples of induced seismicity are i) Pohang, South Korea with a moment magnitude of 5.4 caused by a geothermal energy project (Kim et al., 2018), ii) Oklahoma, US, an order of magnitude 5.7 earthquake due to the waste-water injection (Keranen & Weingarten, 2018), and three events above the magnitude of 3 in Basel, Switzerland during an Enhanced Geothermal Systems (EGS) project (Bachmann et al., 2012). From a physical perspective, reactivating pre-existing faults relies on the interplay of effective stress and the Coulomb failure criterion. Elevating the fluid pressure diminishes the effective normal stress acting on the fault plane. Consequently, the shear resistance decreases, enabling movement under tectonic shear stresses in natural settings (Ellsworth, 2013a; Keranen & Weingarten, 2018; Nicol et al., 2011; Zang et al., 2014; Zoback & Gorelick, 2012). Mitigating and managing seismic hazards caused by injection operations with the uninterrupted functioning of geo-storage operations is essential for society. Comprehending the key factors influencing injection-induced seismicity can contribute to improved management and mitigation strategies. Several attempts have been conducted to mitigate and reduce injection-induced seismicity on laboratory and field scales (Bommer et al., 2015; Hofmann et al., 2018; Ji, Yoon, et al., 2021; Ji, Zhuang, et al., 2021; Naderloo et al., 2023). There are two injection/production-related critical factors influencing seismicity. The first is the rate at which fluid pressure is increased during injection and the second, the pattern of fluid injection.

6

To first consider the effect of fluid injection rate: lowering fluid injection rates has been shown to lead to reduced seismic hazard and risk (Alghannam & Juanes, 2020; Ciardo & Rinaldi, 2022; French et al., 2016; Ji et al., 2022; Passelègue et al., 2018; L. Wang et al., n.d.). High injection rates during experiments performed on a saw-cut Westerly granite sample (extremely low permeable) under triaxial stress conditions facilitated the transition from drained to locally undrained conditions. High injection rates create local fluid pressure perturbations (heterogeneous distribution of fluid pressure) capable of reactivating faults (Passelègue et al., 2018). The same phenomenon occurred with stepwise increasing fluid pressure into faulted granite samples with different roughness (Ye & Ghassemi, 2018). Rutter and Hackston (2017) conducted triaxial shear experiments on sandstones with saw-cut fracture, both permeable and impermeable, revealing that fluid pressurization can readily induce seismogenic fault slip in low-permeable rock. Conversely, in permeable sandstone rock, fluid can permeate the fault plane through the rock matrix, following the law of effective stress, and this can lead to aseismic fault sliding (Rutter & Hackston, 2017). Therefore, in low permeable rocks, localized fluid overpressures due to the high injection rates can initiate episodes of quasi-static, partial fault slip, which can then progress to the nucleation and propagation of earthquakes. Injection-induced fault slip experiments on high-permeable saw-cut sandstone using high and low fluid pressurization rates showed that slip behaviour is determined by pressurization rate rather than injection pressure (L. Wang et al., n.d.). While several studies have explored the mechanism of fault reactivation with different injection rates on impermeable rocks, few studies have been allocated to reveal fundamental physical mechanisms linking the rate of fluid injection to induced earthquakes in permeable rocks (Alghannam & Juanes, 2020; Ji et al., 2022; Passelègue et al., 2018; Rutter & Hackston, 2017; Ye & Ghassemi, 2018, 2020). A systematic experimental study that focuses on whether different injection rates, which influence the stress path (effective normal and shear stress), will cause different slip behaviors, is currently lacking. The increased use of the subsurface, particularly of permeable reservoirs underlines the urgency of understanding the impact of slip behaviors on the evolution of microseismicity.

Second, it has been shown that there is a difference in the occurrence and distribution of induced seismicity between constant (monotonic) injection, or injection following a pre-specified pattern for both high-permeable and low-permeable reservoirs. Studies on either intact specimen (Naderloo et al., 2023; Zang et al., 2019; Zhuang et al., 2020) or faulted granite samples (Ji, Yoon, et al., 2021; Ji, Zhuang, et al., 2021) suggest that the seismic response to cyclic fluid injection differs from that of monotonic injection, with cyclic injection potentially leading to reduced levels of induced seismicity (Ji, Yoon, et al., 2021; Ji, Zhuang, et al., 2021; Naderloo et al., 2023; Niemz et al., 2020; Zang et al., 2019; Zhu et al., 2021; Zhuang et al., 2020). In other words, cyclic injection provides a potential mechanism to replace the big magnitude events with many small ones. Ji, Yoon, et al. (2021) conducted an injection-induced fault reactivation test on a critically stressed natural fracture in granite to investigate the slip behaviour under cyclic and monotonic injection patterns (Ji, Yoon, et al., 2021; Ji, Zhuang, et al., 2021). When the cyclic injection is conducted with a limited peak injection pressure, it induces aseismic fracture slips at significantly lower peak slip rates compared to those observed during the monotonic injection. The more uniform reduction in effective normal stress caused by cyclic injection promotes gradual and stable fracture slip, characterized by smaller peak slip rates (Ji, Zhuang, et al., 2021). Cyclic fluid injection facilitates the diffusion of fluid pressure along faults due to the sequence of fluid flowback and re-injection. Yet, the decrease in seismic moment release hinges on various cycle-related elements, including the critical injection pressure and injection frequency (Ji, Yoon, et al., 2021). Oscillating fluid pressure during fault reactivation experiments on permeable sandstone promotes seismic behavior rather than aseismic slip. This was interpreted to be due to the alterations in critical stiffness of the fault plane (Noël et al., 2019). The conflicting conclusions drawn regarding the effectiveness of cyclic injection primarily stem from the influence of the different fault's drainage and different boundary conditions (Ji, Yoon, et al., 2021; Ji, Zhuang, et al., 2021; Noël et al., 2019). Heimisson et al. (2022) showed that altering the bulk's poroelastic response through different undrained Poisson's ratio values and bulk hydraulic diffusivity is as pivotal for rupture stability. Therefore, it is essential to investigate and compare the effects of different injection patterns under the same boundary conditions on a simulated fault in permeable rock.

The aim of this chapter is twofold: to reveal the effect of, first, injection rates and second, injection patterns on seismicity parameters (radiated acoustic emission (AE) energy, total number of generated events, and magnitude-frequency distribution of the events) and the fault reactivation mechanism in permeable faulted rock. To this end, we conduct injection-driven fault reactivation experiments on saw-cut permeable Red Felser sandstones under three different injection rates (high, medium, low) and using three different patterns (monotonic, stepwise, and cyclic recursive injection patterns) whilst monitoring the fault slip and microseismic (MS) activities. Our results highlight that monotonic injection and low pressurization rate can reduce radiated acoustic energy, which may mitigate seismicity in a highly permeable and porous medium.

6.2. MATERIALS AND METHODS

6.2.1. SAMPLE PREPARATION

A high-porosity Red Felser sandstone was selected as the reservoir rock for the injection-driven fault reactivation experiments. This particular sandstone was collected from a quarry in the vicinity of Kaiserslautern, Germany. Cylindrical samples were drilled with a diameter of 30 mm and cut to a nominal length of approximately 75 ± 0.8 mm. The average density and porosity of the samples were determined to be 2.1 ± 0.015 g/cm^3 and 20.14 ± 0.7%, respectively, using a gas expansion (Helium) pycnometer. Only those with porosity falling within the range of the average porosity ± 1% standard deviation were selected to minimize experimental variability. Table 6.1 provides information about the saw-cut samples, experimental conditions, and the analysis of various parameters.

6

Table 6.1: Information about the saw-cut samples (porosity ρ), the experimental protocol (injection patterns: cyclic recursive injection (CRI), stepwise injection (SI), monotonic high-rate injection (MHI), monotonic medium-rate injection (MMI), and monotonic low-rate injection (MLI)), injection rates, and confining pressure (C_p), as well as other result parameters including b-value, total radiated AE energy (E_{total}), maximum slip velocity (V_{max}), and total number of events (N_{total}), is provided.

Sample	Injection Pattern	Injection Rate (MPa/min)	b-value	ρ (%)	C_p (MPa)	E_{total} (J)	V_{max} (mm/s)	N_{total}
RF133	CRI	2	1.84	19.3	20	4.9e-4	16e-4	425
RF126	SI	2	2.05	20.5	20	4.4e-4	13e-4	450
RF128	MHI	2	2.168	19.8	20	3.0e-4	12e-4	428
RF132	MMI	1	2.510	21.3	20	1.5e-4	4.1e-4	322
RF134	MLI	0.2	2.502	19.4	20	1.1e-4	2.2e-4	231

Furthermore, all samples were cut at a 30° angle relative to the vertical cylinder axis to simulate a fault plane. The saw-cut surfaces were carefully cleaned with a soft fabric to ensure removing leftover particles and grains due to the saw cut (see Figures S1). Red Felser sandstone is composed of 95% grain minerals, including 89% quartz and 6% orthoclase, and 5% matrix minerals, featuring 4% kaolinite, 1% albite, and trace amounts of haematite, chlorite, Ca-apatite, pyrite, and halite (van Uijen, 2013). To characterize mechanical properties of the Red Felser sandstone, five uniaxial compression tests were performed. The Red Felser sandstone has a UCS strength of 46 ± 3 MPa and a Young's Modulus of 16 ± 1.5 GPa. The permeability (water permeability) of the saw-cut sample was assessed using the steady-state Darcy flow method at a confining pressure of 21 MPa (similar as confining pressure used for the injection-driven fault reactivation tests), resulting in an approximate permeability of ~ 1.5 Darcy. The following equation (Equation 6.1) was utilized to estimate the diffusion time of the fluid within the saw-cut samples. With a sample length L of 70 mm and taking into account the viscosity of water

$\eta = 1 \times 10^{-3}\,\mathrm{Pa \cdot s}$ and the bulk compressibility of water $C_f = 0.5\,\mathrm{GPa}^{-1}$, the estimated diffusion time was calculated to be $t_c < 1.5 \times 10^{-4}\,\mathrm{s}$.

$$t_c = \frac{L^2 \times C_f \times \eta}{K}, \tag{6.1}$$

Pore fluid ramps are on the order of 0.2-2 MPa/min, therefore fluid pressure throughout the sample is considered to be always at equilibrium.

6.2.2. TESTING APPARATUS

For the triaxial fault reactivation tests, an instrumented Hoek cell was utilized, capable of applying confining pressure ($\sigma_2 = \sigma_3$) up to a maximum of 70 MPa. This cell was positioned beneath a uniaxial servo-control loading machine with a maximum capacity of 500 kN and a resolution of ±0.1 kN to provide the axial stress (σ_1), (see Figure 6.1). To isolate the rock sample and prevent interference from the confining oil, we employed a silicon jacket. Within this jacket, we embedded 8 piezoelectric transducers, each measuring 5 mm in diameter and 1 mm thick, making direct contact with the rock surface. These transducers recorded microseismicity or acoustic emission (AE) signals. To amplify these signals, we utilized pre-amplifiers (with a gain set to 40 dB) connected to a Richter system, which is a continuous data acquisition system (see Figure 6.1). The Richter system is a multi-channel setup with 16-bit ADC resolution, comprising four units that can be synchronized, and offers expandability up to 20 channels. Using the ExStream software, we recorded continuous waveforms at a 2 MHz sampling rate while maintaining an input impedance of 50 Ω. We processed and managed the captured raw data or continuous waveforms using Insite Seismic Processor software. A trigger logic was employed to convert the continuous waveform data into single waveforms for further analysis. Regarding background noise, number of sensors (8 sensors used), and array distribution, an event was recorded if three or more transducers exceeded a voltage threshold of approximately 0.07 V within a time window of 480 μs, with a sampling rate of 2 MHz. The axial displacement (L) was measured by averaging the readings from two linear variable differential transformers (LVDTs) positioned at the surface of the loading plate adjacent to the Hoek cell with a precision of ±1 μm and a 2 mm range (Figure 6.1). ISCO pumps model 100DM were used for the pore fluid injection and confining pressure systems, which are highly precise with a precision of 0.5% in reading pressure. The pore pressure system utilizes distilled water, while the confining pressure system operates with silicon oil. Pore pressure was introduced into the sample from the bottom end by the injection pump, while the top end was linked to the reservoir pump. This setup created a drained boundary condition, as illustrated in Figure 6.1.

6.2.3. EXPERIMENTAL PROCEDURE

Before conducting the tests, the samples underwent complete saturation using a vacuum system located outside the loading system. Following this, saw-cut samples were meticulously positioned within the instrumented Hoek cell, and after applying 0.5 MPa of confining pressure, they were integrated into the loading system. Once the cell was

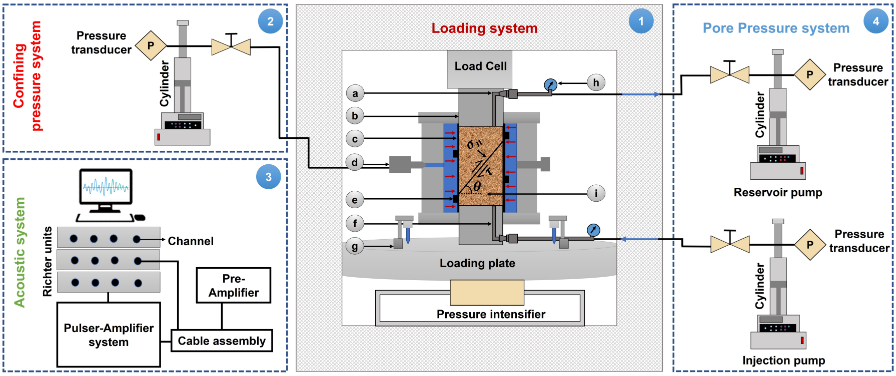

Figure 6.1: Schematic of the experimental setup including different units: 1) Loading system ((a) outlet fluid line, (b) loading piston, (c) silicon jacket, (d) confining oil inlet, (e) acoustic emission sensor, (f) inlet fluid line, (g) Linear Variable Differential Transformer (LVDT) for measuring axial deformation, (h) pressure sensor, (i) saw-cut sandstone), 2) Confining pressure system, 3) Acoustic system, and 4) Pore pressure system).

integrated into the loading system, an initial 5 MPa of isostatic pressure ($\sigma_1 = \sigma_3$) was applied. Subsequently, the injection lines were flushed to eliminate air from the system. With this primary preparation completed, the main phases of the experiments proceeded as follows (see Figure 6.2):

Phase 1: The axial stress and confining pressure increased hydrostatically until the desired confining pressure of 21 MPa was achieved.

Phase 2: The pore pressure was built up until it reached 3 MPa in pressure gradient control mode (fluid was injected from the bottom of the sample at a rate of 0.5 MPa/min) as the background pore pressure. A waiting period of 15 minutes (sufficient time for equilibrium based on pore pressure diagram) followed, allowing the system to equilibrium before the next phase commenced.

Phase 3: While maintaining constant pore pressure and confining pressure, the axial stress increased by continuously advancing the axial piston at a rate of 0.0005 mm/s. This process aimed to reach the shear strength through displacement-driven fault reactivation. After the fault was reactivated, the axial piston was halted, and due to system relaxation, the shear stress dropped to 96% of the shear strength, resulting in a near-critically stressed condition for the fault (L. Wang et al., n.d.; Ye & Ghassemi, 2020).

Phase 4: Following a 10-minute relaxation period, the injection process began, involving an increase in pore pressure to induce fault reactivation. Different injection patterns and rates were applied until reaching the target pressure. This phase allowed for the investigation of fault behavior under varying injection conditions.

During phase 4, three different injection schemes were used to investigate the effect of injection patterns on microseismicity and slip behavior, as shown in Figure 6.2. The first pattern, Monotonic Injection (MI), involved gradually increasing the pore pressure from the background pore pressure of 3 MPa at a constant rate until reaching the target pore pressure of 19 MPa. In the second scheme, the Stepwise Injection (SI) pattern, the pore pressure was raised stepwise by 4 MPa at each step, starting from 3 MPa. There was a 5-minute waiting interval between each step, continuing this process until the target pressure was achieved. Lastly, the third scheme, the Cyclic Recursive Injection (CRI) pattern, entailed reducing the pore pressure to 3 MPa after each cycle and increasing it by 4 MPa per cycle until reaching the final target pore pressure of 19 MPa. The waiting time in between cycles was 2.5 min (sufficient time for stabilizing the shear stress and AE event cessation). (Figure 6.2). Notably, all injection patterns had the same pressurization rate of 2 MPa/min and reached the same final pore pressure target (19 MPa). Additionally, the MI pattern was subjected to three different injection rates (low, medium, and high rates, 0.2 MPa/min, 1 MPa/min, and 2 MPa/min, respectively) to explore the influence of injection rate on microseismicity and fault slip.

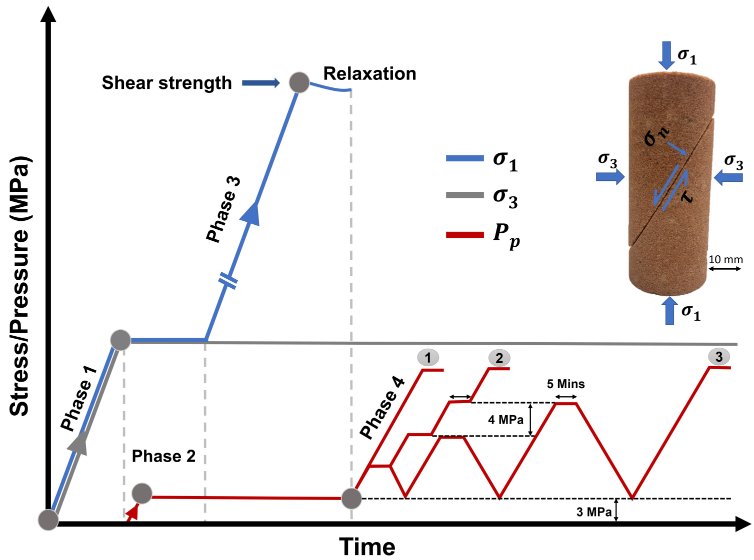

Figure 6.2: Schematic illustration of the experimental protocol and stress path: 1) Monotonic injection (MI) pattern, 2) Stepwise injection (SI) pattern, 3) Cyclic recursive injection (CRI) pattern.

6.2.4. DATA ANALYSIS

The shear displacement along the fault plane (s) was calculated by total axial shortening (L_{ax}), which is calculated by excluding the contributions resulting from the elastic deformation of the test system and rock matrix (L. Wang et al., n.d.). Thus, shear slip along the fault plane (s) can be expressed as,

$$s = \frac{L_{ax}}{\cos(30°)} = \frac{(L_{lvdt} - \frac{F}{K_s} - \frac{F}{K_{rock}})}{\cos(30°)}, \tag{6.2}$$

where L_{lvdt} represents the axial displacement measured by the LVDTs, and F denotes the axial force applied during the experiment. The vertical stiffness of the test loading system (K_s) is 340 kN/mm, and the vertical stiffness of the sandstone matrix (K_{rock}) is 70 kN/mm. The estimation of K_s involved conducting a uniaxial compression test within the elastic regime on a cylindrical aluminum dummy sample with a known elastic modulus.

The slip rate or slip velocity (S_v) of the fracture is defined as the first derivative of shear displacement (s) with respect to time (t), expressed as:

$$S_v = \frac{ds}{dt}, \tag{6.3}$$

To determine the effective normal stress and shear stress, we employ the following equations and estimate the friction along the fault plane as the ratio between shear stress (τ) and effective normal stress ($\sigma'_n - P_f$).

$$\sigma'_n = \frac{(\sigma_1 + \sigma_3 - 2P_f)}{2} - \frac{(\sigma_1 - \sigma_3)}{2}\cos(2\theta), \tag{6.4}$$

$$\tau = \frac{(\sigma_1 - \sigma_3)}{2}\sin(2\theta), \tag{6.5}$$

$$\mu = \frac{\tau}{(\sigma'_n - P_f)}, \tag{6.6}$$

where σ_1 and σ_3 represent the axial and confining pressure, respectively, and θ denotes the angle between the axial stress and the fault plane. Using the shear displacement (s), the τ and σ'_n values are adjusted for a changing effective contact area of the fault plane due to fault slip (Tembe et al., 2010). Based on axial shortening, it is possible to determine the evolution of contact area as follows:

$$\frac{A}{A_0} = \frac{(\Theta - \sin\Theta)}{\pi} \tag{6.7}$$

$$\Theta = \pi - 2\sin^{-1}\left(\frac{L_{\mathrm{ax}}}{2r}\tan\theta\right) \tag{6.8}$$

Where A and A_0 represent the corrected and original cross-sectional areas of the sample ($A_0 = \pi r^2$), respectively, L_{ax} denotes the axial displacement, and r is the radius of the cylindrical rock sample. The true shear and normal stress components are derived by dividing the uncorrected τ and σ_n by the ratio A/A_0. The effective normal stress is then determined by subtracting the pore pressure P_p from the corrected normal stress, under the assumption that the Biot coefficient is equal to 1.

To investigate microseismicity evolution, different acoustic emission (AE) parameters such as AE energy (seismic radiated energy), number of events, and b-value (magnitude-frequency distribution) were quantified. The energy of acoustic emission (AE) is directly proportional to the area beneath its waveform, in which electrical signals are assumed to have energy proportional to the square of their voltage (equation 6.8) (Grosse & Ohtsu, 2008; Khazaei et al., 2015; Naderloo et al., 2019).

$$E_i = \frac{1}{R}\int_{t_0}^{t_1} V_i^2(t)\,dt, \tag{6.9}$$

where V_i represents the voltage of each trace point that surpasses the threshold amplitude, t_0 and t_1 denote the start and end times of the transient voltage record, respectively, while R signifies the input impedance of the AE system, equal to 50Ω.

The Gutenberg-Richter relationship describes the statistical relationship between the occurrence frequency of earthquakes and their magnitudes, often used in seismic hazard assessment. This concept can be expressed or measured in terms of a magnitude-frequency relationship (Gutenberg & Richter, 1944; Lombardi, 2003).

$$\log_{10} N = a - bM_l, \tag{6.10}$$

where N is the number of events with a magnitude larger than or equal to M_l, and a and b are empirical constants. The b value represents the inverse of the slope in the logarithmic frequency-magnitude graph. A higher b value indicates a higher proportion of small events than larger ones, a favourable characteristic for mitigating seismic activity (Lei et al., 2018).

6.3. RESULTS

6.3.1. EFFECT OF INJECTION RATE

Figures 6.3a, 6.3b, and 6.3c illustrate the results of three different injection rates (high, medium, and low), showcasing the temporal variations in shear stress, slip velocity, and cumulative microseismic (MS) events following the injection or pore pressure increase. Upon reaching the shear strength and allowing for a 10-minute relaxation period just before the injection commenced, the shear stress consistently stabilized at approximately 22.5 ± 0.5 MPa for all experiments. The shear stress decreases as the slip rate increases and fault reactivation begins, as indicated by the brown zone (stage II) in Figures 6.3d, 6.3e, and 6.3f. Pore pressure values for reactivation are very similar for all injection rates (4.8 MPa, 4.5 MPa, and 4.1 MPa for high, medium, and low injection rates). This suggests that the initiation of fault reactivation is mostly governed by the magnitude of pore fluid rather than the pressurization rate. Thus, employing a rate ten times lower induces fault reactivation at a 0.7 MPa lower pressure, i.e., more than a 10% difference in absolute pore pressure value. Additionally, microseismic events are observed to commence when fault reactivation starts.

In the high injection rate scenario, fault reactivation initiates when slip increases (depicted by the brown zone in Figure 6.3d, stage II). As injection progresses, velocity rapidly increases, culminating in a peak, and drops quickly, resembling a slow slip event (depicted by the grey zone in Figure 6.3d, stage III). Aseismic (creep) slip velocity for natural faults is generally less than 0.001 mm/s, and slow slip events have peak slip rates of less than 1 mm/s (Bürgmann, 2018; Leeman et al., 2016)). The peak slip velocity is 0.0012 mm/s, thus can be considered as a slow slip. After a slow slip event, slip velocity maintains a consistent level and increases slightly by the end of the injection operation (stage IV). Similar behavior is observed for the microseismic behavior in which event generation starts with the initiation of fault reactivation (Figure 6.3d brown shaded zone, stage II). There is a rapid surge in the number of MS events (stage III), followed by a continuous generation of microseismicity proportional to the injection rate as pore pressure

6

increases (see Figures 6.3a and 6.3d). On the other hand, the medium and low injection rates exhibit a distinct pattern, with no sharp increase in microseismic activity (see Figure 6.3b, 6.3c, 6.3e, and 6.3f), and the MS events increase slowly and gradually relative to their respective injection rates. Also, in the low-rate injection scenario, there is no slow slip (velocity acceleration and drop) during fault reactivation; instead, the slip velocity gradually increases from stage II to stage IV and the top part of the sample slides (creeps) over the bottom part with a constant velocity as an injection or pore pressure buildup progresses. This observation shows that the likelihood of slip nucleation and a drastic increase in the number of events at the onset of fault reactivation is minimized by reducing the injection rate. In other words, the high injection rate is characterized by higher maximum slip and continuous slip velocity compared to the medium and low injection rates.

Frictional evolution for all the injection rates is shown in Figure 6.4. As the injection initiates and pore pressure builds up, the friction coefficient increases linearly for all injection rates (Figures 6.4a, 6.4b, and 6.4c, stage I). In the case of a high injection rate, following the linear increase of the friction coefficient to a static friction coefficient (Figures 6.4a, 6.4d, stage II), it subsequently drops, coinciding with the maximum slip velocity and the occurrence of a slow slip event (stage III). After the friction drop, it gradually recovers and increases with the further increase in pore pressure, indicating frictional strengthening (stage IV). There is no drop in friction for the cases of medium and low injection rates (Figures 6.4b, 6.4c, 6.4e, and 6.4f). After slip velocities reach their constant rates (Figures 6.4b, 6.4c, 6.4e, and 6.4f), a nearly linear frictional strengthening is observed with a further increase in pore pressure, similar to the high injection rate case after the friction drop (slow slip). At the end of the injection operations (i.e. after building up 19 MPa pore pressure in the system), the total shear stress drop and total shear slip are 17.5 ± 0.3 MPa and 0.32 ± 0.005 mm, respectively, very similar for all three injection rates (Figures 6.3 and 6.4). The initial fault displacement due to displacement-driven fault reactivation was set to zero up to the start of the injection for easy comparison.

While the total shear displacement and total shear stress drop remain consistent across various injection rates, and all cases experience stable sliding and frictional strengthening, the seismicity pattern and slip velocity differ. Figure 6.5 directly compares the number of events (Figure 6.5a), total radiated AE energy (Figure 6.5b), maximum slip velocity (Figure 6.5c), and b-value (Figure 6.5d) across tests with different injection rates. There is a clear difference between the high injection rate experiments and the low or medium injection rate experiments. With a high injection rate the radiated total AE energy, maximum slip velocity, and the total number of events, all exhibit higher values than in the other experiments. Moreover, the b-value is slightly elevated in the medium and low-rate injection cases (Figure 6.5d). Together this suggests the high injection rate leads to more pronounced seismic activity and slip motion.

6.3.2. Effect of Injection Pattern

Figure 6.6 depicts the evolution of shear stress, slip velocity, and microseismic (MS) events while building up pore pressure through stepwise and cyclic recursive patterns (Figure 6.6). The data can be divided into 5 stages. The SI and CRI patterns share stages

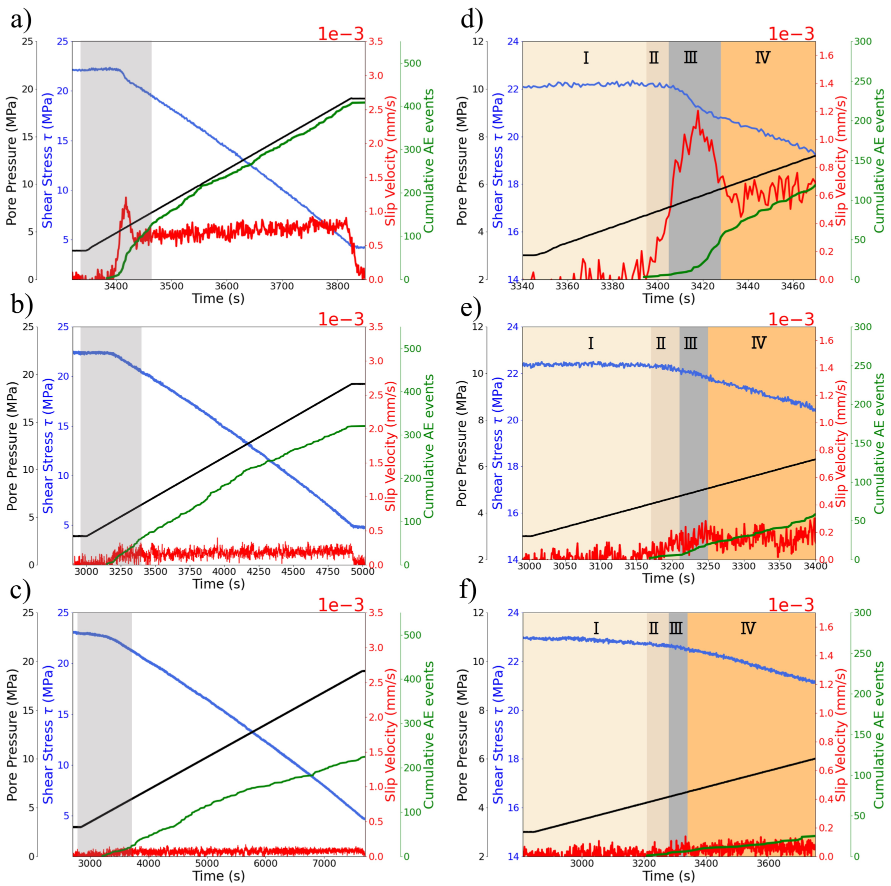

Figure 6.3: Temporal evolution of shear stress, microseismicity, and slip velocity with increasing pore pressure (injection) in tests with different injection rates, (a) high rate, (b) medium rate, and (c) low rate. Figures 6.3d, 6.3e, and 6.3f show a zoomed-in view of the shaded area in Figures 6.3a, 6.3b, and 6.3c, respectively. The stages I-IV represent the onset of an increase in pore pressure, the initiation of fault reactivation accompanied by an increase in slip velocity, the subsequent increase of slip velocity reaching a peak and then declining (slow slip), and continuous sliding, respectively.

I-IV with the MI pattern, including stage I (silent zone based on MS activity and without fault movement), stage II (start of MS activity and reactivation), stage III (the further acceleration of slip velocity reaching a peak and then declining (slow slip)), and stage IV (continuous sliding), (Figure 6.6). However, there is another stage when injection stops or reduces between cycles in which MS activity remains absent, and slip velocity approaches near-zero values (stage V). To focus first on stage V of the SI pattern, once the pore pressure reached 7 MPa during the first step, the injection pump was halted and pressure maintained at a constant level for 5 minutes (see Figures 6.6a and 6.6c). Throughout this waiting period, the shear stress experienced a gradual decline and stabilized, accompanied by the absence of microseismic activity (stage V in Figure 6.6). Ad-

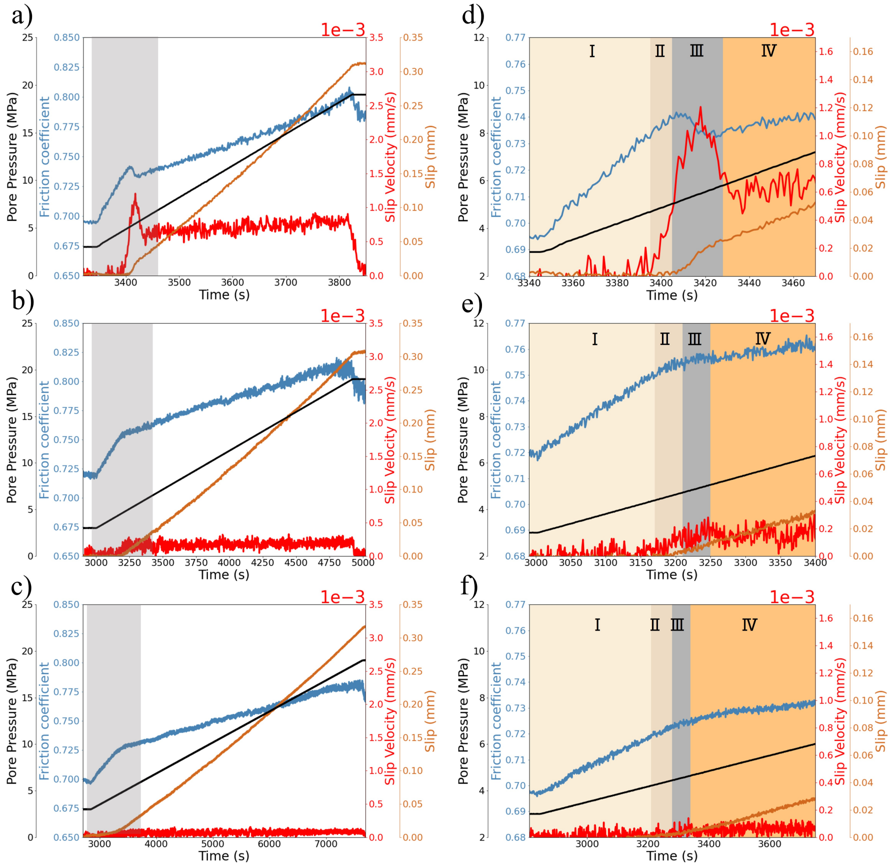

Figure 6.4: Evolution of friction coefficient, shear slip, and slip velocity with building pore pressure (injection) in tests with different injection rate, a) high rate, b) medium rate, and c) low rate. Figures 4d, e, and f show the zoomed view of shaded area in Figure 4a, b, and c, respectively.

ditionally, the slip velocity diminished nearly to zero. Comparing that to phase V of the CRI pattern, following the first cycle, a waiting period of 2.5 minutes followed, sufficient for the relaxation of shear stress and MS activity cessation (Figures 6.6b and 6.6d, stage V). After waiting time, the pore pressure was reduced (depleted) to 3 MPa, serving as a reference or background pore pressure. For both SI (waiting time only) and CRI (waiting time plus time spent for pressure depletion), injection recommences to elevate the pore pressure within the system further to reach the next target (11 MPa). The MS activity shows that the fault reactivates when pore pressure is 8.5 MPa during the second cycle/step, and reactivation stages are similar to the prior step/cycle (see the colors for stages of reactivation in Figures 6.6c and 6.6d). Although the reactivation stages are the same for the SI and CRI patterns, increasing the total number of injection cycles (CRI) or steps (SI) shows a noticeable rise in peak slip velocity (Figure 6.6). However, the increase in maximum slip velocity per step for the SI pattern is less significant than the change in

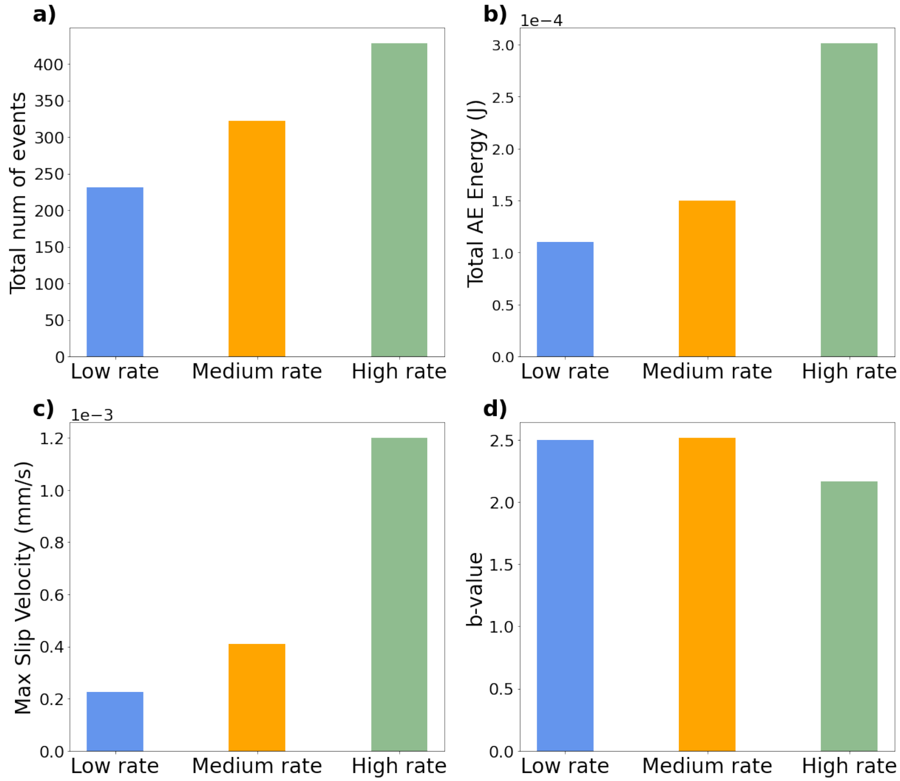

Figure 6.5: Comparison of different seismicity parameters obtained from experiment with different injection rate: a) total number of MS events, b) total radiated AE energy, c) maximum slip velocity, and d) estimated b-value.

maximum slip velocity per cycle in the CRI pattern.

Figure 6.7 further investigates the evolution and correlation of friction coefficient and AE amplitudes with pore pressure changes. Throughout the course of the experiment, there is a semi-continuous frictional strengthening trend in the friction coefficient (Figure 6.7). In stages I and II, with increasing pore pressure in each cycle/step, a slight and almost immediate increase is observed for the friction coefficient of 0.045. During each cycle/step the friction coefficient follows a linear progression. In stage III, once reactivation starts, the friction coefficient drops, concurrent with a sharp increase in slip velocity. In stage IV, friction recovers and starts to increase again as the pore pressure further increases until injection stops for that cycle or step. Each step or cycle comes with a cluster of microseismic (MS) events during injection (depicted in Figure 6.7), and the amplitude of the events increases during each successive step/cycle.

Figures 6.8 and 6.6 show how the injection pattern influences the evolution of shear and effective normal stress. There is a clear difference between the CRI and SI patterns. In the case of the CRI pattern, the effective normal stress increases and decreases as a di-

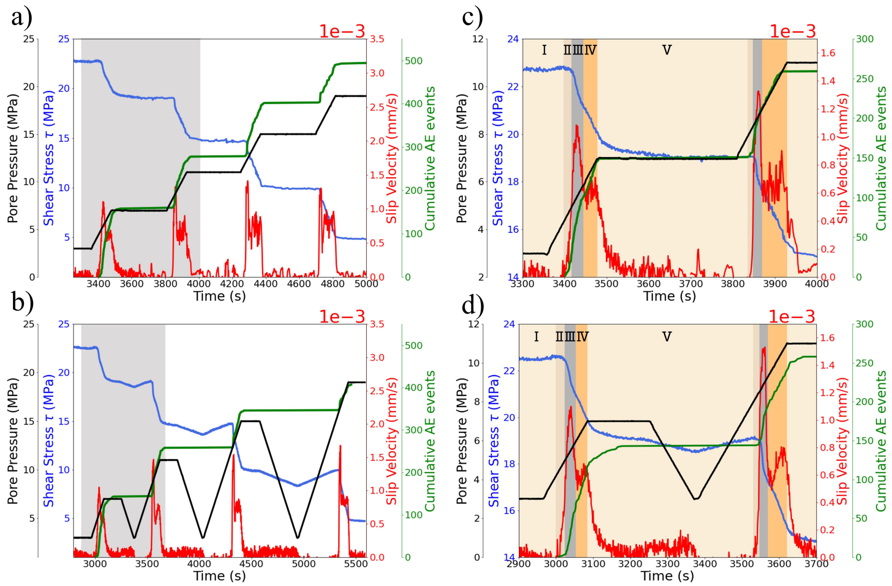

Figure 6.6: Evolution of fault reactivation by SI and CRI patterns. (a) Stepwise injection (SI) pattern. (b) Cyclic recursive injection (CRI) pattern. (c) and (d) show a zoomed-in view of the shaded area in Figures 6a and b, which includes the first and second step/cycle of injection for SI and CRI patterns, respectively. The stages I-V represent the onset of the increase in pore pressure (silent area), the initiation of fault reactivation accompanied by an increase in slip velocity, the subsequent further increase of slip velocity reaching a peak and then declining (slow slip), and continuous sliding, and decline in slip velocity following by the cessation of fault slip, respectively.

rect function of pore pressure (increase and decrease), whereas for the SI pattern, the effective normal stress drops in a stepwise manner. The evolution of shear stress and effective normal stress is accompanied by differences in slip behavior and MS activity. While monotonic injection triggers a single instance of a slow slip event (slow stick-slip), the SI and CRI patterns elicit episodic occurrences of slow events, one for each cycle or step (compare Figure 6.3a to Figures 6.8a, and 6.8b).

Similar to experiments conducted at various injection rates, total shear displacement and shear stress drop remain equal across tests with different injection patterns (Figures 6.9c and 6.9f). Additionally, there is no significant discrepancy in the total number of generated events (Figure 6.9a). However, it is noteworthy that the maximum peak slip velocity and the total radiated AE energy resulting from the CRI pattern surpass those of the MI and SI patterns. This observation indicates that the larger events generated during the CRI pattern may be attributed to the higher slip velocity resulting from abrupt shear stress drops. Furthermore, the same interpretation can be drawn from b-value estimation, which reveals that using the CRI pattern decreases the b-value by 15% compared to the MI pattern (Figure 6.9d). This implies a relatively more significant occurrence of larger seismic events than small ones when employing the CRI pattern. Consequently, it suggests that the CRI pattern leads to more prominent seismic activity and

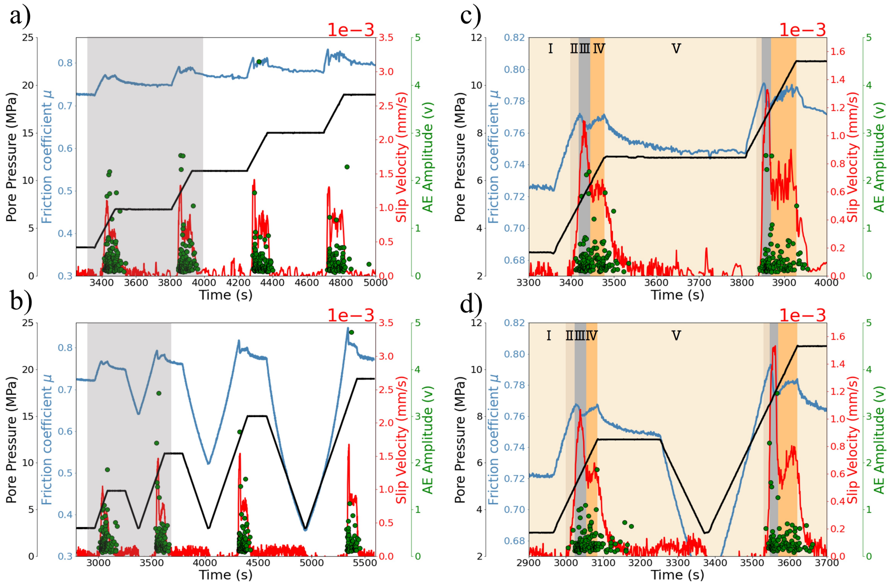

Figure 6.7: Friction coefficient evolution with clustering of the MS events per cycle/step. (a) Stepwise injection (SI) pattern. (b) Cyclic recursive injection (CRI) pattern. (c) and (d) show a zoomed view of the shaded area in Figures 7a and b, which includes the first and second step/cycle of injection for the SI and CRI patterns, respectively.

slip motion in comparison to the SI and MI patterns.

6.4. DISCUSSION

Over the past few years, there has been a growing interest in fine-tuning injection operations for a range of applications, including geothermal projects, hydraulic fracturing, and temporal energy storage endeavors (Patel et al., 2017; Zang et al., 2013). This increased attention is driven by the desire to minimize induced seismicity and implement effective seismic risk management. Our results showed different behaviour in seismicity and fault slip corresponding to different injection rates and patterns, which may provide more information to adjust injection operations and traffic light systems for subsurface-related projects.

6.4.1. DESTABILIZING EFFECT OF HIGH INJECTION RATES IN FAULTED PERMEABLE ROCKS

Studies into the effects of fluid pressure change on fault reactivation in impermeable rocks demonstrate that localized fluid overpressures (where the pressure locally exceeds what is anticipated based on a uniform Coulomb criterion) can instigate periods of quasi-static or partial fault slip (Huang et al., 2021; Labuz & Zang, 2012; Passelègue et al., 2018; Viesca & Rice, 2012). Subsequently, this may be followed by earthquake nucleation and propagation, extending well beyond the initially pressurized region (Rutter & Hackston,

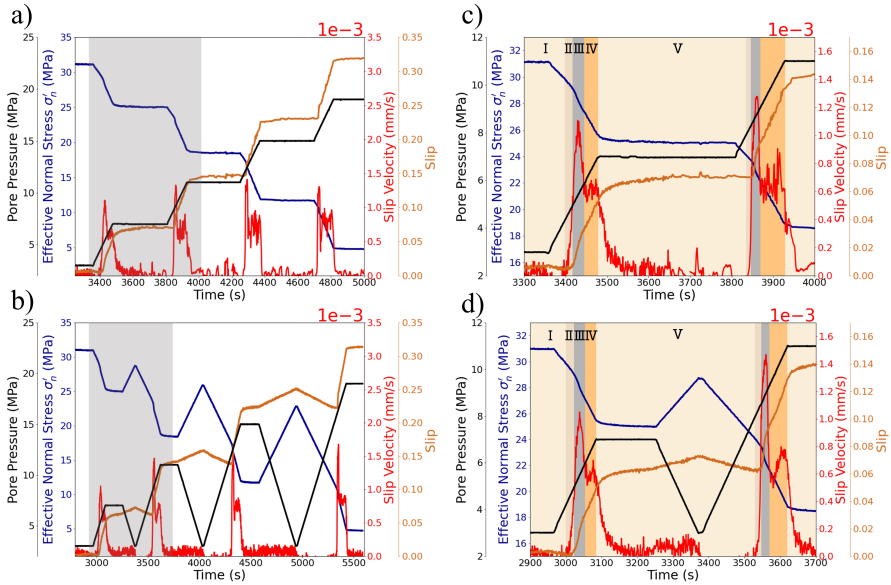

Figure 6.8: Evolution of effective normal stress and shear slip by SI and CRI patterns. (a) Stepwise injection (SI) pattern. (b) Cyclic recursive injection (CRI) pattern. (c) and (d) show a zoomed-in view of the shaded areas in Figures 8a and b, which includes the first and second step/cycle of injection for SI and CRI patterns, respectively.

2017). High injection rates can increase the chance of localized fluid overpressures and slip nucleation (Passelègue et al., 2018). However, in a highly permeable medium, the chance of localization of pore pressure is low due to the drainage conditions along the fault. L. Wang et al. (n.d.) showed that in the context of permeable fault structures, the mode of fault slip is predominantly influenced by the rate of fluid pressurization rather than the magnitude of pore pressure. We observed a similar result: a high injection rate induced a slow slip event at the beginning of fault reactivation. In contrast, with medium and low injection rates, fault reactivation started without the nucleation of slow slip events, and exhibited a gradual increase in slip velocity, despite the same level of pore pressure. (Figure 6.3). Our results also show that injection rate influences the seismicity response, specifically maximum slip velocity, radiated AE energy, and the total number of events and b-value (Figure 6.5).

To explain how and why the pressurization rate can influence the fault slip behaviour and subsequently, seismicity response we will discuss our results within the context of frictional models. The process of frictional evolution is described through the utilization of rate-and-state constitutive laws, enabling the accurate replication of a diverse array of observed seismic and aseismic fault phenomena (Dieterich, 1979; Hunfeld et al., 2020; Marone, 1998; Ruina, 1983). Combining the rate-and-state friction approach with a one-dimensional spring-slider model, the critical stiffness marks the point of transition from stable to unstable slip (Dieterich, 1979; Noël et al., 2019; Rice, 1993; Ruina, 1983). As a

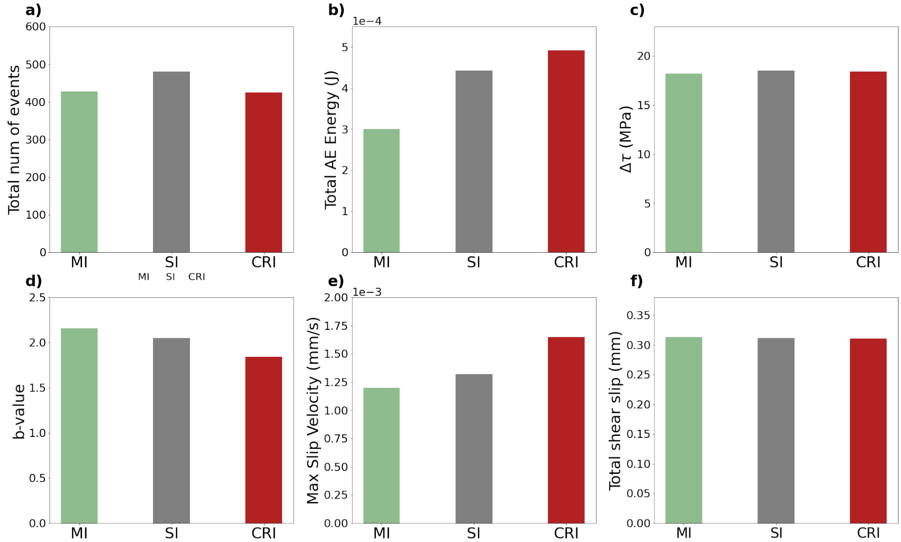

Figure 6.9: Comparison of different parameters obtained from the experiment with different injection patterns (MI (monotonic injection), SI (stepwise injection), and CRI (cyclic recursive injection): a) total number of MS events, b) total radiated AE energy, c) Total shear stress drop, d) b-value estimation e) maximum slip velocity, and d) total shear slip at the end of the injection operation.

consequence of fluid injection, there is a change in the effective normal stress. Alghannam and Juanes (2020) adopted a one-dimensional spring-slider model as outlined by Linker and Dieterich (1992) to the poroelastic spring–slider system with an evolving pore pressure in which the critical stiffness (K_{crit}) is given by:

$$K_{\text{crit}} = (b-a)(\sigma_n - p) + \frac{\alpha}{v_0}\dot{p} \tag{6.11}$$

where a and b are experimentally derived parameters and α is the scaling factor, all of which are normalized by frictional parameters. Dimensionless parameters p and $\dot{p}$ represent the pore pressure and pressurization rate, respectively and v_0 is the loading velocity. Slip occurs through stick-slip behavior (unstable) when the dimensionless stiffness of the loading system (k) falls below a critical threshold ($k < K_{\text{crit}}$), while it transitions to stable sliding when the stiffness surpasses this critical value ($k > K_{\text{crit}}$). For the poroelastic spring–slider system, frictional instability hinges on both pore pressure magnitude and its rate of change. The influence of $\dot{p}$ prevails during the rapid early growth of pore pressure, elevating the critical stiffness. However, as pore pressure diffuses and stabilizes, p takes over, causing a decline in critical stiffness (Alghannam & Juanes, 2020; Heimisson et al., 2019).

The initial destabilizing impact of the pressurization rate ($\dot{p}$) is likely linked to a transient influence on contact interlocking (Alghannam & Juanes, 2020). Figure 6.10 depicts changes in normal effective and shear stress due to the pore pressure increase for different injection rates. Notably, the high-rate injection scenario exhibits approximately a sudden 1.5 MPa drop in effective normal stress (red arrow), distinct from the behavior corresponding to the medium and low-rate injection at the start of fault reactivation. This abrupt drop likely results in fault opening and the disruption of asperity contacts (W. Wang & Scholz, 1994), leading to a phase of slow slip (Figure 6.3d, stages II and III). Additionally, Figure 6.11 presents the calculated total hydraulic energy and evolution of hydraulic power across all injection rates. The input power of the system, known as hydraulic power, is calculated by multiplying the injection fluid pressure (p) by the flow rate (q). By integrating hydraulic power over the injection interval, we were able to determine the hydraulic energy involved (Goodfellow et al., 2015). Although there is no substantial difference in the total hydraulic energy input into the system (With the same volume of injected water), a significant contrast exists in the magnitude of hydraulic power. Specifically, there is a noticeable surge in hydraulic power in the case of high injection rates (Figure 6.11). This rapid increase in hydraulic power may plausibly explain the sudden decrease in effective normal stress. Consequently, higher injection rates enhance the likelihood of a sudden reduction in effective normal stress, leading to fault opening and the disruption of asperity contacts. This sequence of events can ultimately trigger slow slip and contribute to the occurrence of high-energy microseismic events.

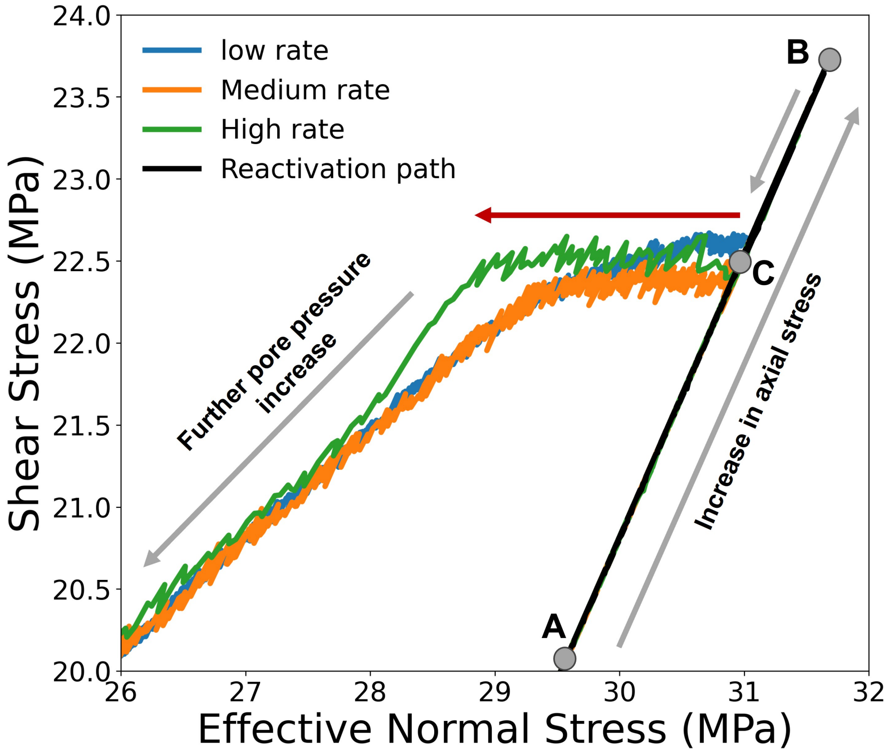

Figure 6.10: Stress path for different injection rates. The black line shows displacement-driven fault reactivation (from point A to B, axial stress increase) and following relaxation before injection starts (from point B to C). Pore pressure build-up starts from point C and changes the stress path by changing shear and effective normal stress.

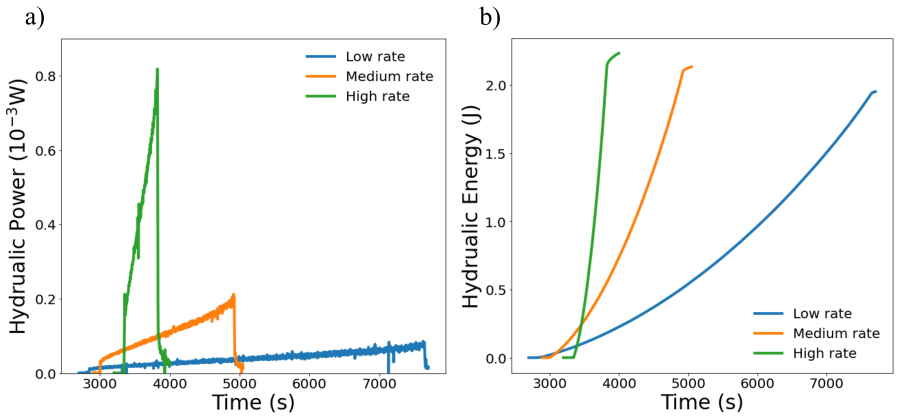

Figure 6.11: (a) Evolution of hydraulic power and (b) imposed total hydraulic energy into the system for the tests with different injection rates.

6.4.2. STABILIZING EFFECT OF PORE PRESSURE IN PERMEABLE FAULTED ROCKS

As mentioned in the previous section (Equation 6.11), after pore pressure diffuses and reaches a steady state, the stabilizing influence of pore pressure (p) starts by reducing the critical stiffness (k_{crit}), which is likely due to its impact on interface locking. Elevated pore pressure reduces effective normal stress, which, in turn, diminishes the extent of interface locking. Consequently, such reductions play a role in constraining the potential magnitude of stress drops (Alghannam & Juanes, 2020; Moreno et al., 2010; Segall et al., 2010). This interpretation is consistent with our findings. As depicted in Figures 6.4a and 6.4d, the behavior is as follows: following the initial slow slip (stages II and III), a notable frictional strengthening is observed for the high injection rate scenario (stage IV). Also, for the low and medium injection rates, an increase in pore pressure leads to a subsequent rise in the friction coefficient or frictional strengthening (Figures 6.4b and 6.4c). This can also be observed in cumulative MS events and MS rates, which display no abrupt spikes. Furthermore, it is worth noting that the calculated fault stiffness remains constant at approximately $k_f \approx 58$ MPa/mm (slope of the shear stress versus shear slip plot) across all tests conducted, regardless of varying injection rates and patterns. The system's stiffness measures approximately 270 MPa/mm, well above the stiffness of the fault ($k > k_{\text{f}}$), and therefore the behavior of fault slip remains mechanically stable throughout all tests conducted with different injection rates. Hence, the combined effects of pore pressure build-up and the high stiffness of the system serve to ensure stable sliding behavior across all test scenarios, even though slow stick-slip is observed in cases of high injection rates.

6.4.3. EFFECT OF INJECTION PATTERN ON FAULT REACTIVATION

Many investigations into seismicity in low permeable intact or faulted rock have suggested that the seismic reaction to cyclic fluid injection contrasts with that of monotonic injection, hinting at the possibility of cyclic injection resulting in diminished levels of induced seismic activity (Ji, Yoon, et al., 2021; Ji, Zhuang, et al., 2021; Naderloo et al., 2023;

Niemz et al., 2020; Zang et al., 2019; Zhuang et al., 2020). Our findings reveal distinct behaviors among different injection patterns on saw-cut permeable sandstone. When using the CRI pattern, we observe the occurrence of slow slips in each cycle, whereas, with the MI pattern, slow slip initiation only nucleates at the start of fault reactivation (Figures 6.3a, 6.6b). Additionally, slow slip events occur at each step of pore pressure increase in the SI pattern (Figure 6.6a). Notably, the CRI pattern induces a higher maximum slip velocity than MI and SI patterns (Figure 6.9e). Furthermore, our microseismic analysis underscores that while there is no significant difference in the total number of events generated across all three injection patterns, employing the CRI pattern generates larger magnitude events in contrast to the MI and SI patterns. This discrepancy is attributed to the higher total radiated AE energy observed in the CRI pattern (Figure 6.9). Moreover, the b-value extracted from the CRI pattern is lower than that of the MI and SI patterns, indicating a prevalence of larger-magnitude events (as illustrated in Figure 6.9d). The four slow slips induced by the CRI pattern exhibit each a higher maximum velocity (Figure 6.6b) than the single slow slip of the MI pattern (Figure 6.3a), summarized in Figure 6.9. Having four slip events that each have a higher peak velocity compared to just one event with a lower velocity, should intuitively lead to larger events. In other words, more frequent and higher peak velocities can be the explanation for the higher MS activity associated with the CRI pattern. Next, we will discuss the differences in slip behaviour and seismicity resulting from the different injection patterns in terms of (1) the effect of pressure rate front (rate ($\dot{p}$)), (2) the hydraulic energy budget, and (3) fault compaction and dilation.

6

1- Figure 6.12 illustrates the stress path for all patterns. Specifically, at the start of each cycle or step in the CRI and SI patterns, we observe a notable and sudden drop in effective normal stress (orange arrows). Since both patterns were conducted with a high injection rate (2 MPa/min), the initial destabilizing influence of the pressure front ($\dot{p}$) will result in a sudden drop in effective normal stress (i.e. Figure 6.12). This pressure front leads to fault opening and the disruption of asperity contacts and subsequently initiates a phase of slow slip (Alghannam & Juanes, 2020; W. Wang & Scholz, 1994). During both the SI and CRI patterns, when pore pressure stops increasing between each cycle/step, we allow the system to stabilize and reach equilibrium. Each time when pore pressure rises the perturbing and destabilizing impact of the pressure rate ($\dot{p}$) comes into play.

2- Figures 6.13a and 6.13b show the evolution in different parameters by increasing the number of cycles for the CRI pattern. The imposed or available hydraulic energy increases by increasing the number of cycles. However, in the case of the MI pattern, hydraulic energy was imported gradually (Figure 6.11b). As depicted in Figure 6.13a, a greater hydraulic energy budget is available with each cycle, leading to an increase in shear slip, maximum slip velocity, and shear stress drop per cycle.

3- In the case of CRI, by reducing the pore pressure, the effective normal stress (σ'_n) exerted on the fault rises (as indicated by the red arrow in Figures 6.12c and 6.13b), resulting in fault compaction. The compaction is illustrated in Figure 6.13b, which increases sample axial shortening. The absence of any associated event or change in slip velocity during the reduction of the pore pressure suggests that shear slip is not occurring, and the observed behavior is solely attributable to fault compaction. The effective normal stress acting on the fault plane decreases again through elevating pore pressure (Figures 6.12c and 6.13b, black arrow). This reduction in effective normal stress leads to fault dilation. Fault dilation is evident in Figure 6.13b, where the re-injection results in a decrease in estimated axial shortening, indicating the occurrence of opening and dilation. Primarily, fault compaction can enhance the likelihood of healing even in the time scale of depressurization ramp (minutes) which increases the shear strength of the quartz-rich fault plane (see Figure S3) (Hunfeld et al., 2017; Seyler et al., 2023). In fact, frictional healing would promote the strengthening of the fault by effectively locking it during the compaction phase (as pore pressure decreases). Consequently, overcoming the high shear strength can trigger abrupt slips. Additionally, the interplay of fault dilation and compaction through fluctuations in effective normal stress can influence and oscillate the critical stiffness of the fault shown in Equation 6.11 (Noël et al., 2019).

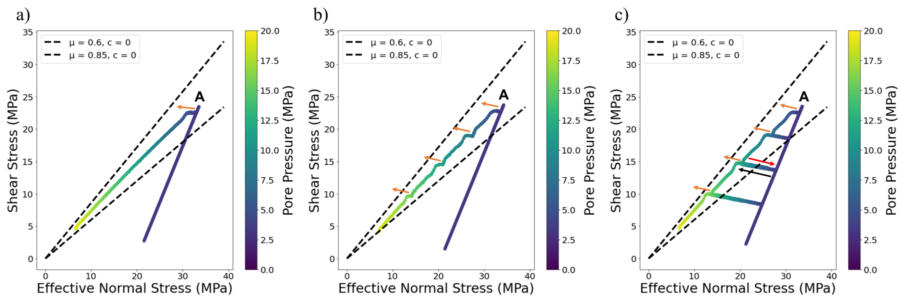

Figure 6.12: Illustrating the evolution of stress paths in the shear stress-effective normal stress space. Initially, up to point A, the stress path undergoes changes solely due to variations in axial stress (displacement-driven), while pore pressure and confining pressure remain constant. Following point A and the associated relaxation period, injection commences, with the color bar indicating the increasing pore pressure. The figure includes three scenarios: a) Monotonic injection (MI) pattern, b) Stepwise injection (SI) pattern, and c) Cyclic recursive injection (CRI) pattern. The orange arrows indicate the moments of reactivation and stress drop, while the red and black arrows mark the depletion of pore pressure and the re-injection process.

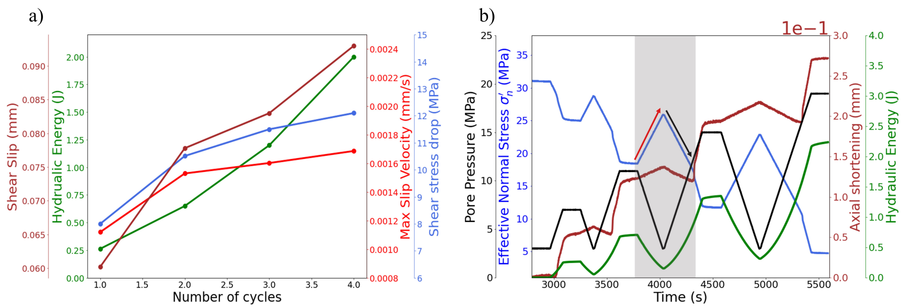

Figure 6.13: (a) Evolution of hydraulic energy budget, shear slip, maximum slip velocity, and shear stress drop per cycle during the CRI pattern. b) Change in effective normal stress and hydraulic energy budget per cycle till the end of the injection operation. shaded area in Figure 6.13b shows fault compaction (red arrow) and fault dilation (black arrow) by increase and decrease in effective normal stress.

6.5. CONCLUSION

We conducted triaxial fault reactivation experiments on saw-cut Red Felser sandstones under different injection rates and patterns to reveal the effect of pressurization rate and pattern on microseismicity pattern and fault slip. The results show that:

1. A high injection rate enhances the likelihood of a sudden reduction in effective normal stress, leading to fault opening and the disruption of asperity contacts, whereas, during a low injection rate, there is enough time for diffusion of pore fluid and a slow drop in effective normal stress.
2. A low injection rate is characterized by a lower maximum slip velocity, resulting in lower total radiated AE energy and a reduced total number of microseismic events. In contrast, it exhibits a higher b-value compared to a high injection rate.
3. A cyclic recursive pattern in highly porous and permeable sandstone resulted in more frequent and abrupt slow slow-slip events compared to a monotonic injection pattern.
4. Available hydraulic energy budget, shear slip, shear stress drop, and maximum slip velocity all increase from the first to the fourth cycle during the cyclic recursive injection pattern.
5. Comparing different injection patterns, the monotonic injection pattern shows a high potential for reducing seismicity in high permeable media compared to cyclic recursive injection and stepwise injection patterns.

Bibliography

Alghannam, M., & Juanes, R. (2020). Understanding rate effects in injection-induced earthquakes. *Nature communications*, *11*(1), 3053.

Bachmann, C. E., Wiemer, S., Goertz-Allmann, B. P., & Woessner, J. (2012). Influence of pore-pressure on the event-size distribution of induced earthquakes. *Geophysical Research Letters*, *39*(9).

Bommer, J. J., Crowley, H., & Pinho, R. (2015). A risk-mitigation approach to the management of induced seismicity. *Journal of Seismology*, *19*(2), 623–646.

Bürgmann, R. (2018). The geophysics, geology and mechanics of slow fault slip. *Earth and Planetary Science Letters*, *495*, 112–134.

Ciardo, F., & Rinaldi, A. P. (2022). Impact of injection rate ramp-up on nucleation and arrest of dynamic fault slip. *Geomechanics and Geophysics for Geo-Energy and Geo-Resources*, *8*(1), 28.

Deichmann, N., & Giardini, D. (2009). Earthquakes induced by the stimulation of an enhanced geothermal system below basel (switzerland). *Seismological Research Letters*, *80*(5), 784–798.

Dieterich, J. H. (1979). Modeling of rock friction: 1. Experimental results and constitutive equations. *Journal of Geophysical Research: Solid Earth*, *84*(B5), 2161–2168.

Ellsworth, W. L. (2013a). Injection-Induced Earthquakes. *341*(July), 1–8.

Ellsworth, W. L. (2013b). Injection-induced earthquakes. *science*, *341*(6142), 1225942.

French, M. E., Zhu, W., & Banker, J. (2016). Fault slip controlled by stress path and fluid pressurization rate. *Geophysical Research Letters*, *43*(9), 4330–4339. https://doi.org/10.1002/2016GL068893

Goodfellow, S. D., Nasseri, M. H. B., Maxwell, S. C., & Young, R. P. (2015). Hydraulic fracture energy budget: Insights from the laboratory. *Geophysical Research Letters*, *42*(9), 3179–3187.

Grigoli, F., Cesca, S., Rinaldi, A. P., Manconi, A., Lopez-Comino, J. A., Clinton, J. F., Westaway, R., Cauzzi, C., Dahm, T., & Wiemer, S. (2018). The November 2017 Mw 5.5 Pohang earthquake: A possible case of induced seismicity in South Korea. *Science*, *360*(6392), 1003–1006.

Grosse, C. U., & Ohtsu, M. (2008). *Acoustic emission testing*. Springer Science Business Media.

Gutenberg, B., & Richter, C. F. (1944). Frequency of earthquakes in California. *Bulletin of the Seismological society of America*, *34*(4), 185–188.

Heimisson, E. R., Dunham, E. M., & Almquist, M. (2019). Poroelastic effects destabilize mildly rate-strengthening friction to generate stable slow slip pulses. *Journal of the Mechanics and Physics of Solids*, *130*, 262–279.

Heimisson, E. R., Liu, S., Lapusta, N., & Rudnicki, J. (2022). A spectral boundary-integral method for faults and fractures in a poroelastic solid: Simulations of a rate-and-state fault with dilatancy, compaction, and fluid injection. *Journal of Geophysical Research: Solid Earth*, *127*(9), e2022JB024185.

Hofmann, H., Zimmermann, G., Zang, A., & Min, K. B. (2018). Cyclic soft stimulation (CSS): a new fluid injection protocol and traffic light system to mitigate seismic risks of hydraulic stimulation treatments. *Geothermal Energy*. https://doi.org/10.1186/s40517-018-0114-3

Huang, Y., Lei, X., & Ma, S. (2021). Numerical study of the role of localized stress perturbations on fault slip: Insights for injection-induced fault reactivation. *Tectonophysics*, *819*, 229105.

Hunfeld, L. B., Niemeijer, A. R., & Spiers, C. J. (2017). Frictional properties of simulated fault gouges from the seismogenic Groningen Gas Field under in situ P–T-chemical conditions. *Journal of Geophysical Research: Solid Earth*, *122*(11), 8969–8989.

Hunfeld, L. B., Chen, J., Hol, S., Niemeijer, A. R., & Spiers, C. J. (2020). Healing behavior of simulated fault gouges from the Groningen gas field and implications for induced fault reactivation. *Journal of Geophysical Research: Solid Earth*, *125*(7), e2019JB018790.

Ji, Y., Wang, L., Hofmann, H., Kwiatek, G., & Dresen, G. (2022). High-Rate Fluid Injection Reduces the Nucleation Length of Laboratory Earthquakes on Critically Stressed Faults in Granite. *Geophysical Research Letters*, *49*(23), e2022GL100418.

Ji, Y., Yoon, J. S., Zang, A., & Wu, W. (2021). Mitigation of injection-induced seismicity on undrained faults in granite using cyclic fluid injection: A laboratory study. *International Journal of Rock Mechanics and Mining Sciences*, *146*, 104881.

Ji, Y., Zhuang, L., Wu, W., Hofmann, H., Zang, A., & Zimmermann, G. (2021). Cyclic Water Injection Potentially Mitigates Seismic Risks by Promoting Slow and Stable Slip of a Natural Fracture in Granite. *Rock Mechanics and Rock Engineering*, 1–17.

Keranen, K. M., & Weingarten, M. (2018). Induced seismicity. *Annual Review of Earth and Planetary Sciences*.

Khazaei, C., Hazzard, J., & Chalaturnyk, R. (2015). Damage quantification of intact rocks using acoustic emission energies recorded during uniaxial compression test and discrete element modeling. *Computers and Geotechnics*, *67*, 94–102.

Kim, K.-H., Ree, J.-H., Kim, Y., Kim, S., Kang, S. Y., & Seo, W. (2018). Assessing whether the 2017 Mw 5.4 Pohang earthquake in South Korea was an induced event. *Science*, *360*(6392), 1007–1009.

Labuz, J. F., & Zang, A. (2012). Mohr–Coulomb failure criterion. *Rock mechanics and rock engineering*, *45*, 975–979.

Leeman, J. R., Saffer, D. M., Scuderi, M. M., & Marone, C. (2016). Laboratory observations of slow earthquakes and the spectrum of tectonic fault slip modes. *Nature communications*, *7*(1), 1–6.

Lei, X., Li, S., & Liu, L. (2018). Seismic b-value for foreshock AE events preceding repeated stick-slips of pre-cut faults in granite. *Applied Sciences*, *8*(12), 2361.

Linker, M. F., & Dieterich, J. H. (1992). Effects of variable normal stress on rock friction: Observations and constitutive equations. *Journal of Geophysical Research: Solid Earth*, *97*(B4), 4923–4940.

Lombardi, A. M. (2003). The maximum likelihood estimator of b-value for mainshocks. *Bulletin of the Seismological Society of America*, *93*(5), 2082–2088.

Marone, C. (1998). Laboratory-derived friction laws and their application to seismic faulting. *Annual Review of Earth and Planetary Sciences*, *26*(1), 643–696.

Moreno, M., Rosenau, M., & Oncken, O. (2010). 2010 Maule earthquake slip correlates with pre-seismic locking of Andean subduction zone. *Nature*, *467*(7312), 198–202.

Naderloo, M., Moosavi, M., & Ahmadi, M. (2019). Using acoustic emission technique to monitor damage progress around joints in brittle materials. *Theoretical and Applied Fracture Mechanics*, *104*, 102368.

Naderloo, M., Veltmeijer, A., Jansen, J. D., & Barnhoorn, A. (2023). Laboratory study on the effect of stress cycling pattern and rate on seismicity evolution. *Geomechanics and Geophysics for Geo-Energy and Geo-Resources*, *9*(1), 137. https://doi.org/10.1007/s40948-023-00678-1

Nicol, A., Carne, R., Gerstenberger, M., & Christophersen, A. (2011). Induced seismicity and its implications for CO2 storage risk. *Energy Procedia*, *4*, 3699–3706.

Niemz, P., Cesca, S., Heimann, S., Grigoli, F., Specht, S. V., Hammer, C., Zang, A., & Dahm, T. (2020). Full-waveform-based characterization of acoustic emission activity in a mine-scale experiment : a comparison of conventional and advanced hydraulic fracturing schemes, 189–206. https://doi.org/10.1093/gji/ggaa127

Noël, C., Passelègue, F. X., Giorgetti, C., & Violay, M. (2019). Fault Reactivation During Fluid Pressure Oscillations : Transition From Stable to Unstable Slip Journal of Geophysical Research : Solid Earth, 940–953.

Passelègue, F. X., Brantut, N., & Mitchell, T. M. (2018). Fault Reactivation by Fluid Injection: Controls From Stress State and Injection Rate. *Geophysical Research Letters*, *45*(23), 12, 837–12, 846. https://doi.org/10.1029/2018GL080470

Patel, S. M., Sondergeld, C. H., & Rai, C. S. (2017). Laboratory studies of hydraulic fracturing by cyclic injection. *International Journal of Rock Mechanics and Mining Sciences*, *95*(March), 8–15. https://doi.org/10.1016/j.ijrmms.2017.03.008

Rice, J. R. (1993). Spatio-temporal complexity of slip on a fault. *Journal of Geophysical Research: Solid Earth*, *98*(B6), 9885–9907.

Ruina, A. (1983). Slip instability and state variable friction laws. *Journal of Geophysical Research: Solid Earth*, *88*(B12), 10359–10370.

Rutter, E., & Hackston, A. (2017). On the effective stress law for rock-on-rock frictional sliding, and fault slip triggered by means of fluid injection. *Philosophical Transactions of the Royal Society A: Mathematical, Physical and Engineering Sciences*, *375*(2103), 20160001.

Segall, P., Rubin, A. M., Bradley, A. M., & Rice, J. R. (2010). Dilatant strengthening as a mechanism for slow slip events. *Journal of Geophysical Research: Solid Earth*, *115*(B12).

Seyler, C. E., Shreedharan, S., Saffer, D. M., & Marone, C. (2023). The role of clay in limiting frictional healing in fault gouges. *Geophysical Research Letters*, *50*(20), e2023GL104984.

Tembe, S., Lockner, D. A., & Wong, T.-F. (2010). Effect of clay content and mineralogy on frictional sliding behavior of simulated gouges: Binary and ternary mixtures of quartz, illite, and montmorillonite. *Journal of Geophysical Research: Solid Earth*, *115*(B3).

van Uijen, W. M. (2013). Rotliegend geology in the Southern Permian Basin: the development of synrift sediments and its relation to seismic imaging.

Viesca, R. C., & Rice, J. R. (2012). Nucleation of slip-weakening rupture instability in landslides by localized increase of pore pressure. *Journal of Geophysical Research: Solid Earth*, *117*(B3).

Wang, L., Kwiatek, G., Rybacki, E., & Bonnelye, A. (n.d.). Laboratory Study on Fluid - Induced Fault Slip Behavior : The Role of Fluid Pressurization Rate Geophysical Research Letters, 1–12. https://doi.org/10.1029/2019GL086627

Wang, W., & Scholz, C. H. (1994). Micromechanics of the velocity and normal stress dependence of rock friction. *pure and applied geophysics*, *143*, 303–315.

Ye, Z., & Ghassemi, A. (2018). Injection-induced shear slip and permeability enhancement in granite fractures. *Journal of Geophysical Research: Solid Earth*, *123*(10), 9009–9032.

Ye, Z., & Ghassemi, A. (2020). Heterogeneous Fracture Slip and Aseismic-Seismic Transition in a Triaxial Injection Test. *Geophysical Research Letters*, *47*(14), 1–9. https://doi.org/10.1029/2020GL087739

Zang, A., Oye, V., Jousset, P., Deichmann, N., Gritto, R., McGarr, A., Majer, E., & Bruhn, D. (2014). Analysis of induced seismicity in geothermal reservoirs–An overview. *Geothermics*, *52*, 6–21.

Zang, A., Yoon, J. S., Stephansson, O., & Heidbach, O. (2013). Fatigue hydraulic fracturing by cyclic reservoir treatment enhances permeability and reduces induced seismicity. *Geophysical journal international*, *195*(2), 1282–1287.

Zang, A., Zimmermann, G., Hofmann, H., Stephansson, O., Min, K.-B., & Kim, K. Y. (2019). How to reduce fluid-injection-induced seismicity. *Rock Mechanics and Rock Engineering*, *52*(2), 475–493.

Zhu, J. B., Kang, J. Q., Elsworth, D., Xie, H. P., Ju, Y., & Zhao, J. (2021). Controlling Induced Earthquake Magnitude by Cycled Fluid Injection. *Geophysical Research Letters*, *48*(19), e2021GL092885.

Zhuang, L., Gyu, S., Melvin, J., Kwang, D., Kim, Y., Hofmann, H., Bok, K., & Arno, M. (2020). Laboratory True Triaxial Hydraulic Fracturing of Granite Under Six Fluid Injection Schemes and Grain - Scale Fracture Observations.

Zoback, M. D., & Gorelick, S. M. (2012). Earthquake triggering and large-scale geologic storage of carbon dioxide. *Proceedings of the National Academy of Sciences*, *109*(26), 10164–10168.

6

7

FAULT REACTIVATION MECHANISM IN DISPLACED FAULTS[1]

Abstract: *It is essential to understand fault slip nucleation within the reservoir interval and its propagation beyond the reservoir. Analytical and numerical studies have shown that, depending on the type of operation (injection/depletion), fault slip can nucleate at external or inner reservoir-fault corners along a displaced fault system, driven by positive peak shear stresses. In the case of depletion, slip patches gradually start at the inner corners and grow towards the reservoir, merging with further depletion. Conversely, injection or increased pore pressure leads to slip patches at external corners, potentially propagating beyond the reservoir into the overburden and underburden. We conducted triaxial experiments on large-scale and small-scale samples containing a displaced fault to investigate fault reactivation and slip nucleation in such settings. For this purpose, we utilized acoustic emission techniques to localize slip patches in large-scale cubic samples, and strain gauges for direct measurements along the displaced fault in small-scale samples. The large-scale cubic sample results showed that inelastic deformation was induced by applying cyclic stress conditions. However, using the acoustic emission technique did not allow the detection of the slip patches' growth, which may be due to the special geometry of the large-scale samples. Direct measurements with a strain gauge network adjacent to the displaced fault system during the monotonic test revealed that differential compaction intensifies from the top of the sample towards the internal corner at the center of the fault where different layers are juxtaposed vertically, indicating a variation in the stress field surrounding the fault plane. Furthermore, results from the cyclic test showed that the differential compaction increases with an increasing number of cycles. Our direct measurements near the displaced fault plane confirm/match the anomalies and peaks in stress observed in previous numerical and analytical studies.*

[1]The large-scale experiment described in this chapter has been a joint effort between Aukje Veltmeijer and myself. Also, the numerical simulation has been provided by Aleks Novikov

7.1. Introduction

Changes in the stress path within and surrounding the reservoir, due to either injection or extraction operations, can lead to the reactivation of pre-existing faults in the subsurface (Kisslinger, 1976; Rathnaweera et al., 2020). A well-known example of production-induced seismicity is the Groningen gas field in the Northern Netherlands, the largest natural gas field in Europe (A. Muntendam-Bos & De Waal, 2013). Seismic activity was first recorded in the Groningen region in 1986 with a magnitude of ML = 2.4. By the early 1990s, studies concluded that this seismicity was linked to gas production (A. G. Muntendam-Bos et al., 2022; Roest & Kuilman, 1994). After 2000, both the total number of seismic events and the number of significant magnitude events ($ML \geq 1.5$) increased. The largest event occurred in 2012 with a magnitude of ML = 3.6, causing damage to houses and leading to anxiety among the residents of the Groningen region (A. Muntendam-Bos & De Waal, 2013; Van der Voort & Vanclay, 2015). There have been several studies allocated to understand the mechanism of production-induced seismicity or fault reactivation due to fluid depletion (Buijze et al., 2017; Haug et al., 2018; Jansen & Meulenbroek, 2022; Jansen et al., 2019). Fault reactivation commences to compensate for the disequilibria build-up from differences in deformation caused by changes in effective normal stresses driven by extracting fluid (decreasing the pore fluid pressure) inside the reservoir and its surroundings (Haug et al., 2018). In other words, reduction in pore fluid pressure by production leads to an increase in effective stress acting on the reservoir and causes reservoir compaction (volume reduction) which alters the stress path within and around the reservoir (poroelastic effect) (Hettema et al., 2000; Segall, 1989). Segall (1985) and Segall and Fitzgerald (1998) proposed that alterations in stress paths (poroelastic effect) around a reservoir can destabilize pre-existing faults. They concluded that fault stress and reactivation are significantly influenced by the reservoir's geometry and the rock mechanical parameters that govern the relationship between stress and changes in pore fluid pressure. Also Orlic and Wassing (2013) demonstrated the significance of reservoir geometry in the redistribution of stress induced by fluid production. The presence of differential compaction in scenarios involving offset or displaced faults, combined with the superimposition of stress changes induced by external factors, is proposed to be a key factor affecting the reactivation of faults in seismic events triggered by production activities (Haug et al., 2018; Mulders, 2003; Roest & Kuilman, 1994; Yerkes & Castle, 1976). Differential compaction is associated with variations in total production, production rates, reservoir thicknesses, and elastic or poroelastic properties.

Understanding the nucleation of fault slip within the reservoir interval, which can propagate outside the reservoir is essential. Analytical approaches (Jansen et al., 2019; Lehner, 2019) and numerical studies (Buijze et al., 2019; van Wees et al., 2018) showed that in the case of depletion/production, the nucleation of the slip along the displaced fault starts from the internal and/or external reservoir/fault corners (see Figures 7.1 and 7.2). The beginning of (usually aseismic) slip in inner corners is because of positive peak shear stresses at these corners, and two patches grow gradually toward the reservoir and merge by further depletion (Further depletion increases the shear stress on the fault plane). On the other hand, injection or increasing pore pressure in the reservoir leads to the development of slip patches at the external corners, which can further propagate outside of the reservoir and into overburden and underburden (Figure 7.3) (Jansen et al., 2019).

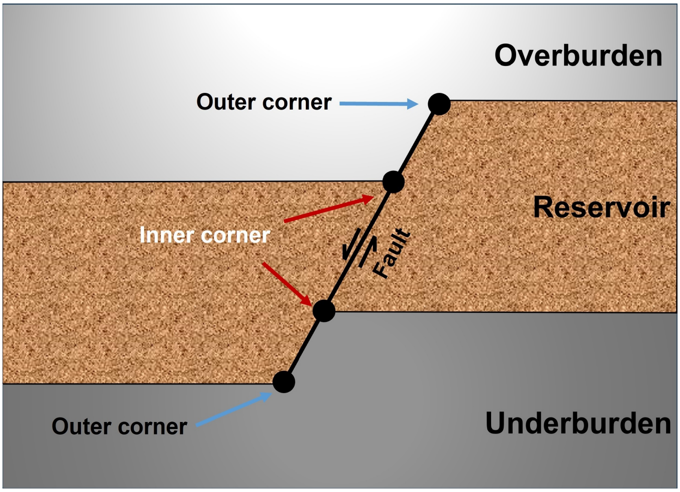

Figure 7.1: Schematic illustration of the displaced reservoir, including two inner and two outer corners indicated with the four solid circles

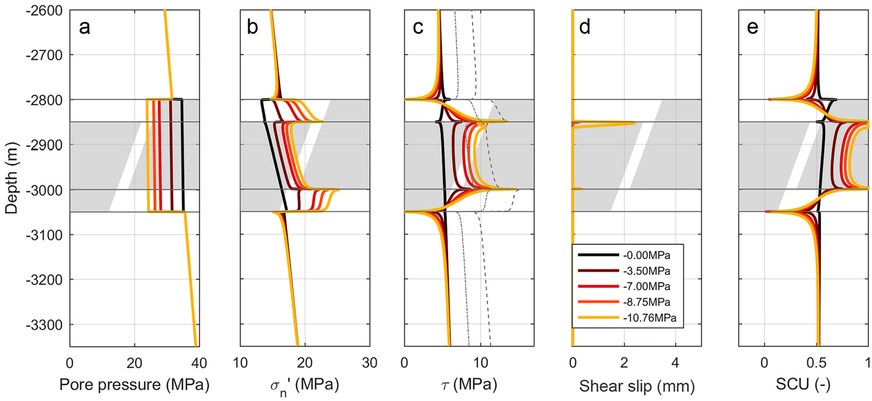

Figure 7.2: Result from 2D finite element modeling of the effects of depletion in a displaced reservoir (grey color), which investigates the evolution of effective normal stress (b), shear stress (c), and slip patch growth (d) by different stages of pore pressure depletion (a) (Buijze et al., 2019). It can be observed that shear stress has positive peaks in inner corners, and also, shear slip starts to nucleate from the inner corners of the displaced reservoir.

Although several numerical and analytical studies address fault reactivation driven by production or injection in the context of displaced fault geometry (Buijze et al., 2019; Jansen et al., 2019; Lehner, 2019; van Wees et al., 2018), to our knowledge, there is no experimental work directly investigating fault reactivation and slip nucleation in such a displaced fault setting. This chapter aims to examine and validate the initiation of

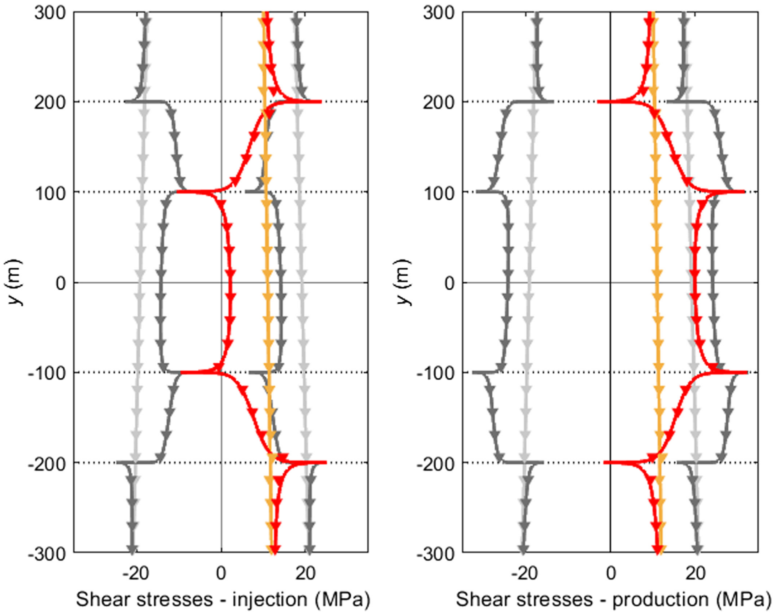

Figure 7.3: Shear stresses generated from injection and production in a displaced reservoir. In the case of depletion/production, the nucleation of the slip along the displaced fault starts from the internal and/or external reservoir/fault corners. On the other hand, injection or increasing pore pressure in the reservoir leads to the development of slip patches at the external corners, which can further propagate outside of the reservoir and into overburden and underburden (Jansen et al., 2019).

slip nucleation patches in both the inner and outer corners of the displaced fault setting under both true-triaxial and triaxial stress path conditions. To achieve this goal, we construct two experiments with two scales of samples. Firstly, large-scale cubic samples with dimensions of 30 × 30 × 30 cm incorporate a displaced normal fault path traversing three layers, including a reservoir formed by highly permeable Red Felser sandstone. Secondly, small-scale (mm scale) cylindrical samples containing an entirely displaced vertical fault (i.e. a fault with a throw equal to the reservoir thickness) are also developed. Note that numerical modeling of the lab-scale sample was also established to find a proper stress regime for slip patch nucleation and fault reactivation and compare the lab results with lab-scale numerical modeling.

7.2. Sample Preparation and design (large-scale)

The construction of large-scale cubic samples featuring a faulted reservoir with dimensions of 30 × 30 × 30 cm involved several preparation stages. The final geometry and configuration of the large-scale sample are depicted in a 2D schematic in Figure 7.4. Red Felser Sandstone, sourced from the vicinity of Kaiserslautern, Germany, was chosen as the reservoir rock from the Rotliegend formation (see Figure 7.5a). The sandstone was cut into two pieces with a 70-degree smooth saw cut relative to the horizontal axis (see Figure 7.5b). After preparing the faulted reservoir, the top and bottom layers, made of mortar (sand, cement, and water composition), were cast using a special mold. Mortar was chosen for its ease of casting symmetrical layers and desirable stiffness.

After casting the top and bottom layers, the sample was stored in a curing room (90% humidity and 23°C temperature) for up to one month to allow the top and bottom mortar layers to reach their final strength. The sample was prepared for sealing using a special AL resin (with properties outlined in the glue specifications) following the curing process. For this stage, a designed mold casts a 0.5 cm glue covering over the reservoir, including the top and bottom layers (see Figure 7.5c). Subsequently, the final layer of mortar was cast around the sample, serving two purposes: adapting the sample size to fit our true-triaxial machine and aiding the sealing layer (AL resin, AE conductive) in preventing pore fluid leakage (see Figures 7.5d and 7.5e). Similar to the top and bottom mortar layers, the sample was kept in the curing room for another month to prevent dehydration and cracking. Once the sample was ready, fluid injection and depletion lines were drilled, as shown in Figure 7.5e.

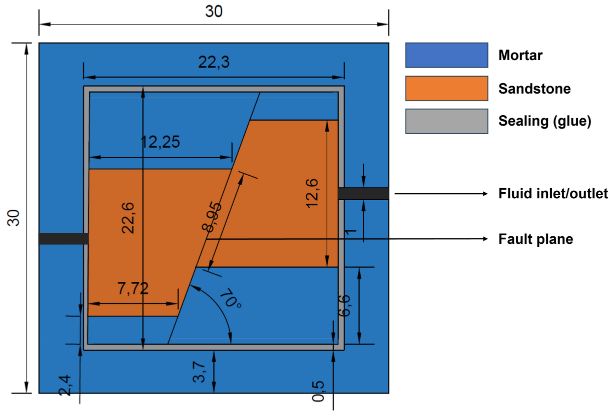

Figure 7.4: The final geometry of the large-scale cubic sample, including a normal-displaced fault system.

A comprehensive series of rock mechanical experiments was conducted to ascertain the mechanical properties of all materials utilized in constructing the sample, including sandstone, mortar, and AL resin. This involved determining the elastic modulus and static friction coefficient for each component. A total of 9 uniaxial compressive tests were conducted on intact cylindrical Red Felser sandstone, mortar, and AL resin. The results for elastic properties, notably Young's modulus and Poisson ratio, are presented in Table 7.1. The findings indicate that mortar exhibits the highest Young's modulus and the lowest Poisson ratio, while the reverse is observed for AL resin samples. Additionally, nine triaxial fault reactivation tests were performed to obtain the static friction coefficient between sliding materials. Figure 7.6 illustrates the prepared saw-cut samples for triaxial fault reactivation tests. All tests were conducted under the same confining pressure (20 MPa).

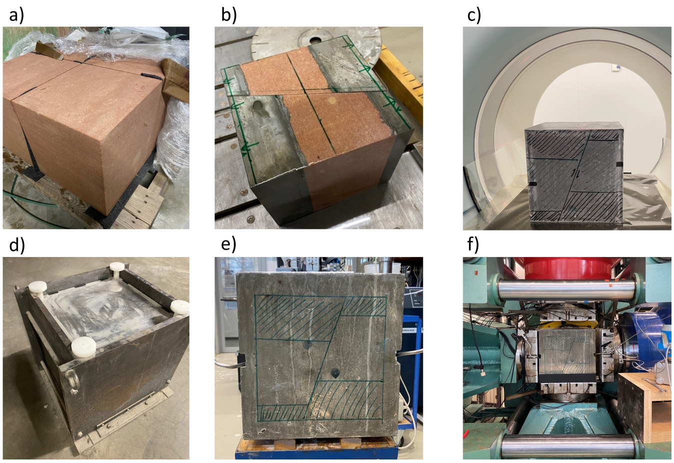

Figure 7.5: different stage of sample preparation: a) Cubic Red Felser sandstone, b) reservoir with top and bottom mortar layer in a normal displaced fault configuration, c) sample after casting the sealing (AL resin), d) casting the outer mortar layer, e) final configuration and embedding injection/depletion lines, and f) sample embedded in the true-triaxial machine.

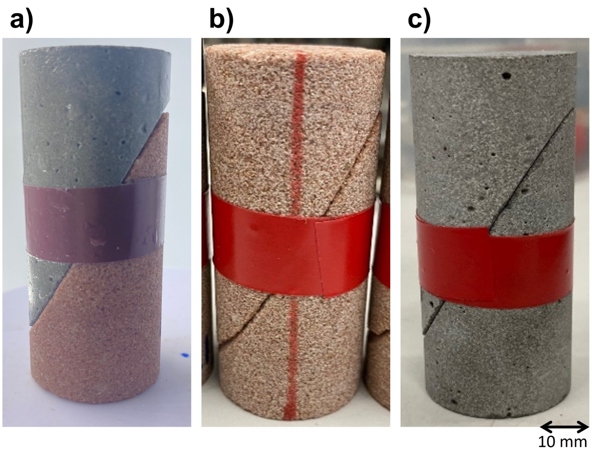

Figure 7.6: Saw-cut samples: a) Mortar-sandstone, b) sandstone -sandstone, and c) mortar-mortar.

Table 7.1: Elastic modulus and friction coefficient for different materials

Sample	Friction coefficient	Young's Modulus (GPa)	Poisson ratio
Mortar-Mortar	0.67	-	-
Mortar-Sandstone	0.62	-	-
Sandstone-Sandstone	0.61	-	-
Intact mortar	-	19.8	0.115
Intact sandstone	-	17	0.3
Intact glue	-	5.2	0.34

7.3. MODELLING THE LARGE-SCALE TRIAXIAL LOADING EXPERIMENT

The numerical modeling (performed by Alex Novikov of TU Delft) was based on the sample's geometry (see Figure 7.7) and the various material properties presented in Table 7.1. The primary objective of the numerical modeling was to identify an appropriate stress regime to induce slip patch nucleation and fault reactivation, as well as to compare the laboratory results with lab-scale numerical modeling.

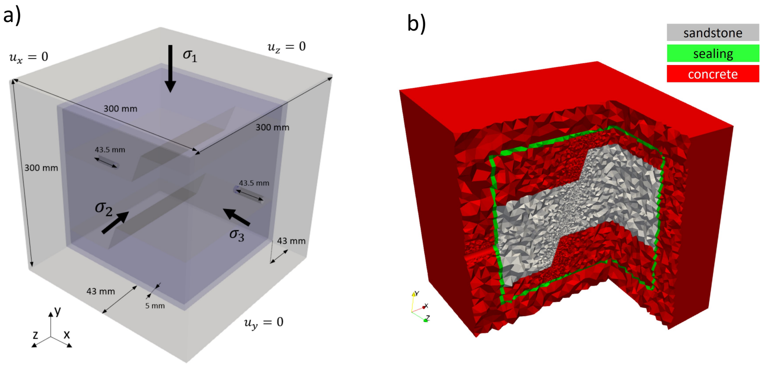

Figure 7.7: Displaying: a) the domain geometry and boundary conditions and b) . 3D view of different material with the structure hexahedral grid.

For modeling the current experimental geometry and configuration, an open-source multiphysics numerical simulator named GEOS was utilized (Huang et al., 2023). GEOS employs a combination of Finite Volume and Finite Element numerical methods for fully implicitly integrating fluid mass and momentum balance equations. In order to analyze the beginning of the slip path growth, the Coulomb stress (σ_c) was used (equation 7.1), which, in principle, shows the difference between resolved shear stress on the fault plane and shear strength (σ_{strength}) of the fault plane.

$$\sigma_c = \sigma_{\text{shear}} - \sigma_{\text{strength}} \tag{7.1}$$

The shear strength of a fault plane is the maximum shear stress it can withstand which can be described by the Mohr-Coulomb failure criterion, which is commonly expressed as follows (Hoek, 1990; Jaeger et al., 2009):

$$\tau_s = C + \mu(\sigma_n - p), \tag{7.2}$$

where τ_s is the shear strength of the fault plane, σ_n is the normal stress acting across the fault, C is cohesion, μ is the coefficient of friction, and p is pore pressure.

Figure 7.8 shows the Coulomb stress distribution over the fault plane in stress condition of $\sigma_1 = -25$ MPa and $\sigma_3 = \sigma_2 = -10$ MPa and pore pressure (p_p) of 0.1 MPa. Analyzing the Coulomb stress changes reveals stress peaks at both inner and outer corners. Notably, the Coulomb stress exceeds zero at the outer corners, signifying the initiation of slip patches in these areas. This observation aligns with the analytical findings of Jansen

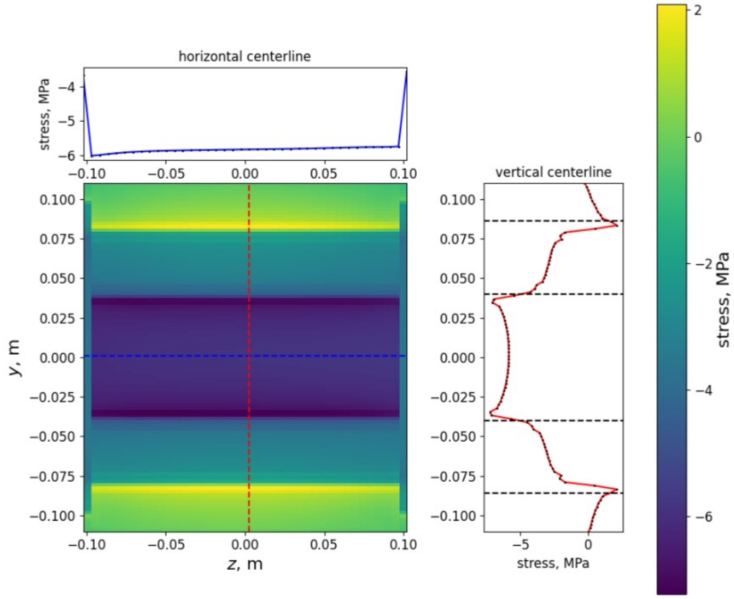

Figure 7.8: The distribution of Coulomb stress over the fault plane. The middle two dotted lines in the right-hand figure correspond to the vertical position of the inner corners and the top and bottom dotted lines to those of the outer corners.

et al. (2019), who elucidated that slip patches tend to initiate and grow at outer corners during injection. We note that the paper by Jansen et al. (2019) considered an infinitely wide reservoir with mechanical properties identical to those of its surroundings. In our experiment, however, the reservoir has a finite size while also the mechanical properties of the reservoir rock and its surroundings (mortar) are different. The resulting stress pattern is therefore more complex.

After conducting many simulations considering various stress paths and conditions while taking into account experimental limitations such as loading capacity and time, a proposed stress path has been developed for large-scale experiments. The stages of this proposed stress path, as depicted in Figure 7.9, are as follows: Under the isostatic stress condition, where $\sigma_1 = \sigma_2 = \sigma_3 = 7$ MPa and zero pore pressure is maintained, pore pressure build-up begins (stage 1). This build-up progresses until it reaches 2 MPa (stage 2). Simultaneously, the principal stresses are increased to 10 MPa. As the pore pressure rises, reaching 5 MPa, slip patches commence due to the Coulomb stress exceeding zero. Further, an increase is implemented to induce more differential stress, intensifying shear stress on the fault plane and consequently elevating the Coulomb stress.

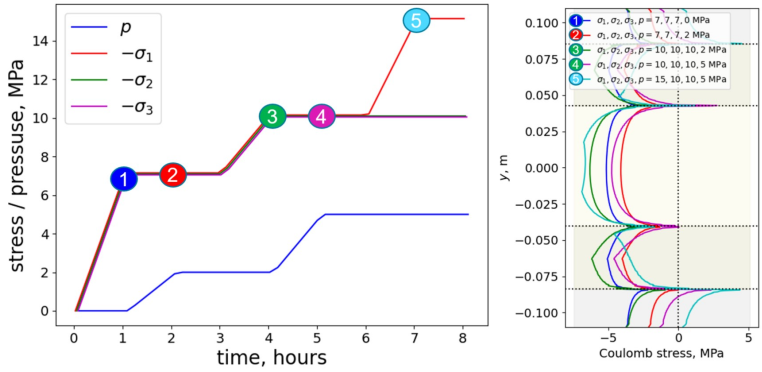

Figure 7.9: The proposed stress path is based on modeling results for large-scale experiments. The figure on the left-hand side shows the proposed experimental protocol, while the figure on the right-hand side illustrates the Coulomb stress changes on the fault plane during each step of the protocol.

7.4. LARGE-SCALE EXPERIMENTS

7.4.1. EXPERIMENTAL APPARATUS

We utilized the True Triaxial System (TTS) to conduct testing on large-scale blocks. This system is an advanced technology for rock deformation, seamlessly incorporating both passive and active acoustic systems. It is also compatible with installing a fluid injection/depletion system (see Figure 7.10). The TTS enables the application of vertical and two independent horizontal stresses, up to 38 MPa (3500 kN) in each direction (σ_1, σ_2, and σ_3) simultaneously on a 30 cm cube of rock. To clarify, three cylinders labeled XC, YC, and ZC independently push the sample against three fixed plates, XD, YD, and ZD (Figure 7.10). These cylinder pressures are controlled by servo valves fixed to the loading frame. The deformation along each axis was measured using the average from two Linear Variable Differential Transformers (LVDT) strategically positioned near the platen–rock interface (Figure 7.11b). Vaseline and Teflon sheets covered the loading plates during the tests to minimize friction between sample interface and loading plates. The loading process can be controlled either manually or via a computer. Acoustic transducers are incorporated into the loading plates. These piezoelectric transducers, such as model V103-RM and VI53-RM (Olympus), can generate compression or shear waves and can also function as receivers (Figures 7.12b and 7.11c). Each transducer has a unit size of 17 mm in diameter, and a spring behind it pushes the transducer face against the sample surface. An ultrasonic coupling agent is utilized to optimize contact coupling. This ensures that the Acoustic Emission (AE) sensor maintains full contact with the sample surface, thereby improving the accuracy of the acquired signals. Teflon sheets cover the loading plates, featuring holes at the transducer locations to allow direct contact with the block. The system boasts a maximum capacity of 48 transducer channels. However, 20 transducers are employed for this specific test, representing the maximum number of channels that can record simultaneously in our acoustic system. The position and quantity of sensors are illustrated in Figure 7.12.

We utilized a Richter acoustic emission system to detect and capture microseismic activity, performing active acoustic measurements with a dynamic range of 5 V. The Richter system is a versatile, multi-channel data acquisition system featuring 16-bit ADC resolution, enabling simultaneous and synchronous sampling across all input channels. Continuous waveforms were meticulously recorded at a sampling rate of 2 MHz, utilizing an input impedance of 50 Ω through the ExStream software. While the ExStream software handled the recording of acoustic emission data, the subsequent processing and management of raw continuous waveform data were conducted using the Insite Seismic Processor software. This processing involved converting continuous waveform data into individual waveforms for subsequent analysis, following a predefined trigger logic. During the experiment, triggered events were identified when at least ten channels recorded a voltage exceeding 500 mV within a window length of 512 sample points. A 1024 sample point waveform was extracted for each channel and saved in the events files for each triggered event.

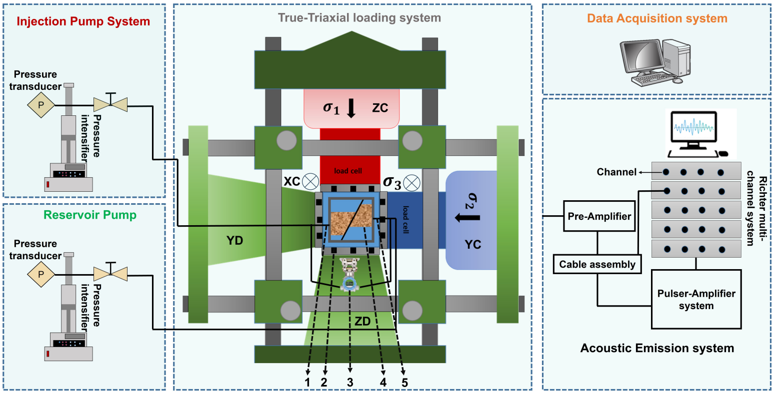

Figure 7.10: Schematic illustration of the different units of experimental set up. 1) Injection line, 2) acoustic sensor, 3) differential pore pressure transducer, 4) cubic sample including displaced fault, and 5) depletion line.

The initial Acoustic Emission (AE) signals underwent amplification by 40 dB using preamplifiers. Continuous recording of amplified waveforms from 20 AE sensors was maintained throughout the experiment. The preamplifiers were designed with a switching mechanism that enabled each Acoustic Emission (AE) sensor to function alternately as a source and receiver. The pulse amplifier system systematically delivered a sequential 500 V pulse to each AE sensor throughout the velocity surveys. In our setup with 20 AE sensors, while one sensor emits or sends the wave, the remaining 19 sensors operate as receivers. This process continues until all sensors have emitted a wave and acted as an active source. Every 1 minute, the system seamlessly transitioned to an active state, engaging in velocity surveys that collectively took 6 seconds to complete. Figure 7.12b shows the array and type of sensors in each loading palate.

7.4.2. EXPERIMENTAL PROTOCOL

We employed a multistage experimental protocol to investigate the mechanism of displaced fault reactivation during both injection and depletion, as illustrated in Figure 7.13.

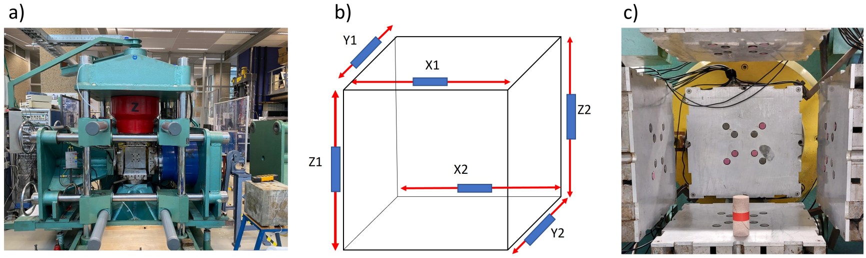

Figure 7.11: Showing a) a picture of the true-triaxial system and b) the position of six LVDTs for recording deformation in principal directions (Z, X, and Y directions). c) A zoomed-in view of the loading plates, which are instrumented with multiple holes for the attachment of acoustic transducers.

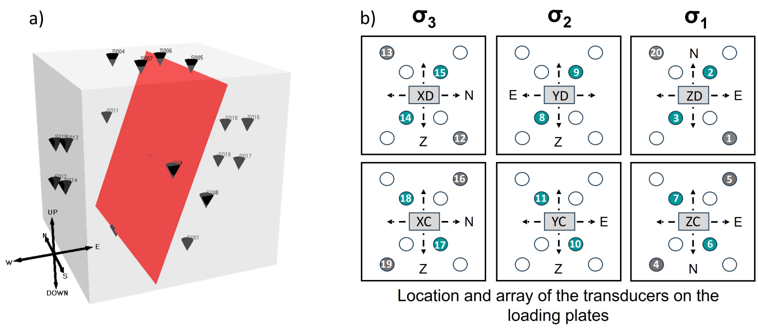

Figure 7.12: Illustration of a) 3D distribution or arrangement of the acoustic sensors around the cubic sample and b) an array of sensors in each loading palate (grey circles show s-wave transducers and green circles show the p-wave transducers).

The first part of the protocol was designed based on the modeling results (Figure 7.9), indicated by the light blue shaded area in Figure 7.13. This design encompasses various stages:

- Isostatically increasing the principal stresses ($\sigma_1 = \sigma_2 = \sigma_3 = 7$ MPa) with a rate of 1 kN/s up to 7 MPa.
- Initiation and gradual buildup of pore pressure up to 2 MPa.
- Simultaneous increase in principal stresses to 10 MPa.
- Further increase in pore pressure to 5 MPa.
- Elevation of the maximum principal stress (σ_1) with a rate of 1 kN/s while maintaining the other two principal stresses and pore pressure constant.

In the subsequent phase of the protocol, depicted by the grey shaded area in Figure 7.13, a stress cycle was initiated by incrementally raising the maximum principal stress to 17 MPa and subsequently reducing it back to 10 MPa, equivalent to the other principal stresses ($\sigma_1 = \sigma_2 = \sigma_3 = 10$ MPa). Shortly after this stress cycle, depletion and injection cycles were initiated. Following this recursive cycle and depletion/injection cycles, we introduced three progressive cycles, with the maximum stress amplitude increasing by 5 MPa per cycle, along with three corresponding depletion/injection cycles during the peak stress of each cycle. The primary objective of this addition was to expose the sample to high-stress levels, enhancing the likelihood of capturing seismic events or the growth of slip patches. Additionally, we sought to examine the impact of cyclic stress induced by both pore pressure and principal stress on the mechanism of displaced fault reactivation. In the final segment of the protocol, when the maximum principal stress reached (σ_1 = 34.8 MPa), two rapid depletion cycles were applied to simulate extreme and rapid depletion conditions.

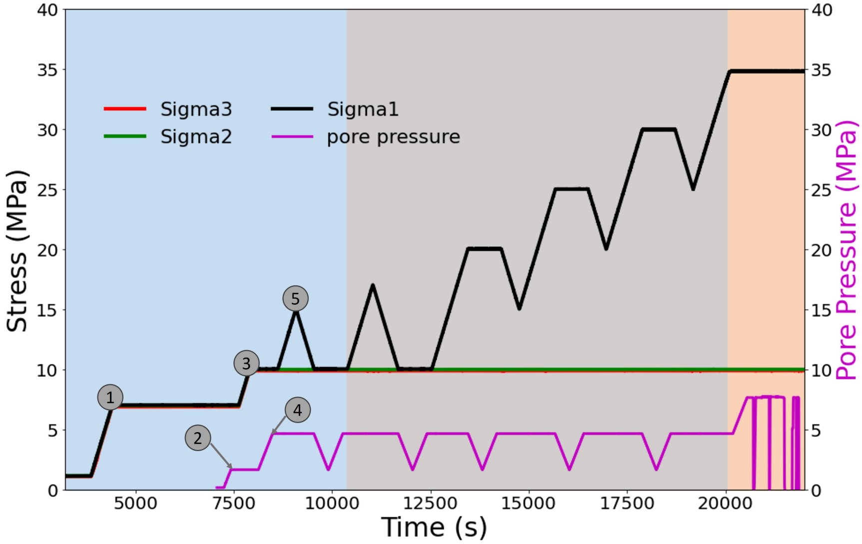

Figure 7.13: Schematic illustration of the experimental protocol and stress path. Shaded light blue area is based on the modeling results (Figure 7.9). See section 7.4.2, experimental protocol for comprehensive information.

7.4.3. RESULTS AND DISCUSSION

MECHANICAL RESPONSE

Figure 7.14 illustrates the evolution of sample deformation from three principal directions (X, Y, and Z) in response to changes in stresses and pore pressure. Note that the X direction corresponds to the minimum principal stress (σ_3) (perpendicular to the fault strike), the Y direction to the intermediate principal stress (σ_2), and the Z direction to the maximum principal stress (σ_1). From stage three of the experimental protocol (see Figure 7.13), where principal stresses increase isostatically, displacement in all directions increases. However, deformation in the Z direction is significantly greater than in the other two directions. This disparity could be attributed to the sample's geometry and the fact that the Z direction is perpendicular to the layering direction of the sample, which could allow more deformation between layer interfaces and along the fault plane due to compaction. Moreover, the stiffness contrast (differences in Young's modulus and Poisson ratio) between the sandstone and the mortar is likely to play a role. After stage

5, or upon initiating an increase in deviatoric stress (increasing stress in the Z direction), displacement in the Z direction increases, culminating in a 3.42 mm deformation at the highest deviatoric stress level. Although the stresses in the X and Y directions were maintained constant and equal, the deformation in these directions was influenced by both the change in stress in the Z direction and the change in pore pressure. As a result, displacement in both the X and Y directions decreased gradually with the increasing number of cycles of Z direction stress. However, at the end of the tests, under the highest deviatoric stress condition, the reduction in displacement in the X direction was greater than in the Y direction. This phenomenon is also an effect of the geometry, indicating that increasing stress in the Z direction makes it easier for the sample to expand in the X direction rather than in the strike direction of the fault. Figure 7.15 presents a zoomed-

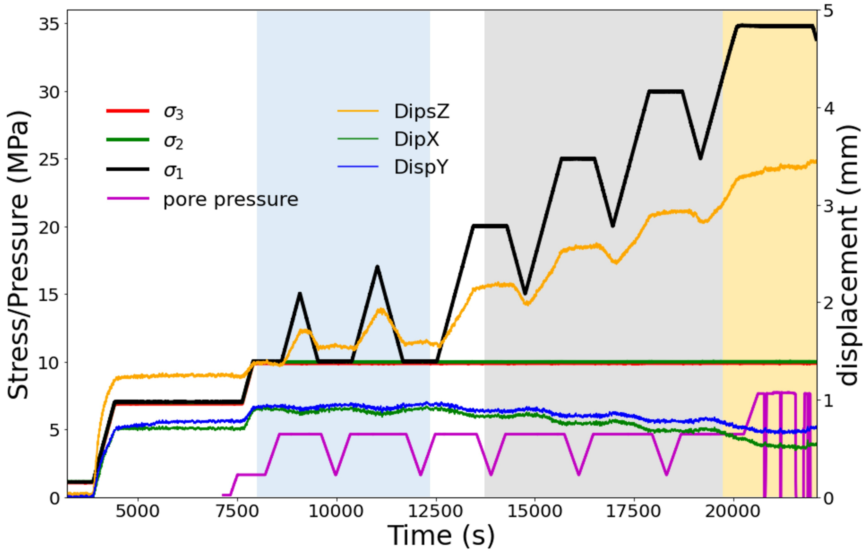

Figure 7.14: Evolution of the sample deformation from three principal directions (X, Y, and Z) by change in stresses and pore pressure.

in view of the blue-shaded area in Figure 7.14, offering a clearer depiction of changes in displacement in different directions from the first to the second cycles. At the end of the first two cycles, the evolution of deformation in the Z direction indicates inelastic deformation. Focusing on point A, which marks the start of the first cycle and the increase in differential stress, inelastic deformation becomes evident after each cycle, as indicated by the differences in magnitude at points A, B, and C in Figure 7.15. With a decrease in pore pressure (depletion), deformation slightly increases in all directions.

Figure 7.16 presents a detailed view of the progressive cycles, as indicated by the grey-shaded area in Figure 7.14. Similar to the recursive cycles, inelastic deformation is observed cycle after cycle during the progressive cycles, as evidenced by points A to D. With an increasing number of cycles, there is a slow and gradual decrease in deformation in the X and Y directions. However, it's important to note that since an outer sealing layer and mortar encase the displaced reservoir, the LVDT measurements reflect the entire sample, not just the changes in the reservoir. Consequently, interpreting fault reactivation and slip nucleation based solely on changes recorded by the external LVDTs is challenging.

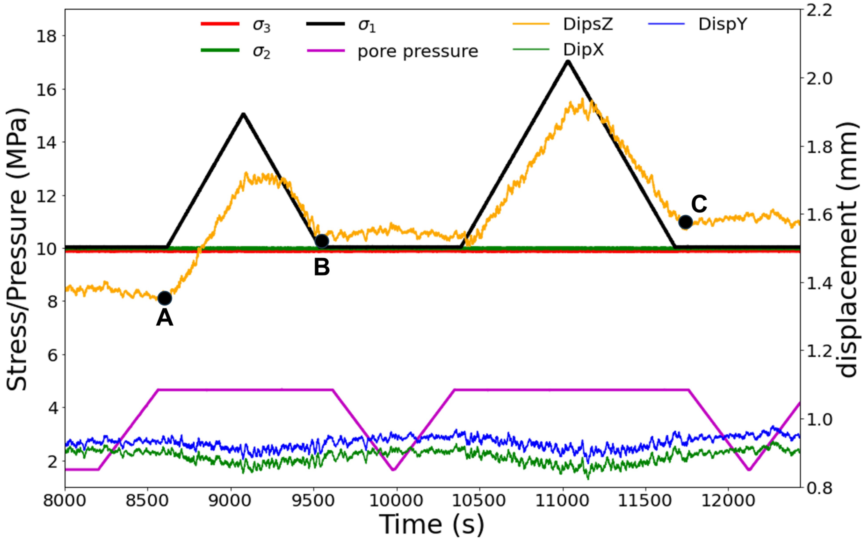

Figure 7.15: A zoomed view of the blue-shaded area in Figure 7.14 showing the evolution of deformation from three principal directions (X, Y, and Z) by change in stresses and pore pressure.

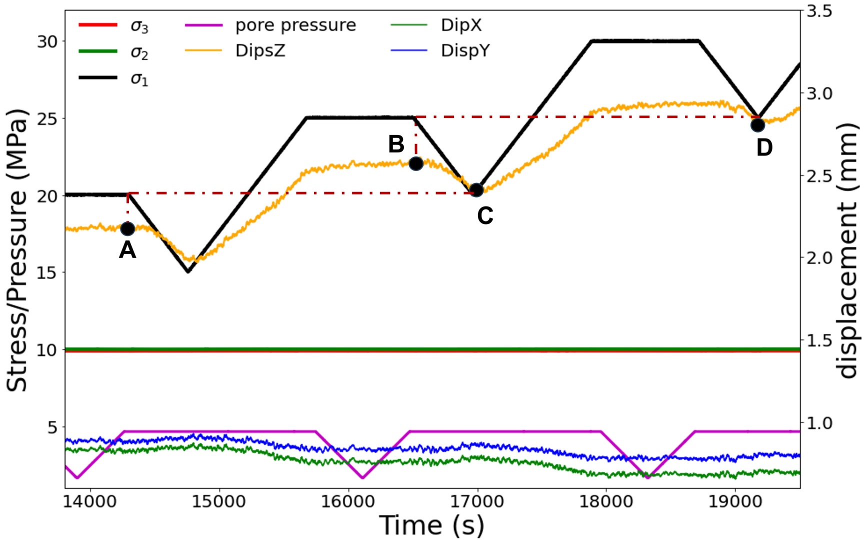

Figure 7.16: A zoomed view of the grey shaded area in Figure 7.14 showing the evolution of deformation from three principal directions (X, Y, and Z) by change in stresses and pore pressure.

The final part of the experimental protocol involved rapid depletion of pore pressure (decreasing it to zero) under the highest differential stresses, as depicted in Figure 7.17, which is a zoomed view of the light orange shaded area in Figure 7.14. The displacement in the Z direction exhibits two peaks in response to the rapid depletion, as indicated by circles A and B. Interpreting the causes of these peaks in Z direction deformation is challenging. To this end, we can utilize acoustic data (both passive and active). However, one possible explanation could be the rapid compaction of the reservoir due to the complete removal of pore pressure from the porous reservoir. As previously discussed and demon-

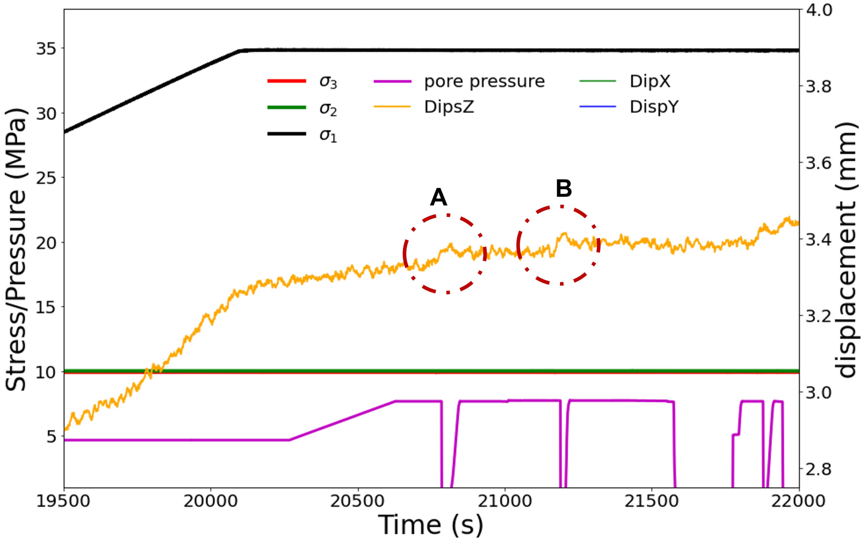

Figure 7.17: A zoomed view of the orange-shaded area in Figure 7.14 showing the evolution of deformation in Z direction by fast depletion.

strated, inelastic deformation is observable with the application of each stress cycle. Additionally, hysteresis loops are evident in Figure 7.18 when considering the unloading and reloading of stress in each cycle. Focusing on Point X, which marks the beginning of the increase in differential stress and the end of the experiment (returning σ_1 to isostatic conditions) on point Y, a total of 0.6 mm inelastic deformation was induced, accounting for approximately 29% of the total deformation from point Y. As mentioned before, interpreting the growth of slip patches from the expected corners or generally interpreting fault reactivation using deformation changes and stress information proves challenging.

7.4.4. MICROSEISMICITY AND ACOUSTIC MONITORING

Regrettably, only a single acoustic emission (AE) event was recorded, and it could not be located due to the insufficient number of P-wave arrivals for the source location algorithm. We speculate that the failure to record more AE events may be attributed to the sample geometry, where a concrete layer and AL resin sealing may have hindered the detection of AE events. Additionally, numerous instances of noise were recorded, probably stemming from friction between the sensor surfaces and the sample. Various studies have indicated that inelastic deformation can be identified through AE event activities (Hernandez et al., 2022; Naderloo, Veltmeijer, et al., 2023; Naderloo, Kumar, et al.,

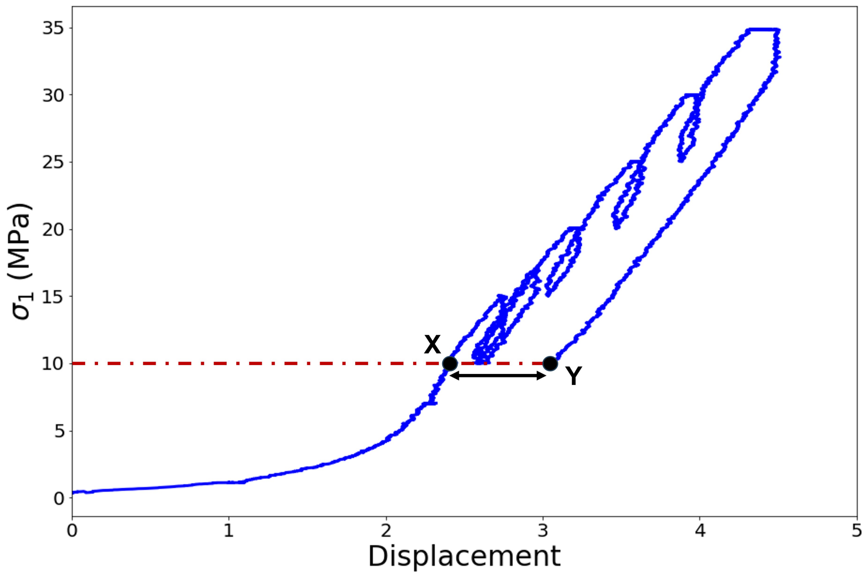

Figure 7.18: Axial stress versus deformation in Z direction showing the total inelastic deformation at the end of the experiment (point Y).

7

2023). In our experiment, we observed considerable inelastic deformation; however, no AE events were recorded while this inelastic deformation was forming. Therefore, the experimental setup impacts the likelihood of recording AE events from slip patch growth at inner and outer corners, and slip patches may have developed at the anticipated corners. Consequently, we recommended simplifying the experimental setup, and including direct deformation measurements, close to the fault plane.

7.5. SMALL-SCALE EXPERIMENTS (HARLEQUIN)

We used a triaxial setup with a simple geometry and a small cylindrical sample to simplify the experimental setup and facilitate direct measurements close to the fault plane. Secondly, strain gauges were employed to measure deformation near the fault plane. Figure 7.19 illustrates the transition from the previous large-scale geometry (normal displaced fault geometry) to a small-scale sample (fully displaced vertical fault). A special geometry was designed for the samples to mimic a fully displaced fault (i.e. a fault with an offset equal to the reservoir height), separating the two compartments of the reservoir from each other (see Figure 7.19b). As shown in Figure 7.19, we simplified the displaced fault design. The sample resembles the theater character known as 'Harlequin,' hence we have named the small-scale sample after this character, abbreviated as HQ. Initiation of the slip is expected to occur at the center of the sample. We note that in this simplified experiment differential compaction between the different rock types (sandstone, mortar, and/or resin) only takes place because of differences in material properties (Young's modulus and Poisson ration) in response to vertical loading. Unlike in the large-scale experiment, pore pressure is not separately controlled.

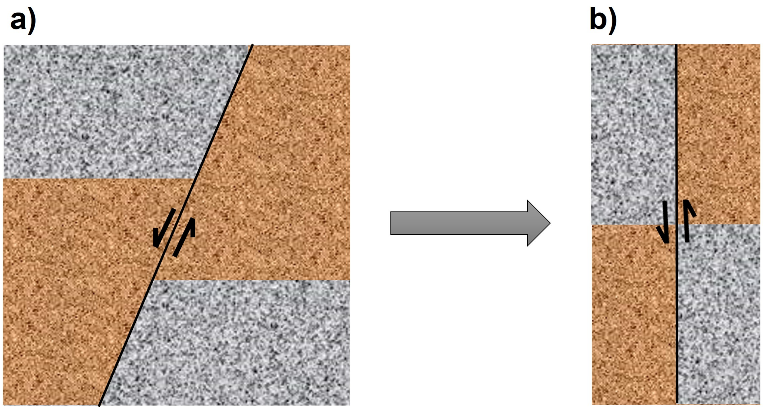

Figure 7.19: a) Normal-displaced inclined fault and b) Complete fully-displaced vertical fault.

7.5.1. Sample preparation and material

Two types of Harlequin (HQ) samples and strain gauge (SG) patterns were constructed. The first HQ sample (HQ1) was made using Red Felser sandstone and AL resin, as depicted in Figure 7.20. The arrangement of SGs on HQ1 is shown in Figure 7.20a, featuring three SGs mounted on the top, middle, and bottom of the sample, precisely on the fault plane. The second HQ sample (HQ2) was created using AL resin and mortar, incorporating more SGs, as illustrated in Figure 7.20b. These strain gauges have dimensions of 5 mm in length and a grid width of 3 mm, with a gauge factor of 2.1.

7

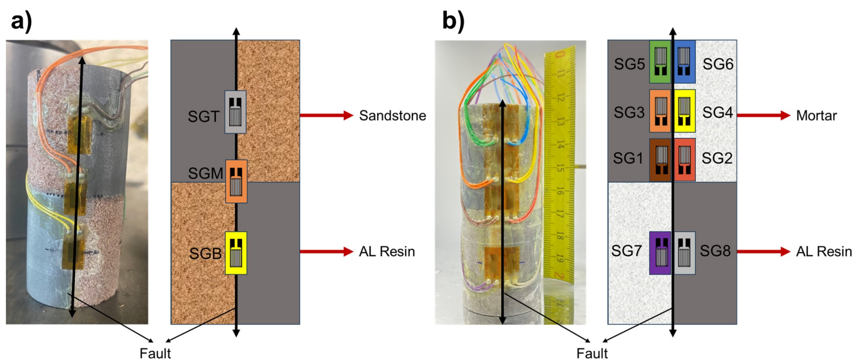

Figure 7.20: Two types of HQ samples: a) HQ1, sandstone and AL resin, and b) HQ2, mortar and AL resin.

7.5.2. Experimental protocol

Uniaxial stress conditions ($\sigma_2 = \sigma_3 = 0$) were applied to the first Harlequin (HQ1) sample, while the second Harlequin (HQ2) sample was subjected to triaxial stress experiments ($\sigma_2 = \sigma_3$). The employed stress paths for HQ2 included monotonic and cyclic variations, as depicted in Figure 7.21. During the monotonic stress path, axial and radial stresses were increased hydrostatically up to 20 MPa. After this, while keeping the radial stress constant, the axial stress was further increased (with a displacement rate of 0.0007/s) to induce differential stress. For the cyclic stress path, a similar initial increase in axial and radial stress up to 20 MPa was followed by an additional increase to 80 MPa. Cyclic stress was then implemented with an amplitude of 15 MPa and a frequency of 0.0024 Hz, repeated over seven cycles. The purpose of incorporating these two stress paths was to explore the effects of different stress patterns on the growth of slip patches.

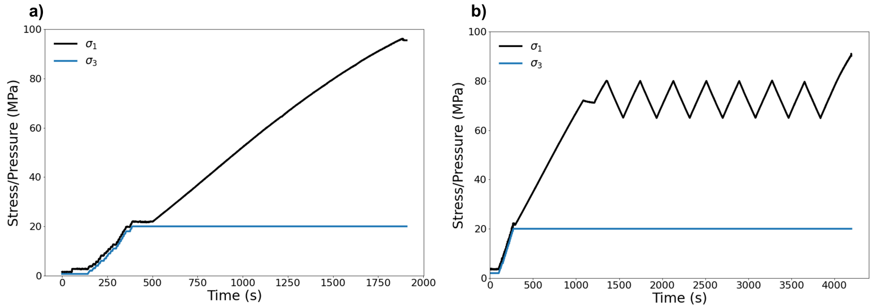

Figure 7.21: Illustration of the stress path or experimental protocol in triaxial stress conditions for HQ2 sample. a) monotonic stress path and b) cyclic stress path

7.5.3. RESULTS AND DISCUSSION

Figure 7.22 illustrates the results of SGs measurements obtained from the uniaxial compression experiment conducted on the HQ1 sample. Even a slight increase in axial stress induces deformation, and the SGs respond to this deformation. The middle SG begins to deviate from both the top and bottom SGs. As the stress further increases, this deviation intensifies, and the slope or gradient of change for the top and bottom SGs becomes very similar. The deviation in the middle SG indicates variations in stress and deformation at the central corner.

Moreover, the similar gradient observed for the top and bottom SGs signifies a consistent stress and deformation field at the symmetric points where they are mounted. Therefore, these were the first direct deformation measurements close to the fault plane and at the anticipated location where slip patches can grow (central corner). Subsequently, we increased the number of SGs and enhanced the mechanical properties contrast between layers of the displaced fault system for the HQ2 sample, a topic discussed next.

HQ2 SAMPLE UNDER MONOTONIC AND CYCLIC STRESS

Figure 7.23 illustrates the variations in all SGs under increasing axial stress during triaxial conditions. As the axial stress increases, all SGs exhibit compression or shortening in the material they are mounted on, except for SG5. The anomaly in SG5's response could be attributed to the loading piston's contact with the end surface of the sample. However, at around 30 MPa axial stress, SG5 also responds to the increase in stress and deformation.

Some SGs exhibit a higher gradient than others, while some show approximately similar gradients. To facilitate the differentiation between the changes in SGs, Figure 7.24 is provided, depicting the alteration in the SGs' row on the top-left side of the fault in the AL resin material. In Figure 7.24, the transition from SG5 to SG1 (from the top to the

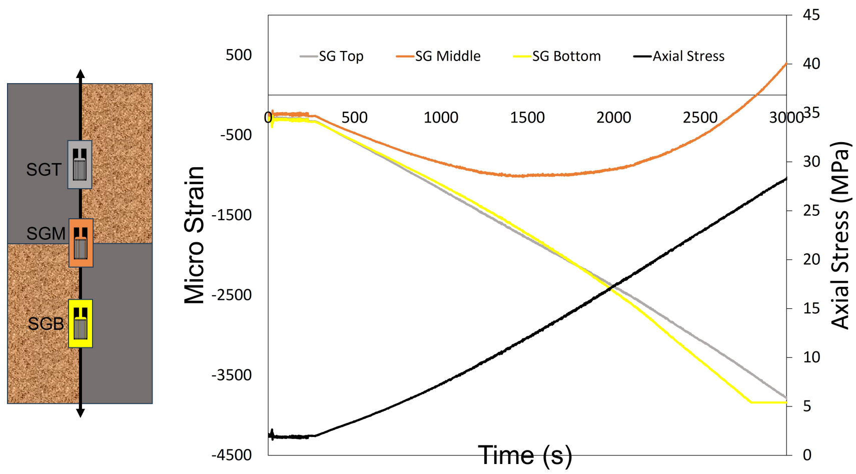

Figure 7.22: SGs measurements result from uniaxial compression experiment on the HQ1

center of the sample) reveals an increasing gradient of deformation, culminating in SG1 recording the maximum amount of deformation. This observation suggests that stress concentration intensifies toward the center of the fault at the inner corner, subsequently inducing more deformation.

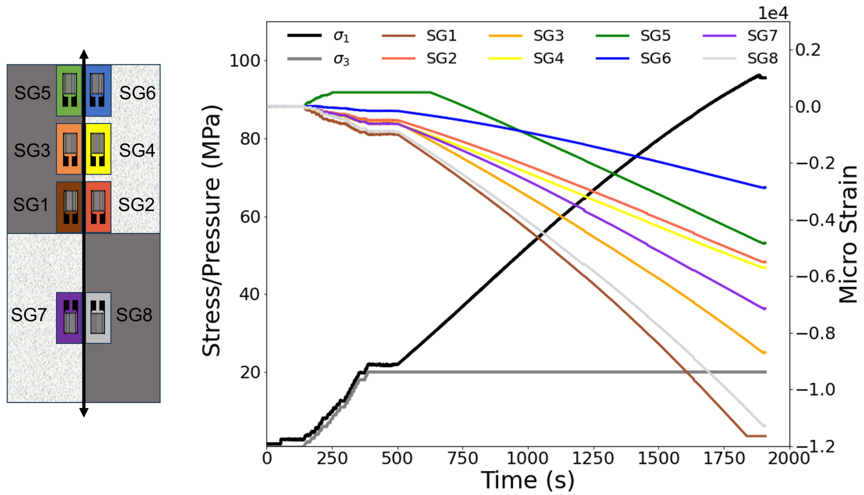

Figure 7.23: Measurements of all the SGs under increasing the axial stress during triaxial condition.

Considering the concept of differential compaction, which can induce fault slip nucleation and reactivation, we present Figure 7.25, which illustrates the differential compaction (deformation which is primarily measured as strain) between SG pairs (SG1SG2, SG3SG4, SG5SG6, and SG7SG8). Differential compaction increases from the top of the sample toward the internal corner at the center of the fault. Additionally, given their sym-

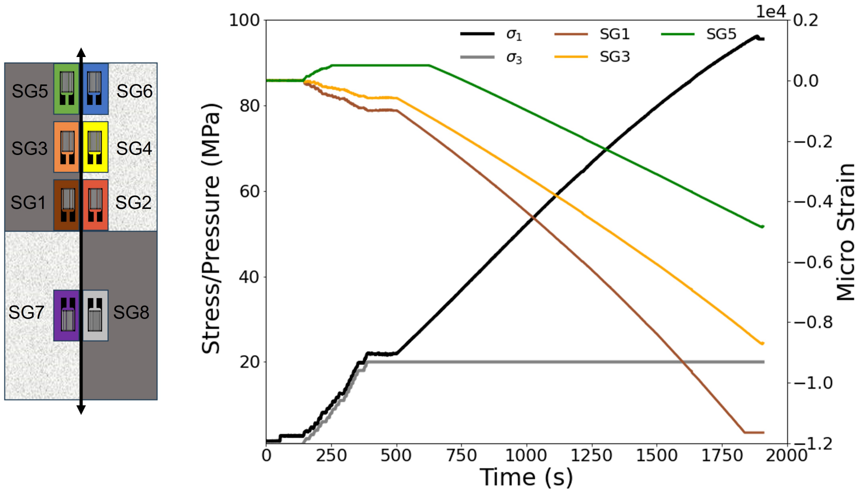

Figure 7.24: Measurements of the SGs row in top left side of the fault in AL resin material (SG1, SG3, SG5).

metrical counterpoint mounting, the gradient of the differential strain between SG3SG4 and SG7SG8 is very similar, as expected. We hypothesize that, similar to the normal displaced fault geometry indicated in various studies where shear stress and effective normal stress exhibit peaks at the internal and external corners based on injection or depletion operations, a simplified version of a displaced fault (fully displaced fault) with one central corner experiences similar stress concentration (Jansen & Meulenbroek, 2022; Jansen et al., 2019). The contrasting mechanical properties of AL resin and mortar lead to differential compaction under stress, as AL resin, being less stiff, deforms more readily compared to mortar. We postulate that fault slip can accommodate or compensate the recorded differential compaction. This is attributed to the boundary conditions, as the fault counterparts at the top and bottom ends of the sample are constrained from moving independently.

The micro strain recorded by the strain gauges (SGs) was converted into millimeters by factoring in the original length of the sample (71 mm) and the gauge factor of the SGs (GF = 2.1). Figure 7.26 illustrates the displacement measurements in millimeters as differential deformation by SG pairs (SG1SG2, SG3SG4, and SG5SG6) at the end of the experiment when the axial stress reached 97 MPa. A progressive increase in differential compaction was observed from the top to the center of the fault. At the experiment's end, the differential displacement recorded by the SG pair (SG1SG2) near the fault's center was 0.92 mm. This displacement is theorized to be a combination of slip and the material matrix's elastic and plastic deformation, including AL resin and mortar.

Figure 7.27 illustrates variations in measurements of all the SGs under cyclic axial stress while maintaining constant radial stress. The recording begins when SGs are subjected to cyclic axial loading. Similar to the case of monotonic stress, SG1 and SG6 exhibit the maximum and minimum deformations, respectively. Analyzing the peaks and valleys

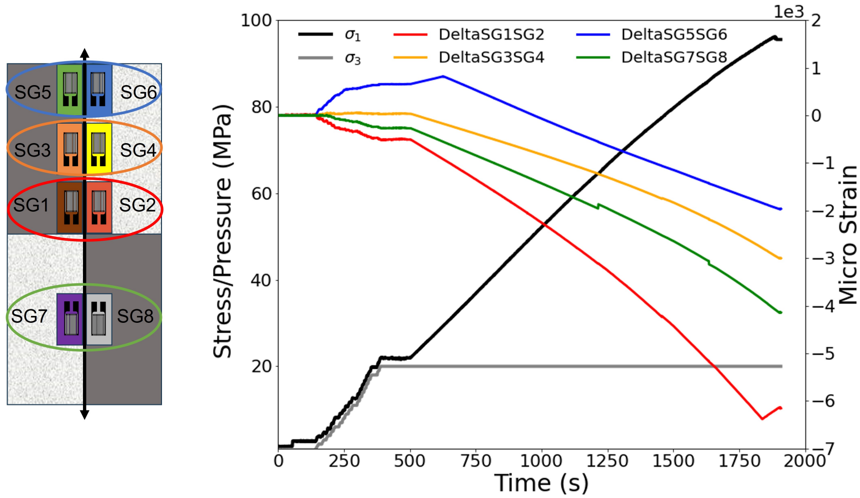

Figure 7.25: The differential compaction between SG pairs (SG1SG2, SG3SG4, SG5SG6, and SG7SG8).

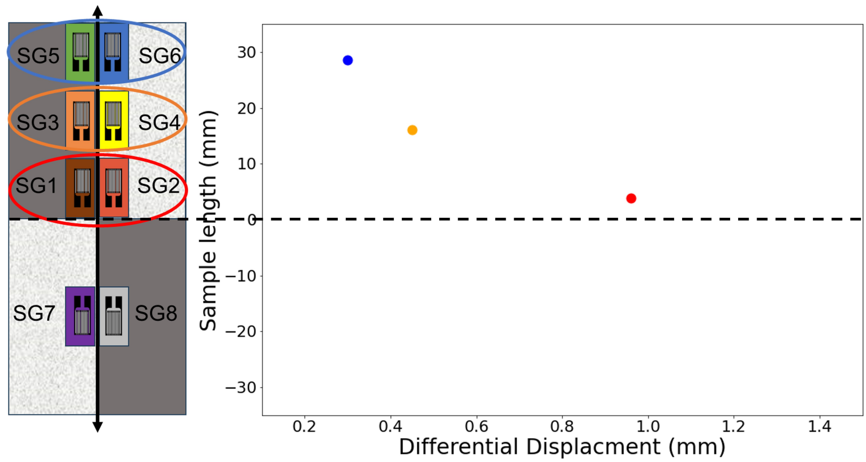

Figure 7.26: Differential displacement recorded at the location of the SGs pairs (markers color refer to SG pairs).

of the cycles reveals a clear decreasing trend, indicating the presence of irreversible deformation recorded by SGs. Similar to the monotonic case, Figure 7.28 is presented to demonstrate the differential displacement between SG pairs (SG1SG2, SG3SG4, SG5SG6, and SG7SG8). Under cyclic stress conditions, the differential displacement increases from the top of the sample towards the internal corner at the center of the fault. Figure 7.29 illustrates the differential displacement at the peak of each cycle at the locations of the SG pairs (SG1SG2, SG3SG4, and SG5SG6). A progressive increase in differential displacement (compaction) from the top to the center of the fault was observed during each cycle. Furthermore, it was noted that the differential displacement increases

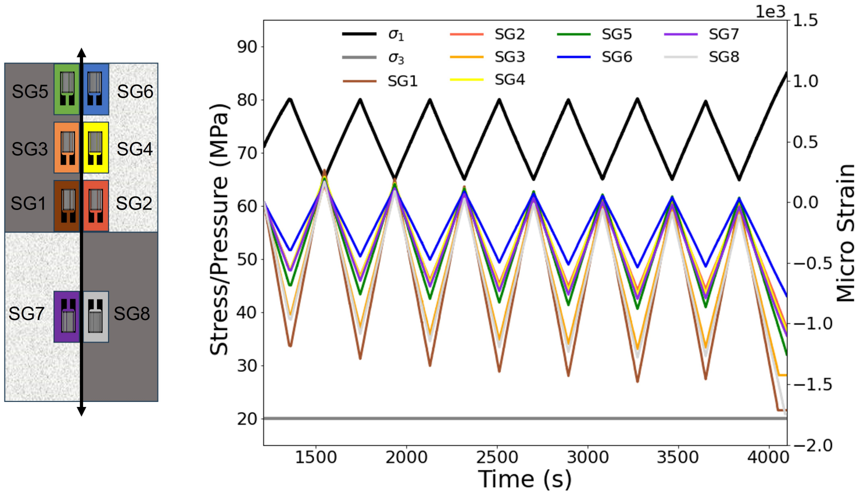

Figure 7.27: Measurements of the SGs under applying the cyclic axial stress.

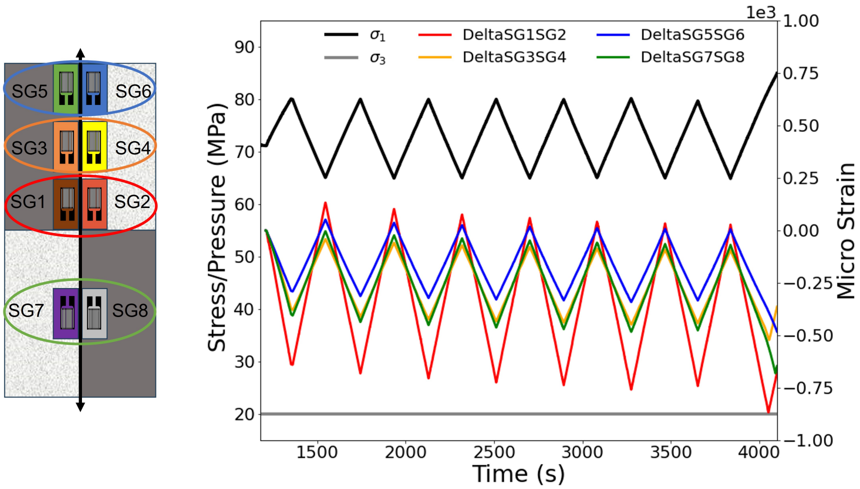

Figure 7.28: The differential compaction between SG pairs under cyclic conditions(SG1SG2, SG3SG4, SG5SG6, and SG7SG8).

with an increasing number of cycles. The most notable increase occurs from the first to the second cycle. As the number of cycles nears seven, the trend of increasing differential displacement starts to weaken. This escalation in differential displacement could be attributed to changes in inelastic deformation. Figure 7.30 demonstrates inelastic deformation induced by an increasing number of cycles. The blue arrow in Figure 7.30 indicates that upon returning the stress to the end of a cycle's waveform (65 MPa), the deformation recorded by SG1 and SG2 does not fully recover, resulting in a level different from that at the start of cycle one (point A).

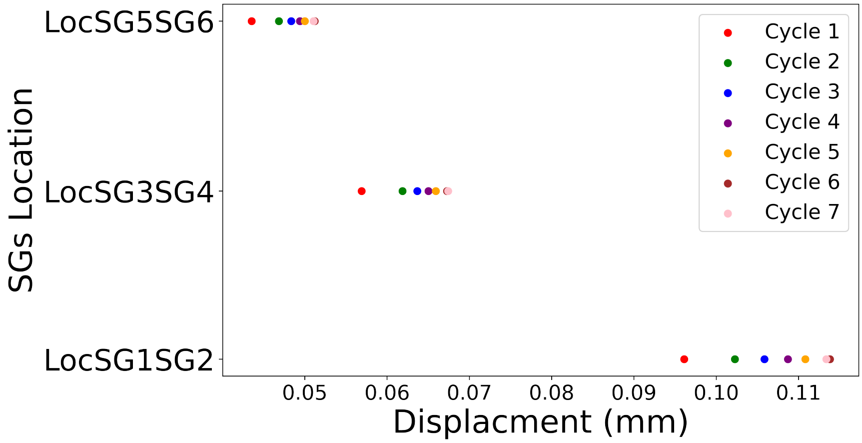

Figure 7.29: Illustration of the differential displacement at the peak of each cycle (maximum stress waveform amplitude) observed at the locations of the SG pairs (SG1SG2, SG3SG4, and SG5SG6).

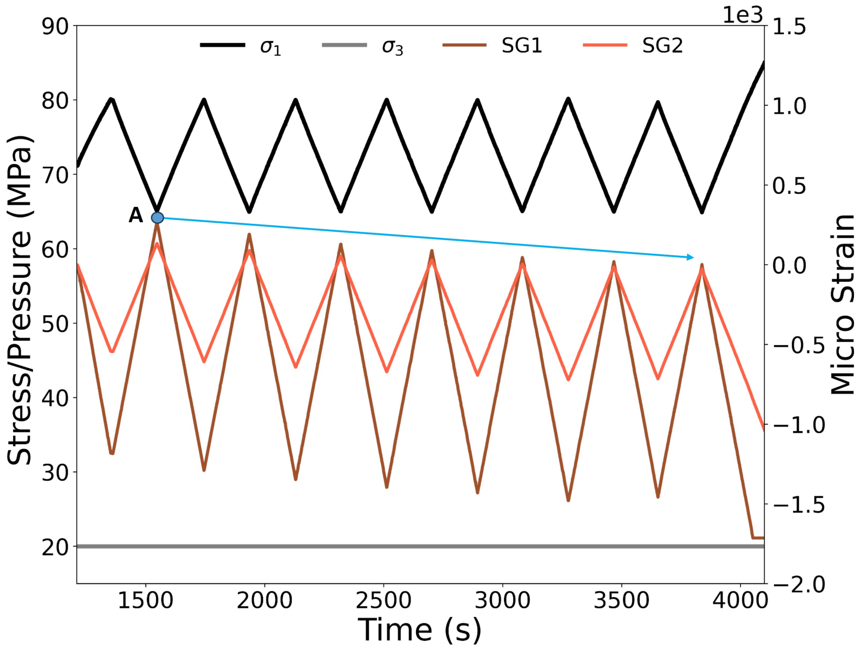

Figure 7.30: Change in deformation recorded by SG1 and SG2 under cyclic stress conditions.

The results obtained from HQ samples indicate matrix deformation and slip along the displaced fault system. However, for a precise investigation and estimation of the pure slip magnitude along the fault, two crucial steps are necessary:

1. Calculation of Absolute Deformation:

It is essential to initially calculate the other component of deformation (elastic and inelastic) using elastic properties and compare it with the total axial shortening of the sample. This step is critical for estimating the shear slip on the fault accurately (Due to time limitations, it was not feasible to perform other experiments).

2. Numerical Simulation:
   A numerical simulation of the current HQ sample is imperative. This simulation will facilitate an understanding of the exact stress distribution and deformation map on the sample, enabling a comprehensive comparison with experimental results.

By undertaking these steps, a thorough understanding of fault slip can be achieved, integrating experimental data with numerical simulations for a more precise and reliable analysis.

7.6. CONCLUSION

We conducted the first triaxial experiment on a large-scale cubic sample containing a normally displaced fault. Subsequently, we performed triaxial experiments on small-scale cylindrical samples, each containing a vertically completely displaced fault (so called Harlequin samples). The results demonstrate that:

1. A technically advanced large-scale experiment featuring injection/depletion operations was technically successfully conducted.
2. Inelastic deformation was induced even with a small amount of differential stress, in both recursive and progressive cycles on large-scale sample. A total of 0.6 mm inelastic deformation occurred, accounting for approximately 29% of the total deformation.
3. The gradient of deformation and the total amount of deformation in the HQ test as recorded by Strain Gauges (SGs) in the same row (composed of the same material) increase from the top to the center, as they approach the central corner.
4. Differential compaction in the HQ test intensifies from the top of the sample towards the internal corner at the center of the fault. This signifies a variation in the stress field surrounding the fault plane.
5. Our direct strain measurements near the displaced fault plane in the HQ test corroborate the anomalies and peaks in stress observed in previous numerical and analytical studies.

Bibliography

Buijze, L., Van den Bogert, P. A. J., Wassing, B. B. T., & Orlic, B. (2019). Nucleation and arrest of dynamic rupture induced by reservoir depletion. *Journal of Geophysical Research: Solid Earth*, *124*(4), 3620–3645.

Buijze, L., van den Bogert, P., Wassing, B. B. T., Orlic, B., & ten Veen, J. H. (2017). Faulting mechanisms and dynamic rupture modeling of depletion induced seismic events in a Rotliegend reservoir. *Netherlands Journal of Geosciences/Geologie en Mijnbouw, this issue*.

Haug, C., Nüchter, J.-A., & Henk, A. (2018). Assessment of geological factors potentially affecting production-induced seismicity in North German gas fields. *Geomechanics for Energy and the Environment*, *16*, 15–31. https://doi.org/https://doi.org/10.1016/j.gete.2018.04.002

Hernandez, E., Naderloo, M., Kumar, K. R., Hajibeygi, H., & Barnhoorn, A. (2022). Modeling of Cyclic Deformation of Sandstones Based on Experimental Observations. *EAGE GET 2022*, *2022*(1), 1–5.

Hettema, M. H. H., Schutjens, P., Verboom, B. J. M., & Gussinklo, H. J. (2000). Production-induced compaction of a sandstone reservoir: the strong influence of stress path. *SPE Reservoir Evaluation Engineering*, *3*(04), 342–347.

Hoek, E. (1990). Estimating Mohr-Coulomb friction and cohesion values from the Hoek-Brown failure criterion. *International Journal of Rock Mechanics and Mining Sciences Geomechanics Abstracts*, *27*(3), 227–229.

Huang, J., Hamon, F., Gazzola, T., Gross, H., Cusini, M., Settgast, R. R., & White, J. A. (2023). Fully Coupled Near-Wellbore Multiphase Poromechanics Simulation for CO2 Storage. *ARMA US Rock Mechanics/Geomechanics Symposium*, ARMA–2023.

Jaeger, J. C., Cook, N. G. W., & Zimmerman, R. (2009). *Fundamentals of rock mechanics*. John Wiley Sons.

Jansen & Meulenbroek, B. (2022). Induced aseismic slip and the onset of seismicity in displaced faults. *Netherlands Journal of Geosciences*, *101*, e13.

Jansen, Singhal, P., & Vossepoel, F. C. (2019). Insights From Closed-Form Expressions for Injection- and Production-Induced Stresses in Displaced Faults. https://doi.org/10.1029/2019JB017932

Kisslinger, C. (1976). A review of theories of mechanisms of induced seismicity. *Engineering Geology*, *10*(2-4), 85–98.

Lehner, F. (2019). An analysis of depletion-induced fault stressing-new closedform analytical solutions. *Assen: Nederlandse Aardolie Maatschappij BV*.

Mulders, F. M. M. (2003). Modelling of stress development and fault slip in and around a producing gas reservoir.

Muntendam-Bos, A., & De Waal, J. (2013). Reassessment of the probability of higher magnitude earthquakes in the groningen gas field. *KNMI confidential final report dd*, 16–01.

Muntendam-Bos, A. G., Hoedeman, G., Polychronopoulou, K., Draganov, D., Weemstra, C., van der Zee, W., Bakker, R. R., & Roest, H. (2022). An overview of induced seismicity in the Netherlands. *Netherlands Journal of Geosciences*, *101*.

Naderloo, M., Veltmeijer, A., Jansen, J. D., & Barnhoorn, A. (2023). Laboratory study on the effect of stress cycling pattern and rate on seismicity evolution. *Geomechanics and Geophysics for Geo-Energy and Geo-Resources*, *9*(1), 137. https://doi.org/10.1007/s40948-023-00678-1

Naderloo, M., Kumar, K. R., Hernandez, E., Hajibeygi, H., & Barnhoorn, A. (2023). Experimental and numerical investigation of sandstone deformation under cycling loading relevant for underground energy storage. *Journal of Energy Storage*, *64*, 107198.

Orlic, B., & Wassing, B. B. T. (2013). A study of stress change and fault slip in producing gas reservoirs overlain by elastic and viscoelastic caprocks. *Rock mechanics and rock engineering*, *46*(3), 421–435.

Rathnaweera, T. D., Wu, W., Ji, Y., & Gamage, R. P. (2020). Understanding injection-induced seismicity in enhanced geothermal systems: From the coupled thermo-hydro-mechanical-chemical process to anthropogenic earthquake prediction. *Earth-Science Reviews*, *205*, 103182.

Roest, J. P. A., & Kuilman, W. (1994). Geomechanical analysis of small earthquakes at the Eleveld gas reservoir. *SPE/ISRM Rock Mechanics in Petroleum Engineering*, SPE–28097.

Segall, P. (1985). Stress and subsidence resulting from subsurface fluid withdrawal in the epicentral region of the 1983 Coalinga earthquake. *Journal of Geophysical Research: Solid Earth*, *90*(B8), 6801–6816.

Segall, P. (1989). Earthquakes triggered by fluid extraction. *Geology*, *17*(10), 942–946.

Segall, P., & Fitzgerald, S. D. (1998). A note on induced stress changes in hydrocarbon and geothermal reservoirs. *Tectonophysics*, *289*(1-3), 117–128.

Van der Voort, N., & Vanclay, F. (2015). Social impacts of earthquakes caused by gas extraction in the Province of Groningen, The Netherlands. *Environmental Impact Assessment Review*, *50*, 1–15.

van Wees, J.-D., Osinga, S., Van Thienen-Visser, K., & Fokker, P. A. (2018). Reservoir creep and induced seismicity: inferences from geomechanical modeling of gas depletion in the Groningen field. *Geophysical Journal International*, *212*(3), 1487–1497.

Yerkes, R. F., & Castle, R. O. (1976). Seismicity and faulting attributable to fluid extraction. *Engineering Geology*, *10*(2-4), 151–167.

8

Conclusion and Implication

8.1. Conclusion

This experimental study aims to explore the impact of parameters related to injection and depletion, such as pattern (monotonic, cyclic) and rate, on the deformation of intact reservoir rock, slip behavior in the faulted reservoir rock, and the evolution of microseismicity with the main focus on how we can mitigate induced seismicity. Also, we investigate the fault slip nucleation in a displaced fault setting. The findings from this research could apply to natural settings or other geo-reservoirs with comparable features, such as those used for geothermal energy extraction, Natural gas, H_2, CO_2 injection and/or production , and wastewater storage, given specific conditions. Five main questions were addressed in this research:

1. How do different stress patterns and rates affect the seismicity and mechanical evolution of intact reservoir sandstone? Can varying stress rates and patterns reduce seismicity?

2. How does cyclic stress with different amplitudes and frequencies influence the deformation of intact reservoir rock?

3. How does stress pattern affect fault slip and microseismic evolution?

4. How do different injection rates and patterns affect injection-induced seismicity in a faulted porous media?

5. What is the mechanism of fault slip in a displaced fault system?

The next section of the conclusion will briefly describe the main conclusions derived from the five central questions of the study.

8.1.1. EFFECT OF STRESS CYCLING PATTERN AND RATE ON SEISMICITY EVOLUTION

In our study on highly porous Red Felser sandstone, we explored the impact of varying stress patterns and rates on seismicity and failure through uniaxial compression tests. Our key findings reveal that cyclic stress patterns, particularly cyclic progressive patterns, tend to induce a high number of Acoustic Emission (AE) events and higher b-values, suggesting a larger number of smaller events than larger ones. The stress rate significantly influences the maximum AE energy and the ultimate strength of the samples; lower stress rates lead to reductions in both metrics and induce intense disintegration and powdering of the rock sample. Furthermore, the stress rate markedly affects the distribution of events in the average frequency versus rise angle (AF-RA) space, with low-rate events clustering in high AF zones and higher-rate events dispersing towards areas with low AF and high RA.

8.1.2. SANDSTONE DEFORMATION UNDER CYCLIC LOADING

We conducted an extensive experimental and modelling analysis on Red Felser sandstone subjected to various cyclic loading conditions, including different frequencies, amplitudes, and stress regimes. Our major conclusions highlight that inelastic deformations occur above and below the brittle yield point, with a decrease in inelastic strain per cycle as the number of cycles increases. The cyclic inelastic deformations are significantly influenced by the mean stress, amplitude, and frequency of the stress waveform, with higher mean stress or amplitude increasing total inelastic strains and lower frequency leading to greater total inelastic strain. A strong correlation exists between the cumulative number of acoustic emissions and cumulative inelastic strain. Based on the governing physics, the proposed constitutive model showed excellent agreement with the experimental data, underscoring the importance of rock viscosity, especially under varying cyclic loading frequencies. The cyclic Modified Cam Clay (MCC) model effectively captures the estimation of inelastic deformation.

8.1.3. ACTIVE AND PASSIVE MONITORING OF FAULT REACTIVATION

Passive and active acoustic techniques were utilised to monitor stress-driven fault reactivation during stress cycling. The combination of these methods successfully detected various reactivation phases, with active acoustic techniques identifying early signs of fault slippage slightly earlier and more sensitively than passive acoustic emission. The combination of these techniques promises enhanced accuracy in monitoring fault reactivations.

8.1.4. MICROSEISMICITY EVOLUTION DURING DISPLACEMENT-DRIVEN FAULT REACTIVATION

During displacement-driven fault reactivation experiments on Red Felser sandstone, the impact of stress patterns, including continuous, cyclic, and under-threshold patterns, on seismicity and slip evolution was investigated. The study revealed that cyclic sliding leads to less seismicity than continuous sliding, as evidenced by higher b-values and fewer large Acoustic Emission (AE) events. Interestingly, increasing the number of sliding cycles tends to decrease the number and energy of AE events, though early cycles still pose a risk of large AE events. However, carefully considering cyclic operation parameters, such as maximum amplitude and rock medium type, is essential. Underthreshold sliding effectively prevents seismicity and pure shear slip, yet seismic risks escalate sharply if shear stress exceeds the prior maximum. Furthermore, healing gouge material during cycle unloading phases contributes to shear strengthening and stress accumulation, potentially leading to increased slip velocity.

8.1.5. INJECTION-INDUCED SEISMICITY IN POROUS MEDIA

Triaxial fault reactivation experiments were conducted on saw-cut Red Felser sandstones to examine the impact of varying injection rates and patterns on microseismicity and fault slip. The findings indicate that a high injection rate increases the likelihood of sudden effective normal stress reduction, leading to fault opening and asperity contact disruption. Conversely, a low injection rate allows for gradual stress reduction due to fluid diffusion, characterized by lower maximum slip velocities, reduced total radiated Acoustic Emission (AE) energy, and fewer microseismic events, but with a higher b-value. The cyclic recursive pattern in porous and permeable sandstone led to more frequent and abrupt slow-slip events than monotonic injection. These patterns also influenced the hydraulic energy budget, shear slip, maximum slip velocity, and shear stress drop across multiple cycles. Monotonic injection was more effective in reducing seismicity in highly permeable media than cyclic recursive and stepwise injection patterns.

8.1.6. FAULT REACTIVATION MECHANISM IN DISPLACED FAULTS

Triaxial experiments on a cylindrical sample with vertically completely displaced faults (Harlequin samples) were conducted to investigate the fault nucleation of such a system. Direct measurements with a strain gauge network adjacent to the displaced fault system during the monotonic test revealed that differential compaction intensifies from the top of the sample towards the internal corner at the centre of the fault where different layers are juxtaposed vertically, indicating a variation in the stress field surrounding the fault plane. Furthermore, results from the cyclic test showed that the differential compaction increases with an increasing number of cycles. Our direct measurements near the displaced fault plane confirm/match the anomalies and peaks in stress observed in previous numerical and analytical studies.

8.2. IMPLICATION

8.2.1. RESERVOIR DEFORMATIONS

As mentioned in Chapter 1, many studies indicated that the frequency and amplitude of stress/loading cycles and stress path can strongly affect reservoir rock deformations (Bagde & Petroš, 2005; Fuenkajorn & Phueakphum, 2010; Peng et al., 2020; Taheri et al., 2016). The amplitude and frequency of the cycles can be translated as the amplitude and frequency of the injection/depletion during geo-storage activities. In this study, we conducted experiments within a controlled laboratory setting regarding time (hours scale) and geometry (centimeter scale). Although directly applying these findings to reservoir-scale scenarios is complex, our results provide foundational insights into the processes affecting reservoir rock deformation under various frequencies and amplitude of the cycles. It has been demonstrated that higher amplitudes and lower frequencies in stress/pressure cycles result in greater inelastic deformation of reservoir rock. Consequently, future energy storage projects utilizing lower frequencies (corresponding to slower injection/depletion rates) may experience increased subsidence over the project's lifetime. This is particularly likely when storage operations aim for greater capacity through increased amplitude of the cycles. Furthermore, our results indicate that the initial cycle is predominantly responsible for most of the inelastic deformation and microseismicity, which should be considered in future reservoir projects. Additionally, the cycle amplitude and frequency design should be tailored to the reservoir's specific stress regime and depth. At greater depths, where the brittle yield point is closer to being reached, higher cycle amplitudes may cause more extensive damage to the reservoir.

8.2.2. MITIGATION OF INDUCED SEISMICITY

Various factors are believed to elevate the risk of large-magnitude seismic events (LMEs). These include operational parameters such as the volume, rate, and pressure of injections, along with permeability of the reservoir and geological aspects like in-situ stress, formation depth, and temperature, proximity to significant faults, and their orientation (Hofmann, Zimmermann, Zang, Yoon, et al., 2018; McClure & Horne, 2014; Raleigh et al., 1976; Wilson et al., 2018; Zang et al., 2019). Our findings contribute additional insights for the development and refinement of mitigation strategies. However, it's important to note that these experiments were conducted on a laboratory scale and did not account for the heterogeneities that would be present at a field scale. Reaching a safe break down pressure (avoiding seismicity) or target fluid pressure is crucial for hydraulic fracturing, geothermal energy production, and water waste disposal. (Hofmann, Zimmermann, Zang, & Min, 2018; Ji, Yoon, et al., 2021; Yoon et al., 2014; Zang et al., 2019). Seismicity mitigation can be considered a balance between different parameters, including maximum magnitude, radiated energy, the total number of events, and b-value (magnitude distribution). Prior research on low-permeability rocks has indicated that cyclic injection techniques, as opposed to continuous monotonic injections, can enhance permeability while reducing seismicity (Patel et al., 2017; Yoon et al., 2014; Zang et al., 2013, 2014). At the Pohang Enhanced Geothermal System (EGS) site, a cyclic soft stimulation method was employed to control the magnitude of induced seismic events, successfully keeping them at or below the target magnitude of Mw 2.0. This was a significant improvement compared to the higher magnitudes observed with previous continuous injection approaches (Hofmann, Zimmermann, Zang, Yoon, et al., 2018; Hofmann, Zimmermann, Zang, & Min, 2018). Our experiments on highly porous sandstone yielded similar findings. Utilizing cyclic stress patterns combined with low stress rates could lead to more favorable outcomes in terms of induced seismicity in subsurface injection operations. In particular, cyclic progressive injection emerges as a potential technique in porous media for minimizing seismic activity. This stress pattern, which resembles the approach Niemz et al. (2020) demonstrated in mini-scale experiments under controlled conditions in crystalline rock, has shown potential in reducing induced seismicity.

The seismicity mechanisms differ between intact media, like hydro-fracturing, and faulted media, such as hydro-shearing. While recent studies have indicated that cyclic injection can mitigate seismicity induced by injection, these have primarily been conducted in low-permeable rocks like granite (Ji, Yoon, et al., 2021; Ji, Zhuang, et al., 2021). The effectiveness of cyclic injection in reducing seismic moment release is influenced by various factors related to the injection cycle, including critical injection pressure and frequency. At the reservoir scale, a cyclic injection strategy might lead to less seismic activity. This reduction could be due to the extended time allowed for pore fluid pressure to spread evenly throughout the reservoir, typically resulting in lower pore fluid pressures than those achieved with continuous, monotonic injections. However, the effectiveness of cyclic injection patterns may vary in highly permeable porous rocks. For instance, (Noël et al., 2019) demonstrated that fluid pressure oscillation could promote unstable sliding. Our findings suggest that in highly permeable media, a monotonic injection pattern is more effective in reducing seismicity compared to cyclic recursive and stepwise injection patterns. Therefore, when designing safe injection protocols for subsurface projects like geothermal energy, wastewater injection, and hydrogen storage, it's crucial to consider the hydraulic properties of the target reservoir.

This thesis also explored the fluid injection rate into reservoirs as another critical parameter. Field-scale studies on wastewater injection projects suggest a positive correlation between the rate of fluid injection and the occurrence of induced seismicity (Passelègue et al., 2018; Wang et al., n.d.). Similarly, our laboratory-scale experiments, conducted on highly permeable media, indicate that fault slip is more influenced by the rate of increase in fluid pressure rather than the absolute fluid pressure level. Our results echo these findings, revealing that during high injection rates, the rate of pressure front advancement is a more significant factor than pore pressure magnitude in destabilizing fault slip and initiating slow slip events. Therefore, it is advisable to adopt lower injection rates to minimize the risk of fault destabilization.

8.3. RECOMMENDATIONS AND FUTURE WORK

Our cyclic triaxial rock deformation experiments were conducted at room temperature and under a low confining pressure of 10 MPa. However, in typical geo-reservoirs located at depths of 1 to 2 kilometers, temperatures can range between 60 to 90°C. Studies have shown that higher temperatures can reduce both the short-term (Friedman et al., 1979; Wong, 1982) and long-term (Heap et al., 2009) strength of rocks in the brittle domain. Therefore, it is advisable to conduct such experiments under conditions that mimic reservoir pressure and temperature. Given that geo-storage systems operate under cyclic conditions of injection and depletion, it's also crucial to study the impact of cyclically induced inelastic deformation on permeability changes, and consequently, on the recovery efficiency of energy-rich fluids.

Besides the reservoir's temperature, the temperature of the injected fluid, often lower than that of the reservoir rock, can alter the in-situ thermal conditions, potentially leading to thermal cracking (Fredrich & Wong, 1986; Vilarrasa & Rutqvist, 2017). This aspect is crucial for understanding injection-induced seismicity, particularly in terms of the effects of thermal shocks or temperature variations on fault reactivation. Consequently, it is recommended to conduct experiments that simulate thermal shocks during the reactivation of faults induced by fluid injection.

Our experiments on injection-driven fault reactivation were conducted using a smooth saw-cut surface. Studies have shown that geometric and structural heterogeneities influence earthquake rupture and slip, including fault roughness (Brodsky et al., 2016; Fang & Dunham, 2013). Typically, natural faults in the Earth's crust feature rough wall structures, requiring higher stress levels for rupture propagation than their smoother, flat counterparts (Fang & Dunham, 2013). Therefore, we recommend incorporating the roughness of fault planes in future injection/displacement-driven fault reactivation experiments.

As previously discussed, the drainage conditions of the fault and its surrounding medium can influence the effectiveness of injection patterns in reducing seismicity (Heimisson et al., 2019). Our injection-driven fault reactivation experiments were conducted exclusively on highly permeable Red Felser sandstone. Therefore, it would be valuable to conduct similar experiments on rocks with varying lithologies and hydraulic properties.

As demonstrated in Chapter 4, combining active and passive methods could enhance the detection and monitoring of fault reactivation. Therefore, developing new experiments that leverage the simultaneous combination of both methods would be valuable. Ultimately, this integrated approach could be tested in the field. Moreover, enhancing the quality of the seismicity recording network is suggested to capture smaller events and improve the overall monitoring system.

Bibliography

Bagde, M. N., & Petroš, V. (2005). Waveform effect on fatigue properties of intact sandstone in uniaxial cyclical loading. *Rock mechanics and rock engineering*, *38*, 169–196.

Brodsky, E. E., Kirkpatrick, J. D., & Candela, T. (2016). Constraints from fault roughness on the scale-dependent strength of rocks. *Geology*, *44*(1), 19–22.

Fang, Z., & Dunham, E. M. (2013). Additional shear resistance from fault roughness and stress levels on geometrically complex faults. *Journal of Geophysical Research: Solid Earth*, *118*(7), 3642–3654.

Fredrich, J. T., & Wong, T.-f. (1986). Micromechanics of thermally induced cracking in three crustal rocks. *Journal of Geophysical Research: Solid Earth*, *91*(B12), 12743–12764.

Friedman, M., Handin, J., Higgs, N., & Lantz, J. (1979). *Strength and ductility of four dry igneous rocks at low pressures and temperatures to partial melting* (tech. rep.). Texas A and M Univ., College Station (USA).

Fuenkajorn, K., & Phueakphum, D. (2010). Effects of cyclic loading on mechanical properties of Maha Sarakham salt. *Engineering Geology*, *112*(1-4), 43–52.

Heap, M., Baud, P., Meredith, P., Bell, A., & Main, I. (2009). Time-dependent brittle creep in darley dale sandstone. *Journal of Geophysical Research: Solid Earth*, *114*(B7).

Heimisson, E. R., Dunham, E. M., & Almquist, M. (2019). Poroelastic effects destabilize mildly rate-strengthening friction to generate stable slow slip pulses. *Journal of the Mechanics and Physics of Solids*, *130*, 262–279.

Hofmann, H., Zimmermann, G., Zang, A., Yoon, J. S., Stephansson, O., Kim, K. Y., Zhuang, L., Diaz, M., & Min, K.-B. (2018). Comparison of cyclic and constant fluid injection in granitic rock at different scales. *ARMA US Rock Mechanics/Geomechanics Symposium*, ARMA–2018.

Hofmann, H., Zimmermann, G., Zang, A., & Min, K. B. (2018). Cyclic soft stimulation (CSS): a new fluid injection protocol and traffic light system to mitigate seismic risks of hydraulic stimulation treatments. *Geothermal Energy*. https://doi.org/10.1186/s40517-018-0114-3

Ji, Y., Yoon, J. S., Zang, A., & Wu, W. (2021). Mitigation of injection-induced seismicity on undrained faults in granite using cyclic fluid injection: A laboratory study. *International Journal of Rock Mechanics and Mining Sciences*, *146*, 104881.

Ji, Y., Zhuang, L., Wu, W., Hofmann, H., Zang, A., & Zimmermann, G. (2021). Cyclic Water Injection Potentially Mitigates Seismic Risks by Promoting Slow and Stable Slip of a Natural Fracture in Granite. *Rock Mechanics and Rock Engineering*, 1–17.

McClure, M. W., & Horne, R. N. (2014). Correlations between formation properties and induced seismicity during high pressure injection into granitic rock. *Engineering geology*, *175*, 74–80.

Niemz, P., Cesca, S., Heimann, S., Grigoli, F., Specht, S. V., Hammer, C., Zang, A., & Dahm, T. (2020). Full-waveform-based characterization of acoustic emission activity in a mine-scale experiment : a comparison of conventional and advanced hydraulic fracturing schemes, 189–206. https://doi.org/10.1093/gji/ggaa127

Noël, C., Passelègue, F. X., Giorgetti, C., & Violay, M. (2019). Fault Reactivation During Fluid Pressure Oscillations : Transition From Stable to Unstable Slip Journal of Geophysical Research : Solid Earth, 940–953.

Passelègue, F. X., Brantut, N., & Mitchell, T. M. (2018). Fault Reactivation by Fluid Injection: Controls From Stress State and Injection Rate. *Geophysical Research Letters*, *45*(23), 12, 837–12, 846. https://doi.org/10.1029/2018GL080470

Patel, S. M., Sondergeld, C. H., & Rai, C. S. (2017). Laboratory studies of hydraulic fracturing by cyclic injection. *International Journal of Rock Mechanics and Mining Sciences*, *95*(March), 8–15. https://doi.org/10.1016/j.ijrmms.2017.03.008

Peng, K., Zhou, J., Zou, Q., & Song, X. (2020). Effect of loading frequency on the deformation behaviours of sandstones subjected to cyclic loads and its underlying mechanism. *International Journal of Fatigue*, *131*, 105349.

Raleigh, C. B., Healy, J. H., & Bredehoeft, J. D. (1976). An experiment in earthquake control at Rangely, Colorado. *Science*, *191*(4233), 1230–1237.

Taheri, A., Yfantidis, N., Olivares, C. L., Connelly, B. J., & Bastian, T. J. (2016). Experimental study on degradation of mechanical properties of sandstone under different cyclic loadings. *Geotechnical Testing Journal*, *39*(4), 673–687.

Vilarrasa, V., & Rutqvist, J. (2017). Thermal effects on geologic carbon storage. *Earth-science reviews*, *165*, 245–256.

Wang, L., Kwiatek, G., Rybacki, E., & Bonnelye, A. (n.d.). Laboratory Study on Fluid - Induced Fault Slip Behavior : The Role of Fluid Pressurization Rate Geophysical Research Letters, 1–12. https://doi.org/10.1029/2019GL086627

Wilson, M. P., Worrall, F., Davies, R. J., & Almond, S. (2018). Fracking: How far from faults? *Geomechanics and Geophysics for Geo-Energy and Geo-Resources*, *4*, 193–199.

Wong, T.-F. (1982). Micromechanics of faulting in westerly granite. *International journal of rock mechanics and mining sciences & geomechanics abstracts*, *19*(2), 49–64.

Yoon, J. S., Zang, A., & Stephansson, O. (2014). Numerical investigation on optimized stimulation of intact and naturally fractured deep geothermal reservoirs using hydro-mechanical coupled discrete particles joints model. *Geothermics*, *52*, 165–184.

Zang, A., Oye, V., Jousset, P., Deichmann, N., Gritto, R., McGarr, A., Majer, E., & Bruhn, D. (2014). Analysis of induced seismicity in geothermal reservoirs–An overview. *Geothermics*, *52*, 6–21.

Zang, A., Yoon, J. S., Stephansson, O., & Heidbach, O. (2013). Fatigue hydraulic fracturing by cyclic reservoir treatment enhances permeability and reduces induced seismicity. *Geophysical journal international*, *195*(2), 1282–1287.

Zang, A., Zimmermann, G., Hofmann, H., Stephansson, O., Min, K.-B., & Kim, K. Y. (2019). How to reduce fluid-injection-induced seismicity. *Rock Mechanics and Rock Engineering*, *52*(2), 475–493.

ACKNOWLEDGEMENTS

First and foremost, I would like to express my gratitude to everyone I've had the pleasure of meeting during my PhD journey, whether online or in person. Each interaction has contributed in some way to my growth and development.

I would like to extend a special thanks to my supervisor, **Dr. Auke Barnhoorn**. In addition to providing exceptional supervision, you have helped me become an independent researcher. Your incredible work ethic and dedication have been truly inspiring. I appreciate your concern and effort during the COVID pandemic to ensure we were doing well, both in our research and in our lives outside of it. I still laugh at some of the moments we've shared—like the times I overslept and missed our run, or when I somehow managed to break plates and glasses at your place, among other things. I truly enjoyed working with you and deeply appreciate your guidance and support. I'm happy that we will be working together for two more years.

I want to sincerely thank **Prof. Dr. Ir. Jan Dirk Jansen** for his guidance and supervision. Your constructive feedback has been instrumental in shaping my research, and I am deeply grateful for the support you provided throughout my Ph.D. I appreciate that, despite your busy schedule with deanship duties, you remained highly invested in our DeepNL project. I truly enjoyed our S4S meetings and gained a great deal from them. I'll never forget the moment at the EGU conference when we were sitting together, and you explained the idea of the Harlequin experiment—I'm really happy that I was able to make it work.

Dr. Anne Pluymakers, I am grateful for the collaboration we had and for the knowledge you shared about all the laboratory experiments and analyses. Your kindness, approachability, and willingness to share your expertise have significantly impacted my research. Anne, I will never forget how you supported me in developing one of the key experiments that formed the foundation of much of my Ph.D. research. I truly enjoyed our chats, both during meetings and outside of them.

I would like to thank **Prof. Dr. Hadi Hajibeygi**. I truly enjoyed our collaboration, which led to an amazing outcome. Beyond our work together, I have learned a great deal from you about storytelling, communication skills, and the importance of being patient in pursuing my passions. You definitely helped me uncover some blind spots in my thinking. I'll never forget our interview in Iran, on the University of Tehran campus, where you challenged me with insightful questions. I am now very happy to be working with you as a postdoctoral researcher.

I would like to extend my appreciation to all the faculty members (professors and doctors) in our department—**Evert**, **Denis**, **Deyan**, **Martin**, **Karl-Heinz**, **Femke**, **Sebastian**, **Tobias**, **Phil**, **Giovanni Bertotti**, and all the others with whom I have chatted and met.

Denis, I particularly enjoyed our discussions and the times we shared over coffee and a smoke.

I would like to thank the support staff of the department—**Marlijn**, **Lydia**, **Rinda**, **Ralf**, **Ingrid**, and **Barbara**—who have always greeted me warmly whenever I approached them with various issues.

Many thanks to my lab buddy **Aukje Veltmeijer**. I really enjoyed working with you, and together we made an amazing team. I'm proud of what we built in the lab throughout all phases of the project. Not just me, but I'm sure everyone in the office will miss how you kept track of who showed up when.

My special thanks to the technicians in the lab. **Marc**, I want to start by saying that this world needs more amazing people like you. Thank you for all the smart experimental setups and the additional support. I consider you like a brother. I should also mention that I owe part of my Dutch language skills to you, even though most of those words can't be repeated here. **Jens**, thank you for all the brainstorming sessions and ideas. I know I often bothered you with small questions. Marc and Jens, you two make a magical combination that brings happiness to everyone's research, and the atmosphere you create is incredible. **Karel**, thank you for designing the acoustic setups and for solving all the problems I faced with the AE device. I truly enjoyed the discussions we had together. Also, special thanks to the other technicians, **Michiel**, **Roland**, **Wim Joost**, **Ellen**, and **Jelle**.

My DeepNL officemates, I am really happy to have shared my PhD journey with all of you—**Jingming**, **Aleks**, **Hamed**, **Aukje**, **Faezeh**, **Sara**, **Samantha**, and **Iban**. Each of you helped me in different ways, and I truly appreciate it. **Jingming**, I'm glad I could turn you into a gym buddy, and I enjoyed our evening chats over my so-called first dinners. **Hamed**, my brother, I really enjoyed our conversations, all the plans for drinks, and parties. I can definitely give you the best friend title—from Cartagena, Colombia. I must confess that I will miss the discussions between **Hamed** and **Aleks**. **Aleks**, it was an amazing experience working closely with you during the last phase of my PhD, and I am very happy with how we helped each other. **Faezeh**, thanks for the Persian chat times. **Samantha**, thanks for promoting left-wing sports like cycling.

Kishan, it was amazing working with you, and I learned a lot from you since you are the most efficient PhD student to ever step foot in TU Delft. Please take that personally! Our collaboration with **Edgar Hernandez**, a very dedicated master's student and a good friend of mine, was also a great experience. Thank you, **Edgar**, for your amazing work.

A special thanks to the DeepNL community—all the PhDs, postdocs, and supervisors, and especially to the coordinators of the project, **Niels van den Berg**, **Ajita Ramautar**, and **Cindy Remijnse-Schrader**.

Being part of the Applied Geophysics section gave me the chance to hang out and spend time with amazing people, and I want to name each of you and thank you all. **David** (you should have moved to our office way earlier), **Eddy** (you know what we say when we see each other), **Ilshat**, **Mohammad** (I truly enjoyed our coffee chats), **Billy**, **Amin**, **Azin**, **Elahe**, **Sverre**, **Shihao**, **Sepideh**, **Camille**, **Menno**, **Mahmoud** (we should keep eat-

ing protein, brother), **Maria** (happy to hang out with you and **Rigo**), **Naomi**, **Mosab**, **Joeri** (come back to reality and stop the video games), **Johno**, **Andrea**, and **Jasper**.

Even though I was in the Geophysics section, I always felt close to the Reservoir Engineering group at heart. Thanks to the amazing people in the Reservoir section: **Kishan**, **Mohsen**, **George**, **Sajjad**, **Kiarash**, **Willemijn**, **Gabriel**, **Carolin**, **Michiel** (I really enjoyed our chats, and now I know you were a DJ before starting your PhD), **Herminio**, **Sian** (thank you so much for all your help in the lab), **Lifei**, **Mahnaz**, and **Thejas**.

I want to give my big thanks to others from our lab group. **Debanjan**, even as I write this, I'm laughing. I can never have a discussion with you without laughing, and you're an amazing and knowledgeable friend, brother. **Kai**, my gallery is full of your pictures, and my mind is still occupied with your sudden statement, 'water is good.' **Entela**, I still regret teaching you some Persian, but I'm happy that we are collaborating. I truly enjoy our chats and party time. Also, a big thanks to **Evgeniia**, **Chris**, and **Parvin**; I enjoyed my time with them in the lab and during meetings. And thanks to my lab friend, **Martijn Jansen**, with whom I shared many great times.

My PhD journey was more enjoyable thanks to getting to know people through MV events and SPE TU Delft. I want to thank all the board members of MV and also the board members of SPE: **William**, **Gertjan**, **Juliette**, **Esther**, **Bengt**, **Ghada**, **Rosita**, **Annique**, and **Wildan**. I also want to thank some other friends: **John**, **Luis**, **Brend**, and **Daan**.

I think it's time to thank my dear Iranian friends. **Aydin**, I truly enjoy hanging out with you and making all the going out plans with you—you are indeed my brother. Also, thanks for being the caring person (the goalkeeper) of our friendship group. **Fardad**, it has been great to build a friendship with you, brother—I think by now you've figured out what to do with egg yolks! **Faezeh**, I'll never forget the first time we met at the Persian BBQ event, and since then, I've really enjoyed spending time with you. **Siamak**, it's been an honor getting to know you, and I've enjoyed how we gave Aydin a hard time together. **Ali Kahatami**, I'm glad you're my gym buddy; I've really enjoyed our time together, both inside and outside the gym. **Ali Golchin**, thank you for helping me at the start of my PhD—even before knowing me well, you were there to support me. Also, thanks to my other Iranian friends: **Behnaz**, **Tina**, **Mahtab**, **Mohammad**, **Saman**, **Aliakbar**, **Saeid**, **Amin**, **Moein**, **Amin**, **Pejman**, **Saba**, **Behrad**, **Iman**, **Amir**, **Sanaz**, **Leila**, and **Ehsan**.

My special thanks to my friends **Alessandro** (I still think your region has the best wine from Italy), **Francesca**, **Emilio**, and **Nazife**. I am so grateful to have you as my friends, and my happiest times are spent with you.

My life gains meaning through the gym, and I want to thank all the gym friends at the X Center, TU Delft: **Arture**, **Daniel**, **Dennis**, **Nicky**, **Hirash**, **Kimberly**, **Djordi**, **Nuno**, and **Sander**. **Arture**, I truly enjoy hanging out, partying, and training with you—you really are like a brother to me.

I couldn't have reached this stage of my life without my dear friends from my bachelor and master: **Hafez**, **Saeid**, **Mehdi**, **Mohsen**, **Salar**, **Farid**, **Alibaba**, and **Hossein**. I think I could write a book about you guys—let's just say you are my family. I am grateful that even though we are all spread across different corners of this Earth, we still talk daily and uplift each other.

I want to thank the family of my girlfriend, who have truly made this country feel like home for me. **Wim**, **Daphne**, and **Junior**, you are amazing, and I'm grateful to have you all in my life. **Wim**, you might have to admit that I'm getting some desirable results in the gym!

Last but not least, I'm thinking about my family back home. **Zahra (Maman)**, I know I don't often express my feelings, and I can never fully convey how much you've sacrificed for me and supported me through every step of my life. **Ahmad (Baba)**, though you are no longer with us, I hope I have made you happy and proud. Thank you for everything you gave me. **Mahdi (brother)**, thank you for being such an amazing and caring brother. But I must say, my biceps are definitely bigger than yours. **Mahdieh (sister)**, thank you (and **Ali**) for all your support and kindness. I'm grateful to have you and your two adorable little kids in my life.

Lastly and most importantly, my girlfriend **Francis**. **Francis**, my love and gratitude go to you. You have definitely made me a better person. Through every challenge and triumph, you have been my confidante and greatest supporter. I can't imagine completing my PhD journey without you. I look forward to continuing the rest of our journey together.

Once again, I would like to express my gratitude to all of the above individuals for their contributions to my Ph.D. journey. I could not have achieved this milestone without your support and encouragement.

Curriculum Vitæ

Milad Naderloo

11-11-1991 Born in Abhar, Zanjan, Iran.

Education

Sep 2010 - Sep 2014	**B.Sc. in Mining Engineering** University of Tehran, Tehran, Iran
Sep 2014 - Sep 2017	**M.Sc. in Rock Mechanics** University of Tehran, Tehran, Iran
Sep 2019 - May 2024	**Ph.D. in Geomechanics and Petrophysics** Delft University of Technology, Delft, The Netherlands Thesis: Fault reactivation and rock deformation mechanism under stress/pressure cycling Promoter: Dr. A. Barnhoorn Promoter: Prof. dr. J. D. Jansen

Awards

2023 MDPI Energies Student Poster Award, InterPore conference

2014 Honor Student Award, Supporter Foundation of the University of Tehran (SFUT)

Work Experience

Sep 2017 - May 2019 **Designer and Rock Mechanics Engineer**
Kan Azin Consulting Engineering Company, Tehran, Iran

Jun 2016 - Sep 2016 **Intern Researcher**
Technical University of Clausthal, Clausthal, Germany
Conducted numerical investigation of slope stability in open-pit mines.

Feb 2016 - May 2016 **Teaching Assistant**
University of Tehran, Tehran, Iran
Principal assistant for the rock mechanics course.

LIST OF PUBLICATIONS

JOURNALS

8. **M. Naderloo**, A. Veltmeijer, A. Pluymakers, J.D. Jansen, A. Barnhoorn, *Microseismicity evolution during displacement-driven fault reactivation in the laboratory: The role of stress pattern*, under preparation.

7. **M. Naderloo**, A. Veltmeijer, A. Pluymakers, J.D. Jansen, A. Barnhoorn, *The Effect of Pressurization Rate and Pattern on Injection-induced Seismicity in Porous Media: An Experimental Study*, Journal of Geophysical Research: Solid Earth, under review.

6. Heimisson, E., **Naderloo, M**, Chandra, D, & Barnhoorn, A., *Applying and Validating Coulomb Rate-and-State Seismicity Models in Acoustic Emission Experiments*, Tectonophysics, under review.

5. **M. Naderloo**, A. Veltmeijer, J.D. Jansen, A. Barnhoorn, *Laboratory study on the effect of stress cycling pattern and rate on seismicity evolution*, Geomechanics and Geophysics for Geo-Energy and Geo-Resources **9.1**, 137 (2023).

4. **M. Naderloo**, K.R. Kumar, E. Hernandez, H. Hajibeygi, A. Barnhoorn, *Experimental and numerical investigation of sandstone deformation under cycling loading relevant for underground energy storage*, Journal of Energy Storage **64**, 107198 (2023).

3. Veltmeijer, A., **Naderloo, M**, & Barnhoorn, A.,*Forecasting of Rock Failure in the Laboratory using Active Acoustic Monitoring Methods*, Geomechanics and Geophysics for Geo-Energy and Geo-Resources **10**, 93 (2024).

2. F. Shirmohammadi, D. Draganov, A. Veltmeijer, **M. Naderloo**, A. Barnhoorn, *Feasibility of reservoir monitoring in the Groningen gas field using ghost reflections from seismic interferometry*, Geophysical Journal International **2**, 237 (2024).

1. Veltmeijer, A., **Naderloo, M**, Pluymakers, A., & Barnhoorn, A., *Monitoring and Forecasting Injection Induced Fault Reactivation and Seismicity in the Laboratory using Active Ultrasonic Methods*, Journal of Geophysical Research: Solid Earth **2**, 129 (2024)..

CONFERENCES

11. **Naderloo, M**, Barnhoorn, A., Veltmeijer, A., & Jansen, J. D. (2021, April). *Laboratory study on seismicity mitigation: The role of loading pattern and rate.* In EGU General Assembly Conference Abstracts (pp. EGU21-13656).

10. Veltmeijer, A., **Naderloo, M**, & Barnhoorn, A. (2021, March). *Monitoring and forecasting failure in laboratory using coda wave decorrelation.* In EAGE GeoTech 2021 First EAGE Workshop on Induced Seismicity (Vol. 2021, No. 1, pp. 1-6). European Association of Geoscientists & Engineers.

9. **Naderloo, M**, Veltmeijer, A., & Barnhoorn, A. (2022, May). *Fault reactivation process in the laboratory: The role of stress cycling and pressurization rate.* In EGU General Assembly Conference Abstracts (pp. EGU22-4177).

8. Veltmeijer, A., **Naderloo, M**, & Barnhoorn, A. (2022, May). *Acoustic Precursors to Laboratory Induced Fault Slip and Failure.* In EGU General Assembly Conference Abstracts (pp. EGU22-4117).

7. Pluymakers, A., Veltmeijer, A., **Naderloo, M**, Kortram, J. D., & Barnhoorn, A. (2022, May). *Hydro-mechano-chemical coupling in rock failure.* In EGU General Assembly Conference Abstracts (pp. EGU22-7156).

6. **Naderloo, M**, Veltmeijer, A., Pluymakers, A., & Barnhoorn, A. (2022, June). *Experimental Investigation of the Effect of Stress Cycling on Seismicity Evolution During Fault Reactivation Process.* In 83rd EAGE Annual Conference & Exhibition (Vol. 2022, No. 1, pp. 1-5). European Association of Geoscientists & Engineers.

5. **Naderloo, M**, Veltmeijer, A., & Barnhoorn, A. (2022, November). *Active and passive monitoring of fault reactivation under stress cycling.* In SEG International Exposition and Annual Meeting (p. D011S083R002). SEG.

4. Veltmeijer, A., **Naderloo, M**, & Barnhoorn, A. (2023). *Seismic monitoring of laboratory fault reactivation by pore fluid injection* (No. EGU23-7596). Copernicus Meetings.

3. Veltmeijer, A., **Naderloo, M**, & Barnhoorn, A. (2023, June). *Active and Passive Seismic Monitoring of Laboratory-Based Injection-Driven Fault Reactivation.* In 84th EAGE Annual Conference & Exhibition (Vol. 2023, No. 1, pp. 1-5). European Association of Geoscientists & Engineers.

2. Shirmohammadi, F., Draganov, D., Veltmeijer, A., **Naderloo, M**, & Barnhoorn, A. (2023, June). *Monitoring pore-pressure depletion in the Groningen reservoir using ghost reflections from seismic interferometry.* In 84th EAGE Annual Conference & Exhibition Workshop Programme (Vol. 2023, No. 1, pp. 1-5). European Association of Geoscientists & Engineers.

1. Hernandez, E., **Naderloo, M**, Kumar, K. R., Hajibeygi, H., & Barnhoorn, A. (2022, November). *Modeling of cyclic deformation of sandstones based on experimental observations.* In EAGE GET 2022 (Vol. 2022, No. 1, pp. 1-5.